CHEMICAL AND PHYSICAL MECHANISMS OF SOOT FORMATION

BY

JULIAN THOMAS MCKINNON, Jr.

B.S. Chemical Engineering
Cornell University
(1979)

Submitted to the Department of Chemical Engineering
in partial fulfillment of the requirements for
the degree of

DOCTOR OF PHILOSOPHY

at the

MASSACHUSETTS INSTITUTE OF TECHNOLOGY

May 1989

Signature of author
Department of Chemical Engineering
May 2, 1989

Certified by
Jack B. Howard
Thesis Supervisor

Accepted by
William C. Deen, Chair
Departmental Committee for Graduate Students

Chemical and Physical Mechanisms of Soot Formation

by

Julian Thomas McKinnon, Jr.

Submitted to the Department of Chemical Engineering on May 2, 1989 in partial fulfillment of the requirements for the degree of Doctor of Philosophy in Chemical Engineering.

ABSTRACT

An experimental and modeling study has been carried out to understand the mechanisms of the nucleation and growth of soot in flames. A low pressure, premixed, flat benzene/oxygen/argon flame was studied. Conditions ranged from pressures of 20 to 40 torr, equivalence ratios from 2.0 to 2.5 (the critical sooting equivalence ratio for benzene/oxygen is 1.9), and argon dilutions from no argon to 45% dilution.

Probe sampling and optical measurements were made on the system. Samples of polycyclic aromatic hydrocarbons (PAH), a key intermediate in soot nucleation, were withdrawn from the flame with cooled quartz probes as a function of height above the burner (time in the reaction zone). Analysis of the PAH samples was done with gas chromatography, UV-visible spectrometry, and gravimetric methods. Coarse size separations were made with gravity column chromatography. Light gases, from hydrogen to benzene, were measured with an uncooled sampling probe coupled to an on-line mass spectrometer. Temperature was measured pyrometrically. Soot diameter, number density, and volume fraction were measured with optical scattering absorption methods. Scattering was done at 488 nm and absorption measurements were made at six wavelengths from 410 nm to 1.4 μm. The longest wavelength was used in the soot particulate analysis. The shorter absorption wavelengths were used for qualitative PAH profile measurements.

The data and published literature allowed the identification of four main mechanisms operative in soot formation. 1) Mass growth of PAH and soot through the addition of C_2H_2. 2) Oxidation of PAH and soot by OH and O_2. 3) Coagulation of PAH to form soot nuclei. 4) Pyrolytic decay of the PAH. Mass growth through C_2H_2 and oxidation have been identified previously in the literature. This work provides the first quantitative support for the concept of soot nucleation through coagulation. The destruction of PAH through a highly activated ($\approx$ 75 kcal/mol) unimolecular process has never before been identified, but yet is crucial for describing the dynamics of soot nucleation in a benzene flame.

A numerical model has been developed which incorporates the four mechanisms above. Inputs to the model are temperature, profiles of stable gas species and free radicals. The model was tested using data from three different flame conditions, from nearly sooting to heavily sooting. Rate parameters for the four mechanisms were fit to the data. It was found that most of the fitted rates were quite close to prototype reactions from the literature. The rate parameters should be fairly universal in nature to allow application of these concepts to different combustion geometries.

Thesis Supervisor:

Dr. Jack B. Howard, Professor of Chemical Engineering

Acknowledgements

As with any work of this kind, many people in an out of MIT provided help, without which, the project would never have been completed. First I would like to thank my advisor, Professor Jack B. Howard, for his foresight in seeing the importance of the work at times when I was buried in thoughts of milling machine cutting speeds and price lists of optical devices. He has allowed me near total freedom in pursuing avenues which I thought were interesting, yet his subtle redirection kept me on a path which led ultimately (if not in a timely fashion) to a valuable product. Professor John P. Longwell deserves much credit for keeping an active interest in the work and providing a different perspective from that of my advisor.

Interaction with the other students is the most productive learning aspect of a place such as MIT. I was fortunate to belong to a very active combustion research group. Our regular seminar meetings, known as 10.731 in MIT jargon, were an extremely fertile ground for discussions on combustion chemistry. I would like to thank the members of that group, Phil Westmoreland, Fred Lam, Craig Vaughn, Rich Shandross, Sam Amponsah, John Pope, Chris Pope, Bob Barat, Carl Wikstrom, and Joe Marr, for their help. Fred Lam and Craig Vaughn deserve note for their assistance in some of the chromatographic methods. Bob Barat, although we had our disagreements, was of great help in some of the optical measurements. Chris Pope provided me with the Bittner data set in machine readable format. Without this, much of the analysis of the Bittner data could not have been done. Although he was not in our seminar group, Tom Griffin deserves many thanks for technical discussions and humorous diversions (and foil technology).

Jim Bittner has to be credited with assembling what has to be the worlds best data set on species concentrations, fluxes, and rates in a rich flame. The data allowed me to test many of the concepts which I use in the analysis of my data. Houston Miller of the George Washington University Chemistry Department and Steve Harris of the Physical Chemistry Department of General Motors helped me with some of the concepts of soot dynamics. Both of them also helped with the development of the mass spectrometric procedures. Steve Harris generously lent me an S-1 infrared photomultiplier tube which I used in absorption experiments.

Peter Dandrige of Atomic Limited helped in the design of the low pressure combustion chamber and did the fabrication for a very reasonable price. Mario DiSilva, a machinist in the Chemical Engineering Department, did many difficult jobs for me very professionally and quickly. I regret that MIT did not have the foresight to keep him here. Tony Modestino lent me several pieces of equipment, without which many of the optical measurements could not have been made. If my acquisitive ways strained his sense of humor, I apologize.

I had assistance from several undergraduates through MIT's UROP program, two of whom deserve special note. Jeanette Burmester worked with me for over a year on a wide variety of projects. She constructed several pieces of equipment and ran many of the GC samples. Ellee Meyer worked on quantifying the visible PAH absorption by determining an effective ensemble absorption cross-section for the PAH as well as did infrared analysis of the PAH samples.

My wife, Jenny Devaud, is the one individual who deserves the greatest thanks of all. Her love and support kept me going through the lean times and her nudging and prodding kept me from extending my residency to sometime into the next millennium. I'm sorry to have kept her waiting over two years after she completed her Ph.D.[1] Sometimes the cards don't always fall the way we like. My children, Daniel and Karen, forced me to keep a reference point in the "real world". My parents deserve thanks for getting the whole process started. They financially supported me through my undergraduate education and emotionally supported me in graduate school.

I would like to thank the National Science Foundation for providing a fellowship for my first three years at MIT through the NSF Graduate Fellowship Program. We are grateful to the Division of Chemical Sciences, Office of Basic Energy Research, Office of Energy Research, U.S. Department of Energy for financial support under Grant No. DE-FG02-84ER13282 for providing project support.

---

[1] I can't help but reflect on the irony of spending nearly seven years to understand a process which a flame manages to figure out in milliseconds.

Table of Contents

List of Figures

Chapter One

Introduction

The formation of soot accompanies many practical combustion processes, often with undesirable consequences. The most familiar are the visible soot emissions from diesel engines and industrial smokestacks. Less obvious are the adverse health effects associated with soot. Soot formation limits the operation of some practical systems. For example, excessive quantities of soot in gas turbines can cause erosion of the turbine blades (Howard and Kausch, 1980). In addition, the emission of soot usually represents some loss of efficiency in the operation of a device since some of the fuel is escaping in a non-oxidized form. On the positive side, soot is responsible for the yellow luminosity from flames due to its black-body emission. It is this bread-band emission, and the associated enhanced radiant heat transfer, that makes soot a useful material in industrial furnaces, provided that burnout of the soot occurs before it exits the stack.

Soot is a carbonaceous solid material formed in flame and pyrolysis conditions. Soots produced in widely different combustion conditions show great chemical and structural similarity, indicating a strong likelihood that similar mechanisms are operative. The H:C ratio of soot decreases as the soot ages in the flame. Newly formed soot has an H:C ratio of about 1:3 with older soot having only one hydrogen per eight carbons (Homann and Wagner, 1967). Physically, soot appears as grape-like clusters of small spheres (more commonly called spherules). The spherules typically reach 20 nm in diameter, but the clusters can grow to macroscopic sizes, depending on the combustion conditions. X-ray diffraction of soot reveals the presence of small (2 nm) graphite-like crystallites, but no long range order across the spherule. The spacing between the carbon planes is 3.63 Å, slightly greater than the 3.35 Å seen in graphite.

In 1775, Sir Percival Pott identified soot as the source of the cancer of the scrotum seen in chimney sweeps in London. This was most likely the first identified environmental carcinogen. The actual cause of the cancers probably was not the soot itself, but some of the polycyclic aromatic hydrocarbons (PAH) produced with it. PAH's are often identified as important intermediates to soot formation. In fact, it has been reported that soot inhibits the mutagenicity of PAH by strong surface adsorption (Boyland, 1983).

Diesel engines are the largest mobil source of soot emissions. As much as 1% of the carbon input to the engine as fuel ends up as soot in the exhaust gases (Wagner, 1981). New regulations by the U.S. Environmental Protection Agency to be enforced in 1991 and 1994 will significantly reduce this emission level on new vehicles, down from the current limit of 0.6 gm/bhphr (brake horsepower-hour) to 0.1 gm/bhphr by 1994.

Soot produced with special properties is an important industrial chemical known as carbon black.[1] In 1904, S.C. Mote discovered that carbon black has a reinforcing effect on rubber and in 1912 B.F. Goodrich first started using large quantities of carbon black to increase the durability of automobile tire rubber (Shreve and Brink, 1977). Now, automobile tires contain 3-4 kg of carbon black, or about 35% of their weight (Cabot Corporation). Ninety-five percent of the carbon black produced goes into rubber products and most of this into tires. The remaining fraction is used in inks (2-3%), conductive plastics, copy machine toners, and many other specialty applications (Donnet and Voet, 1976). In 1988, production of carbon black in the United States was 1.3×10^9 kg, making it the thirty-eighth largest commodity chemical (Reisch, 1989). Feedstocks for carbon black furnaces are usually heavy, highly aromatic "bottoms" by-products from petroleum refining with conversion of feedstock exceeding 65%.

The process of soot formation may be separated into six sequential steps:

- gas phase molecular weight growth
- nucleation or particle inception
- surface growth
- coagulation
- agglomeration
- burn-out

Molecular weight growth is the process under which the fuel molecules undergo homogeneous free

---

[1] The carbon black industry strives to differentiate their product from soot (Rivin and Medalia, 1981). However, on the level of fundamental chemical mechanisms of formation there is probably a great deal of similarity.

radical chemical polymerization reactions. When the molecules grow larger than approximately 2000 amu they are considered to be soot nuclei and the reactions are considered heterogeneous. The somewhat arbitrary designation of the nucleation point at 2000 amu is due to the visibility limit of soot particles using a transmission electron microscope (TEM). Surface growth is a continuation of molecular weight growth and is believed to occur through a free radical mechanism. Concurrently with surface growth, the particles collide and coagulate to form new and roughly spherical particles. As residence time in the flame increases, surface growth virtually ceases, possibly due to the soot becoming less reactive, the depletion of gas phase reactants, or both. The physical collision process changes as well; the particles continue to collide and stick together, but they retain their original shape. That is, clusters or chains of the particles form rather than larger spheres. The individual members of the chains are called spherules . If sufficient oxidant is present,the particles will then be destroyed in the burnout process.

Many different combustion configurations are used in practical systems. We may grossly classify them by the fluid mechanics and by the fuel/oxidant geometry. The fluid mechanics may be either laminar or turbulent and the geometry may be premixed or diffusive. In premixed combustion, the fuel and oxidant are well mixed before entering the combustion zone. In diffusion flames, the mixing occurs simultaneously with the reactions. Most practical combustion systems, such as gas-turbines or diesel engines, are turbulent diffusion flames. Unfortunately, these are the most complex to study because of temporal and spatial inhomogeneities.

In order to modify and control the formation of soot, we need to understand its dynamics. Two approaches are possible here. The first is to work with an existing complex combustion system (*e.g.* a diesel engine on a test stand). The parameters could be adjusted and the effect on emissions observed. This Edisonian approach may be valuable in finding solution to specific problems, but the results are not generally applicable.

In contrast, we have taken the approach of examining an extremely simple combustion system, a laminar, premixed, flat flame. This configuration is temporally invariant and spatially varying in only one dimension. We cannot take any result directly from this flame and apply them to a practical combustor, but instead we can derive fundamental kinetic information from the data. This kinetic knowledge, then is widely applicable to more complex combustion geometries.

Thesis Objectives

The focus of this thesis is to investigate the nucleation phase of soot formation. This is the transition region between molecular dynamics and particle dynamics. In particular, we seek the identity of the molecular species which are responsible for the formation of the nascent particles and the kinetics of their reactions.

Chapter Two

Literature Review

This chapter contains a review of the published literature in the area of soot formation. The presentation is broken down roughly into the grouping of fuel effects, temperature effects, mass growth, oxidation, particle coagulation, polycyclic aromatic hydrocarbon (PAH) formation, and carbon clusters.

Soot has generated a great deal of interest in the literature, more than one unfamiliar with the field might expect. Figure 2.1 shows a plot of the number of publications in the Chemical Abstracts STN electronic database found using the search word "soot" as a function of publication year. One immediate observation is that there has been a steady and rapid increase in the number of papers from the early sixties until the middle eighties (the low numbers in 1963 and 1964 are a reflection of the small number of records in the database in those years). A second salient feature is the discontinuity between 1979 and 1980. This can be attributed to the severe energy shortage in 1979. With the resulting

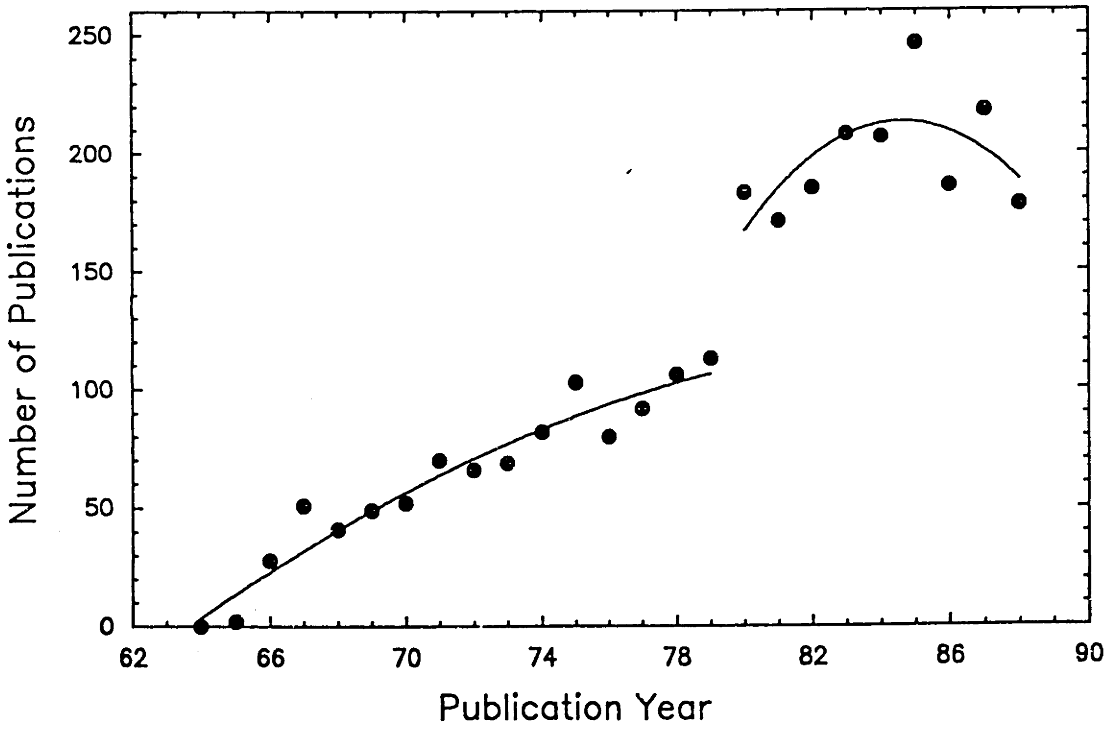

Figure 2.1 Number of publications with "soot" as a key word as a function of publication year.

increase in interest in synthetic fuels came the realization that their greater aromatic content meant greater sooting tendencies.

Yet with thousands of papers published on soot we still do not have a clear picture of the chemical and physical processes involved. One problem is the tremendous number of experimental systems which researchers use for soot studies. Data are published on premixed and diffusion flames, laminar and turbulent flow, with the degrees of freedom in pressure, temperature, diluent content, and additives. Hundreds of different fuels are examined from methane to heavy aromatic hydrocarbons. Shock tubes and flow reactors provide still more sources of data, each with its own experiment idiosyncrasies. Papers are also published correlating soot production to operating parameters of practical systems such as diesels. In trying to draw inferences across different experiments, allowances must be made for the different time/temperature/concentration histories in each system and for steep gradients of concentration and temperature induce diffusive transport which can be greater than the more obvious convective process. One gets the feeling that the secrets of soot formation are already available in our libraries, but that a perfect logician is needed to extract them.

Over the years, the theories and models of combustion and soot formation have become much more sophisticated. This is a reflection not of increasing quality of the scientists but of advances in technology. First, lasers have been refined to the point where they are the most common light source in the laboratory. Measurements of particles and radicals which had been difficult or impossible before lasers have become routine. The second major advance is in computers. Large kinetic models now can be integrated numerically in short periods of time. Whereas early theories were often forced to be qualitative, we can now test complex ideas in a quantitative fashion.

2.1 Early Work

In one of the first systematic studies of the parameters of soot formation, Street and Thomas (1955) discuss some of the mechanisms which had been proposed at that time. The condensation of C_2 is often suggested because C_2 is observed spectroscopically in flames (and also visually be a green emission). This theory was rejected by Street and Thomas on the grounds of insufficient concentration of C_2. Condensation of PAH was considered as a soot formation route because the structure of the resulting soot is graphite-like, similar to an infinite PAH, and also because aromatic fuels tend to produce more soot. Wolfhard and Parker argued against this because they could not find evidence of PAH intermediates spectroscopically. They instead proposed graphitization of droplets of polymerized fuel.

Porter (1953) promoted the idea of direct polymerization of C_2H_2 to carbon. His experiments, flash photolysis of C_2H_4, showed the conversion of substrate to C_2H_2 and then to carbon with no hydrocarbon intermediates. The reaction $C_2H_2 \Rightarrow 2C + H_2$ is thermally favored by 54 kcal/mol. An argument based on transition state theory shows the existence of a threshold temperature, above which direct polymerization of fuel to form soot (Wolfhard and Parker's concept) cannot occur. It is estimated that this threshold is at 1000 °C. Porter recognized that oxidation is a competitive process to the creation of particulate and that oxidation can have an enhancement effect through initiation of chain reactions. The presence of oxygen, however, should not change the soot *formation* mechanism.

Palmer and Cullis wrote the first comprehensive review paper in 1965. In it they made the observation that there is great deal of similarity across different combustion conditions:

> "With diffusion flames and premixed flames, investigations have been made both of the *properties* of the carbon formed and of the *extent* of carbon formation under various experimental conditions. In general, however, the properties of the carbons formed in flames are remarkably little affected by the type of flame, the nature of fuel being burnt and the other conditions which they are produced. Any complete and comprehensive theory of carbon formation must of course be able to account for this striking observation."

As will be shown below, the similarities extend beyond soot to PAH as well. The authors noted the physical structure of soot. It has an elemental composition of C_8H and a morphology of tiny spherules strung together like beads of a necklace. Each spherules contains of order 10^4 crystallites which are identified with X-ray diffraction. Each crystallite has a size of about 20 to 30 Å in the plane (*ca.* 100 carbon atoms per plane) with 5 to 10 planes in a stack. The layers have a turbostratic structure, meaning that there is no orientation between planes, and the plane spacing is 3.44 Å, as opposed to 3.35 Å for graphite.

Bonne, Homann and Wagner (1965) used a molecular beam/mass spectrometer apparatus to study a rich, premixed, low-pressure acetylene flame. In this pioneering study, the authors were able to make direct measurements of stable species and free radicals. Soot was measured with optical absorption.

Bonne *et al.* conclude that polyacetylenes are important in soot nucleation because their profiles peak at the soot nucleation zone.

2.2 Fuel Effects

Sorting out the effects of fuel structure on soot formation can be considered as one of the most difficult problems if viewed on the basis of controversy in the literature.[1] The problem is made difficult by the fact that different fuels have different flame temperatures. Several methods are available to quantify the tendency of a fuel to produce soot. One of the most common is to measure the height of a diffusion flame at which soot just starts to break through the top as the fuel/air ratio is increased. ASTM has developed a simple method to test aviation turbine fuel (ASTM D 1322-85) which correlates the height of a lamp wick at the point of smoke formation to sooting tendency of fuel. A slightly more quantitative method is to measure the critical equivalence ratio (φ_c)[2] at which soot just starts to appear in a flame, usually determined by the visible yellow emission from the flame (black body radiation from the soot particles). This is not, however, a robust technique because the flame type and burner type have major effects.

Kinetically, the critical equivalence ratio represents the point at which the rate of formation of soot precursors is just balanced by the rate of their oxidation. It is important to keep in mind that φ_c is not necessarily related to the soot yield in a richer system. The critical sooting tendencies in *premixed* flames go in the order:

aromatics > alkanes > alkenes > alkynes

In *diffusion* flames the order is some what different:

aromatics > alkynes > alkenes > alkanes

The position of alkynes switches between the two flame types. Glassman (1979) reasoned that the shift was due to temperature. Higher temperature flames induce a greater rate of pyrolytic growth of soot precursors and a greater concentration of OH which destroys the precursors. The temperature sensitivity is greater for OH production so hotter flames produce less soot. This effect is not seen in a diffusion

---

[1] Including fairly vicious battles through letters to editors.

[2] $\varphi \equiv$ (actual fuel/air ratio)/(stoichiometric fuel/air ratio). $\varphi > 1$ means a rich system

flame because the fuel pyrolysis occurs in an oxidant free environment.

Frazee and Anderson (1957) added various aromatic compound to a flow of heated gas and measured the soot formation optically. Temperatures of 700-850°C were reported. The general observation was that aromatics with alkyl side chains produced the most soot, larger ring systems made more soot than smaller, and aromatics with heteroatoms (*e.g.* pyridine) produced the least. It is interesting to compare the isomers phenanthrene and anthracene ($C_{14}H_{10}$). Anthracene, being the less stable thermodynamically, has the greatest sooting tendency. Even more striking is that anthracene has a greater propensity to form soot than pyrene ($C_{16}H_{10}$). Pyrene is one aromatic ring *larger* but is a more stable structure due to the larger degree of condensation.[3] This observation would indicate that the fuel must break apart in the reaction zone to form larger species and that those fuel which crack more readily produce more soot.

Davies and Sculley (1966) did the same sort of experiment by adding aromatics to a rich flame. This work was at a significantly higher temperature, 1400 K, but the results are in accord with Frazee and Anderson. They also noted that hydrogen acts as an inhibitor. Presumably this is due to an increase in the radical pool and oxidation, as in the Glassman argument above.

The general picture emerges that aromatic fuels produce more soot because growth can occur readily on intact rings. Harris and Weiner (1984) clouded that image with an experiment in which toluene was added to an ethylene flame. Care was taken to maintain temperature and equivalence ratio the same between the doped and control flames. The result was *no* difference in level of soot production. Thus, it appeared that the toluene was broken down to the point where it was no more effective than a non-aromatic at producing soot.

2.3 Temperature Effects

Of all the parameters which affect soot formation, temperature is the most profound. Temperature simultaneously affects the rate of molecular weight growth reactions, which have an apparent activation energy of about 60 kcal/mol, and the concentration of OH, which has an Arrhenius-form temperature

---

[3] Highly condensed structures such as pyrene are called *peri*-condensed, as opposed to *cata*-condensed structures such as anthracene.

sensitivity of 70 kcal/mol (Millikan, 1962).[4]

Millikan and Foss (1962) measured the temperature sensitivity of the critical C/O ratio in an ethylene flame. The experimental apparatus allowed temperature and equivalence ratio to be varied independently. It was found that the critical equivalence ratio would shift richer as the temperature was increased. Put another way, a sooting flame could be made non-sooting by increasing the temperature.

Takahashi and Glassman (1984), in a careful study, measured the critical equivalence ratio of 21 fuels and some mixtures in a Bunsen-type flame. The authors defined another normalized fuel/air ratio, ψ, which is the ratio of the actual fuel/air ratio divided by the fuel/air ratio where the products are stoichiometric CO and H_2. The authors state that this is a better parameter for correlating soot formation in rich flames. The data for all the different fuels, when plotted against the number of carbon-carbon bonds in the fuel, all collapses into a single line. The fuels tested range from ethane to methylnaphthalene. Acetylene is the only molecule which does not fit the line; it produces soot sooner than its C-C bond count (=3 for acetylene) would predict. Takahashi and Glassman claim that the good fit is because the number of C-C bonds correlates to both the C/H ratio and the size of the molecule. The C/H ratio is a large determining factor in the OH concentration (at equilibrium for a given temperature C/H ratio fixes [OH]). The size of the molecule affects the pyrolysis rate; large molecules decompose faster. This result indicates that fuel structure has no effect on the equivalence ratio for *incipient* sooting (no claim is made about soot yields).

Harris *et al.* (1986) also analyzed critical equivalence ratio, but for a smaller set of fuels. The authors interpreted the data through a kinetic analysis based on the equality of the rates for soot precursor formation and destruction at incipient sooting conditions. They assumed that precursor formation was first order in fuel concentration and that OH was the only oxidizing species. Equating formation and destruction rates with this set of assumptions yields the expression,

$$k_f\,[\text{fuel}] - k_o\,[\text{precursor}]\,[\text{OH}] = 0. \tag{2.1}$$

The fuel concentration is proportional to the equivalence ratio. Expression of the rate constants in Arrhenius form yields an equation with φ_c as a function of temperature, with three adjustable

---

[4] Although it is not in the literature, this study has identified pyrolytic decay (*ca.* 72 kcal/mol) as a third major effect of temperature. See Chapter 6.

parameters. When the parameters are fit, the data from the five different fuels (all aliphatics) collapse on single line. From Lucht *et al.* (1985) an assumption is made that the OH is at global equilibrium.[5]

Gomez *et al.* (1987) compared critical sooting conditions for four fuels, butene, butadiene, acetylene, and benzene, in a diffusion flame. In all four fuels, the temperature at the point where soot would begin to nucleate was always 1350 K. If N_2 diluent was added to the flame, the location of the soot inception point would shift, but the temperature would stay the same.

Olson and Madronich (1985) also found temperature invariance among different conditions. They studied an atmospheric pressure, laminar premixed flame using toluene and decalin as fuels. Temperature was varied independently of equivalence ratio through nitrogen dilution. The critical sooting threshold temperature was found to be at 1750 K for toluene and 1720 K for decalin, regardless of equivalence ratio. Even more surprising, the soot *yields* were found to be a function of temperature only and insensitive to equivalence ratio.

Böhm *et al* (1989), in a study of pressure and temperature effects on the critical C/O ratio in premixed ethylene-air flames, obtained a result counter to that of Olson and Madronich. The critical C/O ration was found to increase with increasing temperature. There was, however, a minimum in the curve at about 1500 K. Below this temperature the critical C/O ratio rises sharply. There is a slight pressure effect on critical C/O ratio as well. Increasing the pressure over the range of 1 to 10 bar decreases the critical C/O ratio. The pressure effect is much stronger at temperatures less than 1600 K.

Kent and Wagner (1984) found the burnout of soot to be related to a fixed temperature. In a study of a laminar ethylene diffusion flame, the flame height at which soot was emitted was found to vary with fuel flow rate, but temperature of soot breakthrough was always 1300 K. The authors attribute this to a kinetic control of soot burnout in the upper regions of the flame. The temperature decrease is strongly coupled to soot loadings though radiative losses from the flame.

---

[5] This assumption is less valid in the low pressure benzene flame studied in this work. The soot formation reactions of a benzene flame occur simultaneously with primary oxidation making the radical concentrations well above global equilibrium in the soot nucleation zone.

2.4 Soot Mass Growth

Mass growth of soot in premixed flames typically rises to an asymptotic value even though C_2H_2 is present and temperatures are high in the region of no mass growth. This performance can be described through the first order differential equation,

$$\frac{df_v}{dt} = k_{sg}\,(f_v^* - f_v), \tag{2.2}$$

where k_{sg} is a fitted surface growth rate constant and f_v^* is a fitted parameter which represents the ultimate amount of soot formed (Wagner, 1981). The temperature effects for both these parameters (k_{sg} and f_v^*) have been determined. The rate constant, k_{sg}, fits well to an Arrhenius form with an activation energy of 43 kcal/mol and an A factor of $1.56\text{x}10^7\ s^{-1}$ (derived from Figure 4 of Baumgärtner *et al.*, 1985). The ultimate soot volume fraction, f_v^*, has a maximum at around 1600 K (Böhm *et al.*, 1989). This rate growth expression does not predict behavior for new conditions and its simple structure does not reveal the underlying mechanisms.

Harris and Weiner (1983a and 1983b) took a more mechanistic approach to describing the mass growth of soot. Acetylene is almost certainly the source of mass for the growth of soot. If C_2H_2 does not react directly with soot, the species that does must be closely related to C_2H_2 in the reaction network. Harris and Weiner correlated the rate of surface growth as first order in C_2H_2 concentration and first order in soot surface area.

$$\frac{dM}{dt} = k\,[C_2H_2]\,S_{soot} \tag{2.3}$$

The rate constant, determined from light scattering experiments on atmospheric pressure ethylene flames, is the same for several different equivalence ratios. The Harris and Weiner formalism is less of an empiricism than the previous method, but it has the unusual feature that the rate "constant" decrease with increasing residence time of the soot in the flame. The authors give an explanation that the declining rate constant is due to "aging" of the soot. As shall be shown in Chapter Six, the decline in rate constant could be explained by the decay in the radical pool which is responsible for activating the reaction sites.

Dasch (1985) has made an attempt to reconcile the empirical equation of Wagner (Equation 2.2) with the expression of Harris and Weiner (Equation 2.3). In his analysis, he attributes the rate constant of Equation 2.2, k_{sg}, not to surface *growth* but to the kinetics of surface *deactivation*. It is noted that k_{sg}

is only a function of temperature and not flame composition. By expressing the rate constant of Equation 2.3 as $k^o \exp(-\alpha t)$, where t = time, the formulae are shown to be equivalent.

Wieschnowsky *et al.* (1989) have done experiments which question the Harris conclusion that mass addition to soot is controlled by the particulate surface area. Their experiment was the study of low pressure premixed acetylene flames, both unseeded and seeded with CsCl. The salt additive has the effect of reducing the coagulation rate of the particles through electrostatic repulsion. The result was that the same yield of soot was obtained in both the seeded and unseeded flames. However, the soot surface area in the seeded flame was much higher because the particles did not coagulate as fast. If surface area was indeed a controlling factor then the seeded flame should have produced more soot. The authors conclude that a gas-phase process must be rate limiting, and suggest $OH + C_2H_2 \Rightarrow H_2O + C_2H$ as a likely possibility. In this case the radical C_2H would rapidly add to the soot surface.

Brei *et al.* (1987) examined the fate of incremental fuel carbon above the sooting threshold in flames of acetylene, ethylene, and benzene. The carbon was classified as in the soot category or hydrocarbon category. For benzene flames, the carbon present as soot exceeded the carbon present as hydrocarbons in all cases. The reverse was true for the other fuels except for very rich ethylene flames. The authors plotted soot mass as a function of excess in the form of Equation 2.4.

$$M_c = [C/O - (C/O)_{crit}]^n \tag{2.4}$$

The value of the exponent, n, is 3-4 for C_2H_4, 3.5 for C_2H_2, and 3 for C_6H_6. These large exponents are could indicate that the acetylene addition process to soot is of a high order.

2.5 Soot Oxidation

Millikan (1962) postulated that the existence of the dark zone between the primary combustion zone and soot formation zone of aliphatic flames was due to oxidative degradation of the growing soot precursors. He proposed that OH is the species responsible for the oxidation. By the time the soot begins to form, Millikan found that the OH level had decayed to within 50% of its global equilibrium level, down from ten times in excess of equilibrium in the primary reaction zone. Millikan observed that a wire becomes coated with carbon when placed in the sooting zone. Moving this wire down to the dark zone causes the carbon to dissipate, an indication of strong oxidizing conditions. Millikan fitted the OH concentration parametrically in temperature and equivalence ratio. As was stated in §2.3, the temperature sensitivity of the OH is about 70 kcal/mol.

Fenimore and Jones (1967) studied the oxidation of soot by OH in a double-burner premixed ethylene flame. A lower burner produces a supply of soot which is cooled, mixed with more oxidant, and burned out in a second burner. The [OH] was determined assuming partial equilibration of the reaction $O + H_2O \Leftrightarrow 2OH$. [O] was determined from the rate of $O + N_2O \Rightarrow 2NO$, with N_2O being added to the flame. The removal rate of carbon by OH was found to be 1 effective reaction removing one carbon per 10 collisions. Page and Ates (1978) also concluded that OH was the dominant oxidizing agent of the soot produced in an ethylene flame. They computed a reaction probability of 0.25, slightly higher than the one of Fenimore and Jones.

Neoh (1980) conducted a very careful study of the burnout rate of soot produced in a methane flame. H atom was measured using an optical absorption method which involves doping the flame with lithium. O and OH were calculated with partial equilibrium assumptions. The soot burnout rate was measured using optical Rayleigh scattering methods. The observed burnout rate was correlated against all the possible oxidants: O, OH, O_2, H_2O, and CO_2. It was found that only OH gave a reasonable (*i.e.* less than unity) and fairly constant value for reaction efficiency. The reaction efficiency determined was in the range 0.13 - 0.27. Higher in the flame Neoh observed that the soot particles began to break up as evidenced by a large increase in number density. This phenomenon was assumed to be due to oxidation by molecular oxygen. The O_2, being less reactive than OH, has time to diffuse into the pores of the soot before reaction. From inside, the oxygen can reduced the structural integrity of the spherule to the point of rupture.

Wright (1975) measured the oxidation rate of soot by O atom in a thermogravimetric analyzer from room temperature to 850 K. He saw CO_2 as the only product, indicating that the oxidation by O atom at these temperatures involves surface diffusion (*e.g.* $CO(s) + O(s) \Rightarrow CO_2(\uparrow)$). While it was not directly measured, all the soot oxidation experiments in flames made the assumption that CO was the product. Wright also oxidized pyrographite and vitreous carbon and found basically the same rates, indicating a similarity of mechanism. The reaction probability for O atom plus soot at 850 K was determined to be 0.036.

Wicke and Grady (1986 and 1988) measured the oxidation of paraffin candle soot by O atoms at low and high temperatures in a thermogravimetric analyzer, much in the same method as Wright. At room temperature the main product of oxidation is CO_2. As the temperature approaches the maximum measured, 873 K, CO becomes the dominant product. At low temperature, up to one O atom in four carbons becomes chemically adsorbed to the surface. This oxygen can only be desorbed at high temperatures with the oxygen leaving as CO_2. At 873 K, no long term adsorption occurs.

The relative importance of O *vs.* OH as a soot oxidizer is not currently known. Wright makes arguments that O is important due to the higher reactivity of O offsetting the lower concentration. However, his measured reactivity of O is *lower* than that assigned to OH (the Fenimore and Jones paper had been published before Wright's). Equilibrium considerations dictate that [O] will be much less than [OH] for most conditions of interest to soot research: high φ and temperatures below 2000 K. These two points imply that O is not an important oxidizer. Kinetic argument indicate that O could be as important a player as OH. Both O and OH are initially produced at the same rate through the reaction $H + O_2 \Rightarrow OH + O$. Thus their fluxes in the primary oxidation zone will be roughly equivalent.

Park and Appleton (1973) tested the rate of Nagle and Strickland-Constable (1962) on carbon black. This rate expression was developed to model the oxidation of graphite by molecular oxygen. The experimental arrangement was a shock tube filled with a soot aerosol in oxygen and a diluent. The Nagle and Strickland constable expression has terms indicative of adsorption, surface reaction, and desorption kinetics. It also involves two different kinds of reactive sites, *A* and *B* as they call them. The more reactive *A* sites can be thermally converted to the less reactive *B* sites. The equations are solved with a pseudo-steady-state assumption on the concentration of *A* and *B* sites. While the authors do not make this point, the *A* sites could be considered edges of graphite planes and the *B* sites to be the basal planes. Park and Appleton found these kinetics to be an adequate description of the observed data. Given the physical structure of soot presented in §2.1, this would not be expected. Soot, made up of tiny (20-30 Å) platelets with random stacking between planes should have many more edge defects than the graphite modeled by Nagle and Strickland-Constable. Intuitively, the greater number of defects in the more randomly oriented soot particles would mean that the pseudo-steady-state assumption between that A and B sites will not hold.

Felder *et al.* (1988) have studied oxidation of carbon black by O_2 in a high temperature flow reactor. The oxidation rate was found to be lower by about a factor of ten than the Nagle and Strickland-Constable expression would predict. The authors conclude that the sulfur content of their carbon black (about 1% by weight) was responsible for its reduced reactivity. This is an intriguing concept because sulfur content of diesel fuel has been found to be a very good correlating factor to the amount of soot emitted by an engine (Wall and Hoekman, 1984).

2.6 Soot Coagulation

Smoluchowski (1917) studied the coagulation kinetics of colloidal solutions and found the rate of change of number density to be second order in number density.

$$\frac{dN}{dt} = k N^2 \tag{2.4}$$

This relation was found to apply to soot aerosols with a rate constant equal to the gas kinetic collision rate. Prado *et al.* (1983) integrated the Smoluchowski equation (see Equation 4.1 through 4.5) and found that the number density of soot particle in the flame is independent of the initial number density.

Gay and Berne (1986) have done a theoretical study to support the observation that particles can stick on collision. What they showed is that the translational energy of the colliding particles can be dissipated as thermal energy in the lattice of the newly formed double-particle. This calculation was done by computing the molecular dynamics of two clusters of 135 hard spheres each. The hard spheres have Lennard-Jones potential surfaces. The computer simulation showed that the potential energy of the two separated clusters was rapidly converted to thermal energy. The authors contend that this energy accommodation can account for the high sticking efficiency seen in submicron aerosols.

The nucleation, surface growth, and coagulation of soot aerosols have been modeled using the Smoluchowski equation on a discretized particle size distribution (Frenklach, 1985; Frenklach and Harris, 1987; Harris, Weiner, and Ashcroft, 1986). The first two references involved application of the "method of moments" to solution of the set of differential equations which greatly reduces the computation time. Harris *et al.* combine modeling of the nucleation process with optical scattering data in an iterative fashion in order to determine the size distribution of the nucleating aerosol.

Harris and Weiner (1989) have introduced the concept of nucleation caused by the coagulation of high molecular weight PAH molecules. The authors propose that the heavy PAH's are of three classes. Class A is greater than 1000 amu, Class B is between several hundred and 1000, and Class C is smaller than several hundred. Due to high van der Waals forces collisions between Class A and any other class lead to sticking. Class B can stick to itself or Class A, and Class C can only stick to Class A. The authors propose a dynamical scheme in which the Class B molecules are scavenged from the system by collisions with themselves and Class A. These are the collisions which form nuclei. Once the Class B inventory is depleted, nucleation will stop, but mass growth continues as Class A molecules continue to scavenge Class C molecules. When all the PAH has been consumed by the growing soot inventory, the mass growth of soot becomes dominated by surface addition of C_2H_2.

2.7 Growth of PAH

PAH's have long been implicated as important actors in soot formation, due both to their transient presence in the soot nucleation zone of a flame and to the similarity between the PAH structure and the graphite-like structure of soot. Chakraborty and Long (1968) measured the soot and PAH from premixed flames of C_2H_6 and C_2H_4. The authors conclude that the PAH's are formed through a process which first involved fuel breakdown to C_2H_2.

Homann and Wagner (1967) present a qualitative picture of molecular weight growth through polyacetylenes condensation. PAH's are considered unreactive byproducts rather than intermediates in the soot formation process because the rate of soot formation tends to zero while the PAH's are still rising. The authors note the importance of the radical pool in keeping the free-radical growth reactions going at a fast pace. They also link the decrease in soot surface reactivity to the reduction in radical content of soot as it ages. It is noted that the ESR signals from young soot are 100 times those of old particles.

Tompkins and Long (1969) dispute the claim by Homann and Wagner that PAH's are not intermediates. They note two distinct regions of PAH formation. A rapid early growth, followed by a decay in the soot nucleation region, subsequently followed by a more gradual rise.

Crittendon and Long (1976) made measurements of stable light gas species and PAH in low pressure acetylene and ethylene flames. From the data, a conceptual mechanism (but not elementary) is proposed in which PAH and polyacetylenes grow through C_2H_2 addition.

Bittner and Howard (1981a) proposed the first elementary reaction mechanism for growth of PAH from acetylene. The mechanism involves addition of C_2H_2 to phenyl radical forming styryl radial (see Figure 5.1). A second C_2H_2 then adds to the styryl radical and ring closure follows forming naphthalene. Bockhorn *et al.* (1983) and Frenklach *et al.* (1985) have proposed a similar ring growth elementary mechanism (see Figure 5.2). These two differ from the Bittner and Howard process in that the second C_2H_2 adds to a σ-radical site *ortho* to the C_2 ring substituent rather than on the end of the C_2. Ring closure then ensues across the two C_2 groups on the ring forming naphthyl radical. From the point of view of mass addition to large PAH systems or soot where such fine structural points are impossible to resolve, the two mechanisms are equivalent.

PAH formation has been modeled in large reaction networks for shock tube and flame conditions. Frenklach *et al.* (1985) modeled PAH growth and soot formation in a shock tube using a 600 reaction network. They were able to reproduce the characteristic "bell curve" of soot formation *vs.* temperature seen in shock tubes, but the temperature of the peak was off by several hundred degrees and the predicted soot production levels were too high. Frenklach and Warnatz (1987) have modeled light hydrocarbons and PAH's in a low pressure acetylene flame. The result was a correct prediction of the rise and fall of the PAH, but the model prediction of decay rates were much faster than are seen experimentally.

2.8 Carbon Clusters

One of the most intriguing new developments in the soot literature has been in the area of carbon clusters. Kroto *et al.* (1985) conducted an experiment in which graphite was vaporized with a laser with the vapor being mass analyzed with a time-of-flight mass spectrometer with photoionization. The surprising result was that clusters of 60 carbons are the most stable. The authors propose that the cluster has the structure of a truncated icosahedron, or a soccer ball. The name Buckminsterfullerene is proposed to honor Buckminster Fuller for his work with geodesic structures, or it is known more colloquially as a "bucky ball". The authors conclude (with no real evidence) that C_{60} clusters are an important step in soot formation.

The soccer-ball structure has aroused the interest of theoretical and computational chemists leading to a host of papers on its computed properties such as its molecular orbital structure (Elser and Handon, 1987; Mallion, 1987), it optical spectra (Larsson, 1987), and its vibrational modes and frequencies (Wu *et al.*, 1987).

The combustion community has largely reacted negatively toward the proposal that the formation of soccer-ball structures is related to soot formation. Frenklach and Ebert (1988) make that point through a kinetic argument. Ebert *et al.* (1987) did not see any X-ray diffraction patterns in soot samples which were consistent with spherical C_{60} clusters. It is not unreasonable to believe that such a strained structure would not exist in a flame. In a carbon vapor the chemical bond strain involved in the spherical structure may be energetically favored because all the valences of the carbons are satisfied. In a flame, however, hydrogen can satisfy the valences without resorting to a strained carbon network.

This argument notwithstanding, Gerhardt *et al.* (1987) have observed C_{60} and other even numbered carbon clusters in a flame with a molecular beam mass spectrometer. The fuel was replaced with a deuterated one and the peak locations did not shift, indicating that there was only carbon present.

Chapter Three

Experimental

An experimental system was constructed for this project which allowed a sooting flame to be studied by both optical methods and probe sampling. This chapter describes the combustion apparatus and the analytical methods used.

3.1 Combustion Apparatus

The combustion apparatus includes the burner along with its vacuum chamber, and the equipment for supplying fuel, oxidant and diluent to the burner.

3.1.1 BURNER AND CHAMBER

The combustion system employed in this study is a laminar, premixed flat flame. Fuel and oxidant are well mixed and propagate upwards through the burner top plate. The flame propagates downward and is stabilized on the cooled plate. To as high a degree as possible, all quantities (temperature, concentrations, *etc.*) must be maintained constant in the lateral direction. This allows the system to be modeled in one dimension, greatly simplifying the analysis. The burner must also remove heat in order to stabilize the flame. The stabilization relies on the fact that the flame velocity slows with temperature. The flame front rests at the point where the upward gas velocity exactly matches the downward flame velocity.

The experiments are run at pressures from 20 to 40 torr. The thickness of the flame zone scales roughly proportionally to reciprocal pressure, so we obtain much better spatial resolution at lower pressures. The tradeoff comes in added complexity and expense of the experiments.

Figure 3.1 shows a schematic of the burner. The entire device is made of copper and brass to enhance the heat transfer. The top is made of a 100 mm diameter by 12 mm thick OFHC (oxygen-free high-conductivity) copper plate drilled with approximately 1500 1.0 mm holes. The side walls are water-cooled with a cooling coil. This configuration of having a low resistance to conduction through the top plate and a limiting conduction resistance through the side walls ensures minimization of the lateral temperature gradient across the top plate. A drilled plate was used rather than the more traditional sintered plate because the very rich flames used would tend to clog the pores of the sinter with tars. The top plate was instrumented with three Type K thermocouples. These were inserted into the 1 mm holes at different radial positions as a check on the degree of temperature uniformity. In practice, there was a negligible radial temperature gradient. The burner surface operated between 75 and 85° C, depending on the flame condition.

The inner 70 mm of the burner surface is used for the sooting flame under study. Because many of the optical measurements made are line-of-sight integrals over a radial path, any lateral non-uniformity would lead to erroneous results. To avoid this, an annular burner, 15 mm wide, surrounds the test flame. A rich, but non-sooting ethylene flame was burned here to help maintain temperature and concentration uniformity.

The inner cavity of the burner body is filled with stainless-steel wool, which serves two purposes. First, it will quench the flame if there is a flashback, avoiding an explosion. The second function is to provide a flow resistance greater than the drilled top plate, aiding flow distribution.

The burner is mounted on a vertical translation stage which allows for measurements at various heights above burner. The drive shaft of the translation stage protrudes through a vacuum rotary feedthrough to the outside of the combustion chamber. A stepper motor drives the translation stage through a flexible coupling. The stepper is controlled by the laboratory computer (IBM PC). Because stepper motors turn in discrete angular intervals, burner positions were reproducible to better than 0.1 mm. The unavoidable hysteresis in the drive system was dealt with by the motor-control computer program. The initial position of the burner was set in one of two ways. A photodiode-phototransistor pair was mounted on the bottom of the translation stage such that the light beam would be broken at a reproducible location, sending an indexing signal to the computer. Sometimes the photodiode would get blocked by soot, in which case the burner position would be indexed from the laser beam height or probe tip with a cathetometer.

Figure 3.2 shows a schematic of the combustion chamber. The chamber was constructed of stainless steel and is fitted with O–ring seals to allow operation down to pressures of 20 torr or lower. Several ports are mounted radially near the top for optical and probing access. The laser entrance and exit ports are made from high quality Spectrasil windows mounted at the Brewster angle to reduce internal reflections. The scattered light is collected through another Spectrasil window mounted normal to the light path. Across the chamber from the scattering port is a Woods-horn beam dump which cuts the amount of reflected light seen by the scattering collection optics. A large (15 cm) window is mounted on the side to permit observation of the flame. The upper flange of the chamber is water cooled. The side walls of the chamber were left uncooled but the wall temperature never rose over 40 °C.

The feedthroughs for gas flows (test flame and shield flame), cooling water, and the pressure transducer port are mounted on the bottom of the chamber. The system is designed to facilitate, in a subsequent project, the installation of a molecular beam sampling system on the top of the combustion chamber. To keep the chamber top clear for this modification the exhaust vacuum pump lines were situated at the chamber bottom. Thus, the flame gases and soot turn around at the top of the chamber and flow downwards around the outer part of the chamber. All line-of-sight optical measurements (*e.g.* absorption) were made through purged tubes which penetrated this reverse path. The pressure of the chamber is monitored with an MKS Model 390 capacitance manometer. This device has a 5 decade dynamic range and an accuracy of 0.05% full scale.

The flame was ignited using a Tesla coil connected to an electrode inside the chamber which struck an arc to the side of the burner plate. A premixed flame would explode on ignition, so a diffusion flame was started, with pure fuel flowing through the core and pure oxygen flowing through the annulus.[1]

The chamber was pumped with a large vane-type vacuum pump (Mannesmann-Demag Model WPSO 53) with a capacity of 80 L/sec. The pump was mounted about 20 m away from the burner chamber to avoid coupling vibrations from the pump to optical apparatus. Critical flow was maintained across a valve in the vacuum line which ensured that any oscillations of pump pressure would not propagate upstream into the combustion chamber. The pressure in the chamber was maintained with a home-built feedback control system linked to the laboratory computer. The controller monitored the pressure from the digital output of the capacitance manometer and effected the control by opening and

---

[1] Even with this precaution, the chamber sometimes detonated. Since we operated at a maximum pressure of 40 torr, the detonation pressure never exceeded 1 atm; thus, the only damage was to the nerves of the operator. The upper flange of the chamber was never bolted on, so if the pressure did ever climb, the top would lift and the pressure would be relieved without damage to hardware.

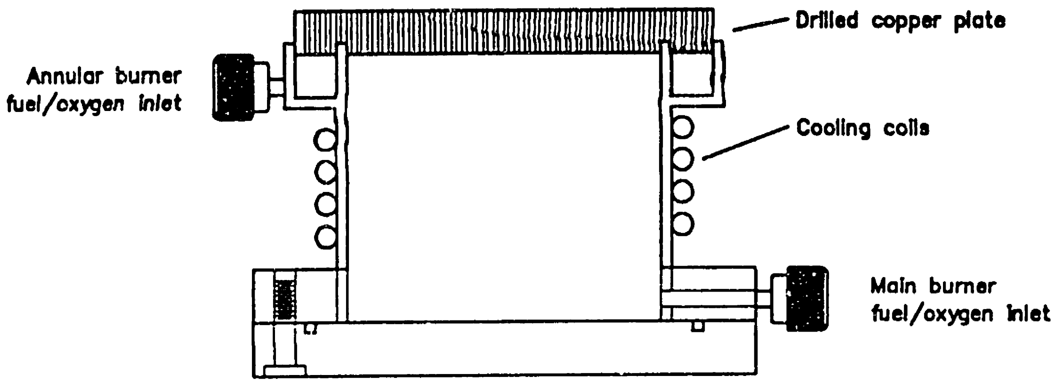

Figure 3.1 Low-pressure premixed flat-flame burner

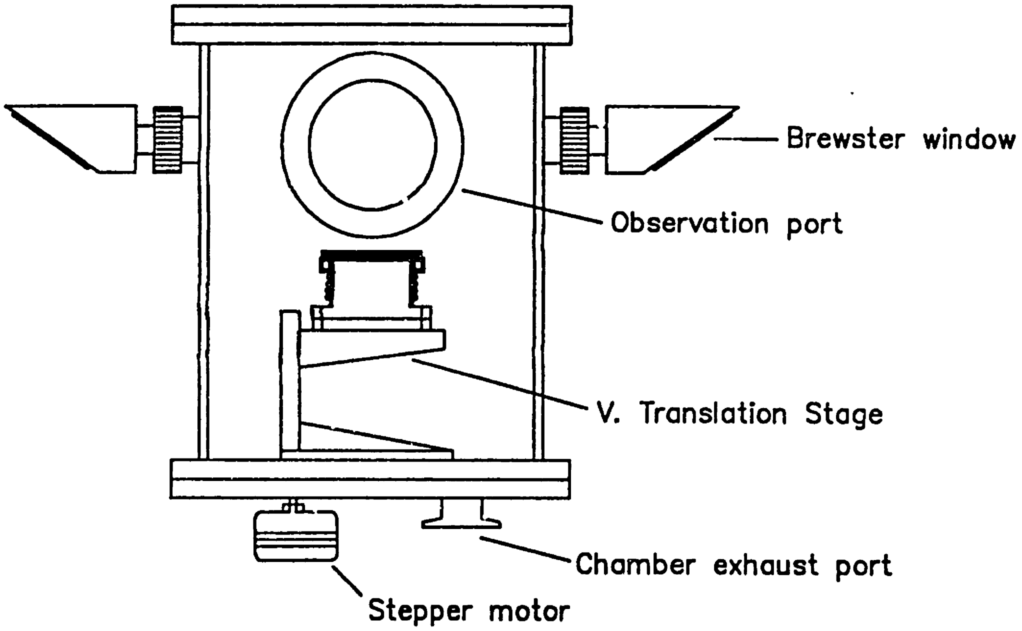

Figure 3.2 Low-pressure combustion chamber with optical access

closing a series of four solenoid valves which bled air into the vacuum line. Each solenoid valve wasattached to an orifice which allowed twice the air flow of the one just below it in the sequence. Operating these four valves in a binary sequence gave 16 control states.

3.1.2 FUEL DELIVERY SYSTEM

Figure 3.3 shows, in schematic form, the fuel metering and delivery system. The function of this device is to deliver vaporized benzene into the flow of oxygen and argon at a low pressure and at flow rates of 1 to 3 g/min. It is a stringent requirement that the flow rate be extremely constant. As can be seen from the data of Bittner *et al.* (1983, Figure 9), a 10% change in equivalence ratio resulted in a 100 fold change in concentration of reaction intermediates of mass greater than 700 amu. Thus every effort was made to limit the variation in flow rate to less than 0.1%.

Originally an HPLC piston pump (Altex Model 110A) was used for fuel supply. This is a finely made (and quite expensive) machine but we found that the pump could not supply fuel at a sufficiently stable rate, presumably because of cycle-to-cycle variations in the seating of the check valves in the pump head. We then installed an ISCO Model LC-5000 syringe pump, which could deliver 500 mL of fuel and

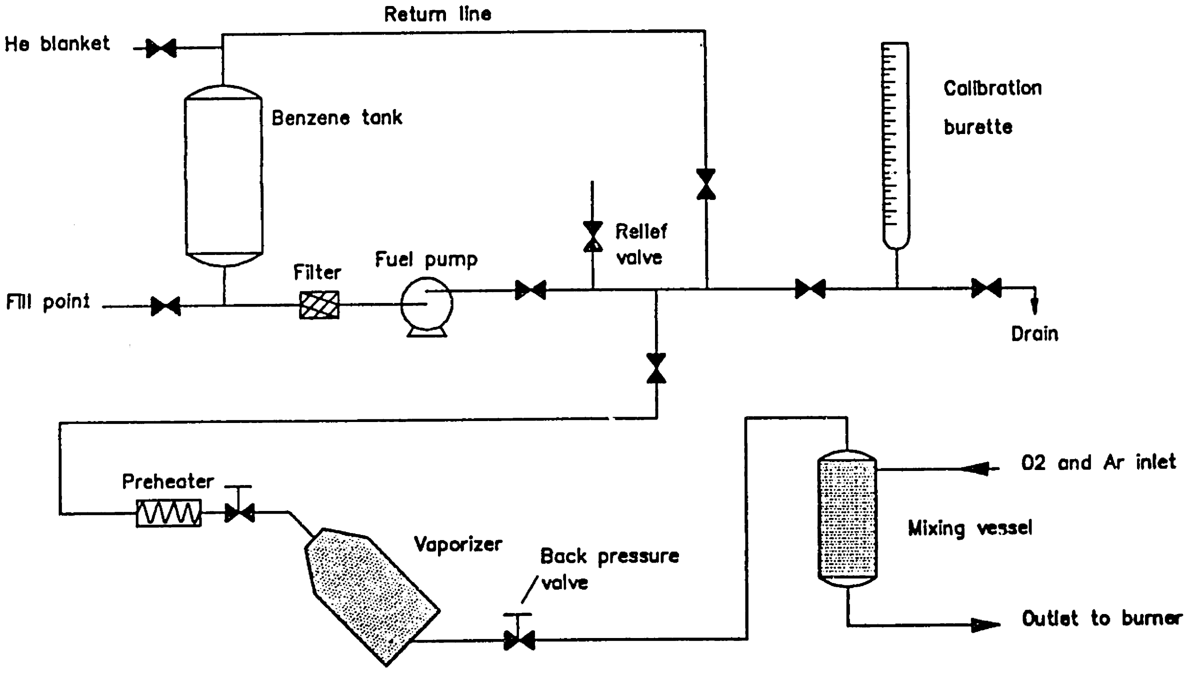

Figure 3.3 Liquid fuel delivery system

had no check valves due to the syringe design. The flow rate was calibrated by diverting the fuel flow from the vaporizer to a 25 mL burette mounted on the side of the vaporizer stand. The rate was timed with a stopwatch. Between calibrations, the burette was dried with a nitrogen flow to keep the droplets clinging to the side of the burette from contributing to the measurement.

The benzene was pumped to a preheater which was maintained at 75 °C with heating tape and a temperature controller. To keep the benzene from vaporizing in the preheater, the pressure was held at 80 psig with a metering valve. The benzene flashed across this valve into a vaporization chamber (*ca.* 1000 mL) which was controlled at 225°C and held at 40 psig. The chamber was filled with small marbles to provide a high surface area on which any slugs of liquid would rapidly vaporize. The vaporized benzene was mixed with the metered oxygen and argon in a heated (40 °C) chamber. The benzene/oxygen/argon mixture went directly to the burner from this point.

During operation, the vaporizer was warmed up for several hours. The pump would then be turned on about 30 minutes ahead of the run to let the pressure in the preheater and vaporizer stabilize. During this time the benzene was diverted to a catch vessel.

All materials which contacted the benzene were constructed of either stainless steel or Teflon, with the exception of the O–rings in the bodies of the metering valves, which were Viton. It was found that Viton, although not rated for benzene service, lasted several years. Then entire vaporization system, except for the pump, was situated inside a fume hood.

3.1.3 GAS METERING SYSTEM

The gas metering system supplied oxygen, argon, and ethylene to the burner at controlled rates. Critical orifice meters were used as control elements. Figure 3.4 shows the basic control system which was replicated for each gas. Critical flow meters employ the principle that the flow across an orifice which has a pressure ratio greater the critical, as shown in Equation 3.1, will be at sonic velocity at the throat and thus the mass flow will depend mainly on the upstream pressure, and to a smaller extent the temperature. The scaling functionalitv for mass flow rate can be seen in Equation 3.2. A calibration is made for each element with the gas for which it will be used.

$$r_c = \left[\frac{2}{\gamma+1}\right]^{(\gamma/\gamma-1)} \tag{3.1}$$

r_c : pressure ratio
γ : C_p/C_v

$$\dot{m} = C A_2 P_1 \left[\gamma \frac{M}{RT}\left[\frac{2}{\gamma+1}\right]^{(\gamma+1/\gamma-1)}\right]^{1/2} \tag{3.2}$$

$\dot{m}$: mass flow rate
C : flow coefficient
A : area

The orifice elements were watch jewels pressed into ¼" tubes and drilled with very fine holes. The orifice sizes range from 0.001 cm to 0.040 cm. The upstream pressures of each element were monitored with a pressure transducer (Omega 240 series) which displayed the pressure on a digital readout and also transmitted them to the computer.

Each element was calibrated in one of two ways. For the meters which required high (*ca.* 100 psig) upstream pressures, the downstream pressure could be 1 atm and the flow would still be critical across

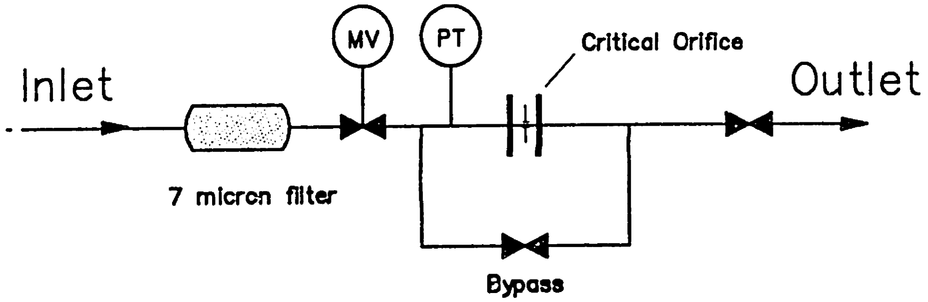

Figure 3.4 Critical Orifice Flow Meter

the orifice. In these cases, the calibration curve was made by connecting the flow element outlet to a bubble flow meter. The meters which required lower upstream pressures were calibrated by directing the exit flow into a large vacuum vessel (68.5 L) and monitoring the pressure rise with a capacitance manometer. Knowledge of the vessel fill rate, volume, and temperature, together with the ideal gas equation is sufficient to determine the mass flowrate. This process was repeated at many upstream pressures to create the calibration curve.

3.1.4 FLAME CONDITIONS

Table 3.1 shows the three flame classes studied. It was a requirement that the combustion conditions be amenable to analysis by both probe sampling and optical methods. With the former method it is desirable that the flame not be excessively sooting as probe orifices tend to clog rapidly. Optical methods, however, demand fairly heavy soot loadings to obtain measurable absorption signal levels. It would also be desirable, but not necessary, to reproduce a flame condition on which literature data exist. This a valuable check on consistency; it may also serve to fill in gaps in our experimental measurements (*e.g.* radical measurements). Below are the details of the flames tested and the rationale for their selection:

Table 3.1 Flame Conditions Studied

	I	II	III
P (torr)	20	40	40
φ	2.0	2.125	2.2, 2.4, 2.5
V_o (cm/s)	50	50	25
[Ar]	0.30	0.45	0.0, 0.10
reference	Bittner (1981)	Bockhorn (1983)	present work

- *φ = 2.0, 20 torr, 30% Ar, V_o = 50 cm/s* - Bittner (1981) made extensive measurements of a nearly sooting benzene oxygen flame with φ = 1.8. His data set included measurements of almost all light radicals except for O atom, molecular species up to 200 amu, and incremental measurements of high mass material in 50 amu increments up to mass 750. He made limited measurements in a sooting flame at φ = 2.0. One striking observation about the transition from non-sooting to sooting conditions is that while the high mass material increased by two orders of magnitude across this boundary, the concentrations of the lighter species changed very little. We make use of this observation by employing the Bittner measurements at φ = 1.8 as an estimate of the profiles of light gases and radicals at φ = 2.0. A series of probe measurements was taken of this flame, with detailed GC analysis of the light PAH's. Soot loadings at this condition were too low in this flame to make optical absorption and scattering measurements.

- *φ = 2.125, 40 torr, 45% Ar* - This is a slight variation of a flame studied by Bockhorn *et al.* (1983) in which soot and molecular species were measured. Bockhorn's group used a pressure of 100 mbar (75 torr); we wanted to achieve the greatest possible spatial resolution so we opted for the same equivalence ratio and velocity, but with a lower pressure. A complete profile of light PAH's was taken of this flame along with UV-visible absorption measurements of the samples. However, the effect of a reduction in pressure on soot loading was underestimated. As in the φ = 2.0 case, insufficient soot was present to make particle measurements.

- *φ = 2.2, 2.4, and 2.5, 40 torr, 0% and 10% Ar, V_o = 25 cm/s* - We dropped the criterion of duplicating a literature flame in order to guarantee that optical soot measurements could be made. This was done by increasing the equivalence ratio and reducing the argon dilution. The effect of reducing the argon diluent is to slow the gas velocity which increases the heat conducted to the burner surface, cooling the flame. It has long been observed that lowering flame temperature increases soot loadings. Three different equivalence ratios were tested within this flame set: φ = 2.2, 2.4, and 2.5. Comparisons of equivalence ratio could be made this way (with some surprising results).

3.2 PAH Sampling

The PAH material was studied by withdrawing sample from the flame using a probe. The samples were extracted with a solvent and subjected to a series of analytical chemistry methods. Probe sampling from a flame is a fairly well established technique (Fristrom and Westenberg, 1965, p. 180) but it has the drawback of being intrusive. The probe tip disturbs the concentration, flow, and (most importantly) temperature fields of the flame, so questions always remain regarding artifacts generated by the probe. These problems are even more extreme under the conditions studied in this project. As the flame becomes more rich or the pressure is reduced, the perturbation of the flame by the radiatively cooled probe tip becomes more and more troublesome. For example, a C_6H_6/O_2/30% Ar flame of $\varphi = 1.8$ (nearly sooting) and 20 torr (the condition studied by Bittner, 1981) shows no visible perturbation at any HAB even when using a fairly large probe. When the oxygen is reduced to a fairly heavily sooting condition ($\varphi = 2.4$), this same probe so severely distorts the flame that the flame front lifts from the burner and "attaches" to the probe.

3.2.1 PROBE DESIGN

The purpose of the probe is to convect a representative sample of the flame gases to a point where they may be analyzed. Besides the perturbation of the flame as discussed above, the probe must also quench the chemistry in a time scale fast compared to the residence time in the reaction zone of the flame. The most common method of quenching the reactions is through an aerodynamic quench, achieved by sampling the gas with a high pressure ratio (> 10) across the orifice. The gas passes the orifice at sonic velocities and expands supersonically while undergoing adiabatic cooling. At some downstream location a shock wave forms, at which point the temperature makes a step increase by converting its translational energy back into thermal energy. By this point some of the energy has been dissipated to the walls before the gas undergoes a shock so the ultimate temperature is well below the flame temperature (Colket, 1982). This works well to terminate highly activated reactions, but many free radical reactions have little or no activation energy. In fact, reactions with low activation energy actually increase in rate as temperature is reduced because gas density increases (Fristrom, 1983). Radical reactions can only be quenched by the injection of a scavenger, such as I_2 or D_2, into the probe. The scavenger, which is not present in the flame, will react with the flame radicals and a unique product may be identified (*e.g.* CH_3I would be indicative of the presence of CH_3 radical; HD likewise for H atom), (Volpani *et al.*, 1986). Probe reactions can also be quenched with a cooling jacket around the probe, but these have the disadvantage of distorting the temperature field of the flame.

The design of an acceptable probe became the most difficult experimental hurdle of the entire thesis. The probe had several conflicting design requirements:

- The temperature of the outside of the probe had to be as close to the flame temperature as possible to minimize the disturbance of the temperature field.
- The inside of the probe had to be cooled to keep the thermally labile PAH from pyrolyzing after they deposited on the probe surface.
- The probe orifice needed to be small to provide good spatial resolution in the flame.
- The orifice must be sufficiently large since heavily sooting flames tend to cause clogging

Obviously, the design had to be a compromise among these requirements. It is worth detailing the experience gained in probe design, both failures and successes, as an aid to any follow-on investigations in this area.

Probe I. All quartz with water jacket - the first design (see Figure 3.5a) tried was a variation on one used by several students in this department (Ritrievi, 1984) for sampling atmospheric pressure flames. The water jacket is formed by solid quartz joints (ring seals) at both ends. In operation this probe disturbed the flame excessively because the cooling extended all the way to the tip. More importantly, the rigid ring seals did not allow stresses which built up as the hot outer jacket expanded against the cooled inner tube to be relieved. This caused the probe to rupture after several minutes in the flame (the Ritrievi probe was much longer and smaller in diameter, allowing the stresses to be non-destructively dissipated).

Probe II. Quartz lower part with flexible seals - The stress problem was addressed by replacing the

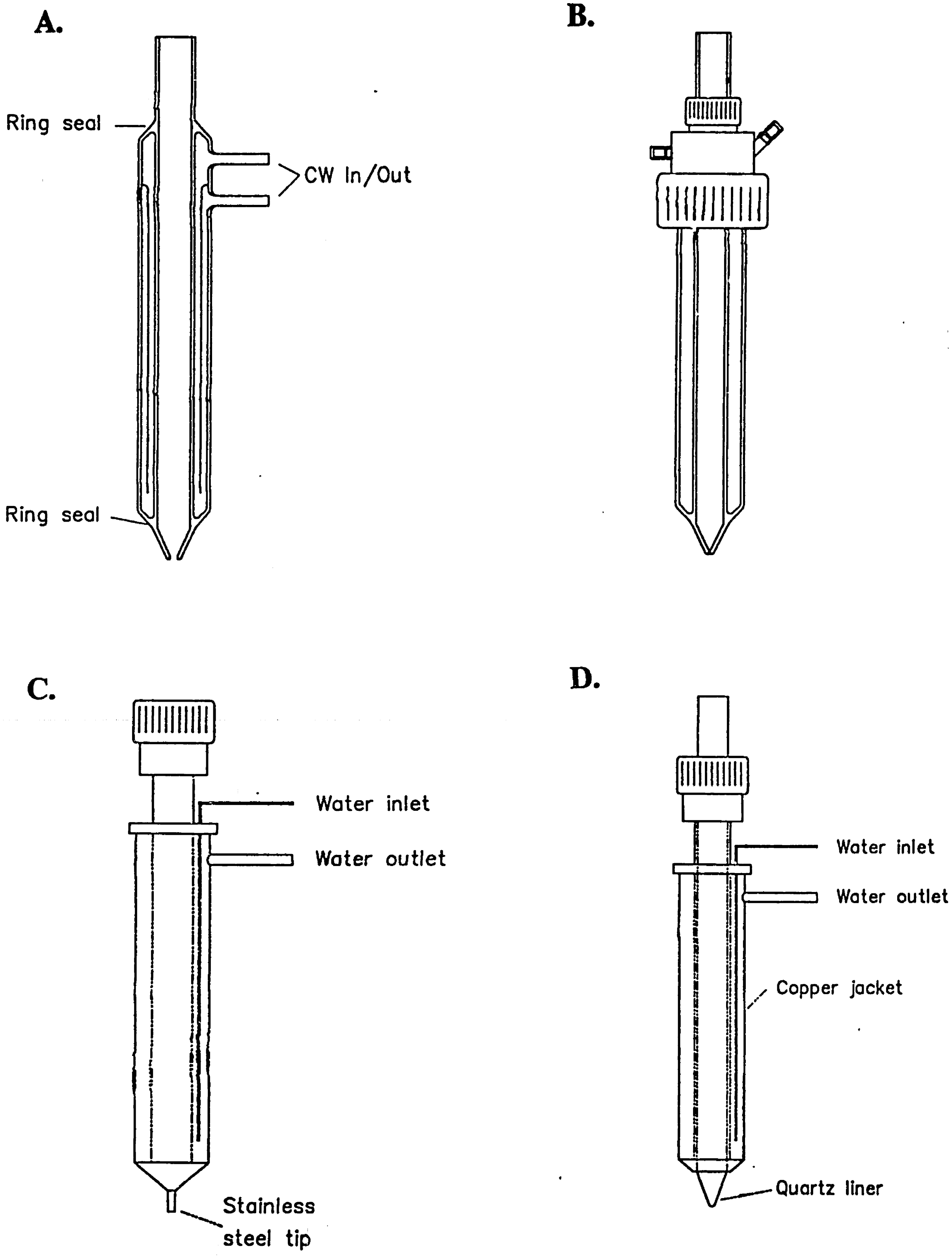

Figure 3.5 Sampling probes used for PAH. a) All quartz probe. b) Quartz lower part with flexible seals. c) Copper probe. d) Hybrid quartz/copper

upper ring seal with a custom fitting made from Cajon Ultratorr fittings (Figure 3.5b). The Ultratorr O-rings allowed the quartz to differentially expand. The lower 2 cm section of the probe were left unjacketed in an attempt to avoid the thermal perturbation of the flame. In practice, this design also disturbed the flame front excessively because the walls of the probe near the tip were thick enough to provide a good conduction channel to the water jacket. The fabrication cost of this probe was sufficiently high ($200) that we could not afford to have it made with a fragile, thin-walled tip.

Probe III. Copper probe - This probe was made entirely of copper except for a 10 mm x 1 mm I.D. stainless steel tip (Figure 3.5c). The PAH collected was cooled very effectively by the copper water jacket. The flame disturbance was minimized by the hot stainless steel tip which protruded ahead of the cold copper. A foil liner was placed inside the probe on which the PAH collected. This probe was used for sampling the $\varphi = 2.0$, 20 torr flame. This design was nearly acceptable except that a significant fraction of the PAH would condense right at the copper cone and before the foil liner. This material would be collected in the solvent, but the insoluble weights would be thrown off (see §3.2.2 for a detailed description).

Probe IV. Hybrid quartz/copper - This design combined the durability and rapid cooling of the copper probe with the ability to form very thin walls from quartz. The quartz probe was surrounded by a copper cooling jacket which started about 2 cm above the tip of the probe (Figure 3.5d). Because the quartz part of this probe is fairly simple, we could fabricate them in our laboratory and avoid the expense and delays of an outside glass blower. We used the technique of Fristrom and Westenberg (1965, Appendix IX–1) with a few modifications. The fabrication procedure is to turn a vertical quartz blank slowly (several rpm) with a motor while heating the lower part with a torch. The torch is held on a lab jack to keep the heating rate even. By carefully controlling heating rate and flame position, probes with very thin walls and controlled contours can be constructed. The technique of scoring the taper with a piece of broken ceramic as describe by Fristrom and Westenberg was not found to work properly. Instead, we broke the taper several mm ahead of the desired point and ground it back by hand on an abrasive wheel. The orifice was sized with fine drill bits and fire-polished to smooth the rough edge. Orifice sizes used ranged from 0.5 mm to 1.0 mm depending on the height in the flame to be sampled (larger orifices are required for greater heights due to increased soot loadings). The wall thickness was much less than 100 μm; this maintained the temperature of the probe tip as high as possible.

3.2.2 PAH SAMPLE COLLECTION AND WORKUP

The PAH sampling apparatus is shown in Figure 3.6 The probe is inserted through a Cajon Ultratorr fitting in the top of the chamber and the burner is moved to the correct HAB for the sample. A tared aluminum foil liner is rolled and slid into the probe, almost to the end. Inside the liner is a tared pyrex wool plug to trap the soot. The probe is connected via 3/4" Teflon lines to a cryogenic trap immersed in liquid N_2. Flow is drawn through the probe and trap with a Sargent-Welch vacuum pump (Model 1376). The exhaust of the pump goes to an inverted water column which serves as an integrating flow meter. The vacuum pump is warmed up for about 1 hour to drive off any volatiles which may have condensed in the pump oil which would corrupt the gas volume measurements. The pressure inside the probe is monitored with a capacitance manometer. Probe pressures are typically one

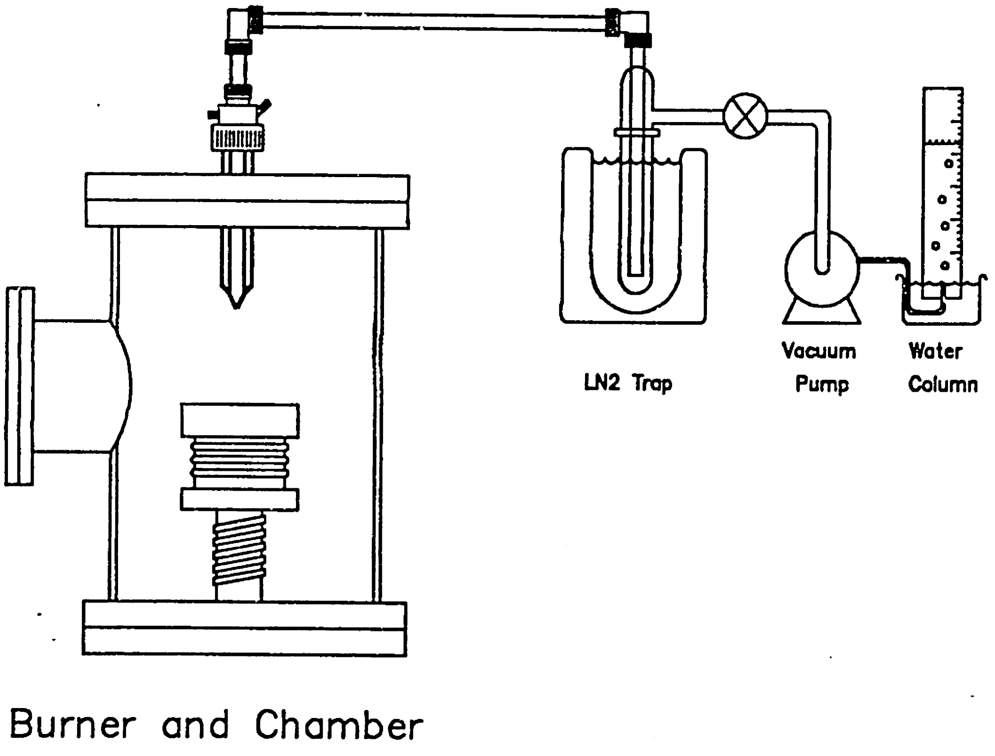

Figure 3.6 PAH sampling apparatus

torr or less when the orifice is clean (for a pressure ratio of better than 20:1). A drop in probe pressure is the indicator of tip clogging.

The high molecular weight component of the PAH (phenanthrene and larger) tends to drop out of the gas phase rapidly. Most of this material condensed on the foil liner of the probe and can be collected. A small portion pyrolyzes on the uncooled tip of the probe, which becomes unavailable for analysis but can be quantified as described below. The unburned benzene and lighter PAH travel to the cryogenic trap where they are frozen out. Sample runs typically last from 20 minutes to 1 hour. When the probe tip clogged before the sample was completed, it was opened by burning the soot off with an oxygen "lance". The "lance" is a stainless-steel tube mounted on a movable bellows seal through which oxygen can be directed to make a locally lean flame in the vicinity of the probe tip. The sampling valve is shut while the probe is being cleaned.

When the run is completed, the flame is extinguished and the combustion chamber is brought up to ambient pressure. The liner of the probe is removed and placed in methylene chloride, along with the pyrex wool plug. A small amount of solvent is used to rinse out the probe to collect any soluble material which slipped past the foil. The lines between the probe and the trap are rinsed with solvent (although not much, if any, PAH collects here). The trap is allowed to warm to room temperature and its contents are dissolved in methylene chloride. The probe liner and quartz wool plug contain soluble PAH, insoluble material, and soot. In order to maximize the amount which will dissolve, the foil and wool are covered with solvent and ultrasonicated for 1 minute. Golden and Sawicki (1975) compared ultrasonic extraction to the much more tedious and time-consuming Soxhlet extraction and found sonication to be superior. Sonication had to be limited to short times; any longer than a few minutes would rupture tiny bits of aluminum from the foil sheet, invalidating the tare weight.

After sonication, the foil and wool are dried and weighed on an analytical balance (Mettler Model H51AR) to find the insoluble content. The solvent fraction contains soluble PAH as well as suspended soot particles. The particle mass in the solvent is quantified by filtering the solvent in a tared cartridge filter (Gellman Scientific Acrodisc–CR, 0.45μm). The filter is dried and its weight gain is added to the insoluble fraction. The last portion of insoluble material appears in the pyrolyzed carbon on the uncooled end of the probe. This is quantified by weighing the probe together with the carbon. The carbon is then burned off by passing a stream of oxygen though the probe while heating the outside with an oxygen/gas torch. The clean probe is then reweighed. About 1 mg of carbon would typically be present on the tip.

The soluble PAH is typically in about 30–40 ml of methylene chloride after filtration. The solution is concentrated to about 5 ml using a blowdown procedure in which a stream of dry, filtered N_2 is directed on the solvent surface. The extremely volatile methylene chloride vaporizes in several minutes, leaving behind the relatively involatile solute and the remaining solvent. The samples are stored in a 4°C dark refrigerator to inhibit further reactions.

3.2.3 PAH ANALYSIS

The size of the PAH's present in a flame range from naphthalene (2 rings) to identified species up to naphthocoronene (Fetzer, 1986) and much higher. The objective of this project is to study the transition from large molecules to small particles, so we are most interested in the high-end fraction of the PAH. However, this is the most difficult region of the size spectrum to study. The problem lies in two areas: 1) the solubility of PAH's drops with size, preventing collection of the largest ones for chemical analysis, and 2) analytical methods have not been developed which can identify large PAH's. The analytical difficulties are due in part to their low vapor pressure (which hinders gas chromatography), their low solubility (limiting liquid chromatography), and their thermal instability (which limits mass spectrometry). *In situ* spectroscopic methods such as fluorescence tend to be non-specific and non-quantitative (Coe and Steinfeld, 1980; Coe *et al.*, 1981; Gomez *et al.*, 1987) due to the broad-banded nature of PAH spectra.

Because the isomer number for a given ring count explodes rapidly as molecular weight becomes large (*e.g.* Lee *et al.* [1981, Appendix 1] list 38 isomers of mass 302), identification of individual PAH's becomes a nearly intractable problem. Fortunately, for soot formation studies this is not a great problem for there do not appear to be any important isomer effects. All PAH's seem to contribute to soot formation according to their size alone. It is in the study of health effects of PAH's that structural effects are dominant (Longwell, 1982). The adverse health effects of the large PAH's appear to be just as severe as the small ones (Schmidt *et al.*, 1987), so we can most likely expect the health field to motivate some advances in analytical capabilities for PAH.

In this study, we have made specific identification of PAH's in the lower range (up to 250 amu) with gas chromatography. While compounds in this size range are a long way from soot nuclei, their profiles and relative proportions provide valuable information on PAH growth mechanisms. Above this size, the PAH's are grouped by operational definitions according to their solubility or affinity for a chromatography column. This created some degree of difficulty in splicing the results from the sampling work into the optical results which had its own set of operational definitions. The ultimate limit for analysis is the requirement that the PAH's be soluble in methylene chloride. On the basis of some preliminary FAB/MS (fast atom bombardment/mass spectrometry) we estimate this limit to be 900 amu (see Figure 3.8). In addition to identification of specific PAH's, we can determine ensemble properties of the group through spectroscopic methods.

Gas chromatography - We used a Perkin-Elmer Sigma One GC with a Hewlett-Packard Model 3390A integrator.[2] The column was a thick film DB–5[3], temperature programmed from −10°C to 280°C. The column was fitted with a splitter injector and a flame ionization detector (FID). Response factors were determined from a standard solution containing 19 compounds. The response factors were fit to a second order polynomial in elution time for interpolation. The method of Lee *et al.* (1979) was used for peak identification. This method is a linear interpolation between several "marker species". A GC/mass spectrometer was also used clarify some uncertain identifications. A GC/FTIR was used for confirmation of ethynyl-substituted PAH by identification of the 3300 cm^{-1} frequency of the C–H stretch.

Typically 1 to 2 μL of solvent would be injected, with a PAH concentration of 1 mg/mL. The GC could identify species up to perylene (5 rings); beyond that, the low vapor pressure and thermal instability of the PAH's caused them to pyrolyze in the injector.

---

[2] Credit for much of the development of the GC procedures goes to Craig Vaughn and Fred Lam of this laboratory.

[3] The DB-5 stationary phase is a 5% phenyl, methyl silicone. It is similar to a SE-52 stationary phase.

Gel permeation chromatography (GPC) - In principle, GPC (a.k.a. size exclusion chromatography) is an ideal method for measuring the size distribution of PAH's in solution. The method, which was developed by polymer scientists to assess the degree of polymerization, separates molecules on the basis of their ability to diffuse in and out of small pores. Large molecules are excluded by size from the pores and thus are eluted first. Smaller molecules spend more time diffusing in the pores and less time in the bulk convection flow and hence come out later. The critical requirement for the size exclusion process is that the solute have no chemical or physical attraction for the stationary phases. The stationary phase we used was a cross-linked divinyl benzene.

However, the unsubstituted PAH's did have a physical attraction for the packing while the substituted PAH's did not. This non size-exclusion behavior has been applied as a method for separating substituted from unsubstituted PAH's for further analysis (Greist *et al.*, 1979; Lafleur and Warnat, 1988), but it rendered the method, as currently developed, unusable for direct determination of molecular weight distributions. Many GPC chromatograms were made of PAH samples, but none are presented in this document due to the uncertainty in their interpretation. Further development will depend on finding the correct combination of solvent and stationary phase which will inhibit these interactions.

Tar weights - The total concentrations of PAH in solution were determined by using a modification of the tar weight method of Lafleur (1986). The concentrations were measured by putting 100 μL of solution onto a small tared boat made of aluminum foil. The solvent and light aromatics (naphthalene and lighter) were allowed to vaporize, then the boat was reweighed on a micro-balance (Perkin-Elmer Model AD-2Z) to find the mass of the involatile material. The Lafleur method prescribes a vaporization period of 3 minutes before weighing. Three minutes was the location off a "knee" in the weight loss curve from a prepared solution of model compounds. For the samples collected from benzene flames, the solvent and light volatiles were far from being completely vaporized after 3 minutes so the time was extended until the weight approach an asymptote (typically 10–15 minutes). The reason for this difference is unclear, but it could be due to the presence of a large fraction of benzene in the samples. The noise limit for the tar weight method is ±0.05 mg/ml.

Infrared Analysis - Infrared (IR) analysis identifies energy levels of the molecule corresponding to molecular vibrations. With this technique, individual bonds or functional groups may be isolated. In the analysis of PAH, one of the most useful identifications to be made is the presence of the ethynyl C–H bond at 3300 cm^{-1}. This feature is clearly separated from the other vibrations and is very sharp. Growth of PAH through acetylene is the most often proposed route for molecular weight growth leading to soot formation. If this is indeed the case then some ethynyl-substituted intermediates must be present in the flame. Figure 3.7 shows an example spectrum of PAH. The 3300 cm^{-1} feature is clearly evident.

IR can also identifies oxygenated functional groups which could be important in assessing oxidation mechanisms. Furthermore, IR has been applied in evaluating the degree of aromaticity of coal samples. Evaluation of aromaticity is more difficult because the spectral features of the aromatic ring systems are more broad and overlap other features.

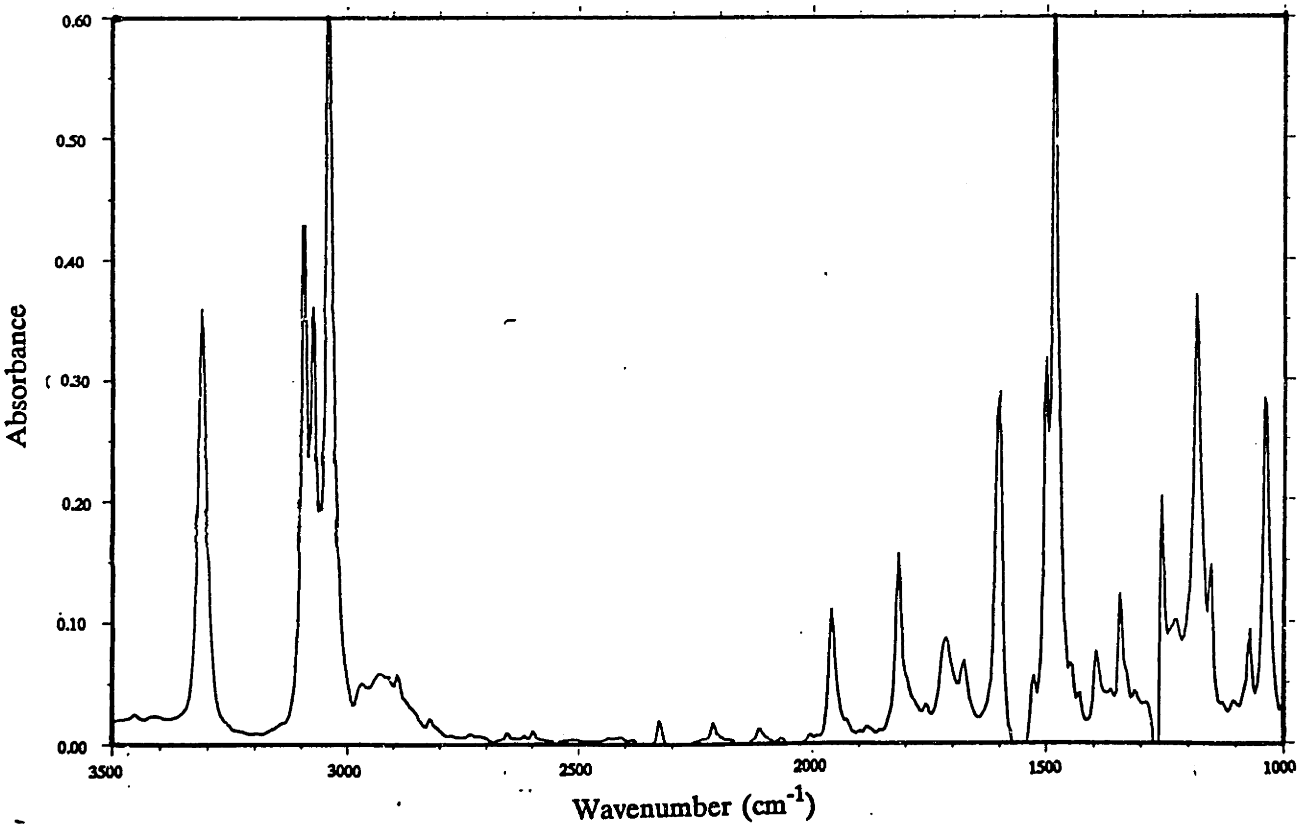

Figure 3.7 Infrared spectrum of PAH sample. φ=2.0, HAB = 5 mm

Nuclear Magnetic Resonance Spectrometry (NMR) - NMR spectra reveal the degree of energy splitting from nuclear spins aligned with and against an applied magnetic field. The degree of shielding which the electrons provide for the nucleus affects the energy levels and thus the spectra. Any nucleus with a net spin (*e.g.* ^{1}H or ^{13}C) may be used in NMR. Proton NMR was used in this study. The energy split is calibrated in terms of a chemical shift in ppm from a standard compound put in the sample (tetramethylsilane). Databases (Karcher *et al.*, 1985) of NMR spectra of PAH's have been developed and can be used for species identification. In complex mixtures, such as flame samples, species identification is not possible, but the highly quantitative nature of NMR makes it possible to determine quantities such as the fraction of carbons which are aromatic (Brown and Ladner, 1960). Another somewhat unusual use of proton NMR is for determination of hydrogen content in a sample (ASTM D 3701-83; Bouquet, 1985). The total area integrated under the NMR spectrum is directly proportional to the number of protons in the sample. Hydrogen analysis by NMR is more sensitive by about an order of magnitude than the more traditional microanalysis method.

Fast Atom Bombardment/Mass Spectrometry (FAB/MS) - Ion mass analyzers (quadrupole or magnetic sector) are clearly the method of choice for determining the molecular weight distribution of a complex, high molecular weight mixture. The problem with this method, however, lies in creating the ion and transporting it to the mass analyzer.

- The molecule usually must be in the gas phase to be ionized. Large PAH's will thermally pyrolyze before vaporizing.
- Most ionization methods fragment the molecule in the process. The cracking pattern can be a useful tool for identification when the molecule is isolated, but the spectrum of a complex mixture with significant cracking loses a great deal of information.
- Molecules have different ionization cross sections. Calibrations must be done on standards to quantify the cross section.

FAB/MS, a relatively new ionization method, addresses the first two problems. Thermal pyrolysis is avoided by ionizing the molecules in a condensed phase. The analyte is dissolved in a liquid matrix (3–nitrobenzylalcohol for PAH's) which is bombarded with high energy Xe atoms (several MeV). FAB is a relatively "soft" ionization method in that fragmentation is fairly low.[4] The relative ionization cross sections are not known and must be estimated since standards do not exist for PAH larger than about 450 amu (decacyclene), .

The MIT Spectrometry Laboratory has a FAB device mounted to a magnetic sector mass spectrometer with a size range of several thousand amu. However, FAB/MS has not yet been developed quantitatively for PAH analysis. There is some degree of reaction in the liquid matrix indicated by changes in the spectrum with the time of bombardment. To date, the usefulness of FAB has been in the identification of the upper solubility cutoff for PAH in methylene chloride. Figure 3.8 shows a FAB mass spectrum of a sample from a $\varphi=2.0$ flame at HAB=10 mm. It can be seen that the upper limit is about 900 amu.

UV-visible Spectrometry - UV-visible spectra are indicative of electronic levels in a molecule. Unlike IR spectra which are sensitive to functional groups on a molecule, UV-visible transitions are related to

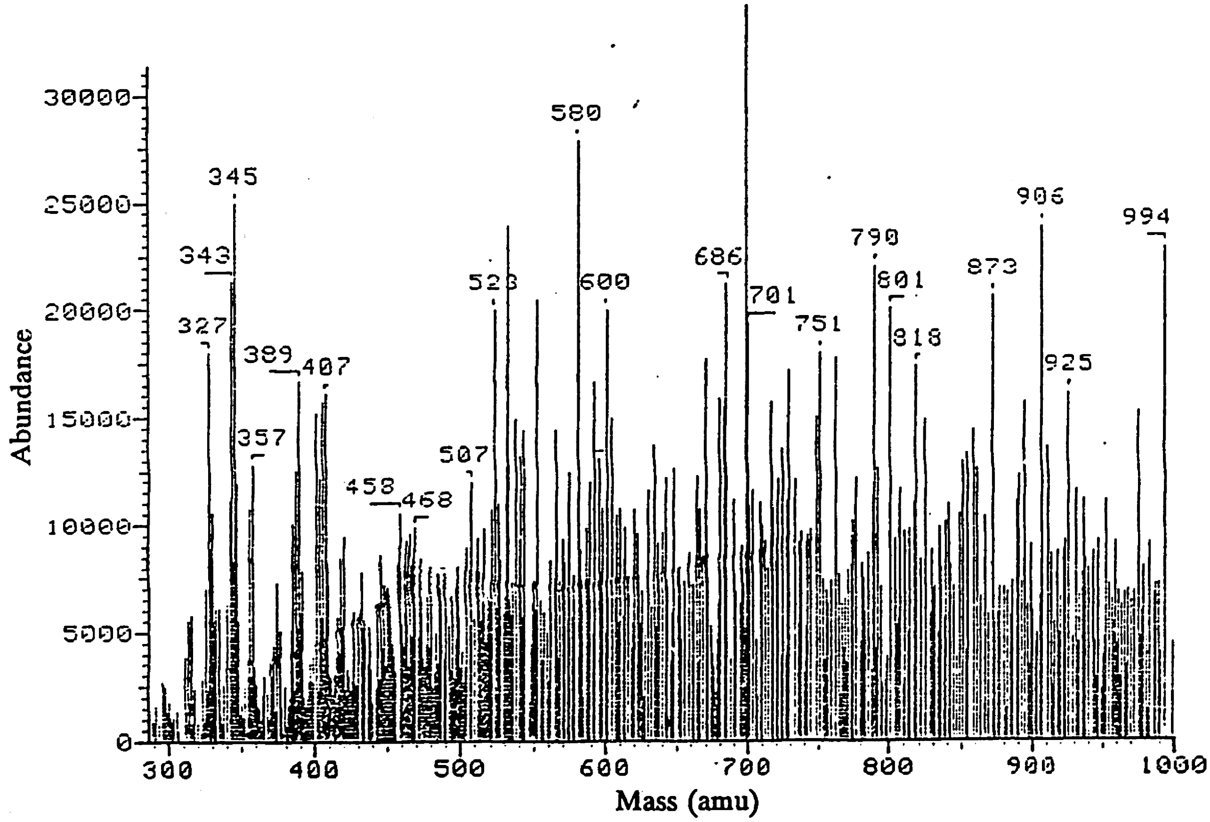

Figure 3.8 FAB mass spectrum. $\varphi=2.0$, HAB = 10 mm

---

[4] The MeV Xe atoms have enough energy to break every bond many times over, but apparently this energy is not coupled vibrationally to the analyte molecule.

the molecule as a whole. In the case of PAH molecules, the UV-visible transition corresponds to a promotion of an electron from the π to π^* molecular orbitals (Streitwieser, 1961). The theory of π symmetry molecular orbitals has been worked out in a fairly simplified form by Hückel (Heilbronner and Straub, 1966). The simplified Hückel Molecular Orbital (HMO) theory does not always predict well all molecular properties of PAH's, however, it is particularly good at estimating the lowest energy gap between the bonding and anti-bonding molecular orbitals (*para* transition). The computational requirement is merely to evaluate the eigenvalues of an N by N matrix, where N is the number of carbon atoms in the molecule, something which can be done on a small computer in seconds. See Appendix C for details of energy calculations from HMO theory. Using HMO we can predict the lowest energy, or longest wavelength, absorption feature of an arbitrary PAH molecule.

UV-visible measurements are made with an Bausch and Lomb (Model 2000 Spectronic) spectrophotometer. The sample, in methylene chloride, is placed in 2 mm path-length quartz cuvettes. The spectrum taken represents the weighted average of the spectrum of each individual component of the complex mixture. In the summation over so many components all fine structure of the spectra are destroyed. The information remaining is in the location of the long wavelength fall-off of the spectrum. Longer wavelengths the spectrum correspond to heavier components present in the sample. Thus, UV-visible spectroscopy of PAH's is a qualitative, indirect measure of molecular weight distribution.

A second use of UV-visible measurements of flame samples is to compute an effective ensemble absorption cross section for the PAH which can quantify *in situ* absorption measurements in flames. Visible absorption has been used to provide a qualitative measure of PAH content (Weiner and Harris, 1988). In order to quantify these, we need an absorption cross section for the collection of PAH. With absorption measurements on the flame samples and concentration data from tar weights we can calculate an ensemble absorption cross section. What makes this feasible is that PAH's appear in roughly the same relative proportions in many different combustion environments (compare the relative PAH proportions of Vaughn, 1988; Lam, 1988; Jones *et al.*, 1989, with this work).

Column Chromatography - As we have seen above, no analytical method is entirely suitable for a direct measure the molecular weight distribution of the PAH sample. What we rely on instead is a fractionation method which can separate the sample into to fairly broad categories. A method developed by Lafleur (1988) has been used in a slightly modified form. The method relies on a solid phase extraction cyano-column (Analytichem International, Bond Elut CN). These columns have an increased affinity for molecules with higher molecular weight and polarity.

In operation, the sample is dried on several grams of sand in an empty syringe barrel. The column which has been preconditioned by washing with all solvents (see below) is placed below the sample on the sand. The sample is first extracted from the sand with hexane (3.5 ml) onto the CN column. The amount which passes the column is collected and weighed. The same procedure is repeated with benzene (5.0 ml), methylene chloride (3.0 ml), and finally methanol (5.0 ml). We modified this procedure slightly in that the solvents are aspirated from the column rather than allowed to gravity flow. Without aspiration, there is about 1 ml of the previous solvent left in the column when the next is added. This results in a "tailing" cross-over and reduces the effectiveness of the separation.

Vapor Pressure Osmometry (VPO) - The number average molecular weights of the samples fractionated with the column chromatography method are measured with VPO. VPO employs the physical principle that a solute depresses the vapor pressure of a solvent. The instrument (Knauer Model 11.00) consists of two thermistors held in a carefully temperature controlled chamber with an atmosphere saturated with solvent. A very precise bridge circuit detects temperature differences between the thermistors to an accuracy of 10^{-3} °C. A droplet of pure solvent is suspended from one of the thermistor beads and a droplet of solvent with solute is placed on the other. Osmotic action forces solvent vapor to condense onto the droplet of solute/solvent because of its lower local vapor pressure. The latent heat of condensation causes the temperature of the thermistor to rise, which is detected at the bridge. In principle, the ΔT for a given solute concentration could be calculated *a priori*, but due to instrumental factors, such as heat conduction up the thermistor leads, a calibration is required. A calibration solution is made using a compound of known molecular weight (benzil, MW = 210) in the same solvent.

The signal from the unknown solution, together with the calibration factor, permits the number density of molecules to be determined. The mass concentration, measured with the tar weight method, allows the number-average molecular weight to be computed.

Vapor pressure depression is a colligative property; that is it depends only on the number of solute "particles". Thus, if some of the molecules form oligomers in solution they will not be counted properly. To avoid this, measurements are made at several different concentrations. The molecular weight is determined by extrapolating back to zero concentration where all the molecules would exist as monomers. In this work, however, no concentration effect was observed with the PAH solutions used.

3.3 *Optical Particle Sizing*

Light scattering and absorption has been used by many researchers to study soot dynamics. It is an ideal particle sizing method in many senses because it is nonintrusive and the data may be produced very rapidly once the apparatus is in place.

3.3.1 THEORY OF LIGHT SCATTERING AND ABSORPTION APPLIED TO SOOT AEROSOLS

One of the first researchers to apply scattering to a sooting flame was Erickson (1961) who used a xenon lamp as a light source. Since then lasers have made the technique much more powerful as well as easier. Several books cover the basics of general purpose light scattering; van de Hulst (1957) and Bohren and Huffman (1983) were used as references in this laboratory. Mie theory is used in the general case to describe light scattering from particles. When the particle diameter is much smaller than the wavelength of light, the much simpler Rayleigh limit theory may be applied. All measurements made in this work were in the small size limit, so only the Rayleigh theory will be discussed.

Light scattering and absorption provide two independent pieces of information about an aerosol from which we may deduce two independent results. An aerosol may be characterized by an infinite number of moments, so we cannot completely describe the system with just two measurements. It is most useful to use the experimental information to compute the zeroth moment (number density) and the first moment (diameter) and assume a form of the size distribution which fixes the rest of the moments. A great deal of discussion has gone on in the literature about the proper form to use for the size distribution of a soot aerosol. Usually this revolves around whether a log-normal distribution or a self-preserving size distribution (which are quite similar in appearance) is more appropriate. The ultimate numerical answers, however, are not very sensitive to the choice of distribution. In fact, even if we assume the simplest possible distribution, monodisperse, the results change by less than a factor of two. Importantly, the form of the size distribution has no bearing on the volume fraction measurement, which is the one used to tie together sampling and optical experiments. We have chosen a log-normal distribution because it is analytically more tractable than the self-preserving size distribution.[5]

In addition to the form of the distribution, we must assume optical properties for the soot. Many workers have measured the index of refraction of soot, both *in situ* and from samples removed from the flame (Stull and Plass, 1960; Howarth *et al.*, 1966; Dalzell and Sarofim, 1969; Chippet and Gray, 1978; Lee and Tien, 1980; Charalampopoulos and Felske, 1987). In this work we have used the values of Lee and Tien. Appendix D. shows the sensitivity of the results to changes in index of refraction of the soot. In general, the range of uncertainty results in a deviation of much less than a factor of two in the desired

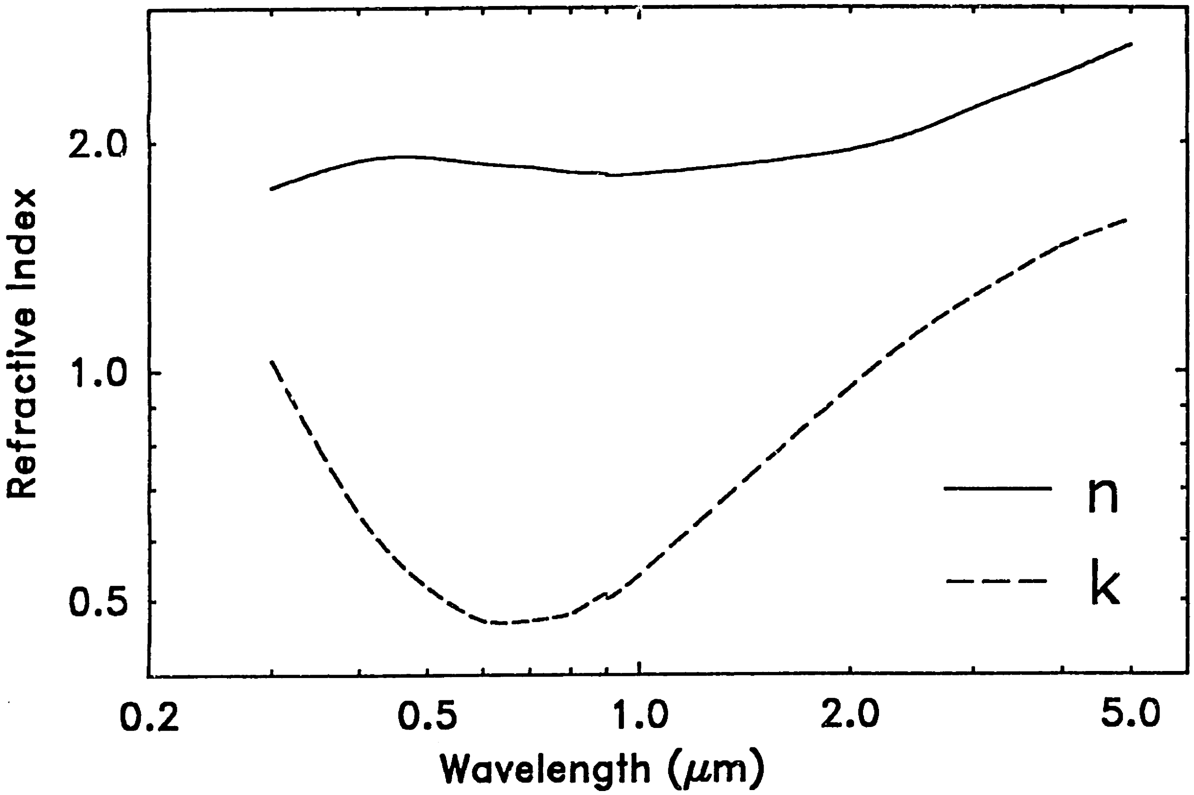

Figure 3.9 Index of refraction vs. λ for soot as measured by Lee and Tien

---

[5] The modeling results which will be presented in Chapter Six indicate that neither of these forms is really correct in the soot nucleation zone. The assumed distributions always rise, peak, then decline. In the nucleation zone, there is a monotonic decrease in concentration with size. The d^6 dependence of scattering, however, helps make this inconsistency unimportant.

quantities. The wavelength dependence of the index of refraction is, however, of great importance to this work because experiments are done at several wavelengths and the results are tied together. Figure 3.9 shows the Lee and Tien dispersion plot along with some data points from other laboratories. The greatest potential difficulty in using published values for index of refraction is that they are measured on "mature" soot which has traversed a high temperature environment for several milliseconds before collection. It is known, however, that the H/C ratio of soot changes with age (Wagner, 1979). Charalampopoulos and Felske (1987) have made an *in situ* measurement of the index of refraction a function of time at a single wavelength in a CH_4/oxygen atmospheric-pressure flat flame and found that assuming an average value for the index of refraction the errors would be less than 25% in number and 15% in diameter.

Scattering - In scattering experiments, we measure the light emitted from the aerosol when illuminated by an incoming beam. The method described here is elastic scattering, meaning that the light measured at the detector is of the same wavelength as the source. In addition, all experiments were done in vertical-vertical configuration. That is, the polarization of the incoming beam and the polarization of the examined light were both normal to the plane formed by the path of the laser beam and the path of the examined light. The subscript "vv" (*e.g.* C_{vv}) indicates a quantity dependent on the orientation of the polarization.

Equation 3.3 describes the light collected by the detector as a function of the incoming light flux, the optical properties of the aerosol, and the geometry of the collection optics (Figure 3.10).

$$\dot{E}(\theta) = Q_{vv}\, \delta V\, \delta\Omega\, I_o \tag{3.3}$$

$\dot{E}(\theta)$: energy flux at the detector
Q_{vv} : energy flux scattered ($cm^{-1}\ str^{-1}$)
δV : scattering volume
$\delta\Omega$: solid angle of collection optics
I_o : Incident laser intensity

We are able, through a calibration procedure, to avoid the difficult (and probably impossible) calculation of the geometrical quantities in Equation 3.3. The quantity Q_{vv} is related to the physical properties of the aerosol through Equation 3.4.

$$Q_{vv} = N\,C_{vv} \tag{3.4}$$

$$C_{vv} = \frac{\lambda^2}{4\pi^2} \left| \frac{m^2-1}{m^2+2} \right| \int_0^\infty f(\alpha)\,\alpha^6\,d\alpha \tag{3.5}$$

N : number density
C_{vv} : scattering cross section
α : $\pi d/\lambda$, d : diameter
m : complex index of refraction $(n + ik)$
$f(\alpha)$: size distribution

Absorption - Absorption, unlike scattering, is a line-of-sight technique. Thus, the measured quantity is an integrated average over the beam path. The measurement will be distorted if the aerosol is not uniform over the path. Efforts were made to ensure that this was the case through careful design of the burner. The Lambert-Beer law (Equation 3.6) describes the absorption phenomenon.

$$\frac{I_\lambda}{I_{\lambda o}} = \exp(-NC_{ext}L) \tag{3.6}$$

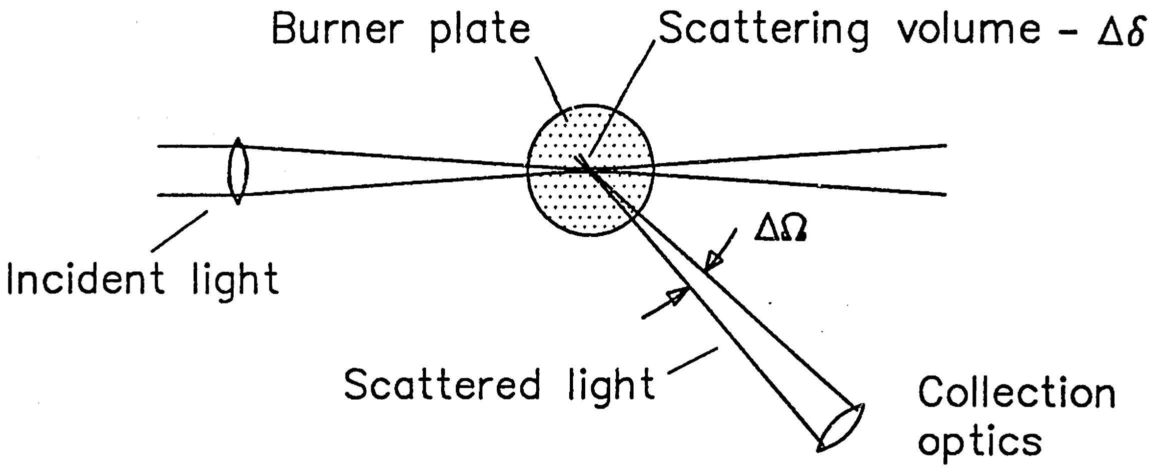

Figure 3.10 Simplified scattering schematic

$$\frac{I_\lambda}{I_{\lambda o}} = \exp(-NC_{ext}L) \qquad (3.6)$$

I_λ : attenuated beam intensity at λ
$I_{\lambda o}$: incident beam intensity at λ
C_{ext} : extinction cross section
L : absorption path length

The Rayleigh theory allows physical quantities to be deduced from the absorption measurement (Equation 3.7). Alternatively, the absorption equations may be cast with the dependent quantity as volume fraction (f_v), as in Equation 3.8.

$$C_{ext} = \frac{-\lambda^2}{\pi} \text{ Im}\left(\frac{m^2-1}{m^2+2}\right) \int_0^\infty f(\alpha)\alpha^3 \, d\alpha \qquad (3.7)$$

$$f_v = \frac{\lambda}{6\pi L} \; \frac{\ln(I/I_o)}{\text{Im}\left(\frac{m^2-1}{m^2+2}\right)} \; \exp(-\frac{9}{2}\sigma^2) \qquad (3.8)$$

C_{ext} : extinction (absorption) cross section
σ : standard deviation of log-normal distribution

Several problems can confound the measurement of physical properties with scattering and absorption. In the nucleation zone of the flame, the soot scattering signal is low because the small particle size coupled with the sixth power dependence of signal on size. In this region the scattering from the gas molecules can exceed the particle scattering. We can deal with this problem if we know the gas concentration and the scattering cross sections for the major species (C_6H_6, CO, H_2O, CO_2, H_2, *etc.*). The gas concentrations are measured and the optical properties of the gases are published (CRC, 1974, p.E-223). The light gas component to the scattering signal is thus computed and subtracted away.

A more serious problem is that PAH molecules absorb visible light along with the soot. Because scattering has a d^6 dependence on diameter, the PAH do not contribute to that signal. Serious errors will result from combining absorption measurements which contain a PAH component with scattering measurements which do not. We partially avoid this problem by making the absorption measurements in the near infrared (1.4 μm). Any species which is large enough to absorb at this wavelength is operationally *defined* to be a soot particle.

3.3.2 OPTICAL APPARATUS

Scattering system - The light source for the scattering measurements is a three-watt argon-ion laser (Spectra Physics Model 2020–03). The laser has a single-line prism mounted ahead of the high reflector which can be tuned to a single wavelength. In our case, we selected the 488 nm line. Figure 3.11 shows a schematic of the laser scattering system. The laser is mounted on the optical table with the beam directed by a series of mirrors to the combustion chamber. The beam is focussed by a 40 cm F.L. lens and modulated at 400 Hz with a mechanical chopper (Laser Precision, Model CTX–534). The beam waist is approximately 100 μm at the focal point. Both the entrance and exit windows of the chamber are mounted at Brewster angles (55°) which virtually eliminate reflections which would wipe out the small scattering signal. The beam exits the back side of the chamber into a beam dump. The scattered signal is collected at 135° (particles in the Rayleigh regime backscatter as strongly as they forward scatter). The scattered light is collected with a 10 cm F.L. lens with a 2 cm diameter aperture. The image of the beam focussed with a 1:1 magnification ratio onto the entrance slits of an S–20 type photomultiplier tube (Centronics Model 4283R). Behind the slits is a narrow band (1 nm FWHM) interference filter tuned to 488 nm. The width of the entrance slits and the beam waist determine the scattering volume. In our case the slit width is 3.2 mm; with a beam waist of 100 μm, this gives a volume of $2.5\text{x}10^{-5}$ cm^3. The height of the slits must be enough to allow all the image of the beam waist to pass, but be small enough to keep out an excessive amount of incandescent radiation from the soot. The PMT is mounted in a thermoelectrically cooled housing (Products for Research, Model TE 104–TS) which is maintained at –25 °C. Cooling the PMT dramatically reduces the dark current, which is primarily due to thermally generated electrons, rather than photoelectrons. The PMT was operated at the highest bias possible while still keeping the cathode current within an acceptable range (< 50 μA). The nominal bias was –1200 V.

The PMT current was converted to a voltage through a 300 KΩ resistor with a parallel capacitor of 510 pF, creating a low-pass filter with $\tau \approx 1$ ms. The signal was sent to a lock–in amplifier (PAR Model 5101). The lock–in amplifies the signal in–phase with the reference signal from the chopper.

background incandescent radiation from the soot because the soot background is both broadband and D.C. However, the D.C. rejection limit of the lock–in is only about 1 part in 10^3. In the zone of the flame where nucleation is the dominant process, the black body soot emission at 488 nm within the 1 nm filter bandwidth is four orders of magnitude greater than the scattering. . This problem caused quite a bit of consternation (plus a month or so of lost time), but was finally solved by the placement of a band-pass filter tuned to the chopper frequency in the line ahead of the lock–in. The D.C. background continued to be the limiting noise level, but it was manageable with the band-pass filter.

Absorption system - Figure 3.12 shows the absorption equipment in schematic form. The absorption light source was a tungsten filament lamp (G.E. Model 20A/T24/2) driven with an D.C. power supply (Hewlett-Packard Model 6264B). Tungsten lamps are among the most stable of light sources. The absorption levels needed to be measured are on the order of 1 part in 10^3, so tiny drifts in source intensity can nullify the measurement. The current to the lamp was monitored by noting the voltage drop across a low-resistance precision resistor (Dale Model SP R 390–1, 4.962 mΩ) in series with the power line. An image of the filament was focussed to the axis of the chamber with a 20 cm F.L. lens. The focussing lens was blocked with a rectangular aperture, 20 mm wide by 1.5 mm high. This arrangement greatly increased spatial resolution of the measurements by limiting the vertical divergence of the light, but the wide horizontal slit allowed an ample amount of light to reach to the collection optics. The beam was chopped by the same device used for scattering. The image of the filament was focussed onto a set of adjustable slits in front of the light detector. This set of slits further defined the spatial resolution. Several light detectors were used in the absorption experiments, depending on the wavelength. For the shorter wavelengths (410 nm to 633 nm), we used the same PMT (S–20) as for scattering. In the intermediate range (725 nm and 900 nm), we used an S–1 PMT at room temperature. For the near infrared, the detector used was a Ge photodiode (Hammamatsu Model B2538–05) which had a thermoelectric cooler built into the chip package. The diode was cooled to –20 °C with 1 amp D.C. current. The diode has broad band sensitivity from 0.8 to 1.8 μm, but for absorption purposes it has an effective wavelength of 1.4 μm.

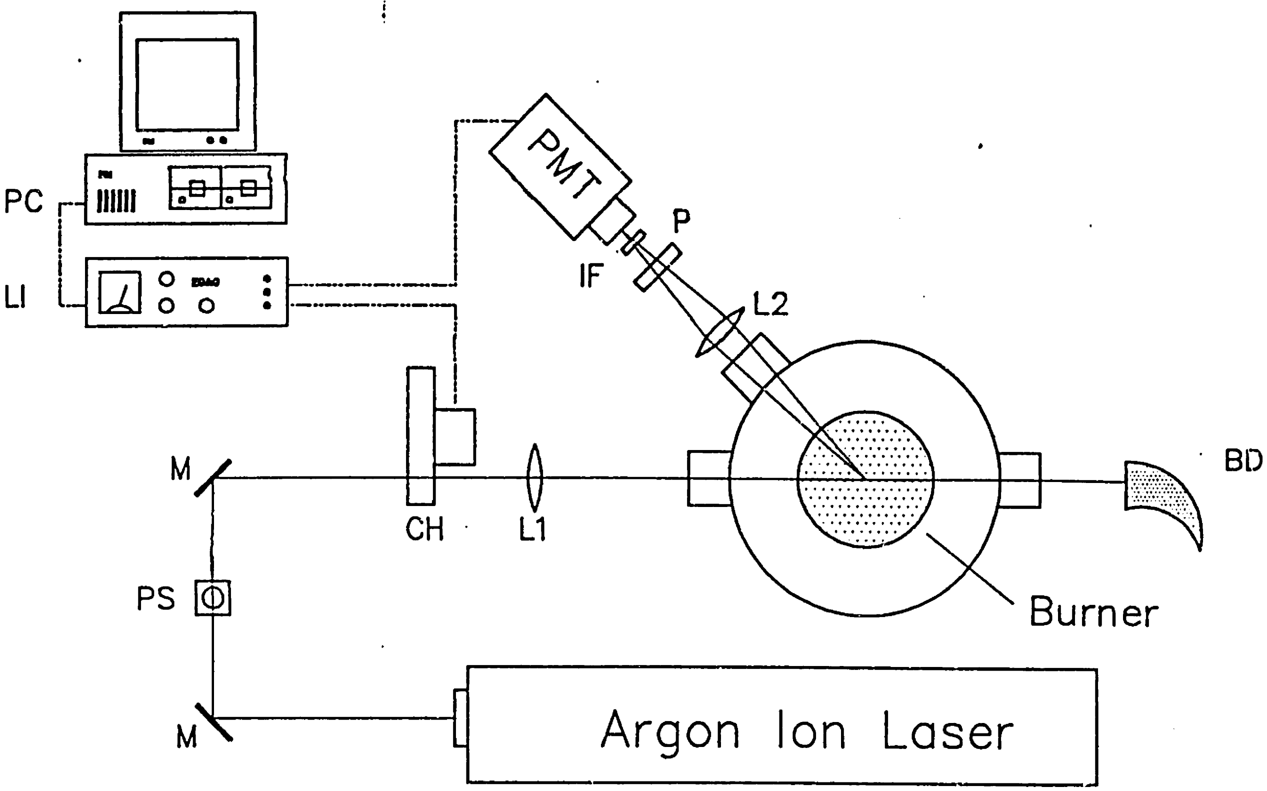

Figure 3.11 Laser scattering apparatus. CH - chopper; L - lens; BD - beam dump; M - mirror; PS - periscope; P - polarizer; IF - interference filter; LI - lockin amplifier.

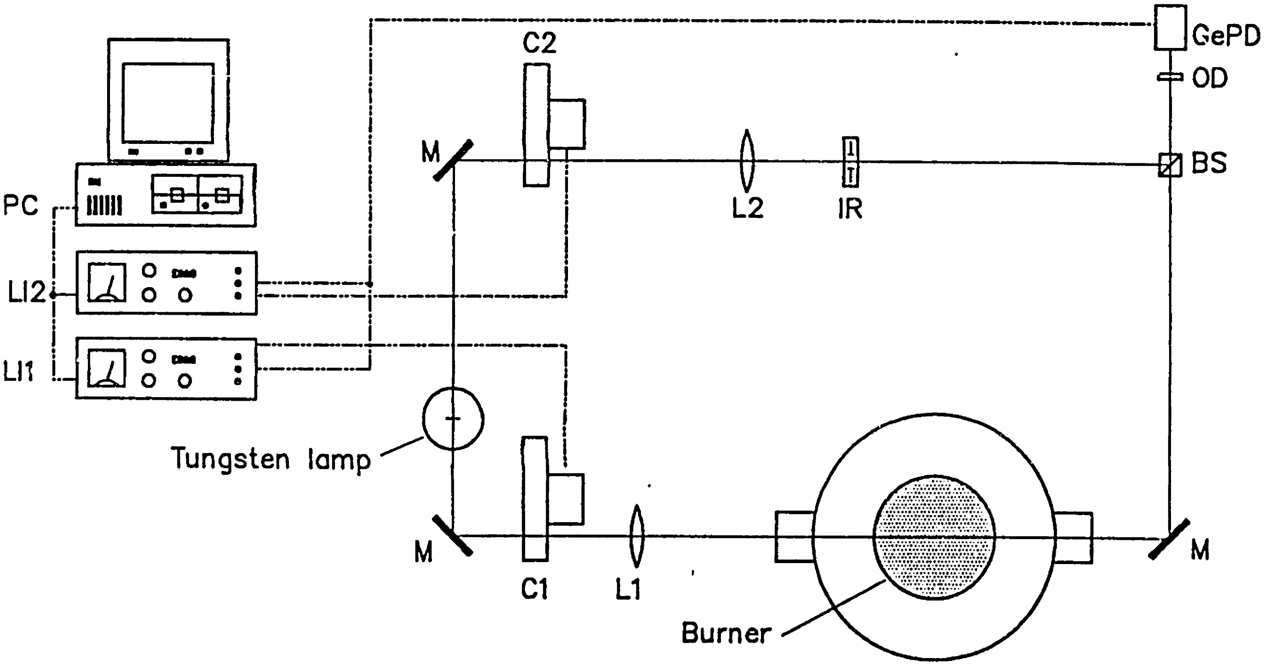

Figure 3.12 Absorption apparatus. C - Chopper; BS - beam splitter; OD - opal diffuser; GePD - germanium photodiode; LI - lockin amplifier; M - mirror; IR - iris.

Although the tungsten lamp was quite stable, the combination of its drift and the drift of the detector proved to be too much for the low level measurements. A reference channel was constructed which had the effect of nulling out any common mode drift. A portion of the light from the bulb was directed around the chamber with mirrors and a lens and was combined with the main beam using a beam splitter at the entrance of the detector. The intensity of the reference beam was adjusted, using an iris and a variable neutral-density filter, to exactly equal the I_0 of the main beam. The reference beam was also chopped, but at a different frequency than the main beam. The signal from the detector contained both frequency modulated measurements. By sending the signal to two lock–in amplifiers, one triggering off the main chopper and the other triggering from the reference chopper, we could extract the independent measurements.[6] By ratioing these two signals, any drift from the lamp or detector will be common to both channels and can be divided away.

The burner height was indexed against the beam position by placing a horizontal razor blade on the burner plate and raising the burner until half the transmitted light was blocked. At that point, the HAB equalled the distance from the razor edge to the burner plate.

Optical alignment - Both the scattering and absorption systems were aligned in the same general method, as described below. First all lenses, apertures, *etc.* were removed from the beam path. A cathetometer was sighted down the beam path (with the light source off!) in the reverse direction and all mirrors were aligned so the beam is level and orthogonal. The source focussing lens was placed in the beam path and the cathetometer was focussed over the burner plate. The lens was positioned such that a sharp image of the source was projected over the burner plate. The focus of the cathetometer was then backed off to the plane of the detection device. The collection lens was mounted and adjusted until the image of the image was cast on the detector entrance. The system was fine-tuned with the source turned on by tweaking the micro-adjusts of the lens holders to maximize the signal. The laser high reflector was adjusted in the same manner.

---

[6] This concept is most easily visualized in the frequency domain. Each signal would exist as a delta function, widely separated in frequency space. The only concern is that none of the harmonics (only odd ones exist for square waves) lie on top of each other. Frequencies were selected to avoid this.

Stray light from reflections off windows, the burner surface, and the chamber walls was a major problem. The reflections were dealt with mainly by placing carefully aligned stops ahead of the entrance window to block off all the laser light not collimated. Outside the chamber, the beam path was enclosed to prevent reflected light from the optics from entering the detector.

The scattering system was calibrated by measuring the scattered signal from a gas with a known scattering cross section at a known temperature and pressure. Obtaining a scattering calibration factor avoids the requirement of estimating the geometrical the parameters in Equation 3.3. The calibration is performed directly before the flame measurement, ensuring that all the optics, laser, *etc.* are the same for both calibration and measurement.

We can guarantee that all reflections are removed in two ways. First, the calibration is repeated with two gases (N_2 and CO_2). We know the refractive index of each gas, so the ratio of the signals must be the same as the ratio of the C_{vv}'s if no reflections are present. A second test is to make the calibration at several different pressures (10 torr to 80 torr). A least-squares linear fit of the scattering signal versus pressure will have an intercept of zero with no reflections. A reflection signal of less than 5% of the lowest flame signal was determined acceptable.

3.4 Light Gas Analysis

Light gases (up to benzene) were measured using uncooled sampling probes coupled to an online mass spectrometer. The probes were the same ones described above for PAH sampling, but they were used without the water cooling jacket. Figure 3.6 is a schematic of the sampling apparatus. It is largely the same as the sampling train used for PAH, but the cryogenic trap has been replaced with a trap at 0 °C filled with pyrex wool. The cooled high-surface-area glass wool is intended to adsorb the PAH, keeping them from clogging the frit at the inlet of the mass spectrometer, but allow water vapor to pass.

The mass spectrometer is a VG Model Q7B. It has a quadrupole mass filter and a tungsten-filament ionizer at 70 eV ionization energy. The system was maintained at 10^{-7} torr with a 4" diffusion pump. The analog output from the quadrupole amplifier was fed to the lab computer. Spectra were taken at 0.1 Hz (100 amu scan) and ten spectra were averaged per sample. Figure 3.14 shows a typical mass spectrum from the flame.

A given peak of the mass spectrum contains the linear sum of all the fragments from the molecules present in the sample. The literature contains fragmentation patterns (Stenhagen *et al.*, 1974) of all the major species present in the flame. The ionization cross sections are also published (Otvos and Stevenson, 1956; Lampe *et al.*, 1957), but as there is quite a bit of scatter in the values it is better to calibrate for them directly.

The calibration procedure went as follows. A calibration gas was made up containing the test gas diluted by argon. Concentrations of the calibration gas represented roughly those present in the flame. The calibration gas was made by evacuating a 6 L vessel, filling it to a known pressure with the test gas using a Hg manometer, and then diluting to atmospheric pressure with argon. The vessel contained several hundred 4 mm glass beads. These were used to ensure mixing of the gases by shaking the vessel, inducing gas mixing by the bead motion.[7] Table 3.2 shows the measured ionization cross sections for the gases of interest. Table 3.3 shows the fragmentation patterns.

A problem encountered with the mass spectral measurements was that the oxygen would tend to reduce to carbon monoxide and carbon dioxide on the hot, catalytic tungsten filament. The carbon source appeared to be from a coke layer that would form on or near the filament.[8] This problem was handled by calibrating the device with an oxygen/hydrocarbon (benzene) mixture fairly representative of what was present in the flame. The fraction of O_2 converted to the carbon oxides was taken into account in the calibration factor. Filaments coated with non-catalytic surfaces (rhenium, thoriated iridium, lanthanum hexaboride) can greatly reduce these reactions, but they were not available at the time the experiments were run.

The abundances at each mass observed in the mass spectrum need to be reduced to concentrations of gases which entered the ionizer. Each peak represents the sum of fragments from several molecules and there are more peaks than molecules. Mathematically, this is an overconstrained system of linear equations. In our case we had 13 components which summed to produce 22 major peaks. This can be solved in a least squares sense using Householder orthogonalization with column pivoting. The program

---

[7] It would seem that the gas would intimately mix without shaking. However it was observed that the signals from calibration gases which were not shaken drifted with time, indicative of concentration gradients in the vessel.

[8] We believed this to be true because the amount of oxygen converted just after the machine was switched from an oxygen-free gas source to an oxygen-containing gas source would rise rapidly, then fall after several minutes.

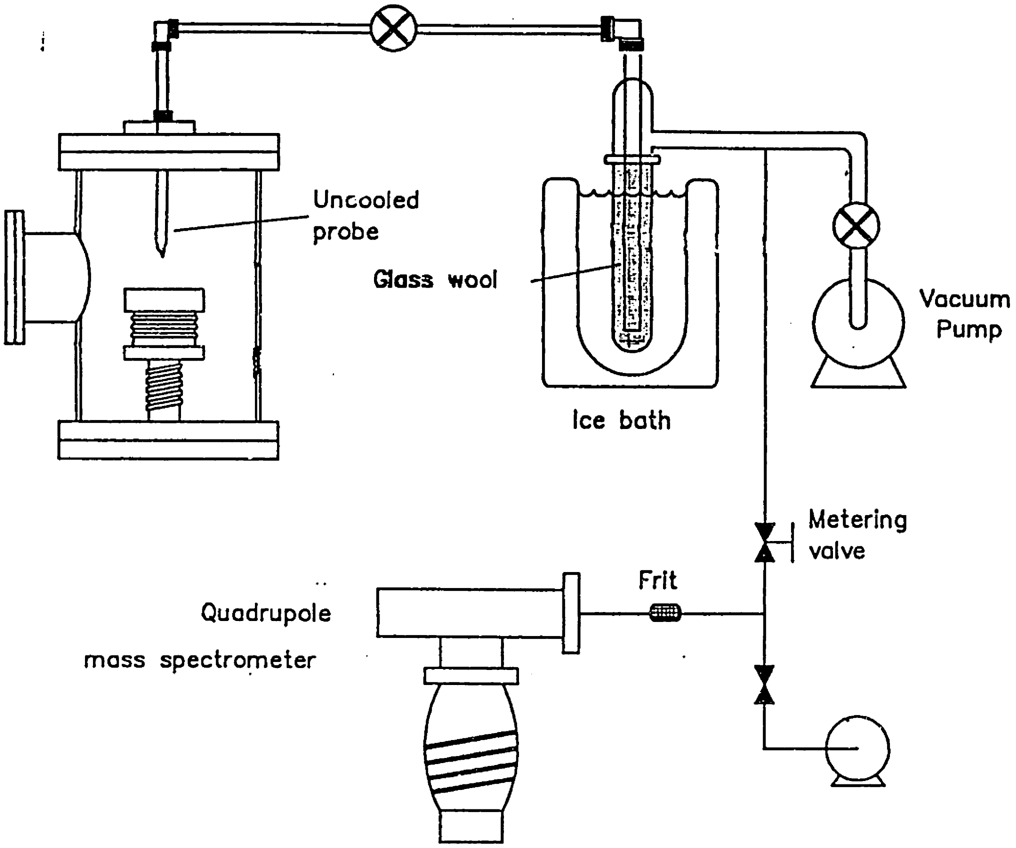

Figure 3.13 On-line mass spectrometer apparatus for sampling and analyzing light gases.

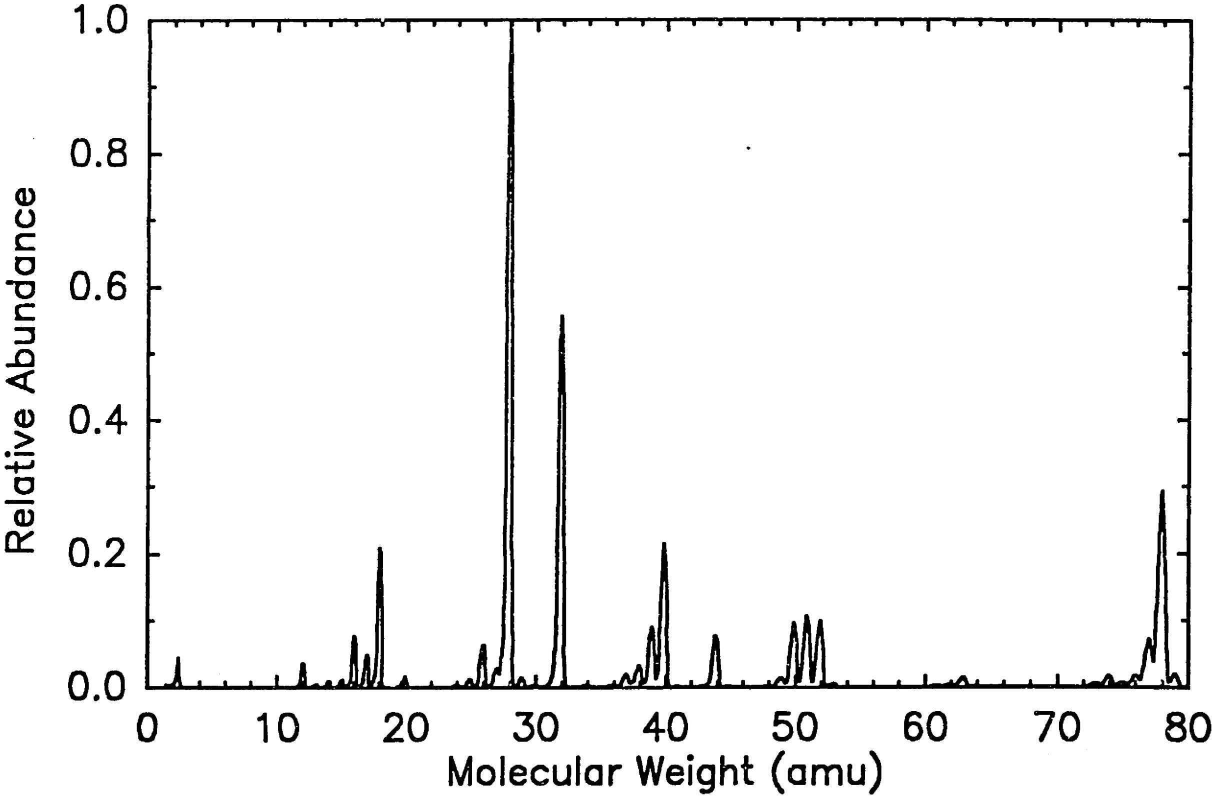

Figure 3.14 Typical mass spectrum from flame sample. HAB = 6 mm, φ = 2.4, 10% Ar, 40 torr

package PC–Matlab (The MathWorks, Inc., Sherborn, MA) does this computation directly.

3.5 Temperature Measurement

Temperature is one of the most critical parameters in interpreting flame data; many reactions have very high activation energies and temperature gradients are extremely steep (order 10^3 °C/mm). Despite this, it is one of the most difficult measurements to make. The commonly used methods are:

- thermocouples
- Na–D line reversal
- Kurlbaum (in sooting flames)
- various spectroscopic methods (Drake *et al.*, 1979)

Each of these methods was unsuitable for our set of conditions. Thermocouples have serious errors due to radiation losses. These may nulled out using an AC heating technique (Gilbert and Lobdell, 1953). However, this method requires that the emissivity of the thermocouple surface be the same during the calibration (in a vacuum chamber) as during the measurement. This requirement could not be met in a sooting flame. Sodium–D line reversal requires adding Na^+ ions to the flame. Numerous studies (Howard and Kausch, 1980; Ritrievi, 1984) have noted that metal additives have an effect on soot formation. Since we are seeking a non-intrusive method of monitoring temperature, Na–D line method was unacceptable. Kurlbaum is an absorption method similar to Na–D line reversal which employs the soot rather than an additive as the absorption medium. It appeared to be the most promising method,

Table 3.2 Ionization cross-sections normalized to argon.

Molecule	Cross Section
H_2	0.25
O_2	0.56
CO	1.26
CO_2	0.88
CH_4	0.70
H_2O	1.00
Ar	1.00
C_2H_2	1.11
C_2H_4	1.23
C_2H_6	1.00
C_4H_2	2.00
C_4H_4	1.20
C_6H_6	0.78

Table 3.3 Cracking patterns of flame molecules. Normalized to largest peak.

Mass	H_2	O_2	CO	CO_2	CH_4	H_2O	Ar	C_2H_2	C_2H_4	C_2H_6	C_4H_2	C_4H_4	C_6H_6
2	100	0	0	0	0	0	0	0	0	0	0	0	0
12	0	0	3.5	5.7	4.9	0	0	2.4	2	0	3	0	0
14	0	0	0	0	79.7	0	0	0	5	2	0	0	0
15	0	0	0	0	100	0	0	0	0	0	0	0	0
16	0	11.4	1.6	13.3	0	1.1	0	0	0	0	0	0	0
17	0	0	0	0	0	23	0	0	0	0	0	0	0
18	0	0	0	0	0	100	0	0	0	0	0	0	0
25	0	0	0	0	0	0	0	22	8	2	10	2	0
26	0	0	0	0	0	0	0	100	45	23	0	9	7.4
27	0	0	0	0	0	0	0	2.5	46	32	0	1	9.9
28	0	0	100	26.9	0	0	0	0	100	100	0	0	0
29	0	0	1.3	0	0	0	0	0	2	22	0	0	0
32	0	100	0	0	0	0	0	0	0	0	0	0	0
37	0	0	0	0	0	0	0	0	0	0	5	3	5.2
38	0	0	0	0	0	0	0	0	0	0	0	1	6.7
39	0	0	0	0	0	0	0	0	0	0	0	0	11.6
40	0	0	0	0	0	0	100	0	0	0	0	0	0
44	0	0	0	100	0	0	0	0	0	0	0	0	0
50	0	0	0	0	0	0	0	0	0	0	100	45	32.6
51	0	0	0	0	0	0	0	0	0	0	5	48	36.5
52	0	0	0	0	0	0	0	0	0	0	0	100	35.1
78	0	0	0	0	0	0	0	0	0	0	0	0	100

but in practice, the soot loadings of our flames were too low for reliable measurements (uncertainties were order 100°C for the best case).

The technique ultimately used was the brightness method (Fristrom and Westenberg, 1965; D'Alessio *et al.*, 1972). This procedure requires the brightness temperature of the flame and the emissivity of the flame. The brightness temperature is the temperature at which a black body would radiate light at the same intensity as the flame. The emissivity, defined as the ratio of actual emission at a given temperature to the black body emission at the same temperature, is the same as the absorptivity as stated in Kirchoff's laws. The absorption measurements made as part of the particle sizing (§3.3.1) are used. Equation 3.9, derived from Wien's formula for radiation by setting the radiance of a black body at T_B equal to the radiance of a grey body of emissivity ϵ and temperature T, allows the true temperature to be calculated (Koskowski and Lee, 1962, Equation 6-3). The brightness temperature of the flame is measured using an optical pyrometer (Pyro Instrument Model 95). An aperture placed in the field of view of the pyrometer is set to ensure that the solid angle of view is the same as that for the absorption optics. The largest source of error with this procedure is in the measurement of absorption. Typically these signals are reproducible to about 10% or better. From Equation 3.10, which is Equation 3.9 differentiated, we can see that 10% error in ϵ leads to an uncertainty in temperature of ±20°C at 2000 K.

The effective wavelength of the pyrometer is 655 nm, determined by the product of a bandpass filter in the instrument and the spectral sensitivity of the human eye. The absorption measurements at 488 nm were used to convert the brightness temperature to flame temperature. The absorbance at 655 nm may be calculated from the 488 nm value using the $1/\lambda$ wavelength dependence of absorption for Rayleigh particles ($d << \lambda$).

$$T^{-1} = T_B^{-1} - \frac{\lambda}{C_2} \ln \epsilon_\lambda \tag{3.9}$$

$$\frac{\Delta T}{\Delta\epsilon/\epsilon} = \frac{\lambda T^2}{C_2} \tag{3.10}$$

T_B : brightness temperature

ϵ : emissivity

λ : wavelength of measurement, 655 nm for optical pyrometers

C_2 : second radiation constant, 1.439 cm deg

3.6 Soot Samples

A limited number of soot samples was taken for analysis by X–ray diffraction (XRD) and transmission electron microscopy (TEM).[9] XRD requires a fairly large sample (>100 mg) so we sampled a very rich flame ($\varphi=2.5$) with no Ar dilution (the main effect of the diluent gas is to increase flame speed, increasing temperature, which reduces soot loading). A large orifice (2 mm) probe was connected to a large area fritted disk. The collected sample was scraped from the fritted disk into the sample vial. A sample of "mature" soot was also analyzed. This specimen was taken from the cooling plate of the upper chamber flange.

---

[9] Analysis done by Larry Ebert of Exxon Research-Sciences Laboratory, Clinton, N.J.

Chapter Four

Results

This chapter contains the results of the combustion experiments and a limited discussion of these experiments. More detailed discussions related to overall mechanisms can be found in Chapter Five.

4.1 PAH Probe Sampling

Probe samples have been analyzed using capillary GC, gravimetric methods, and column chromatography.

4.1.1. LIGHT PAH ANALYSIS

Detailed analyses of the light PAH's using capillary gas chromatography were made for two flames: $\varphi = 2.0$, 20 torr, and $\varphi = 2.125$, 40 torr. The GC was limited to species less than about 250 amu due to thermal instability of the large molecules. As described in §3.2.3, the identifications were made based on the retention index method of Lee (1979). Figures 4.1 through 4.8 show the profiles for most of the identified PAH's. The profiles for all the species are presented numerically in Appendix A.

About 35 species larger than benzene were identified from the chromatogram. The chromatogram typically contained hundreds of peaks, but the total unidentified area an insignificant fraction (*ca.* 10 - 20% of the total). Presumably the unidentified peaks are substituted PAH's. Their low concentrations combined with the large isomer count (*e.g.* there are ten isomers of methyl- cyclopenta(*c,d*)pyrene) could account for the "grass" seen in the chromatogram. Three general classes of species are observed:

- highly condensed PAH's (*e.g.* pyrene)
- substituted PAH's (usually ethynyl substituted, but also methyl)
- PAH dimers with biphenyl-type bridges.

The first two classes are consistent with the concept of PAH formation through sequential addition of C_2H_2 addition to ring structures. This is the sequence typically proposed by many workers (Bittner, 1981, Chapter 10; Frenklach *et al.*, 1986, Bockhorn *et al.*, 1986). The third class is indicative of a second growth mechanism which proceeds through dimerization.[1]

Two main features are readily apparent in the profiles. First, the concentration of all the species drops precipitously right at the soot nucleation zone (as identified by the yellow luminosity). Second, the relative decay of the lighter species is more than the heavier ones. Several other features of the profiles are worthy of note:

- The relative concentrations are generally in inverse proportion to their size. Phenylacetylene is the most concentrated species.
- Among the species with the same carbon number, the most unsaturated is always the most concentrated (*e.g.* phenylacetylene > styrene).
- Benzaldehyde and phenol are the only oxygenated species identified, and they are in low concentrations. No large PAH's were seen with oxygen functionality. This is somewhat surprising since elemental analysis of soot usually identifies oxygen as a component.
- Polyacetylenic species are relatively unimportant. Only triacetylene is seen in the solvent samples. Diacetylene was identified in some preliminary gas samples but was not in sufficient concentration to be seen by the mass spectrometer. In the $\varphi = 2.125$ flame, the triacetylene peaks 2 mm before the PAH's which could be a significant indicator of a mechanism. This early peaking trend, however, is not observed in the $\varphi = 2.0$ case.
- Many species have five-membered rings. Two types of five-membered rings exist. In the first type all the carbons are sp^2 hybridized and all double bonds are conjugated into the rest of the ring π system. Acenaphthalene is an example of this type. The second type contains one sp^3 methylene carbon bridge. The first type is consistent with a growth mechanism through sequential C_2H_2 addition. The type with methylene carbons could be formed through this mechanism, but an equally plausible mechanism is that these species are products of an oxidation reaction. For example, fluorene could be the product of phenanthrene oxidation.
- The isomers phenanthrene and anthracene appear in relative proportions consistent with their

---

[1] We use the term dimer in a slightly non-traditional way: the molecules need not be the same (*e.g.* benzene + naphthalene → phenyl naphthalene).

thermodynamics; anthracene being much less stable. This is indicative of thermodynamic, rather than totally kinetic, control of growth (*i.e.* at least one step in the growth sequence which is reversible).

- Ethynyl substituted benzene, naphthalene, and acenaphthalene were identified. The concentrations are about an order of magnitude lower than the parent compound. Again, this is consistent with the acetylenic growth pathway. It is surprising that no ethynyl-substituted compounds larger than ethynyl-acenaphthalene were identified.
- There is a high degree of similarity between the profile shapes for the φ = 2.0 and the φ = 2.125 flames. Because the fuel is benzene in both cases the similarity is not too surprising. A comparison of results from other totally different fuel and combustion geometries (Vaughn, 1988; Lam, 1988), however, reveals the same relative proportions of PAH's (with the exception of the biphenyl-type compound which are only seen in high concentrations in flames with aromatic fuels).

The match of the retention indices observed to those published by Lee was in general quite good, usually to within ±0.5 index units. The PAH dimers, however, had a deviation of about 2 units from the Lee values. Two factors lead us to believe that we have the correct identifications. First, our column (DB-5) is slightly different from the one used by Lee (SE-52). The operational differences were negligible for the condensed aromatics, but the deviations for biphenyl (+2 units) and 1,1' binaphthyl (-3 units) which are in our standard indicate that the columns perform differently with these classes of compounds. Second, the large presence of biphenyl and the somewhat smaller concentration of 1,1' binaphthyl indicate that a phenyl–type dimerization process was operative; it is reasonable to expect other small dimerization products (terphenyl, phenyl-naphthalene) to be present. By widening the acceptance threshold to ±2 units for these compounds, several otherwise anomalously large peaks can be assigned. The next member of this growth sequence is triphenylene. Lee reported its retention index to be right on top of its isomer chrysene. We do see a small concentration at that retention index and have made the peak assignment to chrysene. It could be triphenylene, but in any case the concentration is low enough that the error, if present, is slight.

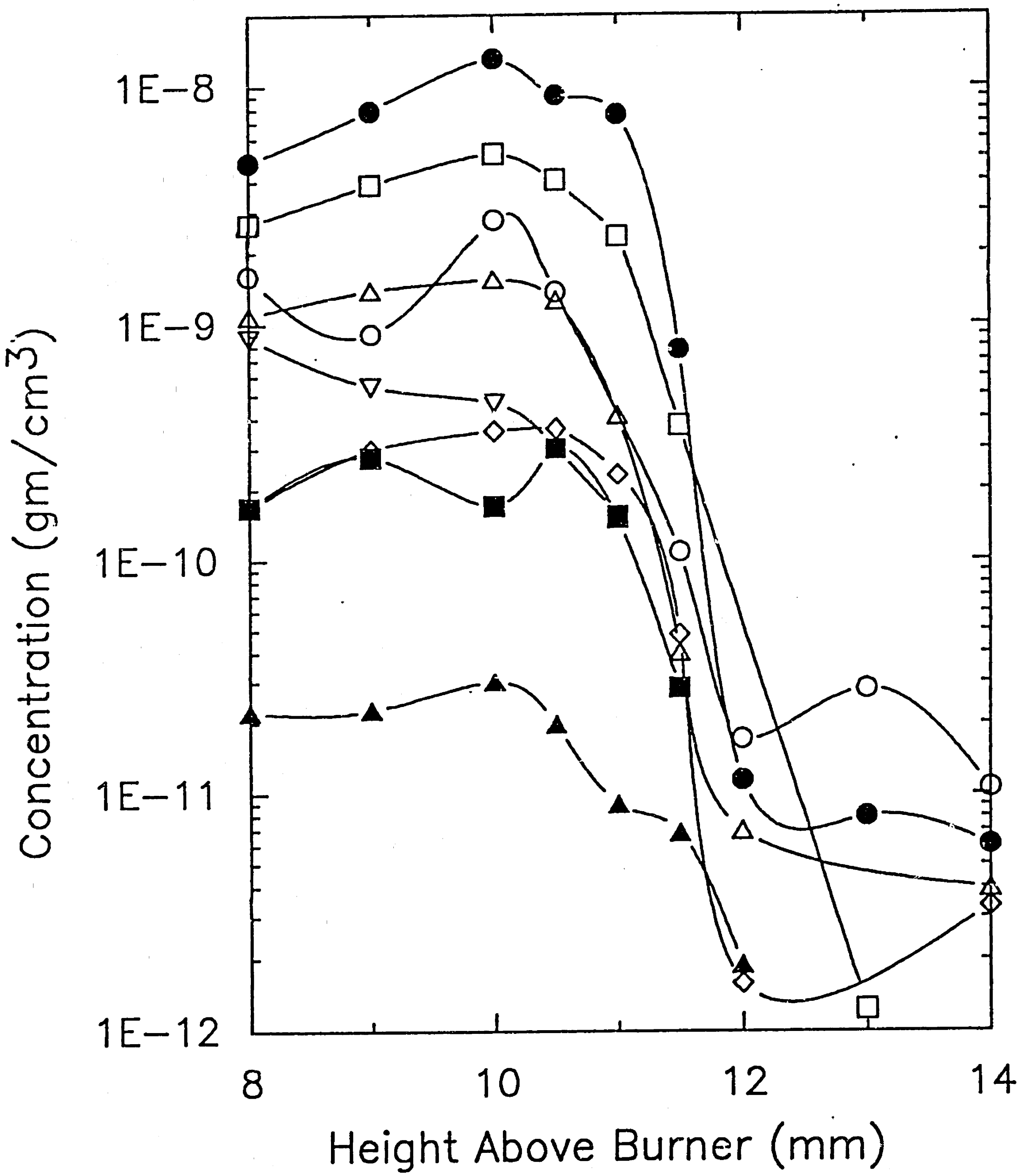

Figure 4.1 **Light PAH profiles. φ = 2.0, 20 torr, 30% Ar. Triacetylene (○), Phenylacetylene (●), Styrene (△), Benzaldehyde (▲), Indene (□), Methyl indene (■), Fluorene (◇). Soot forms at 11-12 mm. Lines are cubic spline fit.**

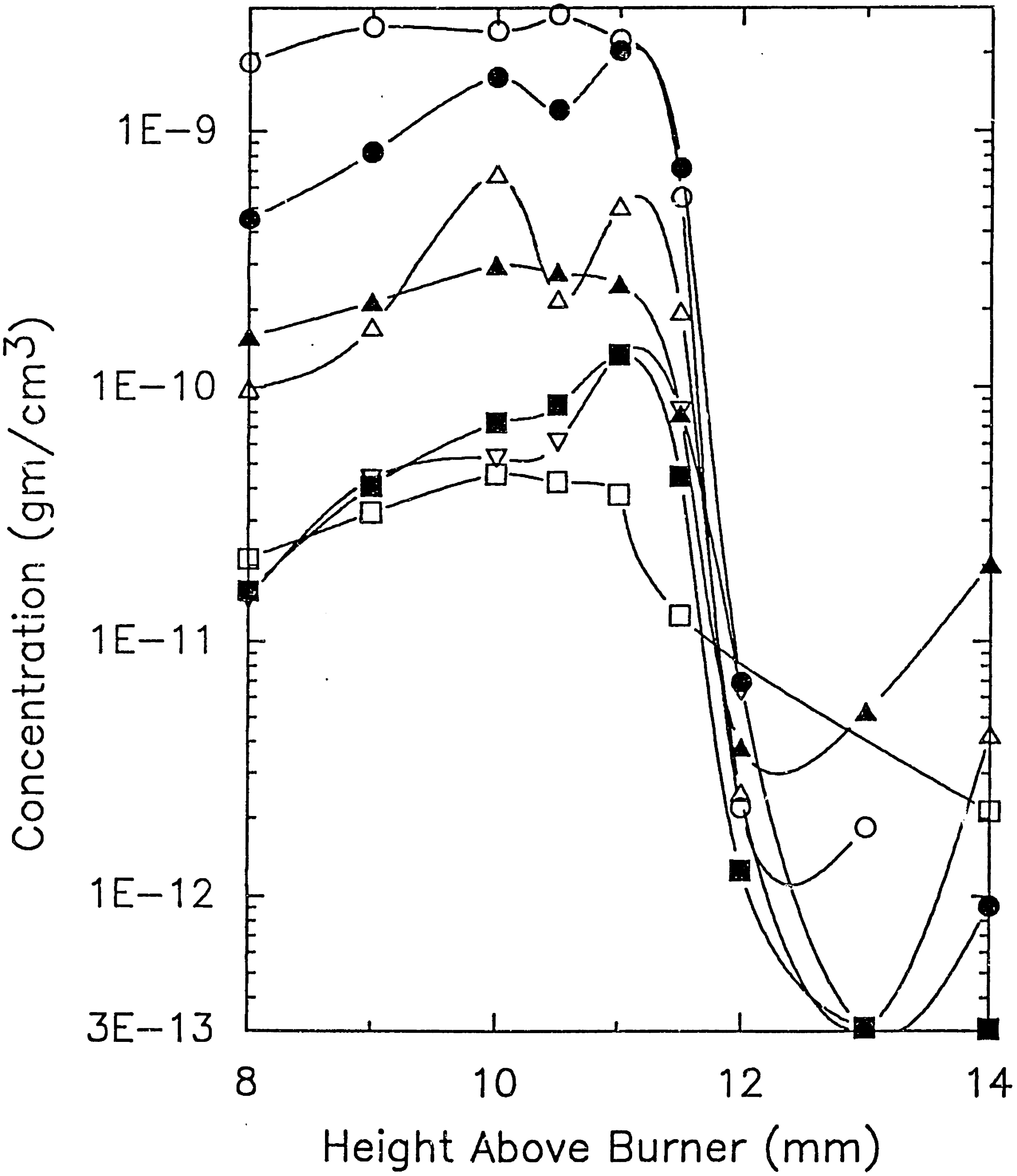

Figure 4.2 Light PAH profiles. φ = 2.0, 20 torr, 30% Ar. Naphthalene (○), Acenaphthalene (●), Ethynyl acenaphthalene (△), Phenanthrene (▲), Anthracene (□), Acephenanthrylene (■), Benzofluoranthene (▽)

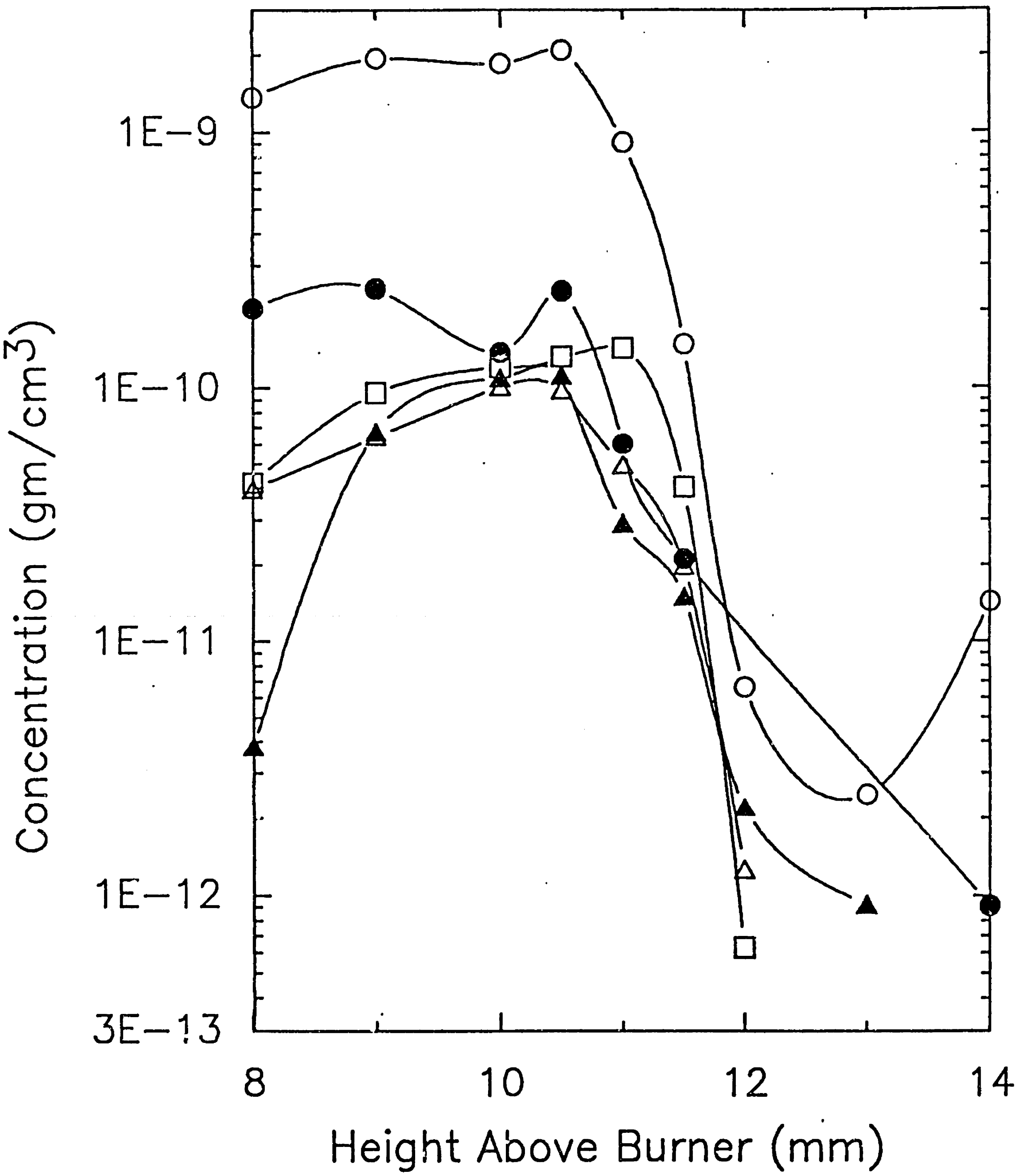

Figure 4.3 Light PAH profiles. φ = 2.0, 20 torr, 30% Ar. Biphenyl (○), Bibenzyl (●), Phenylnaphthalene (△), 1,1'Binaphthyl (▲), Terphenyl (□)

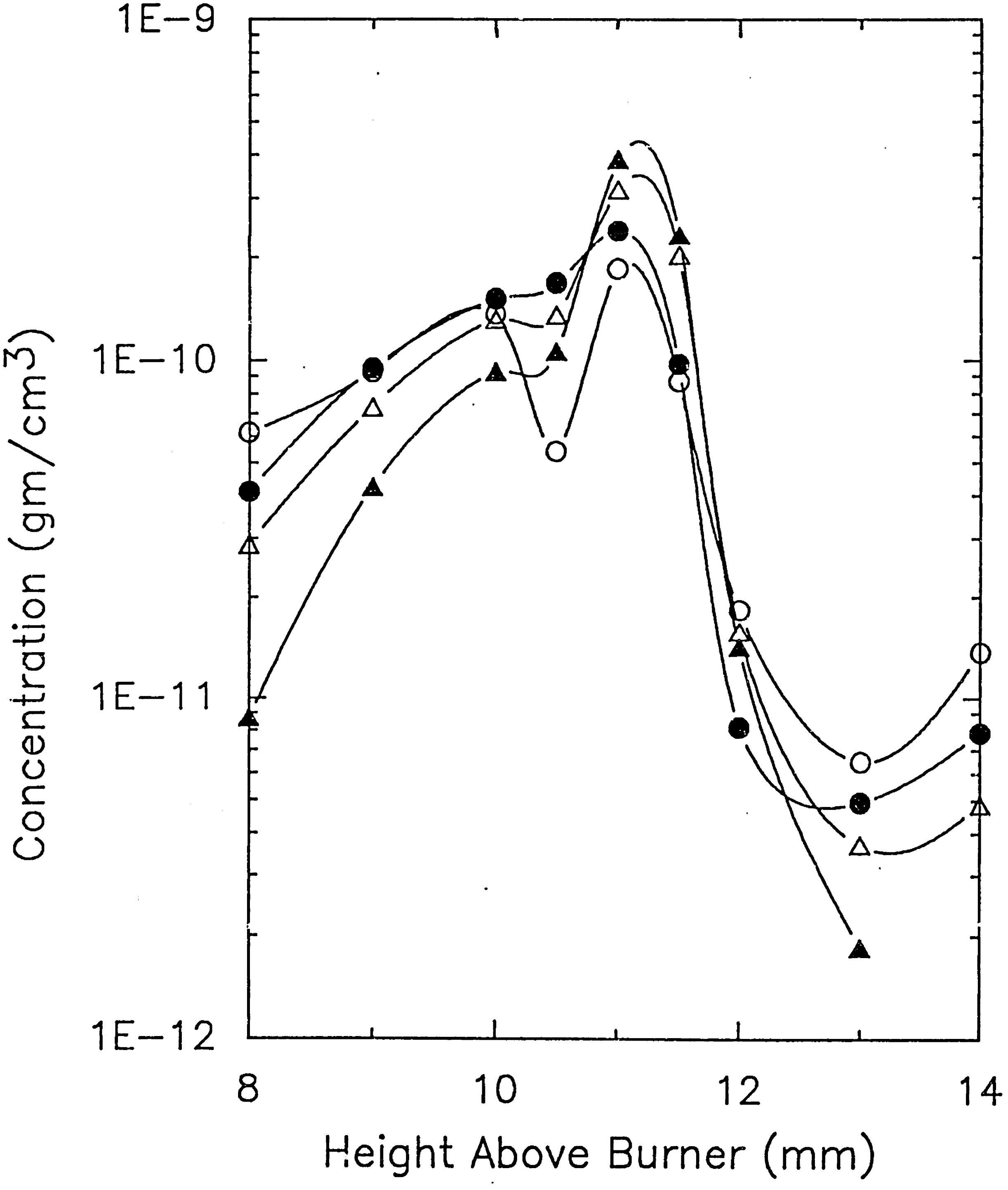

Figure 4.4 Light PAH profiles. φ = 2.0, 20 torr, 30% Ar. Cyclopentaphenanthrene (○), Fluoranthene (●), Pyrene (△), Cyclopenta(*c,d*)-pyrene (▲)

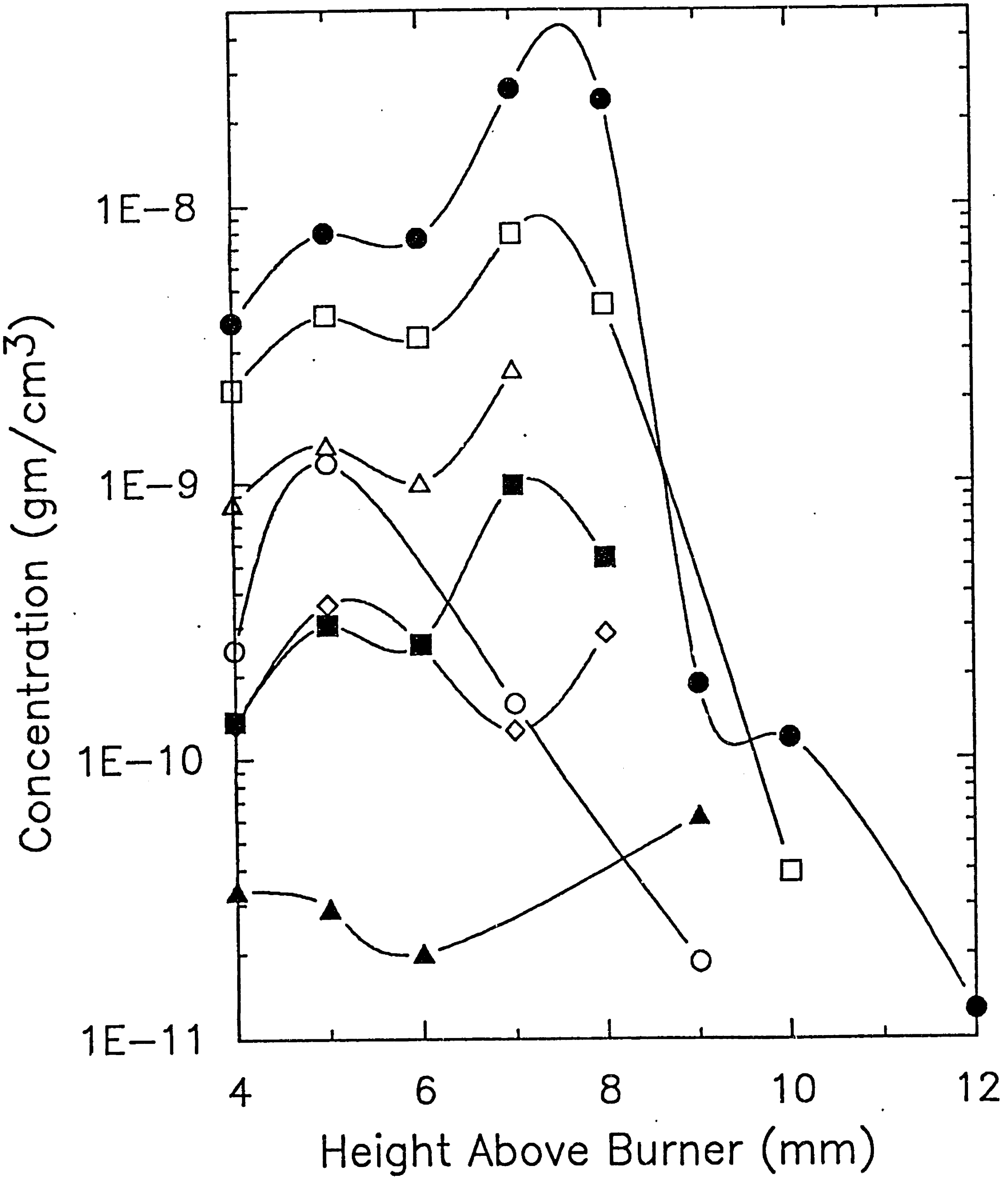

Figure 4.5 Light PAH profiles. φ = 2.125, 40 torr, 45% Ar. Triacetylene (○), Phenylacetylene (●), Styrene (△), Benzaldehyde (▲), Indene (□), Methyl indene (■), Fluorene (◇). Soot forms at 8 mm.

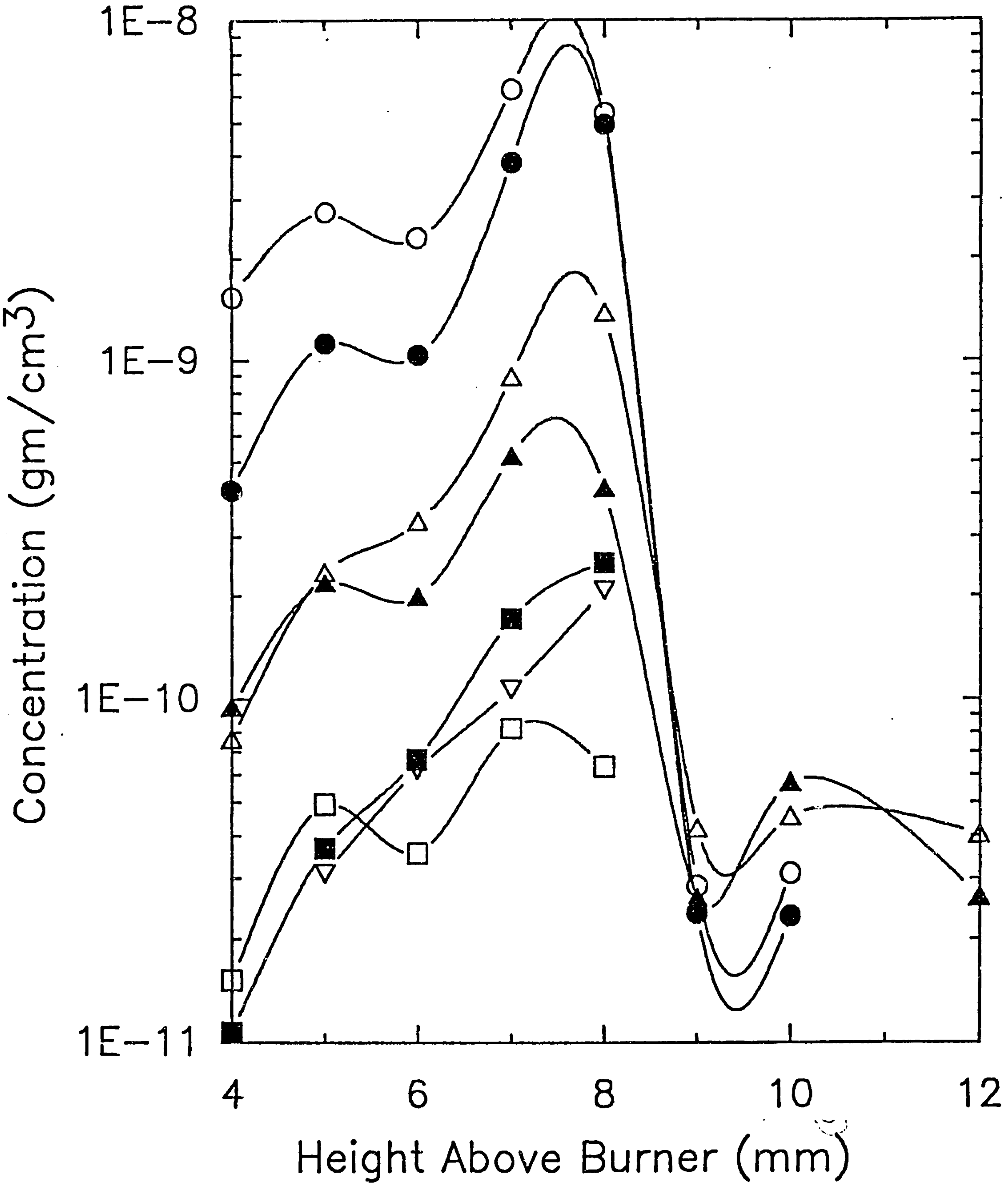

Figure 4.6 Light PAH profiles. φ = 2.125, 40 torr, 45% Ar. Naphthalene (○), Acenaphthalene (●), Ethynyl acenaphthalene (Δ), Phenanthrene (▲), Anthracene (□), Acephenanthrylene (■), Benzofluoranthene (∇)

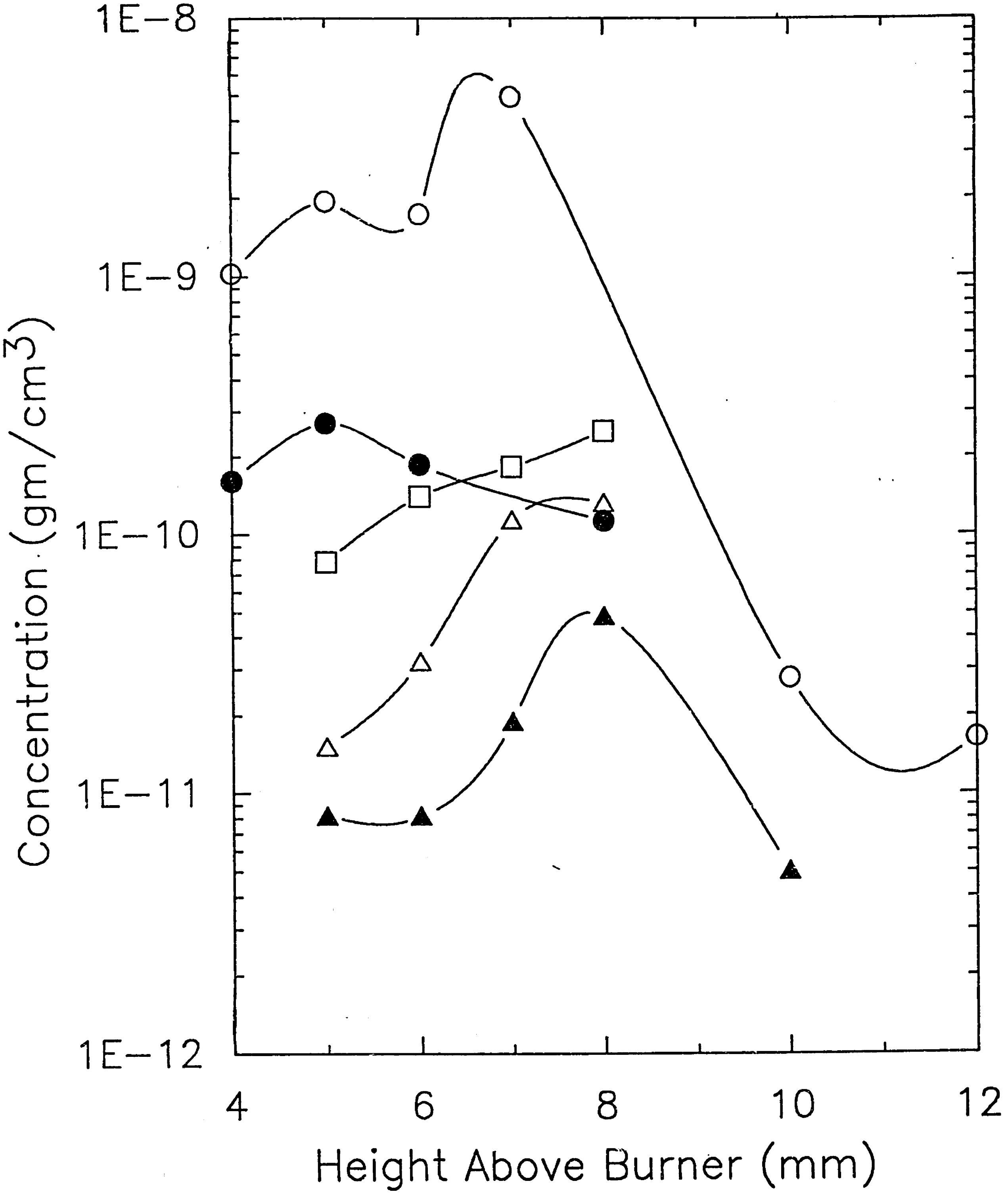

Figure 4.7 Light PAH profiles. $\varphi = 2.125$, 40 torr, 45% Ar. Biphenyl (○), Bibenzyl (●), Phenylnaphthalene (△), 1,1'Binaphthyl (▲), Terphenyl (□)

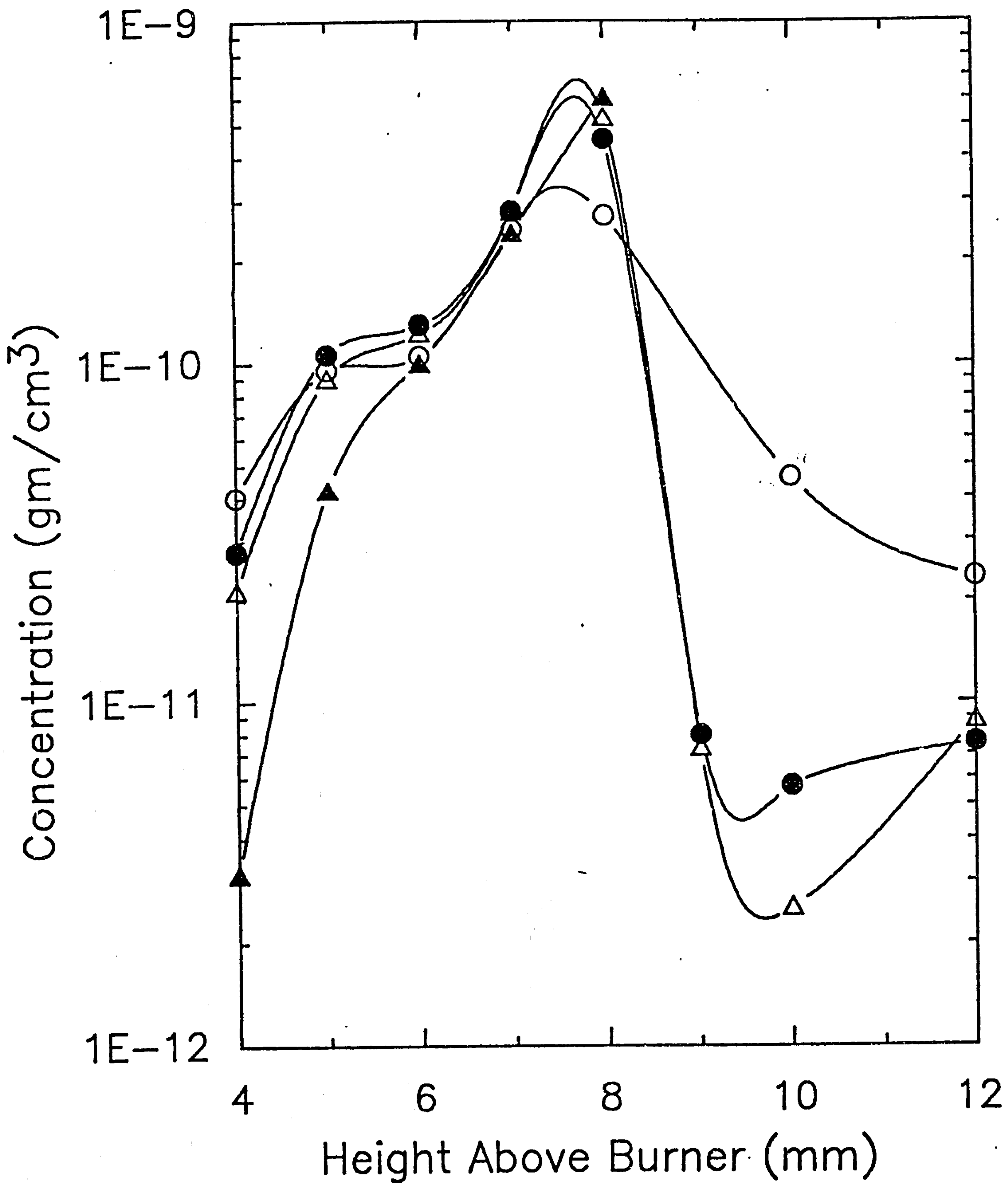

Figure 4.8 Light PAH profiles. $\varphi = 2.125$, 40 torr, 45% Ar. Cyclopentaphenanthrene (○), Fluoranthene (●), Pyrene (Δ), Cyclopenta(*c,d*)-pyrene (▲)

4.1.2 TAR CONCENTRATIONS

Tar weight profiles were made for all four flame conditions. To summarize §3.2.3, the tar weights do not give information on individual PAH species. Instead, they represent concentrations in broad size categories. The upper molecular weight range is only limited by the solubility of PAH in methylene chloride (900 amu). In addition to the weights of the soluble material, we determined the weight of the insoluble material. The insoluble material correlates roughly to soot. There is not a total overlap of the definitions because we define soot to start at 2000 amu. For the samples which were also analyzed using capillary GC, a distinction between heavy solubles and light solubles could be made. The light soluble fraction, representing masses from 130 to 250, was determined by summing all the GC peaks (both assigned and unassigned) which were greater than naphthalene. Recall that molecules of molecular weight less than or equal to naphthalene (128 amu) vaporize in the tar weighing process. The heavy soluble fraction, mass 250 to 900, was then the difference between the total solubles and the light soluble.

The profiles are presented in Figure 4.9 through 4.12. The general trends of the tar profiles is similar for all the flame conditions. The soluble material in all cases grows in the pre-sooting zone and then drops sharply right at the soot nucleation zone.

The $\varphi = 2.125$ tar profile indicates the destiny of the soluble material which decays. We can see that at 8 mm and below, the Total Soluble and Soluble+Insoluble curves are superimposed, meaning that there is no material greater than 900 amu. The curves start to diverge at 9 mm. The Total Solubles decrease about 50–fold but the Soluble+Insolubles decrease only 6–fold. Thus five parts in six of the soluble material is destroyed, either oxidized or pyrolyzed, and one part in six is promoted to the Insoluble category.

A comparison of the $\varphi = 2.2$ and $\varphi = 2.4$ tar profiles clearly shows the effect of the equivalence ratio. Two features are worthy of note. The concentration of soluble material in the two flames is roughly the same. This would not be expected because the insoluble material is a factor of two different and, as will be shown in §4.2.1, the soot varies by a factor of six. The second feature is that the Insolubles of the $\varphi = 2.2$ grow rapidly and then decay slightly, whereas the Insolubles of the $\varphi = 2.4$

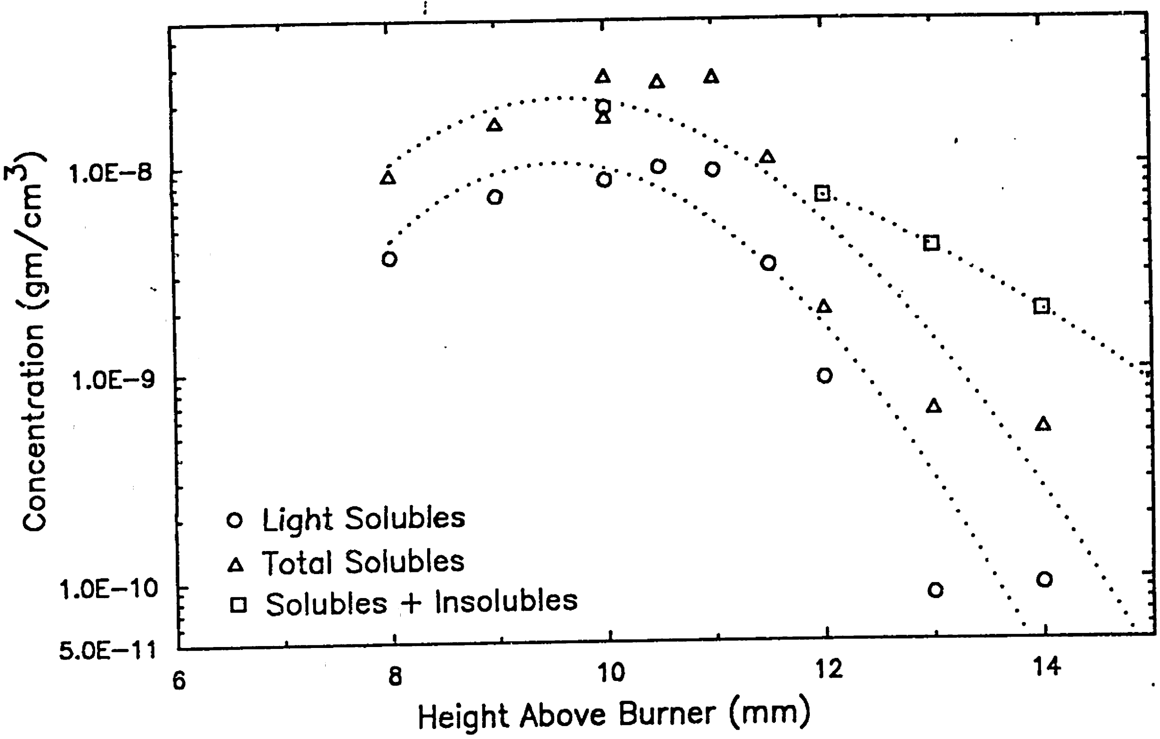

Figure 4.9 Tar profiles. $\varphi = 2.0$, 20 torr, 30% Ar

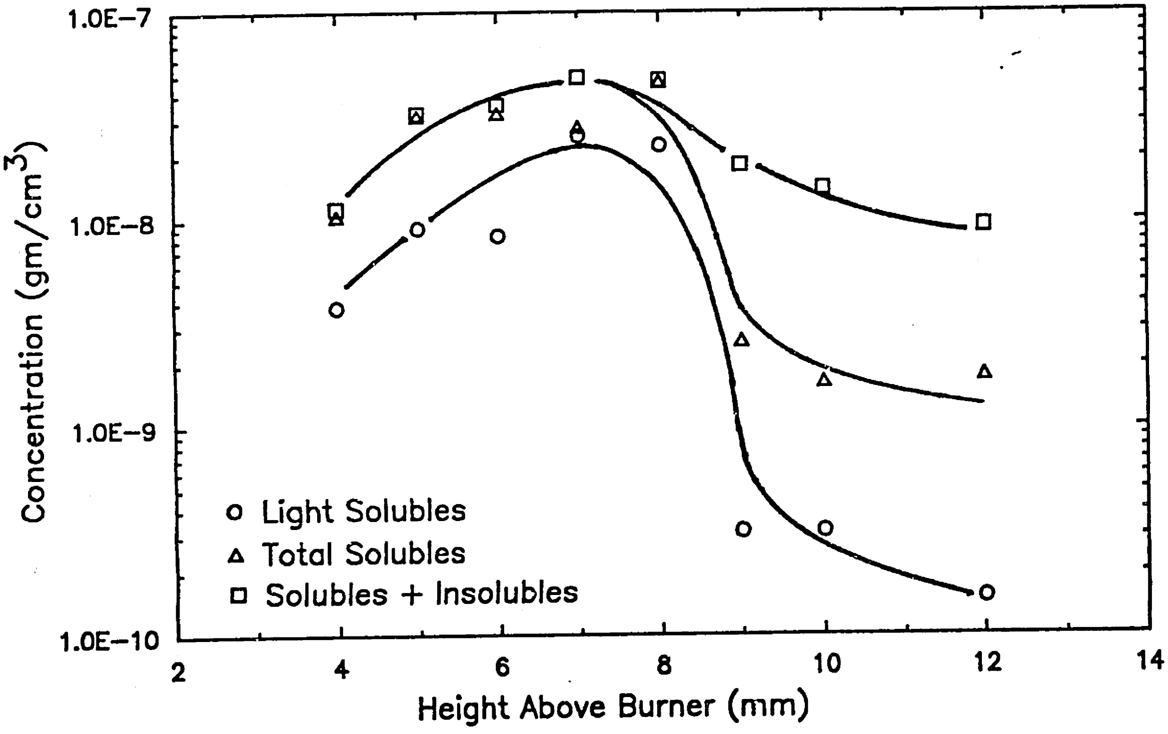

Figure 4.10 Tar profiles. $\varphi = 2.125$, 40 torr, 45% Ar

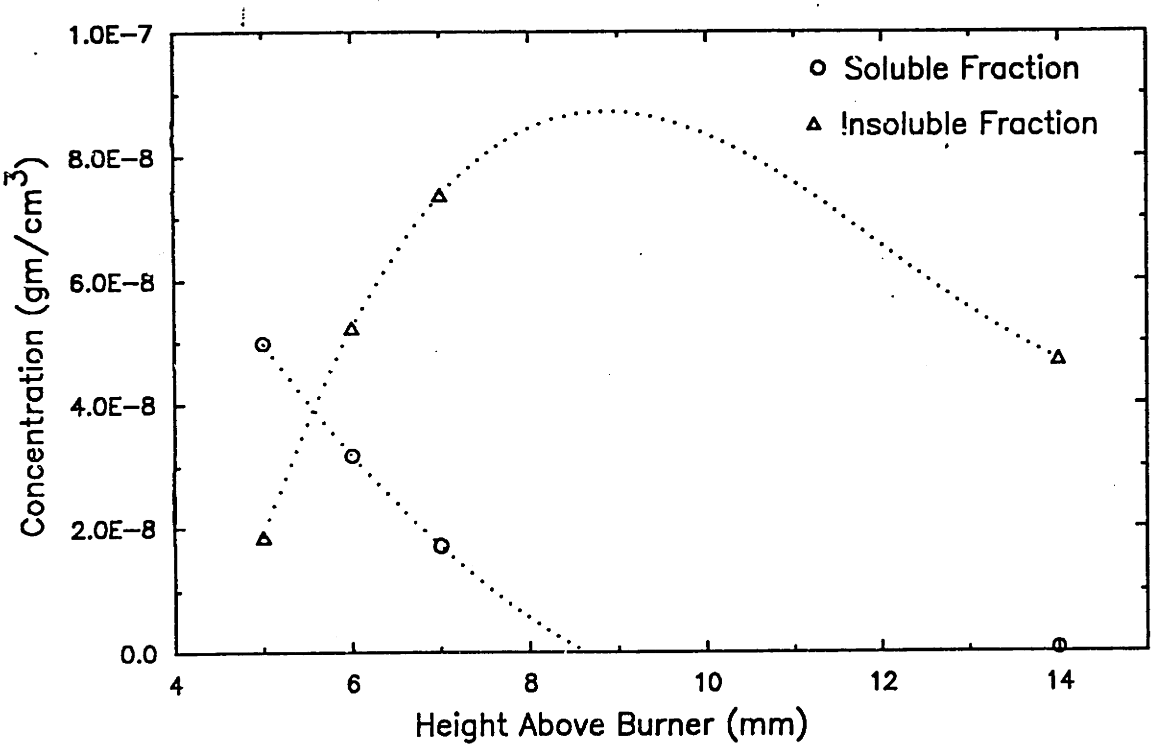

Figure 4.11 Tar profiles. $\varphi \approx 2.2$, 40 torr, 10% Ar

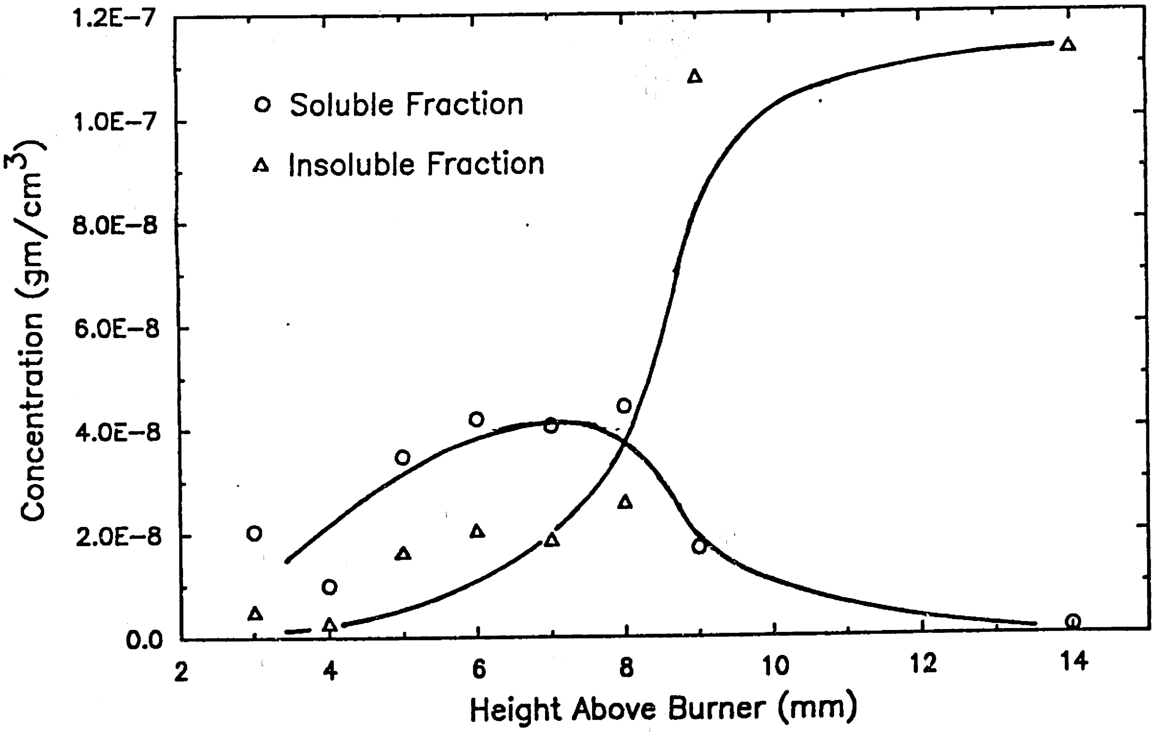

Figure 4.12 Tar profiles. $\varphi = 2.4$, 40 torr, 10% Ar

case grow monotonically. These same trends can be seen from the optical experiments in Figure 4.19.

The column chromatography method was used to fractionate the samples from the φ = 2.4 flame. The fractions are shown in Figure 4.13. Vapor pressure osmometry was used to determine the molecular weight of the fractions. The VPO results are presented in Table 4.1.

The results from the column chromatography are somewhat inconclusive. The following interpretation must be viewed as tentative. The most obvious trend seen is that the lowest molecular weight cut, the benzene fraction, increases with time. The heaviest fraction, methanol, decreases with height above burner except for the last data point (the 14 mm data point, however, has the lowest accuracy because its concentration was much less than the others). The middle fraction, methylene chloride soluble, is slightly peaked. A shift of the size distribution of the soluble material from heavy to light is consistent with a mechanism in which collisions between heavy PAH's have a higher likelihood of reacting than those involving smaller molecules.

The flame concentrations (in g/cm^3) were determined for the light PAH and tars by dividing the mass collected in the sample by the total gas collected in the inverted water column (see Figure 3.6).

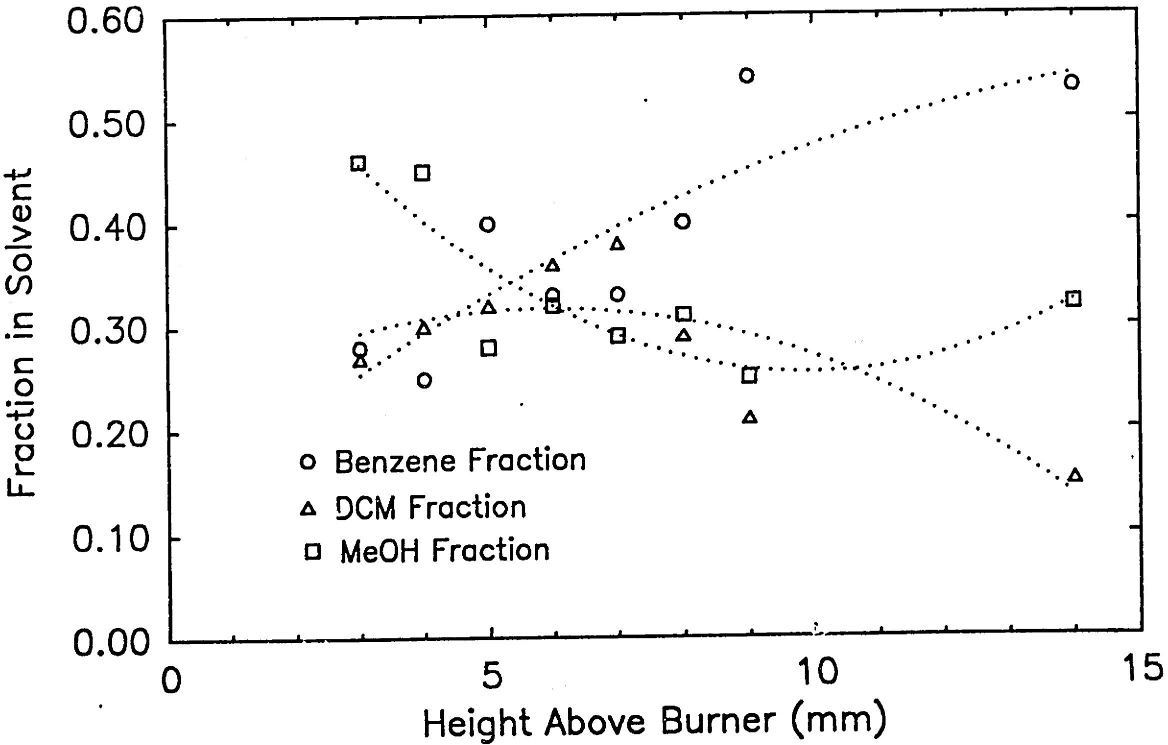

Figure 4.13 Cyano-column tar fractions. φ = 2.4, 40 torr, 10% Ar

Table 4.1 Vapor Pressure Osmometry Results

	Concentration mg/mL	Measured MWn
Benzene fraction	10.31	160
DCM fraction	4.32	250
MeOH fraction	2.20	550
Coronene	0.34	285

MW_n : number average molecular weight
Coronene test shows 5% deviation from true MW (300 amu)

The gas volume had to be corrected to account for the temperature and pressure differences between the laboratory and the flame using the ideal gas law. Also, the fraction of gases which condensed out in the cryogenic trap had to be added back in. The condensable gases (77 K) were CO_2, CH_4, H_2O, C_2H_2, and C_6H_6. For the flame $\varphi = 2.125$, no light gas or temperature measurements were made so we assumed a constant temperature of 2000 K and a constant condensable fraction of 0.20 for the analysis.

4.2 Optical Results

Soot volume fraction, size, and number density, temperature, and PAH profiles were measured using *in situ* optical methods.

4.2.1 ABSORPTION AND VOLUME FRACTION MEASUREMENTS

Absorption measurements were made on five flames: $\varphi = 2.2$, with and without argon; $\varphi = 2.4$, with and without argon; and $\varphi = 2.5$, 10% argon. In this way the effect of equivalence ratio could be separated somewhat from temperature. The absorption measurements were made at wavelengths of

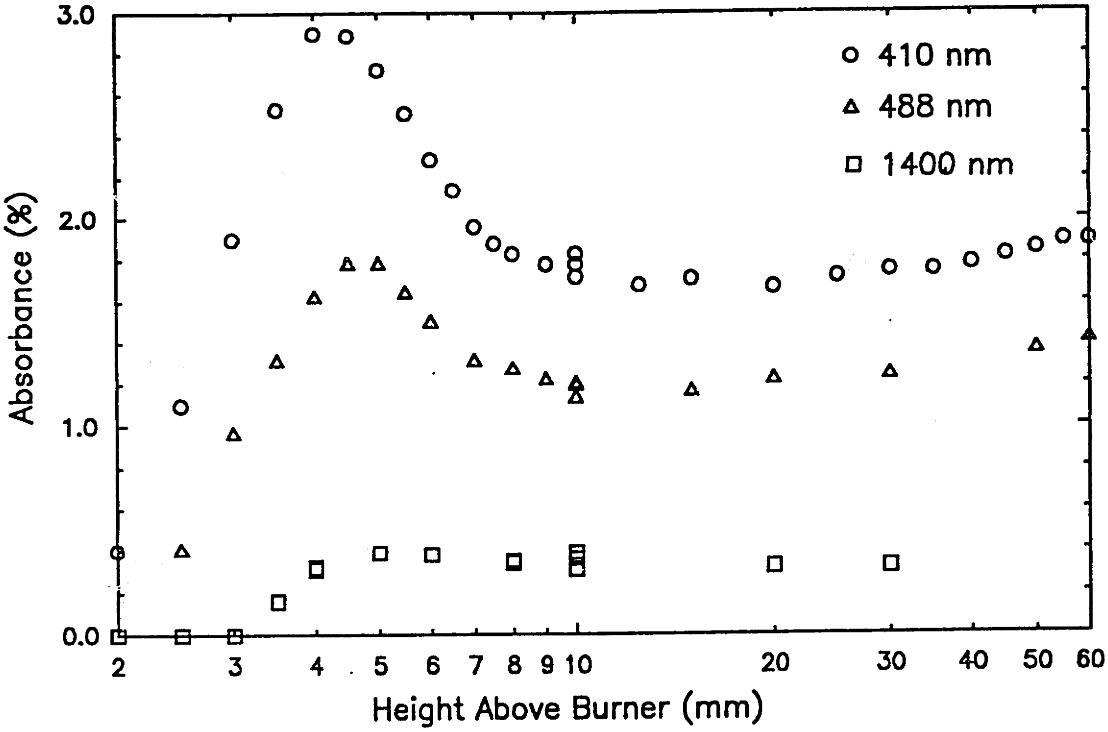

Figure 4.14 Absorption profiles. φ = 2.2, 40 torr, 0% Ar

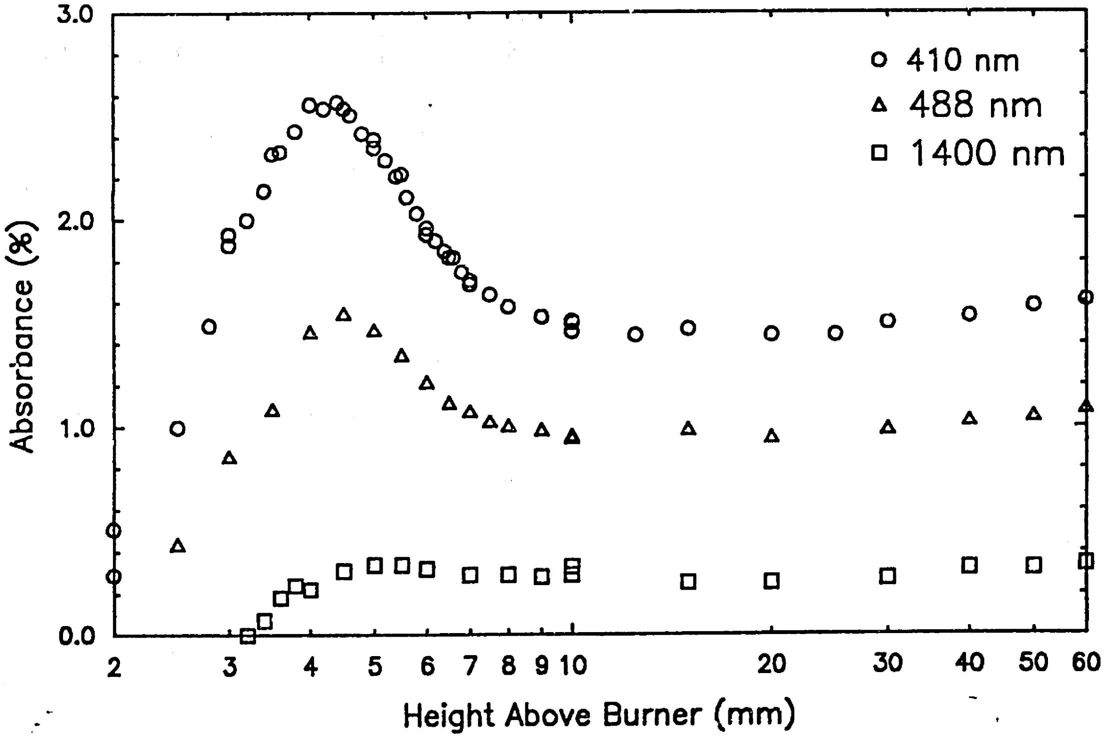

Figure 4.15 Absorption profiles. φ = 2.2, 40 torr, 10% Ar

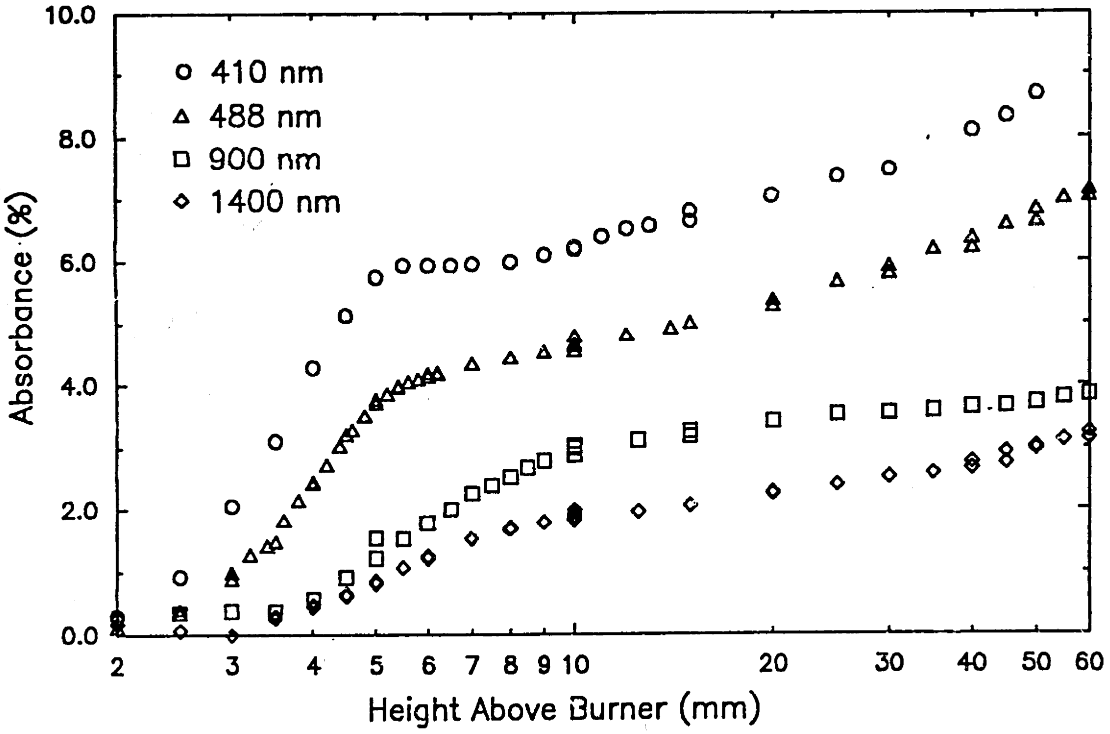

Figure 4.16 Absorption profiles. φ = 2.4, 40 torr, 0% Ar

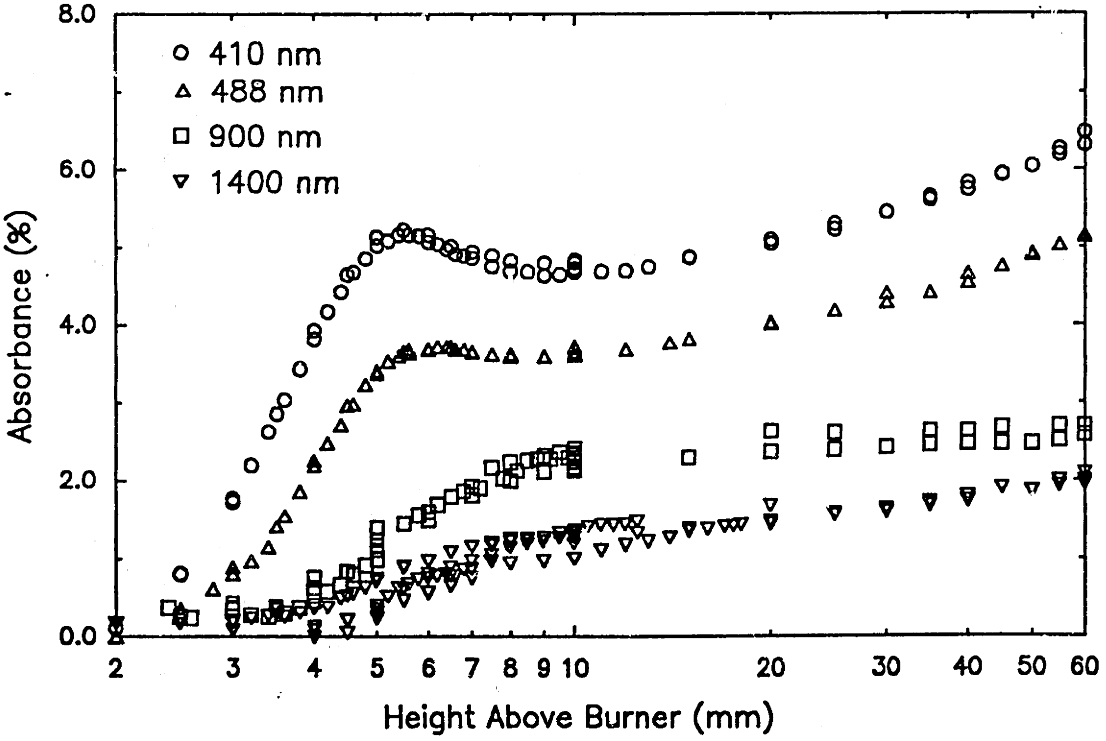

Figure 4.17 Absorption profiles. φ = 2.4, 40 torr, 10% Ar

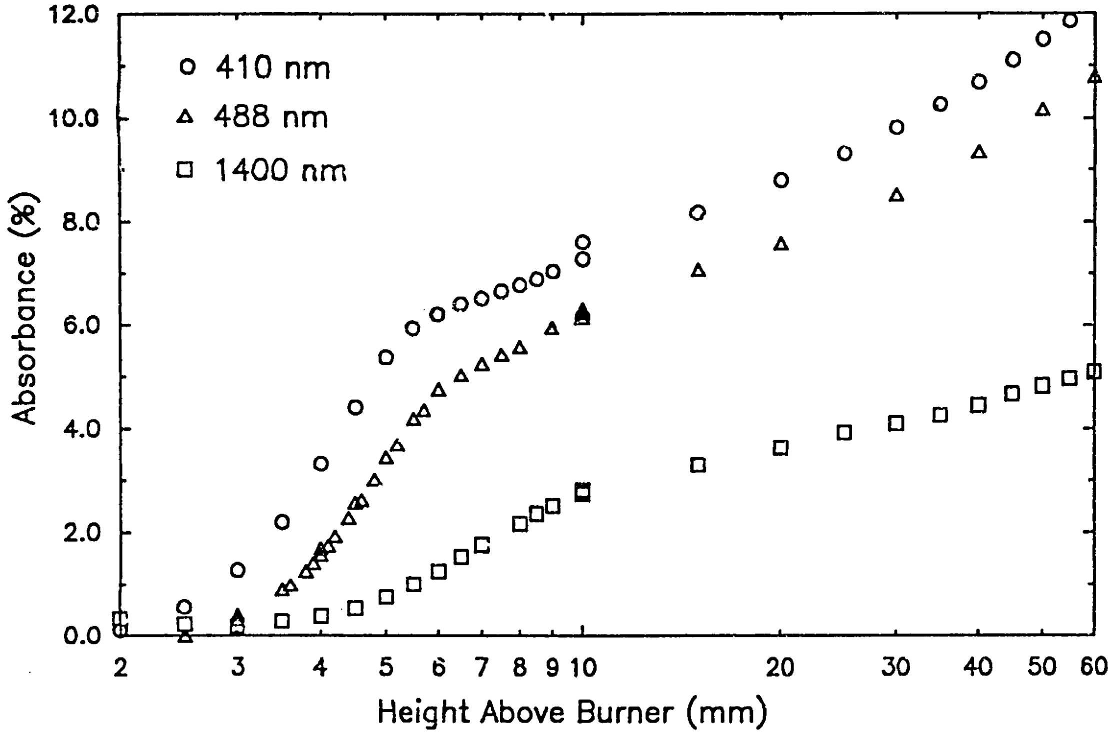

Figure 4.18 Absorption profiles. φ = 2.5, 40 torr, 10% Ar

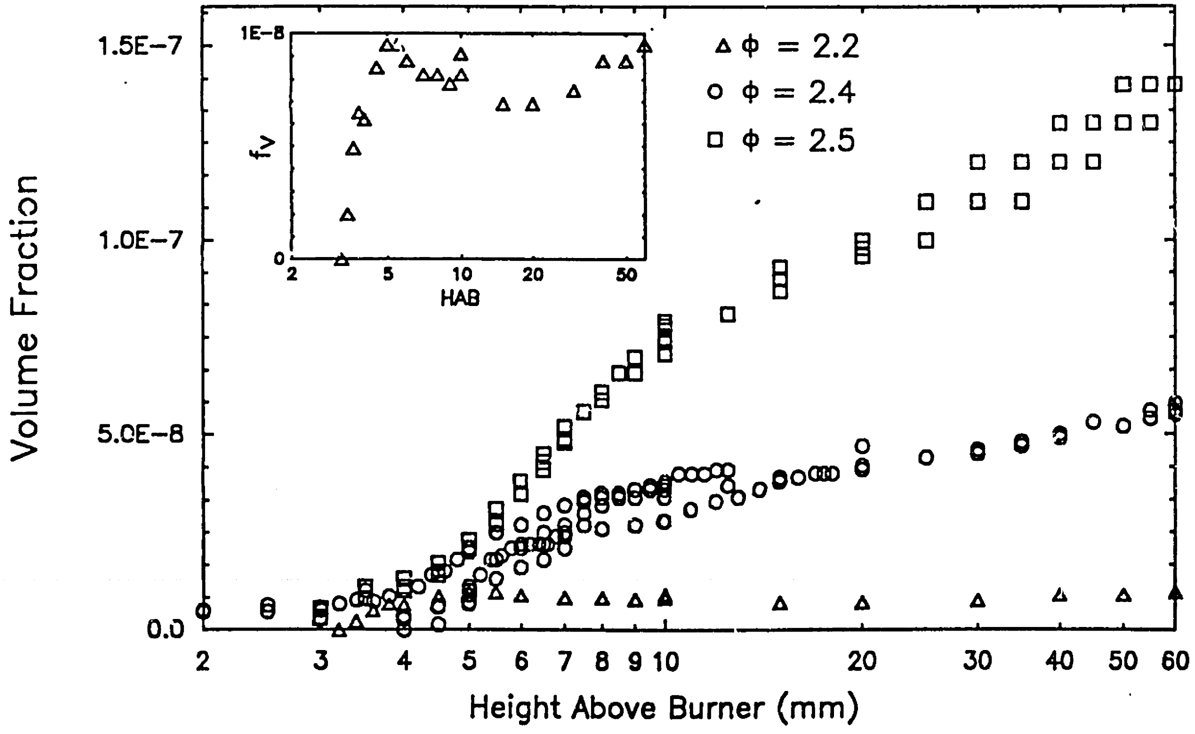

Figure 4.19 Volume fraction profiles. φ = 2.2, 2.4, and 2.5. 10% Ar

410 nm, 488 nm, 632.8 nm, 725 nm, 900 nm, and 1400 nm. Figures 4.14 through 4.18 show the absorption profiles for the five flame conditions. The 632.8 nm and 725 nm curves are not shown to reduce clutter on the plot, but they have the same general trends.

The most prominent trend seen in all the profiles is that the shorter wavelengths absorb more than the longer ones. There are two reasons for this. In the case of Rayleigh absorbers, such as soot, the absorption cross-section scales with reciprocal wavelength (see §3.3.1, Equation 3.7). In the case of PAH, shorter wavelength photons are absorbed by a larger fraction of the molecular weight distribution (*i.e.* it includes more smaller molecules) than longer wavelengths. Since the *in situ* measurement is through a soot aerosol dispersed in a PAH laden gas, both mechanisms are operative.

Probably the most significant feature of these plots is that the shortest wavelength absorption profile (410 nm) for all the runs except the $\varphi = 2.5$ case, exhibit a local maximum right in the soot nucleation zone. This is indicative of a transient PAH inventory and is consistent with the probe sampling results. In the $\varphi = 2.2$, 10% Ar flame the transient peak is 50% higher than the ultimate absorption level, which is predominantly soot.

Because we cannot assign quantitative absorption cross-sections to the PAH ensemble, no concentration values can be assigned to the peaks. In addition, the soot most certainly has different absorption properties than the PAH so the relative quantities cannot be discerned from the measurements.

By definition, we say that only soot absorbs at the longest wavelength, 1400 nm. Using Equation 3.7 the long wavelength absorption measurements may be turned into soot volume fractions as is shown in Figure 4.19. The inset shows the $\varphi = 2.2$ profile expanded and separated from the data clutter to expose the local maximum at 5 mm. The soot concentrations of the other flames showed only a monotonic increase.

4.2.2 TEMPERATURE

The brightness method was used to measure flame temperature. Figure 4.20 shows the temperature profiles *vs.* height above burner. As would be expected, the leanest flame has the highest peak temperature (2150 K). The temperature rises steeply in the early part of the flame, peaks near the soot nucleation zone, and gradually declines. Benzene flames tend to be much hotter than flames of non-aromatic fuels. As will be discussed in the next chapter, temperature is one of the most important parameters in soot nucleation. Thus it is somewhat difficult to reconcile soot data from flames of different fuels.

4.2.3 SCATTERING MEASUREMENTS

Scattering measurements were made on the φ = 2.4, 10% Ar flame only. Figure 4.21 show the raw soot scattering signal at 488 nm. The signal varies over three decades due to the d^6 scaling of signal. The lowest height above burner measurements contain a significant (*ca.* 50%) contribution from gas phase components. This portion was calculated from gas measurements and published indices of refraction of gases and subtracted from the total. The inset of Figure 4.21 show the contribution from molecular species. Benzene is the greatest contributor to the gas phase scattering because of its large index of refraction.[2]

Using the Rayleigh equation of §3.3.1, we can combine the 488 nm scattering and 1400 nm absorption to compute the number density and diameter of the particles. The indices of refraction are the values of Lee and Tien (1981, see Figure 3.9). The noise in the absorption profile was smoothed by least squares fitting the data to an analytical function with linear coefficients. In addition to smoothing the data, the analytical function could provide a value at the heights above burner where the scattering measurements were made.

Figure 4.22 shows these profiles. The diameter increases monotonically, due both to mass growth of the soot through C_2H_2 addition and from sticking collisions. The number of particles continuously decreases in the region of measurement due to collisions. Of course, there must be a region before this where number density increases because the burner surface boundary condition has a particle flux of zero. The scattering signal from such small particles was too low to be measured.

---

[2] An effective soot diameter may be computed for benzene from its index of refraction and the Rayleigh scattering equations. Surprisingly, it is within 5% of the Lennard-Jones diameter.

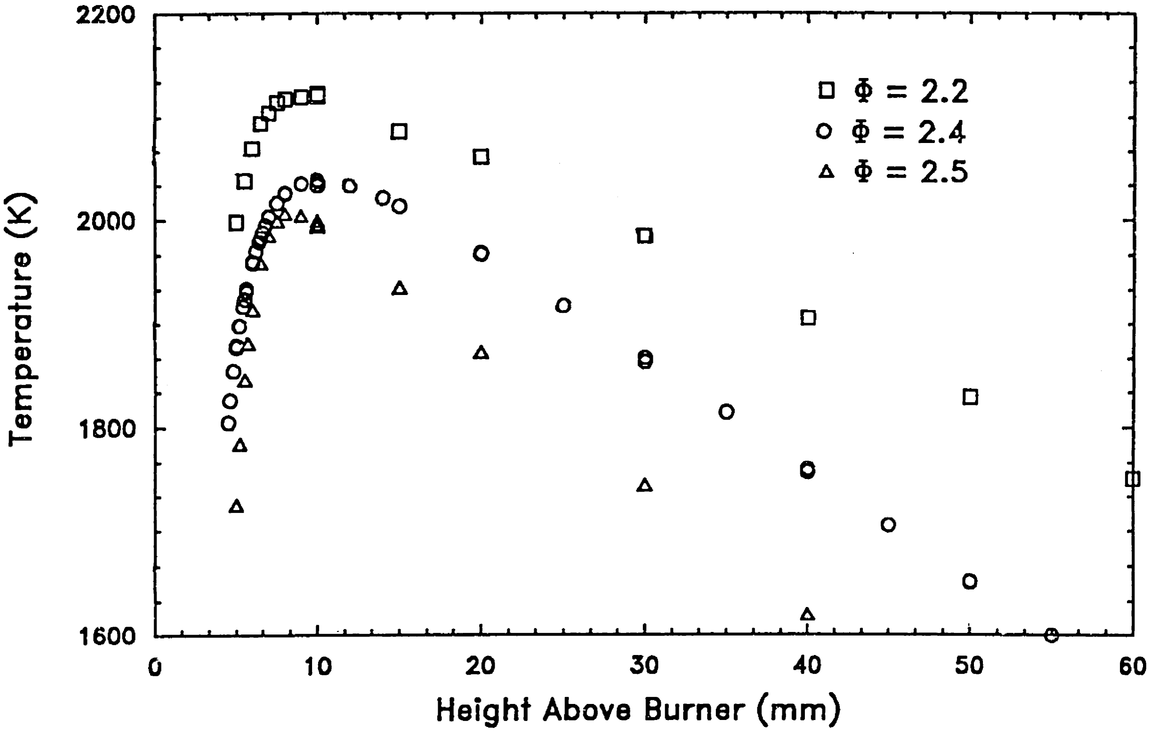

Figure 4.20 Temperature Profiles. φ = 2.2, 2.4, and 2.5, 40 torr, 10% Ar

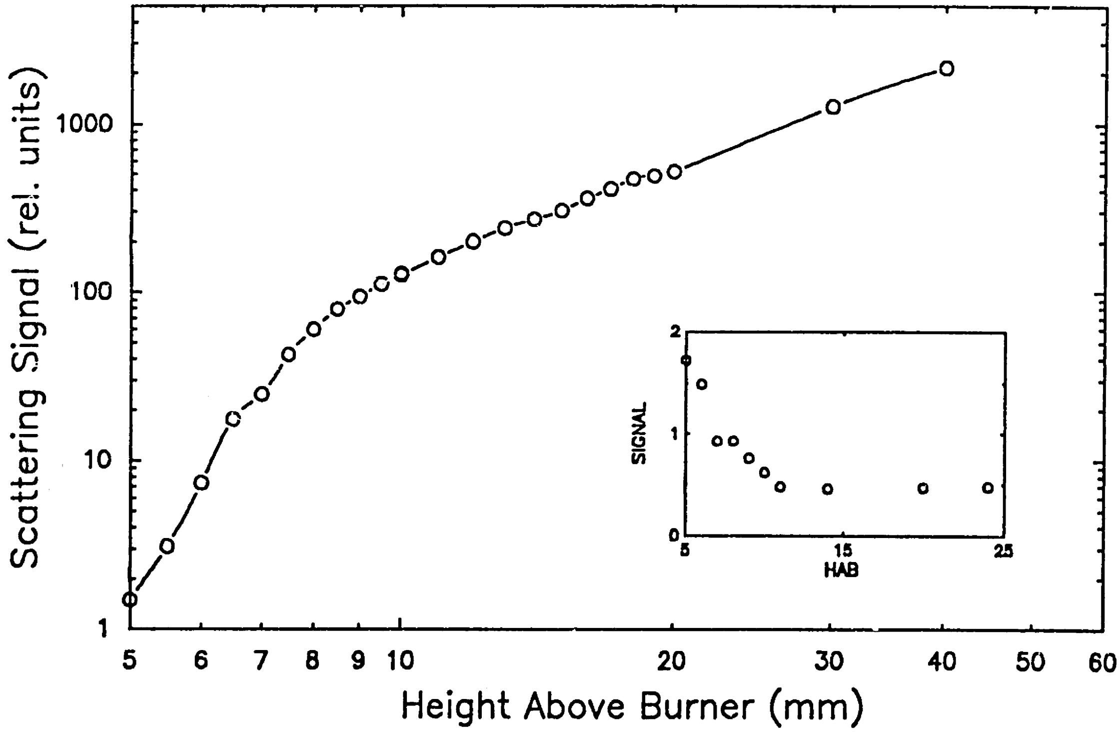

Figure 4.21 Scattering Signal. φ = 2.4, 40 torr, 10% Ar

The dotted line through the number density plot is the fit of the Smoluchowski (1917) equation.

$$\frac{dN}{dt} = -\beta(d)\, N^2 \tag{4.1}$$

$$\beta = \left[\frac{8kT}{\pi\mu}\right]^{1/2} \pi\, \sigma^2\, G \tag{4.2}$$

β : second order rate constant
μ : reduced mass
σ : sum of diameters of colliding species
G : factor which accounts for van der Waals forces, approximately 2

The equation is more easily handled in terms of the number density (N) and volume fraction (f_v). Since volume fraction enters as only the 1/6 power, we can assume volume fraction is constant and integrate as is shown in Equation 4.5 (Prado *et al.*, 1981).

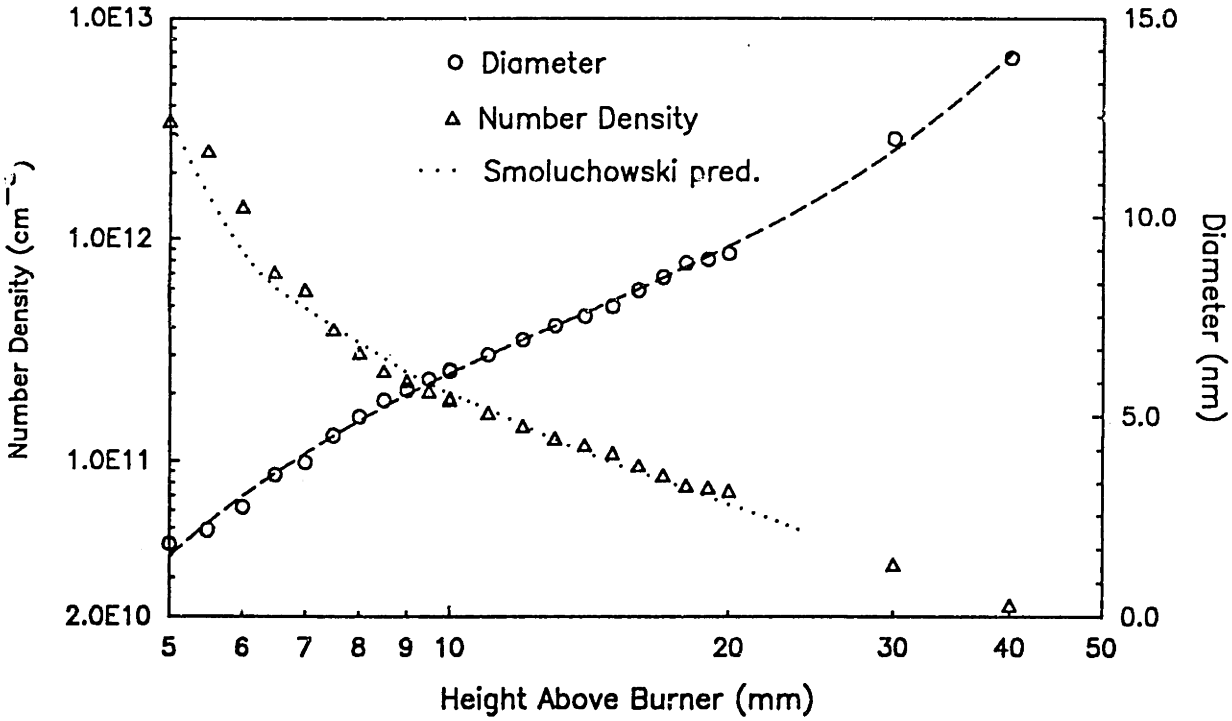

Figure 4.22 Number density and diameter. φ = 2.4, 40 torr, 10% Ar

$$\frac{dN}{dt} = \frac{6}{5}\, k\, f_v^{1/6}\, N^{11/6} \tag{4.3}$$

$$k = \frac{5}{12} \left[\frac{3}{4\pi}\right]^{1/6} \left[\frac{6kT}{\rho}\right]^{½} G \tag{4.4}$$

$$N = N_o \left[1 + 9.03\text{x}10^{-13}\, N_o^{5/6}\, T^{1/2}\, f_v^{1/6}\, t\right]^{-6/5} \tag{4.5}$$

ρ : particle density
N_o : initial number density
S.I. units used in Equation 4.5

The good fit of experiment with prediction is significant in two ways. First, it means that the soot particles do indeed stick with unit efficiency because the β rate constant in Equation 4.1 is the gas kinetic rate constant. Second, it means charged particles are not significant participants in these flames. If they were, the ionic imaging forces would make the effective collision diameter (σ in Equation 4.2) much larger than the physical diameter.

4.2.4 QUALITATIVE PAH PROFILES

We can use the knowledge of soot concentration from the infrared measurements to determine the portion of the visible absorption which is due to PAH alone (Weiner and Harris, 1988). Using the dispersion relation for soot (Figure 3.9) and Equation 3.7, the absorption due to soot at any arbitrary wavelength may be computed from the absorption at 1.4 μm. Subtracting the soot component from the visible signal leaves the PAH component only. Figure 4.23 shows the optical PAH profile for three different equivalence ratios, all with 10% argon. The wavelength used was 410 nm.

The general shapes, a rapid rise followed by decay in the soot nucleation zone, are consistent with results from probe sampling. The concentrations, however, are surprising. The $\varphi = 2.4$ flame has only twice as much PAH as the $\varphi = 2.2$ flame, but it goes on to produce six times more soot. The $\varphi = 2.5$ flame has roughly the *same* amount of PAH absorption as the $\varphi = 2.2$ flame, yet it ultimately produces *15 times* more soot (at 60 mm). Since we are proposing that the PAH are the intermediates to soot nucleation, the decoupling of intermediate inventories from ultimate soot production levels was not

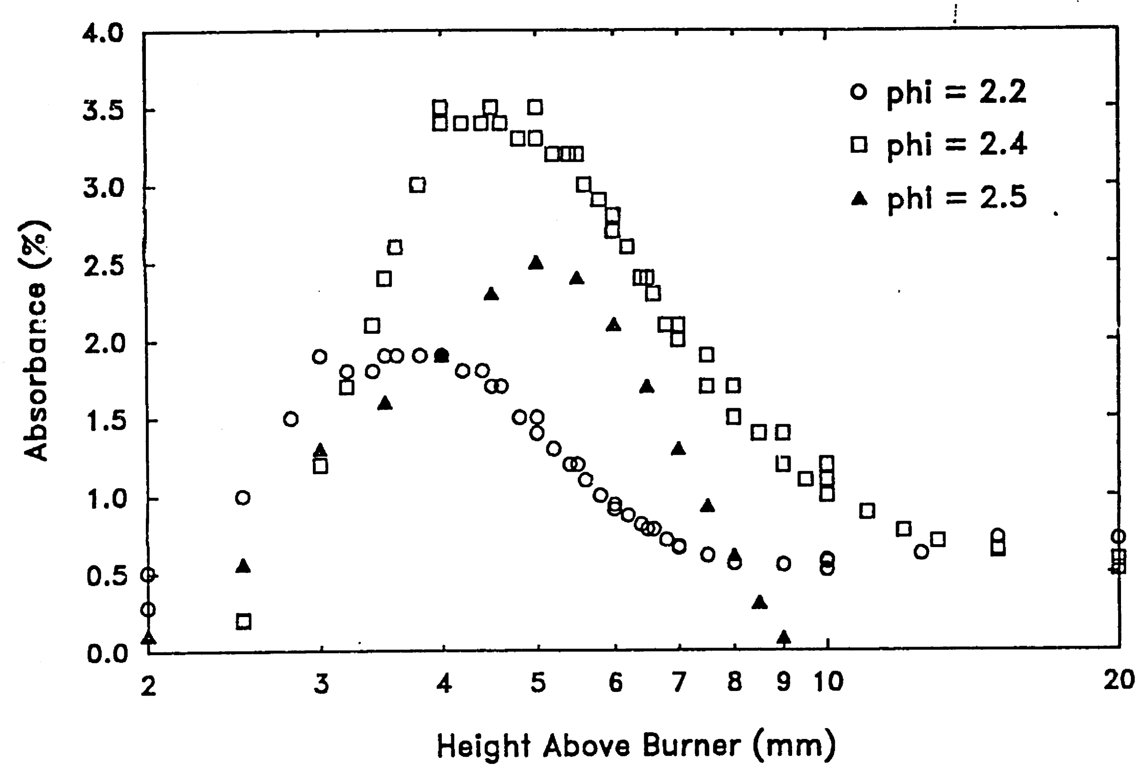

Figure 4.23 PAH absorption profiles. 410 nm and 1400 nm. All flames, 10% Ar

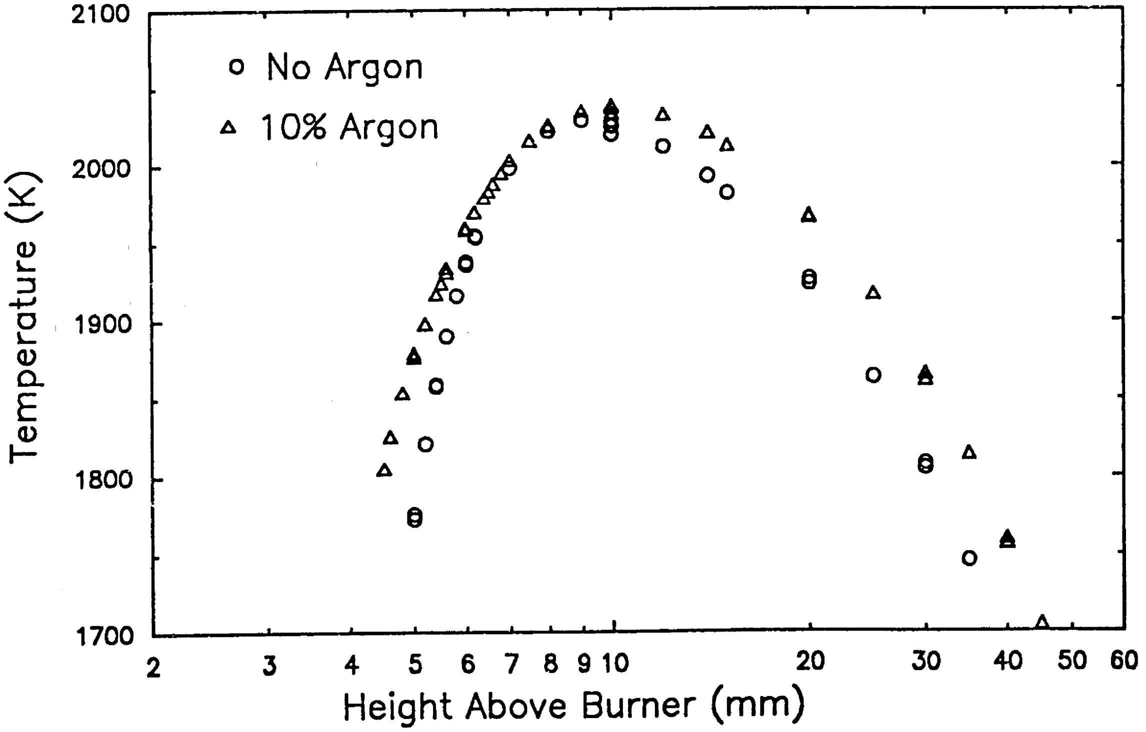

Figure 4.24 Temperature profiles. φ = 2.4, 10% Ar and 0% Ar

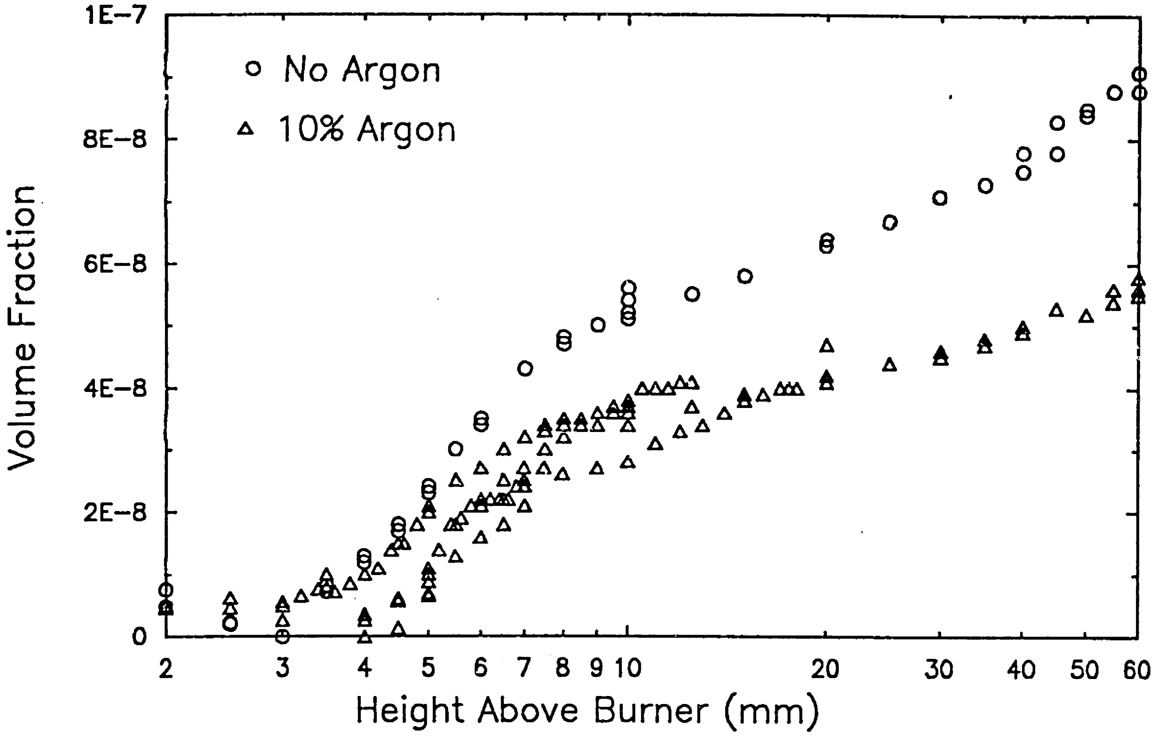

Figure 4.25 Soot volume fraction profiles. $\varphi = 2.4$, 10% Ar and 0% Ar

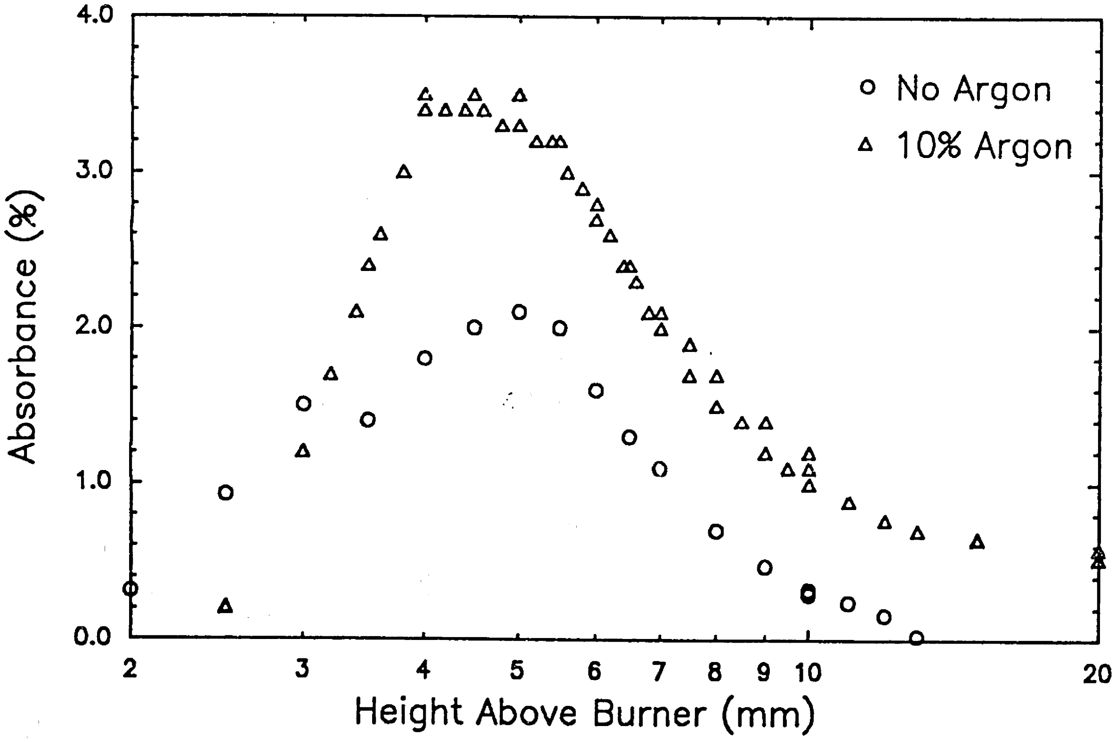

Figure 4.26 PAH-only profiles. $\lambda = 410$ nm. $\varphi = 2.4$, 10% Ar and 0% Ar

expected. In the next chapter some speculation on the cause of this behavior is presented.

A comparison of the $\varphi = 2.4$ flames, with and without argon helps isolate the effect of temperature from equivalence ratio. The temperature profiles are presented in Figure 4.24. The peak temperatures do not differ much, but in the zone where the PAH growth and destruction rates are highest, the no-argon flame is about 50 degrees cooler. Figure 4.25 shows the soot volume fraction profile for the two flames. As is commonly believed, the cooler flame produces more soot. The relative magnitudes are reversed in Figure 4.26 however. This plot of the PAH absorption shows that the hotter flame has a greater inventory of transient PAH even though it produces less soot.

4.3 Light Gas Analysis

Light gases (up to benzene) were measured in the $\varphi = 2.2$ and $\varphi = 2.4$ flames using a quartz sampling probe coupled to an on-line mass spectrometer. Figures 4.27 and 4.28 show the mole fraction profiles for the major species from the $\varphi = 2.4$ flame. The profiles of all species for both flames is presented numerically in Appendix A.

The profiles are in about the form we would expect. Fuel and oxygen decay from their fed values and the combustion products grow. Even though this is a very oxygen deficient flame, the molecular oxygen persists at greater than 1% values up to 11 mm, well past the nucleation zone. As will be shown the next section, this slow decay allowed the radical profiles to be inferred.

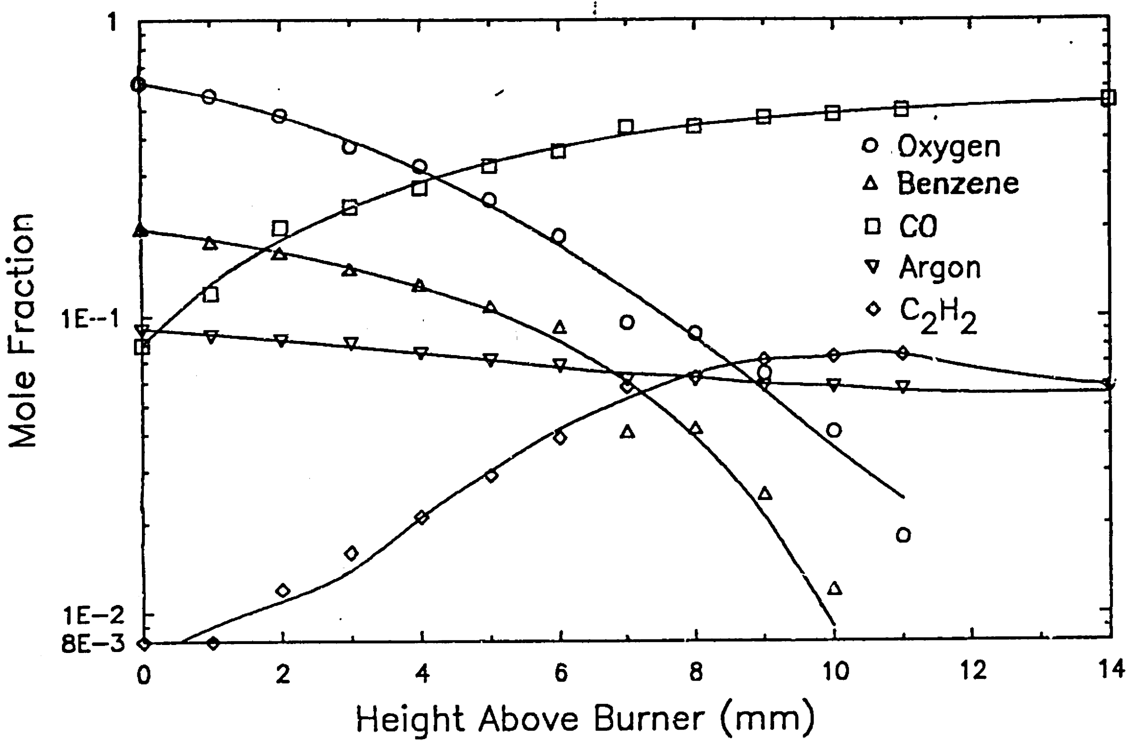

Figure 4.27 Concentration profiles for O_2, C_6H_6, CO, Ar, and C_2H_2. φ = 2.4, 40 torr, 10% Ar

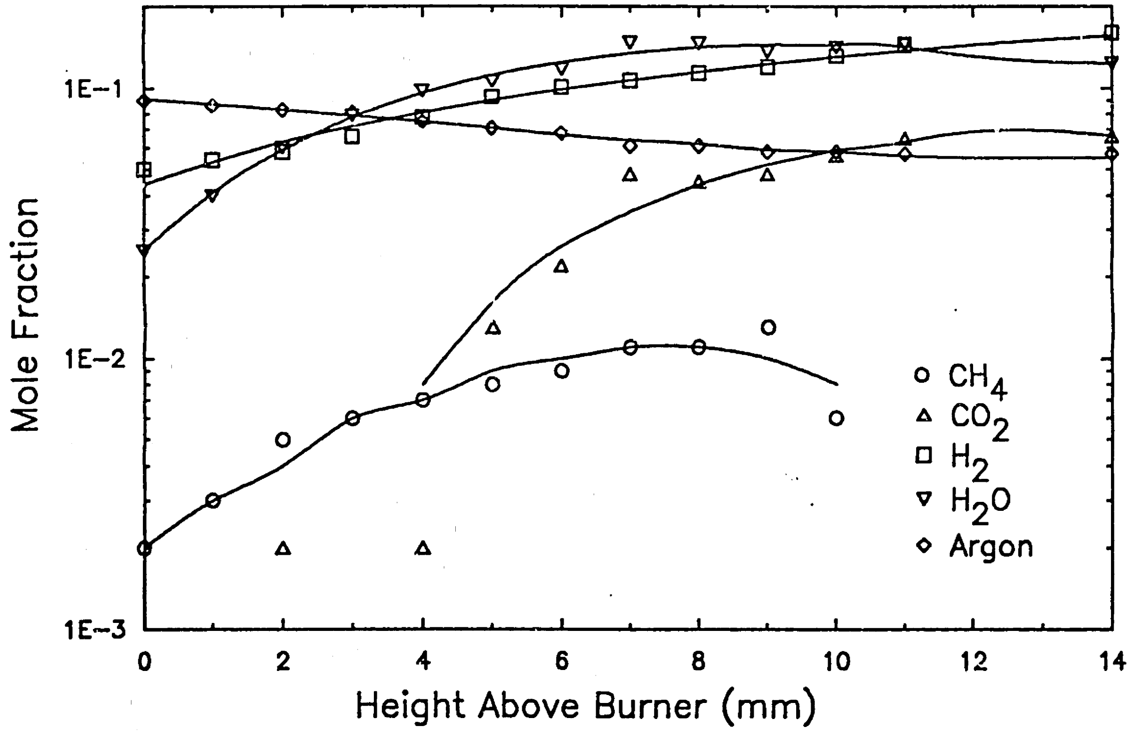

Figure 4.28 Concentration profiles for CH_4, CO_2, H_2, H_2O, Ar. φ = 2.4, 40 torr, 10% Ar

4.3.1 FLUX AND RATE

The one-dimensional flame equation, Equation 4.7, (Fristrom and Westenberg, 1965, p. 76) allows us to compute the flux of each species and, from the flux, the rate of formation or decay.

$$F_j = N_j\,(\nu + V_i) \qquad (4.6)$$

$$\frac{d}{dz}\,[N_i(\nu + V_i)A] = K_i A \qquad (4.7)$$

$$V_i = -\,\frac{D_{i,mix}}{N_i}\;\frac{dN_i}{dz} \qquad (4.8)$$

F_i : Flux of species i
N_i : Concentration of i
ν : convective velocity
V_i : diffusive velocity of species i
A : area expansion ratio
K_i : reaction rate of species i
D_{ij} : multicomponent diffusivity

Multicomponent diffusivities are computed as described in Fristrom and Westenberg (Equations 4.9 and 4.10). Lennard-Jones parameters are computed from literature correlations (Reid *et al.,* 1977).

$$D_{i,mix} = \frac{1 - X_i}{\sum\limits_{\substack{j=1\\ j\neq i}}^{n} X_j/D_{ij}} \qquad (4.9)$$

$$D_{ij} = \frac{1.66\mathrm{x}10^{-3}\,[(M_i + M_j)/M_iM_j]^{1/2}\;T^{1/2}}{P\,\sigma_{ij}^2\,(\varepsilon_{ij}\;/k)^{0.17}} \qquad (4.10)$$

X_i : mole fraction
M_i : molecular weight
σ : Lennard-Jones diameter
ε : Lennard-Jones potential well depth

The data were analyzed given the boundary conditions of no flux at the burner surface (except for O_2, C_6H_6, and Ar) and no reaction at the burner surface. The concentration data were fit to a fourth-order polynomial to smooth the data as well as to provide a differentiable function for calculating the flux.[3] We had no concentration data at the burner surface and the 1 mm and 2 mm data points were somewhat suspect due to probe-burner surface interactions. The burner surface concentration was estimated by adjusting the value until the diffusive flux to the burner just matched the convective flux away.

The flux was fit to a fourth-order polynomial to be differentiated to determine reaction rate. In order to impose the no-flux and no-reaction boundary conditions, the intercept and the first coefficient of the polynomial were forced to zero.

The area expansion ratio was fairly low in this flame. The shield flame seemed to have the effect of keeping the core flame contained. The value from Bittner (1981) was used (Equation 4.11), but it has little effect on the results.

$$A = (1 - 0.0116\ z)^{-1} \tag{4.11}$$

z : height above burner in cm

Figure 4.29 shows the flux profile for the major species. Note that the flux of the H_2 early in the flame is counter to the convective flow. Figure 4.30 shows the rate profile. The signs are adjusted so that the reactants show a positive *destruction* rate and the products show a positive *formation* rate.

4.3.2 ELEMENT FLUXES

The element fluxes provide a means of evaluating the quality of the data. Since no elements are created or destroyed, the fluxes of each element should be uniform. Figures 4.31, 4.32, and 4.33 show the profiles of total C, H, and O along with the major contributors. The fluxes are reasonably uniform, except for a drop at high heights above burner. The reason for this can be seen in a plot of the total mass flux, Figure 4.34. An analysis of the one-dimensional flame equation and the multicomponent diffusivities reveals that all the non-uniformity of the mass flux can be traced to errors in multicomponent diffusivities.

---

[3] Savitsky-Golay (1964) smoothing could have been used instead of the polynomial technique, but at cost of several data points on each end of the set. With the small number of data points collected here that cost was too high.

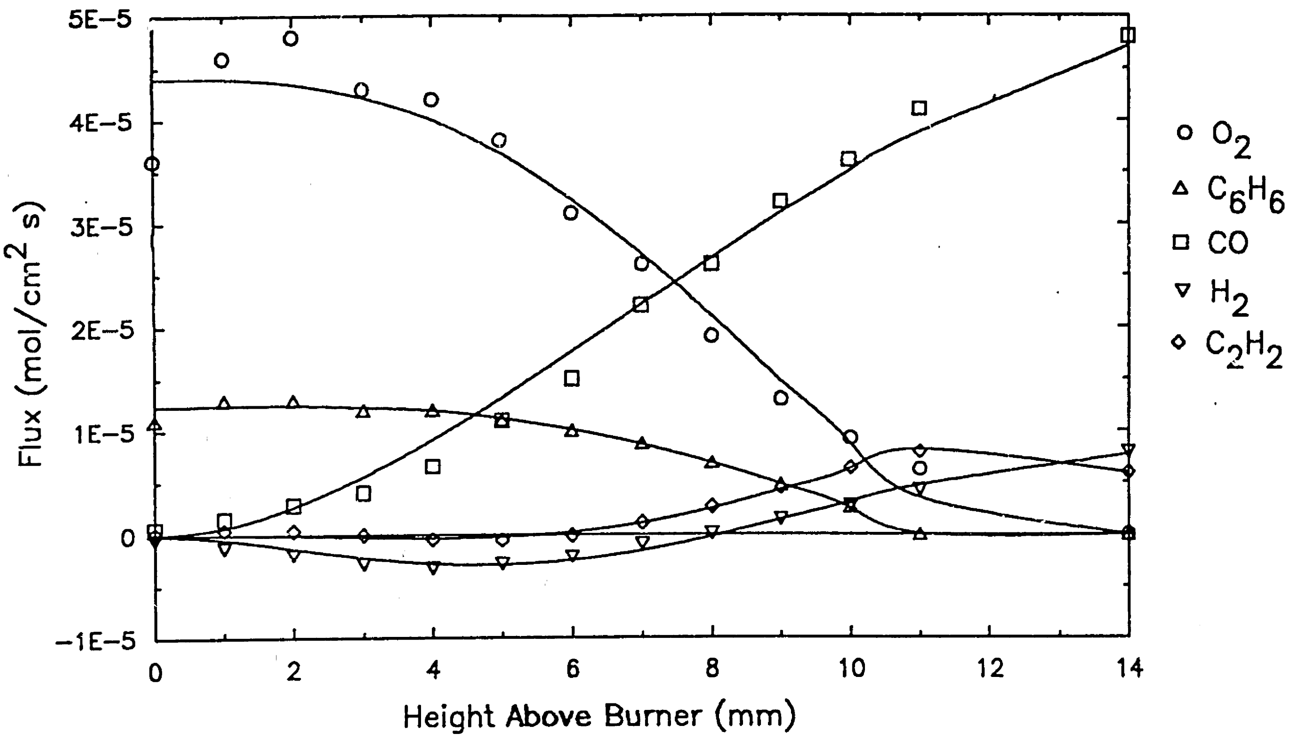

Figure 4.29 Light gas fluxes. φ = 2.4, 40 torr, 10% Ar

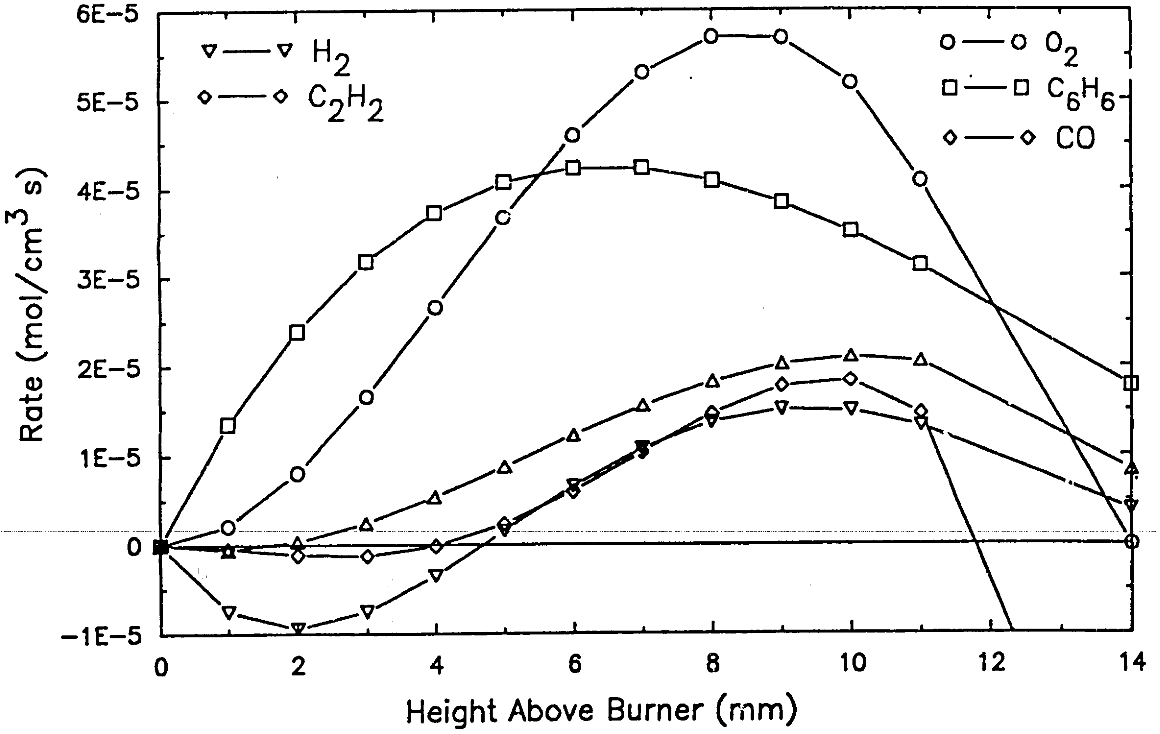

Figure 4.30 Light gas reaction rates. φ = 2.4, 40 torr, 10% Ar

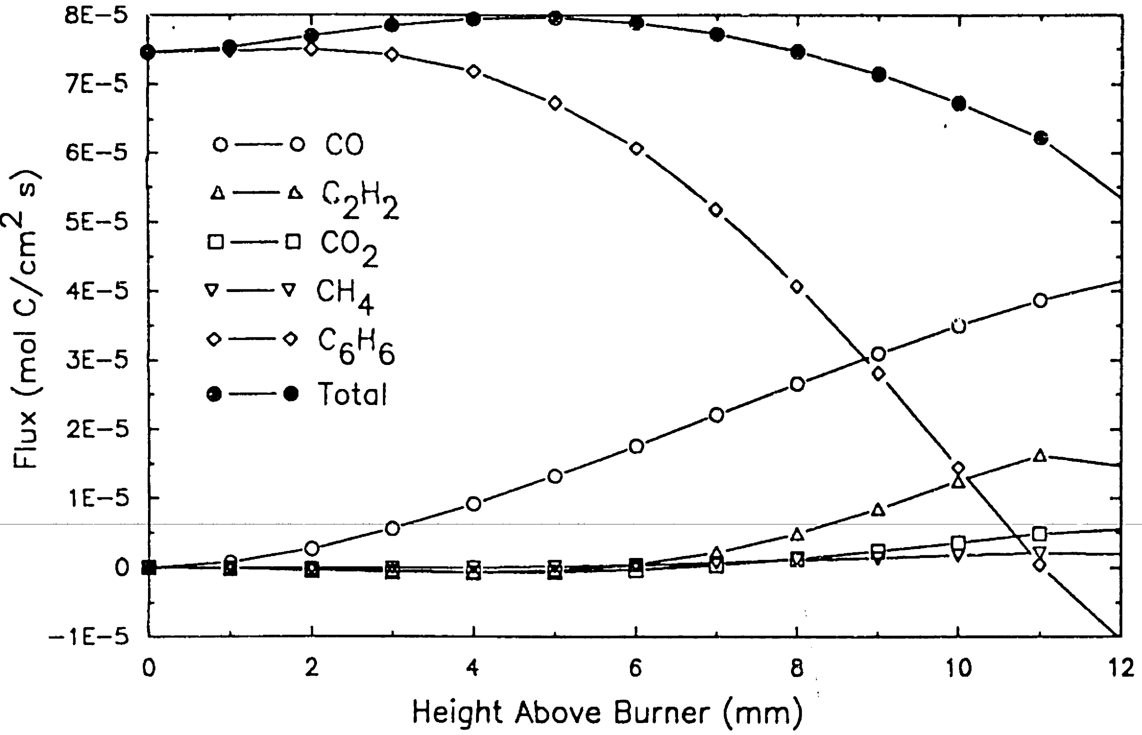

Figure 4.31 Element flux: Carbon. φ = 2.4, 40 torr, 10% Ar

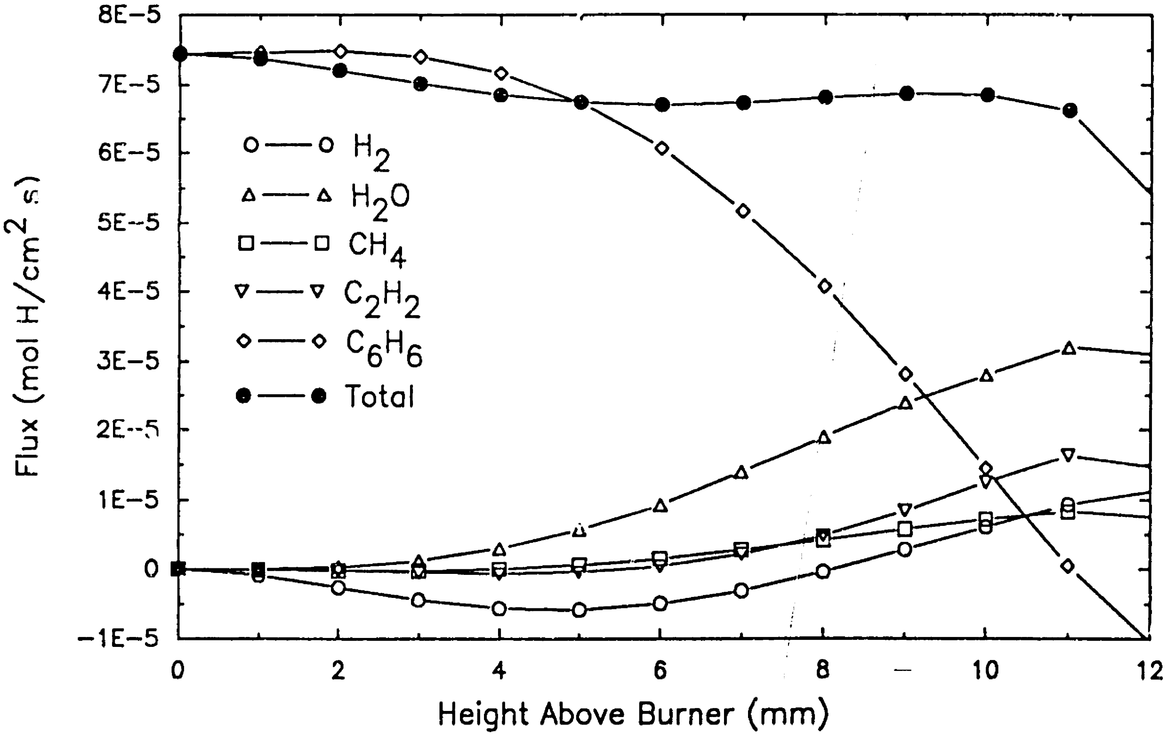

Figure 4.32 Element flux: Hydrogen. φ = 2.4, 40 torr, 10% Ar

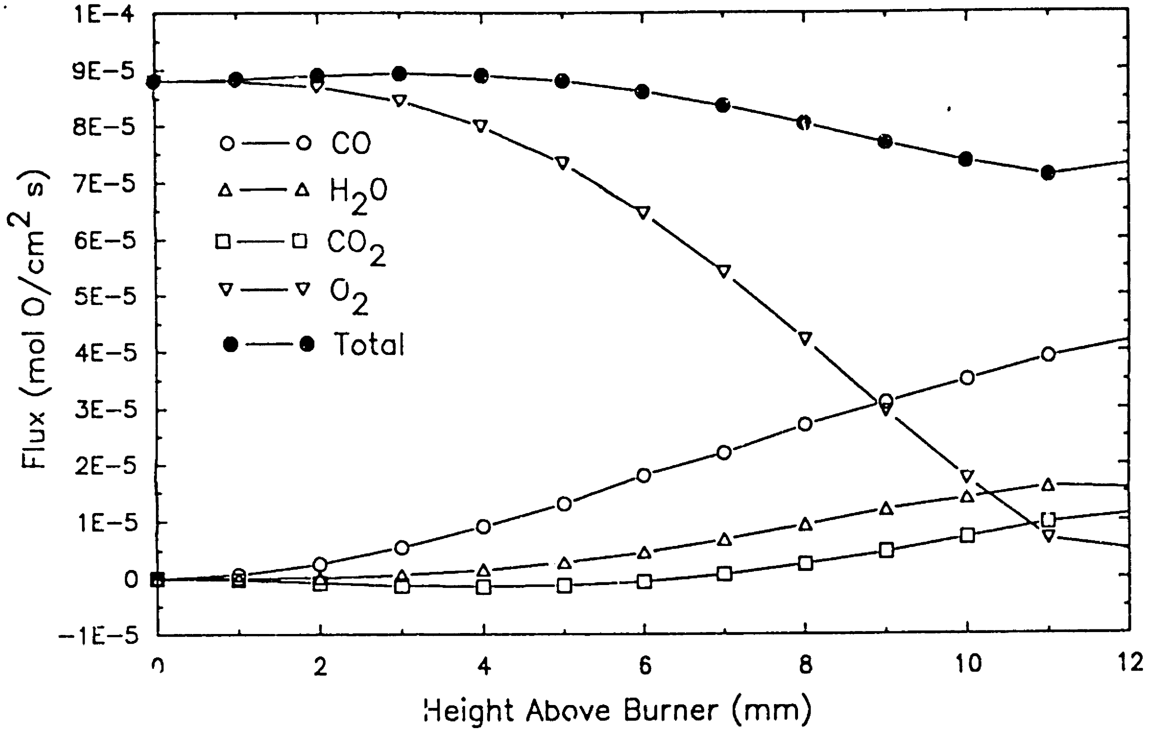

Figure 4.33 Element flux: Oxygen. φ = 2.4, 40 torr, 10% Ar

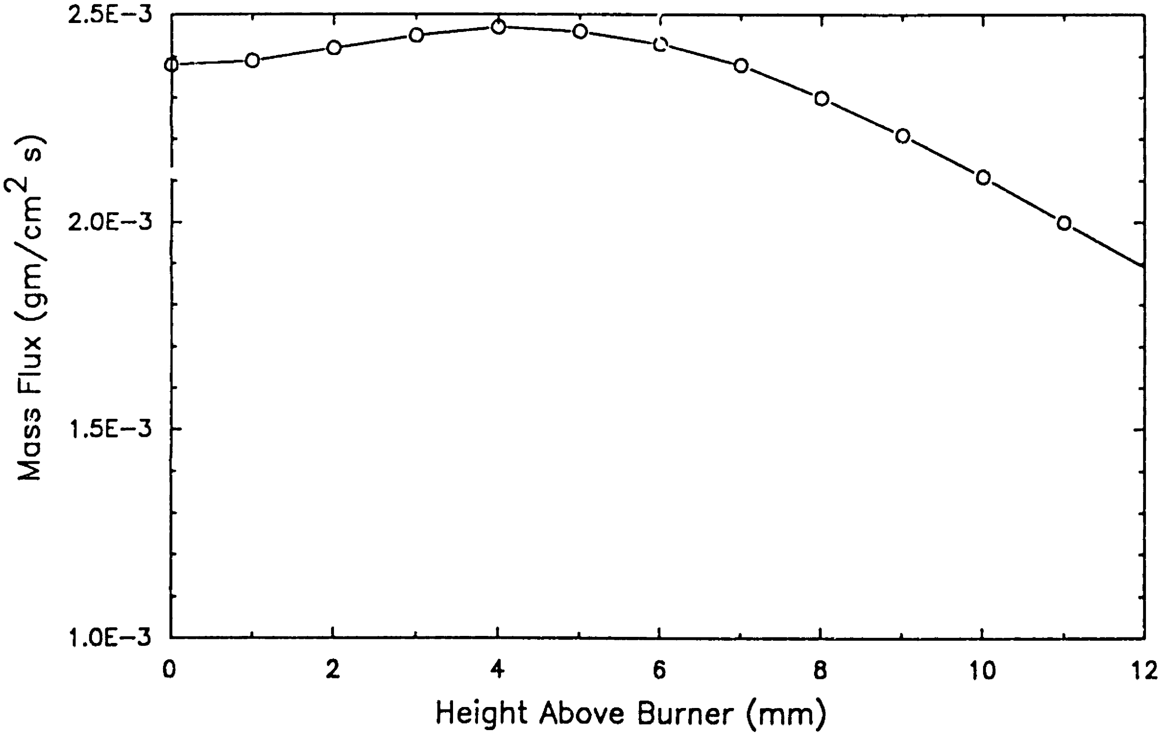

Figure 4.34 Mass flux. φ = 2.4, 40 torr, 10% Ar

4.4 Radical Concentrations

The experimental apparatus used in this study did not allow direct measure of any of the radical species. As will be presented in the next chapter, however, radicals drive most of the chemistry of nucleation.

4.4.1 H ATOM

We may estimate the H atom concentration by noting that almost all of the O_2 is destroyed by the Reaction 4.1 (Fristrom, 1963; Warnatz, 1984). The H atom concentration can then be computed using Equation 4.12.

$$H + O_2 \Rightarrow OH + O \qquad \text{(Reaction 4.1)}$$

$$[H] = -\frac{d}{dt}[O_2]/k[O_2] \qquad (4.12)$$

The rate constant used is that recommended by Warnatz (Schott, 1973).

$$k = 1.2\text{x}10^{17}\,T^{-0.91}\exp(-16.9/RT) \qquad (\text{cm}^3\ \text{sec/mol; kcal/mol})$$

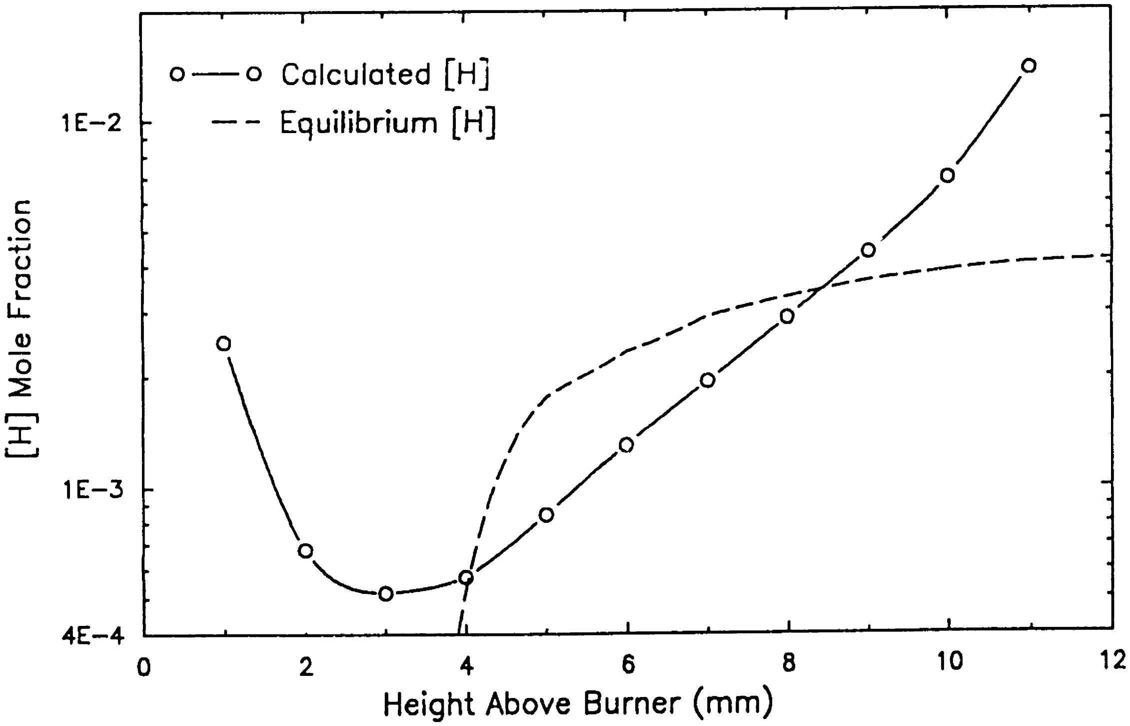

Figure 4.35 H Atom. Inferred concentration and global equilibrium. $\varphi = 2.4$, 40 torr, 10% Ar

This method of estimating H atom concentration was tested against the data of Bittner (1981) where all the variables of Equation 4.12 were directly measured. This result, which is presented in Appendix B, shows that the computed H atom is always within a factor of two of the measured value. The radical can only be calculated in regions of the flame where O_2 is greater than about 1%. Below this, the noise on the concentration signal begins to dominate. The oxygen destruction rate was calculated using the method described in the previous section. Figure 4.35 shows the computed H atom profile along with the global equilibrium value.[4] The concentration dips below the equilibrium value from 4 mm to 8 mm HAB.

4.4.2 OH PARTIAL EQUILIBRIUM

The OH concentration was computed by assuming equilibrium of Reaction 4.2 and the computed [H]. This reaction is equilibrated when the water-gas shift reaction (Reaction 4.3) comes to equilibrium. Analysis of the Bittner data indicates that the radical reaction comes to equilibrium well before the molecular reaction, as is shown in Appendix B.

$$H + H_2O \Leftrightarrow H_2 + OH \qquad \text{(Reaction 4.2)}$$

$$H_2O + CO \Leftrightarrow H_2 + CO_2 \qquad \text{(Reaction 4.3)}$$

Figure 4.36 show the approach to equilibrium of the water-gas shift reaction from the $\varphi = 2.4$, 40 torr flame. By 10 mm the molecular water-gas shift reaction has approached fairly closely to equilibrium. By analogy to the Bittner flame, we assume that equilibrium of Reaction 4.2 can be assumed to hold over the entire domain of interest (3 mm and higher). Figure 4.37 shows the computed OH profile along with the *global* equilibrium value.

4.4.3 ARYL RADICAL CONCENTRATION ESTIMATES

Aryl radicals play a critical role in the soot nucleation sequence which will be described in conjunction with the numerical model (Chapter Six). As in the case of H and OH, no direct measurements were made of these radicals. There is no easy direct experimental technique for

---

[4] Global equilibrium values were calculated using the StanJan computer program available from W.C. Reynolds, Dept. of Mechanical Engineering, Stanford University. This program uses the JANAF thermodynamic data set.

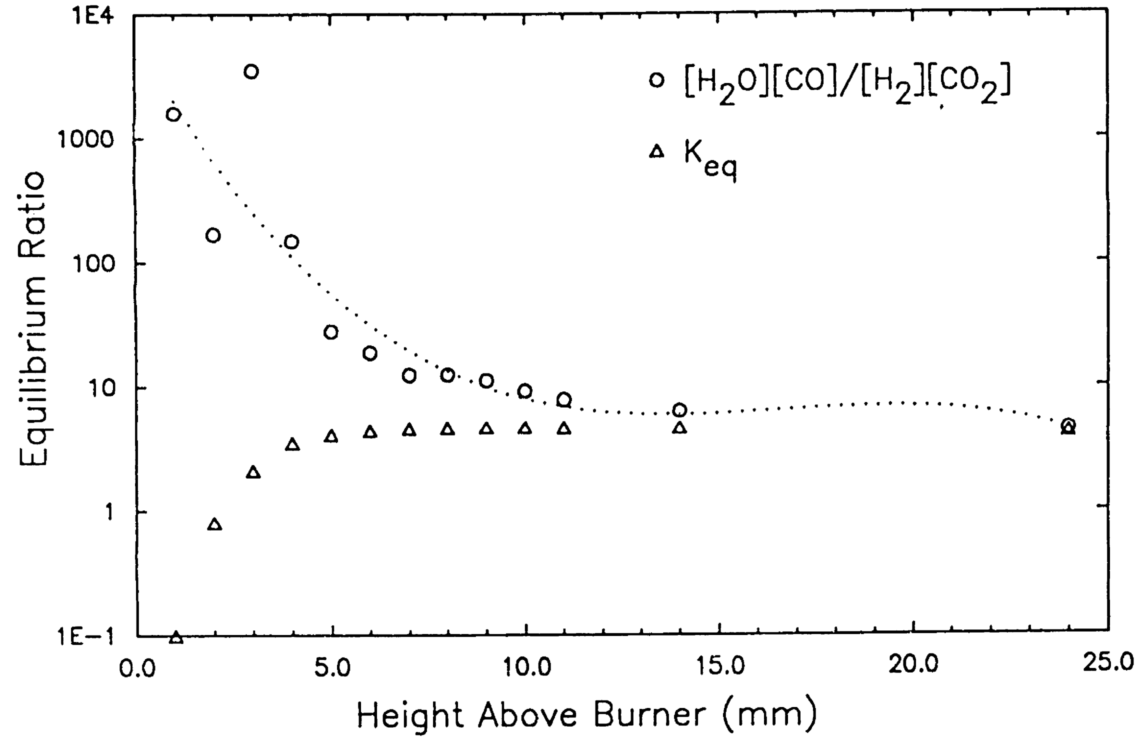

Figure 4.36 Water gas shift reaction. Approach to equilibrium. φ = 2.4, 40 torr, 10% Ar

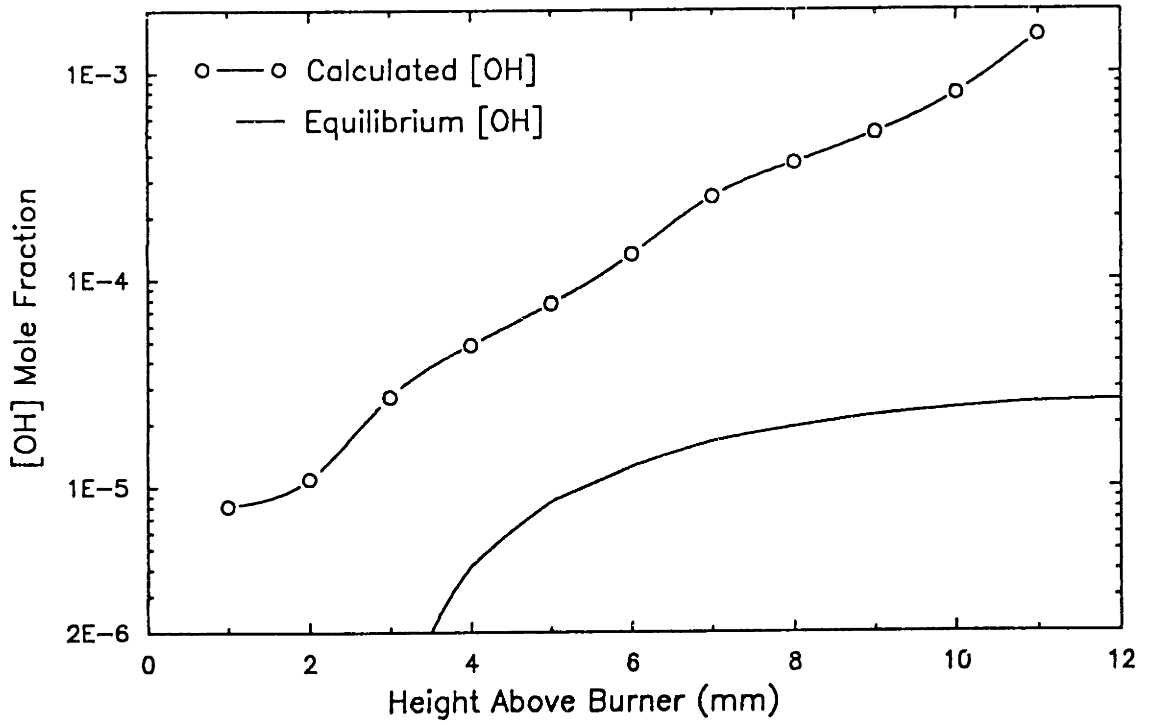

Figure 4.37 OH concentration and equilibrium. φ = 2.4, 40 torr, 10% Ar

determining their concentrations. The large sizes of the molecules makes their spectral features broad, preventing optical *in situ* measurement. Molecular beam mass spectrometry (MB/MS) would be possible on the smaller radicals of the series (phenyl, naphthyl) but even this method becomes intractable at higher molecular weights due to mass isomers. Phenyl is the only aryl radical of which we are aware that has be measured in a flame using MB/MS (Bittner, 1981).

Barring direct measurements we must rely, as before, on kinetics and thermodynamics for an inference on the radical concentration. We assume partial equilibrium of Reaction 4.4.

$$\text{PAH molecule} + \text{H} \Leftrightarrow \text{Aryl radical} + \text{H}_2 \qquad \text{(Reaction 4.4)}$$

Using the rate of Kiefer *et al.* (1985) for $H + C_6H_6 \Rightarrow C_6H_5 + H_2$,

$$k = 10^{14.40} \exp(-16.0/RT) \qquad (\text{cm}^3/\text{mol sec; kcal/mol})$$

we predict that the equilibration assumption is be fairly good. At 2000 K and $X_H = 5x10^{-3}$, the time constant for the forward reaction is approximately $1x10^{-4}$ sec (equivalent to about 0.3 mm at flame velocity). The H_2 and PAH concentrations have been experimentally measured and the H atom was inferred from the molecular oxygen decay rate. The estimation of the thermodynamic properties is done using the group additivity method, employing the values of Stein and Fahr (1985). Figure 4.38 shows

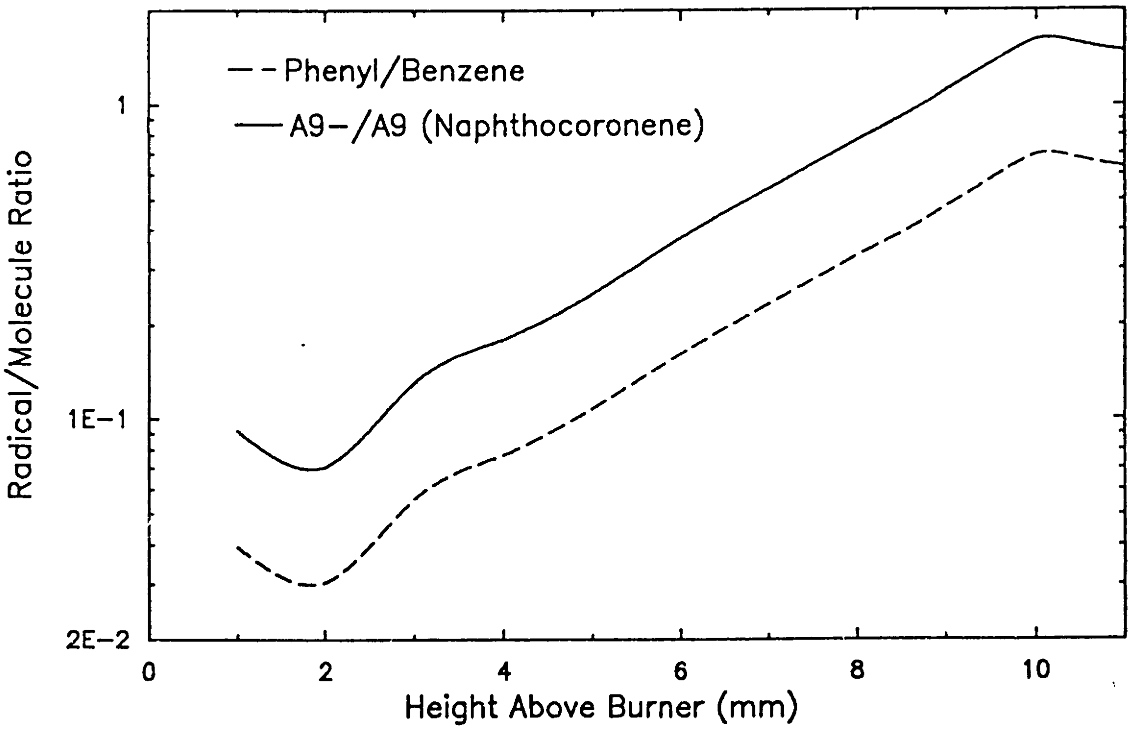

Figure 4.38 Estimated aryl radical concentration. φ = 2.4, 40 torr, 10% Ar

the ratios of aryl radical to PAH molecule using the above estimation method. The major reason for the ten-fold change over burner height is due to the H/H_2 ratio changing. The reaction has an enthalpy of only 4 kcal/mol, so the temperature effect is slight.

4.4.4 PHENYL RADICAL ESTIMATES

The phenyl radical did not come to partial equilibrium in the Bittner (1981) experiments. A plausible reason for phenyl being different from the larger aryl radicals is that the flux of single ring species (benzene) into the system is quite high, and all of it comes in molecular form. The larger aromatic species, however, are formed as radical, either aryl or π-system. It is crucial to have an estimate of the phenyl concentration because it is responsible for pumping a large amount of the mass into the PAH system.

Analysis of the Bittner data reveals an empirical method for estimating phenyl. Figure 4.39 shows the phenyl mole fraction plotted with the benzene destruction rate in mol/cm^3 sec. We can see that there is a striking overlap between the two curves. If we account for temperature, this same proportionality may be used in the flame of this work. We handle the temperature difference by fitting the benzene destruction rate to a unimolecular Arrhenius form. The proportionality between benzene rate and phenyl concentration, as shown in Figure 4.39, then allow the phenyl concentration to be expressed as a function of temperature and benzene concentration.

$$[\text{phenyl}] = [\text{benzene}]\ 10^{5.4} \exp(-62/RT) \qquad \text{(kcal/mol)}$$

4.5 UV-Visible Spectra

Figure 4.40 shows the UV-visible absorption spectrum of DCM soluble material from the $\varphi = 2.4$, torr flame. The trends show an increase in absorption with height above burner. This is indicative of a shift in the molecular weight distribution toward larger molecules.

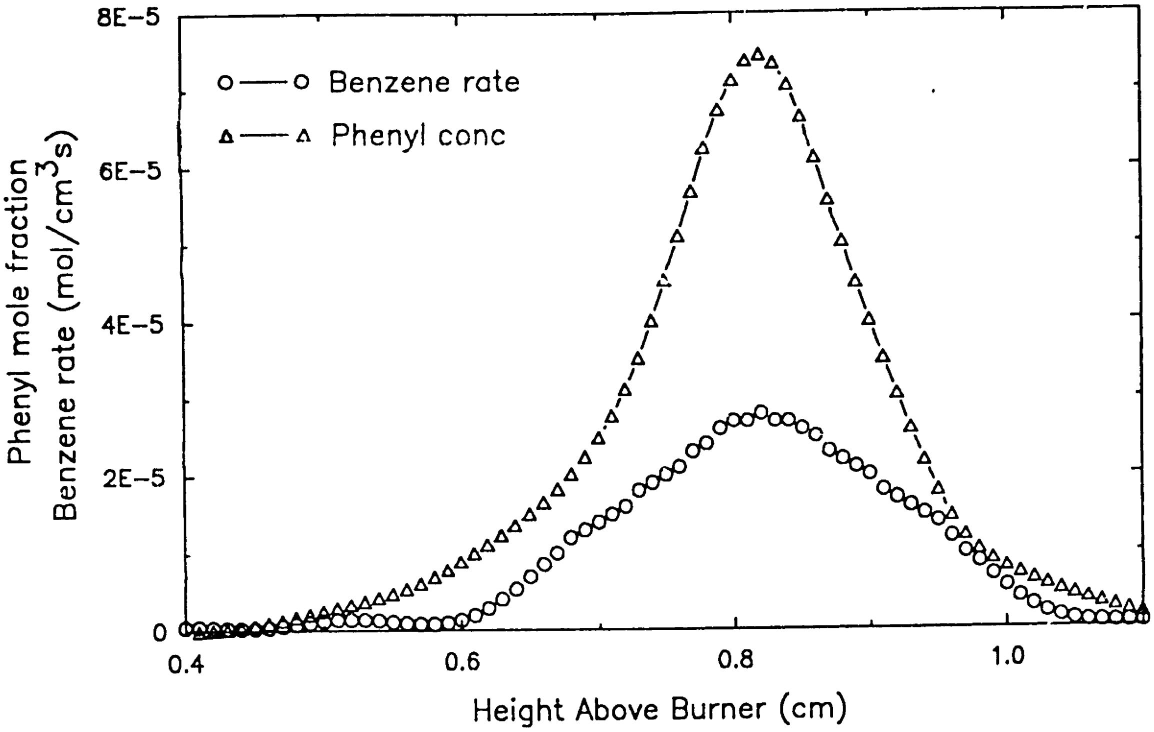

Figure 4.39 Phenyl radical concentration and benzene destruction rate from Bittner (1981). φ = 2.0, 20 torr, 30% Ar

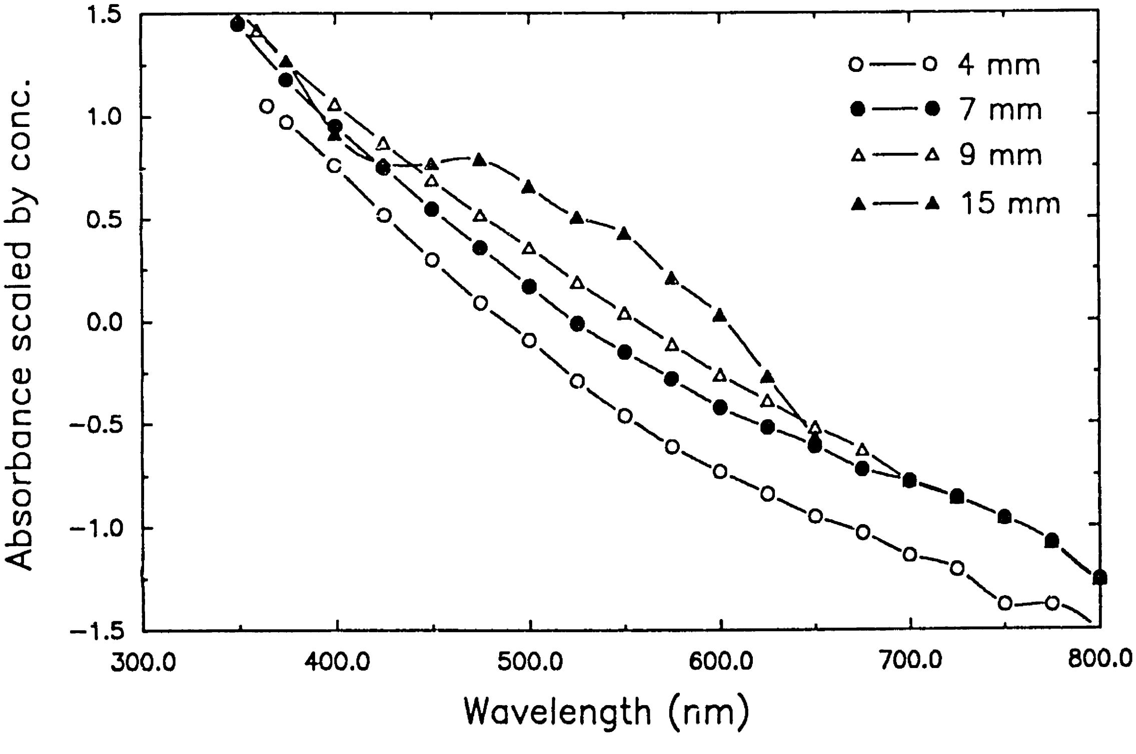

Figure 4.40 UV-visible absorption spectra. φ = 2.4, 40 torr, 10% Ar

Chapter Five

Discussion

This chapter includes discussions of the proposed mechanisms involved in soot nucleation.

5.1 Mechanisms

Four basic mechanisms are operative in the soot nucleation and growth process: mass growth, coagulation, oxidation and pyrolysis.

5.1.1 MASS GROWTH

Acetylene is most often regarded as the species responsible for mass addition to the PAH system. Harris and Weiner (1983a) argued this point on the basis that acetylene was the most abundant hydrocarbon in rich flames. Several mechanisms have been identified in which acetylene can react to form an aromatic ring and then continue to form larger PAH structures. Figure 5.1 from Bittner and Howard (1981) illustrates a growth process starting with phenyl radical and acetylene (Ia). A second acetylene is added to the styryl radical (Id) and the second ring closes (Ie). The viability of this mechanism depends on the branching ratio for the styryl radical. To form a ring, acetylene must add to styryl (Id) at a rate comparable to the other channels for the radical: *beta*-scission to form phenylacetylene (Ib), disproportionation to form styrene (Ic), and *beta*-scission back to reactants (-Ia). In his thesis, Bittner (1981, p.619) computed the lifetime of the styryl radical as a function of activation energy of the decomposition reaction using transition state theory (Benson, 1976). The change in entropy of the transition state ($\Delta S^{\ddagger}$) was assumed to be the same as that for alkyl decomposition. The collision time for styryl with C_2H_2 is $2x10^{-7}$ sec for the concentrations and pressure of the Bittner system. Using these rate estimates, styryl decomposition to phenylacetylene (Ib) must have an activation energy of greater than 70 kcal/mol to give the radical sufficient lifetime for *one* collision with C_2H_2 to occur. It is unlikely that Id would react at gas kinetic rates and also unlikely that Ib would have such a high activation energy. The reaction has a ΔH of 40 kcal/mol, which would put the E_{act} of the reverse reaction at 30 kcal/mol through detailed balancing. Radical plus molecule reactions of this type usually have much lower activation energies. By this analysis, it would appear that the mechanism of Figure 5.1 is infeasible.

Analyzing the same reaction using the model reaction $C_2H_3 \Rightarrow C_2H_2 + H$ and the data of Warnatz (1985) we come to a different conclusion. Warnatz shows that vinyl reaction will be well into the fall-off regime at the Bittner conditions. Using his pressure dependent (second order) rate constant expression of $k = 3.0 \times 10^{15} \exp(-32.7/RT)$, a pressure of 20 torr and a temperature of 1700 K, the calculated lifetime of vinyl is 2.7×10^{-5} sec. If this same rate holds for styryl, then the adduct will suffer of order 100 collisions with C_2H_2 before decomposition. Two factors make direct application of this rate constant to the styryl system risky. First, the greater number of internal vibrational modes of styryl as compared to vinyl make it less likely to be far from the high pressure rate limit. Second, the rate constant from Warnatz is for thermalized vinyl. The styryl produced in reaction Ia will be vibrationally hot (42 kcal), making endothermic unimolecular reactions more accessible.

Bockhorn *et al.* (1983) and Frenklach *et al.* (1986) have presented a slightly different scheme for forming aromatic rings, as is shown in Figure 5.2, which involves closing rings around triple bonds.[1] Acetylene adds to the phenyl radical in the same manner as the Bittner mechanism. However, the styryl adduct then rapidly decomposes to phenyl-acetylene. The phenyl-acetylene must be reactivated by abstraction of a hydrogen *ortho* to the ethynyl substituent. Addition of a second C_2H_2 to this aryl radical site allows the ring to close. One major difference in this scheme, as compared to that of Figure 5.1, is that the second ring is formed as an aryl radical. The radical created in the first mechanism is a delocalized π-radical. Since most of the reactions proposed for soot nucleation involve aryl radicals, the newly formed ring species does not need to be activated by H-abstraction in the Bockhorn/Frenklach (BF) mechanism. The requirement not only that the ring be reactivated after addition of the first acetylene but also that the reactivation occur at a specific site (*ortho*) could keep this path from being operative at the very rapid growth rates observed in flames. At the level of description of soot growth

---

[1] At the time Bittner published his work it was believed that the triple bond was too stiff to allow ring closure.

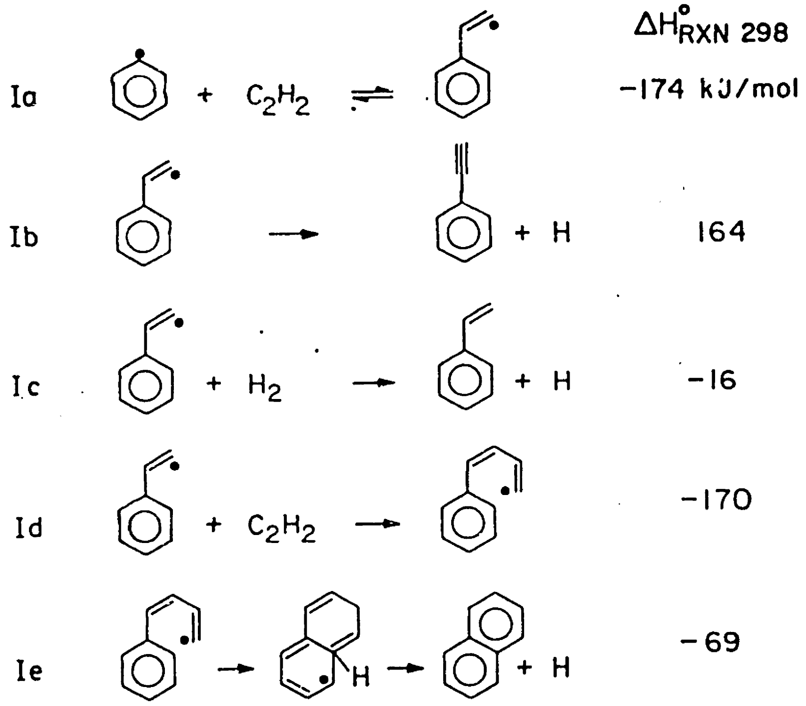

Figure 5.1 Bittner and Howard (1981) ring closure mechanism

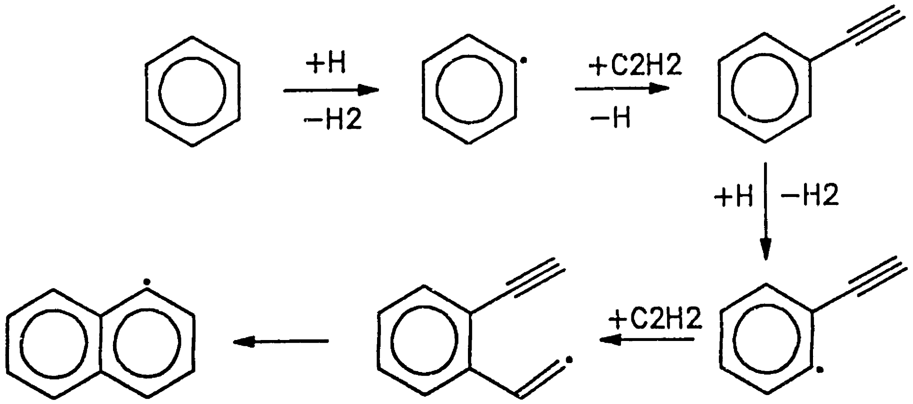

Figure 5.2 Bockhorn/Frenklach ring growth mechanism

where specific structures are not considered, these two mechanisms have more similarities than differences (*i.e.* growth occurs through acetylene addition to a radical).

In this, and all other classes of mechanisms discussed, the π-radicals are considered to be insignificant for the following reasons. It is assumed that these radicals rapidly undergo *beta*-scission, leaving an aromatic ring. As is usually the case, we do not have kinetic data on large PAH species, but data are available for the benzene-hexadienyl system. Nicovich and Ravishnkara (1984) measured the rate for H atom plus benzene. From thermodynamics we can calculate the reverse rate.

$$H + C_6H_6 \Rightarrow C_6H_7 \qquad \text{(Reaction 5.1)}$$

$$k_f = 4.0\text{x}10^{13} \exp(-4.3/RT) \qquad (\text{cm}^3/\text{mol s; kcal/mol})$$

$$k_r = 1.3\text{x}10^{16} \exp(-33.4/RT) \qquad (\text{s}^{-1}\text{; kcal/mol})$$

At 1700 K, the hexadienyl radical decomposed back to benzene and H atom in $1\text{x}10^{-12}$ sec, much less than the time scales of interest in the flame. We would expect some degree of stabilization of the π-radical in the larger aromatic systems of PAH's as compared to benzene, but probably not enough to make the delocalized radicals an important participant in ring-forming reactions.

We have no direct measure of all the reactions presented in Figure 5.1 or 5.2. However, Fahr *et al.* (1988) measured the rate of acetylene addition to phenyl in a low pressure pyrolysis reactor.

$$C_6H_5 + C_2H_2 \Rightarrow C_6H_5C_2H + H \qquad \text{(Reaction 5.2)}$$

$$k = 3.2\text{x}10^{11} \exp(-1.4/RT) \qquad (\text{cm}^3/\text{mol s; kcal/mol})$$

No reactions of acetylene + multiring compounds have measured rate constants, so we must use the Fahr rate as a guide for all mass addition reactions to PAH. This is not as bad as it may appear at first. If the reaction mechanism is as is shown in Figure 5.2, all addition reactions involve C_2H_2 + a localized σ-radical. The energy of these localized radicals is not greatly affected by the size of the ring system,[2] so the rate for phenyl may be a close approximation to the rate for arbitrarily large PAH's. The reaction-path degeneracy must be accounted for, however, due to the larger number of hydrogen atoms of the larger PAH's.

---

[2] This can be seen by the assignment of a group additivity value to an aromatic carbon with a σ-radical by Stein and Fahr (1985). Group additivity thermodynamic values could not be given to a π-radical.

Harris and Weiner (1983b) have measured an apparent rate for C_2H_2 addition to the soot surface. They found the reaction to be first order in soot surface area and first order in C_2H_2, but that the rate constant decreased with height above burner. While the soot they studied is much larger than the PAH of interest in this work, it is interesting to consider the growth processes to be basically the same: addition of C_2H_2 to a σ-radical. In the case of soot, the σ-radicals would be on a surface rather than in the gas phase, but at the local level we can consider the two to be the same. The decrease in rate constant with height above burner can be explained as a reduction in radical density on the soot surface. Decreased radical content of the "old" soot may reflect the balance of radical production due to abstraction (and possibly pyrolysis) and consumption from recombination being shifted toward the latter. Relatively slow radical termination reactions which dominate in the latter parts of the flame reduce the overall radical concentration. The value of the rate constant given represents the maximum soot reactivity.

$$\text{Soot} + C_2H_2 \Rightarrow \text{Larger Soot} \qquad \text{(Reaction 5.3)}$$

$$\frac{dM}{dt} = 2.5\text{x}10^{-2}\, P_{C_2H_2}\, S_{soot} \qquad (\text{gm/cm}^2\ \text{s atm})$$

No activation energy was reported. Since the activation energy of the C_2H_2 + phenyl reaction was only 1.4 kcal/mol, it is not surprising that the activation energy of the soot experiment was not observable.

A common basis to quantitatively compare these Reaction 5.2 and Reaction 5.3, which are presented in different units, is to compute their reaction efficiencies. This is the ratio of the reaction rate to the gas kinetic collision rate. Surprisingly, the two rate constants have virtually the same reaction efficiencies: for Harris and Weiner, η_{react} = 2.5x10^{-4}, for Fahr *et al.*, η_{react} = 2.9x10^{-4}. The fact that these two reactions, both involving C_2H_2 addition but with very different substrates, have such similar rates gives confidence to the notion that the mechanisms are similar.

The data of Bittner (1981) provide data against which these rates may be tested. Bittner measured phenyl radical, acetylene, and phenylacetylene in his benzene flame, allowing computation of an apparent rate constant. Figure 5.3 shows the measured rate of phenylacetylene production and destruction and the calculated production rate using the Fahr *et al.* rate constant. The shape of the production part of the curve is matched quite well by the literature rate constant but the magnitude is about 8-fold too low.

The reason for this large discrepancy may be chemical activation. The phenyl profile in this flame (Figure 4.39) indicates that phenyl is formed through a destruction path of benzene and not through H abstraction.[3] A likely path, which fits fairly well using published rate constants, is $C_2H_2 + C_4H_3$. The ΔH of this reaction is -102 kcal/mol so the phenyl formed this way would be vibrationally hot. Since C_2H_2 is one of the major components of the flame, a collision between C_2H_2 and a phenyl which has not been thermalized is a likely occurrence. The theory of chemical activation, however, has not yet progressed to the point where we can make quantitative predictions of this behavior. As we shall see in the next chapter, the rate required to explain the data is more in line with that observed by Bittner than the other measured rates.

5.1.2 COAGULATION

Coagulation is the term given to the growth of nuclei through reactive (or sticking) collisions between PAH's. As was discussed in Chapter Four, we have evidence of this process on the small end of the size distribution by the observation of biphenyl, phenylnaphthalene, binaphthyl, *etc.* and at the high end through the observation that soot collides with unit sticking efficiency (see Figure 4.22). We postulate that the mechanism for coagulation is through the reaction of aryl radical + PAH molecule.

Fahr *et al.* (1988) have measured the rate for the simplest of these reactions: phenyl + benzene ⇒ biphenyl + H (Figure 5.4).

$$C_6H_6 + C_6H_5 \Rightarrow C_6H_5C_6H_5 + H \qquad \text{(Reaction 5.4)}$$

$$k = 3\times10^{11}\,\exp(-3.75/RT) \qquad (\mathrm{cm^3/mol\ s;\ kcal/mol})$$

Converting this into a collision efficiency yields $\eta_{col} = 2\times10^{-4}$. This leaves a wide gulf between the single-ring rate and the soot rate of about four orders of magnitude. Three factors can help account for this discrepancy. First, the lowered LUMO (*L*owest *U*noccupied *M*olecular *O*rbital) energy of the larger aromatic systems can stabilize the cyclohexadienyl-type adduct and reduce the rate of decomposition of the adduct which reforms the reactants. Second, the van der Waals physical force between the molecules increases with their size. This force could provide a sort of "temporary glue"

---

[3] If H abstraction were operative, then the phenyl concentration profile would start much earlier in the flame. Both benzene and back-diffused H atom are present in fairly large quantities together below 5 mm, but no reaction occurs.

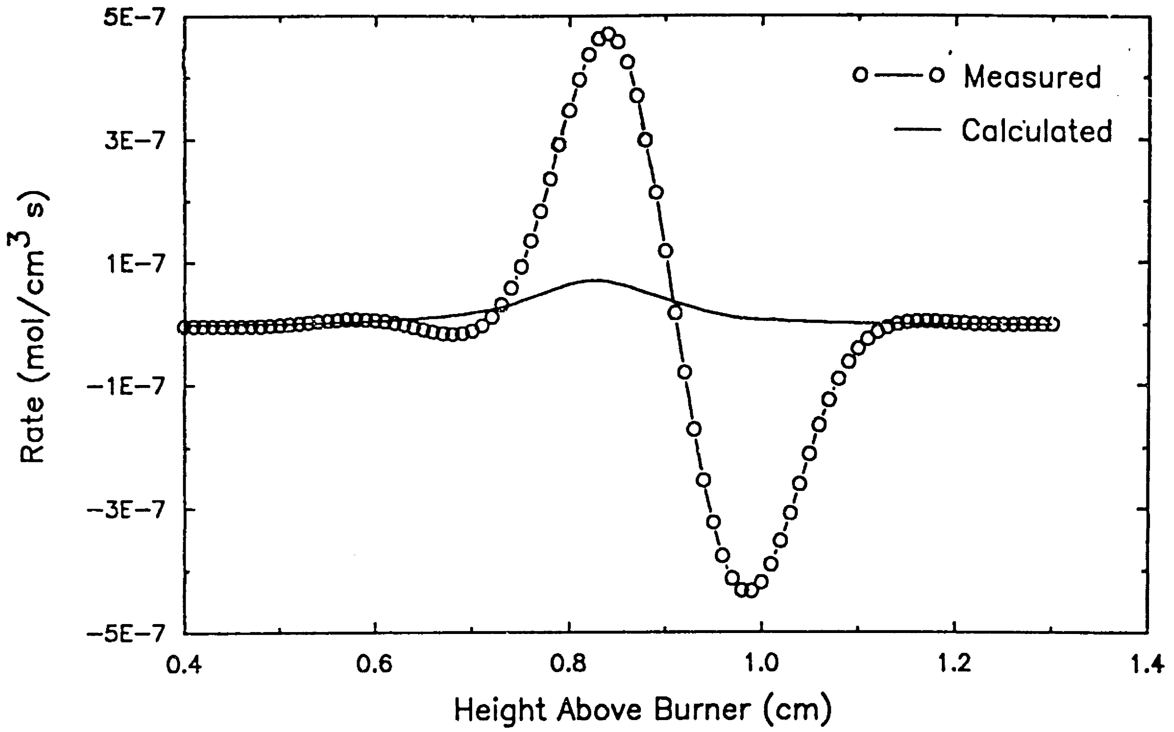

Figure 5.3 Phenylacetylene rate: measured by Bittner (1981) and predicted using the rate of Fahr *et al.* (1988)

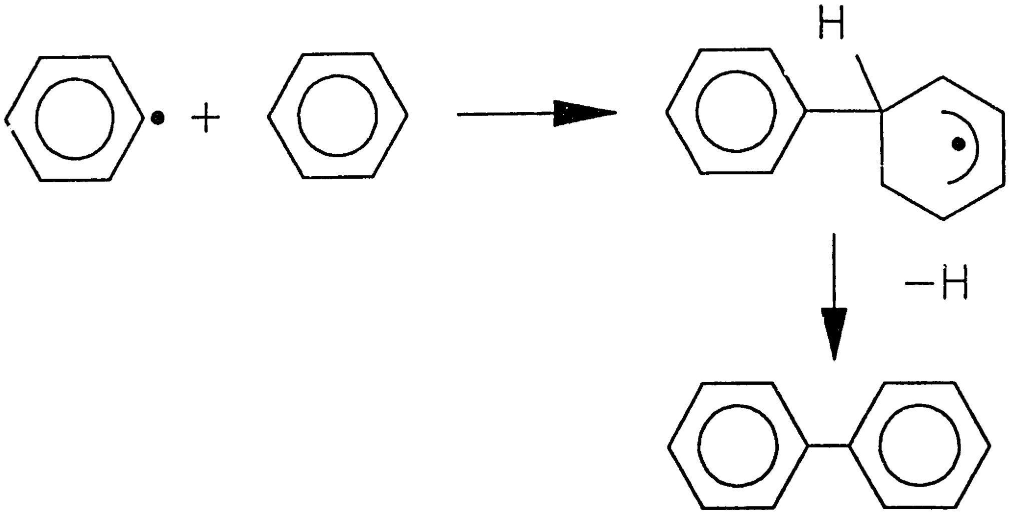

Figure 5.4 Prototype coagulation reaction: benzene + phenyl ⇒ biphenyl + H

which could hold the large adduct together while the chemical bond forms. Miller *et al.* (1984) have computed the van der Waals force between some PAH's. For a pair of circumcoronene molecules (666 amu), the physical force is 22.5 kcal/mol, or about a quarter of a covalent bond. In contrast, a benzene dimer has a van der Waals force of only 2 kcal/mol. Miller *et al.* found that the van der Waals forces *alone, however,* were not sufficient to build up the observed concentration of soot nuclei. A third possible reason for increased sticking efficiency of large PAH relative to single ring species is related to steric factors. The larger PAH have a greater likelihood of existing as radicals with more than one σ-radical site because they have more abstractable hydrogen. With more sites available for reaction, it is more likely that a randomly chosen collision will be favorable. Continuing the same reasoning, the change of radical-radical recombination reaction (as opposed to radical-molecule) is greater for large r PAH. We would expect recombinations to occur at nearly gas kinetic rates.

This growth mechanism does not get much attention in the combustion literature, although Frenklach *et al.* (1988) have included it in a recent paper, and Badger and Spotswood (1960) have studied this type of reaction extensively in a high temperature flow reactor. One reason for it's neglect is due to the difference in structure between a benzene flame and an aliphatic flame. In the benzene flame, the nucleation zone for soot is superimposed on the primary reaction zone. In aliphatic flames, there is a spacial separation between the two zones. Visually, this is seen as a dark band between the blue primary oxidation zone (color due to chemiluminescent CO reactions) and the yellow soot nucleation zone. No such dark band is seen in benzene oxidation. Thus, the concentration of benzene and phenyl in the soot nucleation zone is much higher in benzene flames than aliphatic flames. As will be shown later, the data may be modeled well only by including a route through which PAH's condense.

5.1.3 OXIDATION

The available oxidants in the flame are O_2, OH, and O. Neoh (1980) determined that OH was the dominant oxidizing species for soot in flames and that it occurred with a reaction efficiency in the range 0.13 to 0.27. The only available literature rates are for single ring compounds, as in the case of the previous two mechanisms. He *et al.* (1988) measured the rate for the reaction OH plus benzene.

$$OH + C_6H_6 \Rightarrow C_6H_5OH + H \qquad \text{(Reaction 5.5)}$$

$$k = 1\text{x}10^{13} \exp(-10.7/RT) \qquad (\text{cm}^3/\text{mol s; kcal/mol})$$

The initial part of this sequence involves the addition of OH to a ring forming a hexadienyl-type adduct which undergoes *beta*-scission to form phenol. A major factor in the ultimate rate of this overall reaction is the degree of reversibility of the OH addition to the ring. The *beta*-scission could split off the OH instead of the H, in which case no net reaction takes place. The phenol, once formed, should rapidly decompose to phenoxy radical (Lin and Lin, 1985) through a route similar to that proposed by Cyprus and Bettens (1974, also Vaughn, 1988, p.300) as shown in Figure 5.5. The He *et al.* rate, however, translates into a reaction efficiency of $3x10^{-4}$, three orders of magnitude lower than the apparent rate measured by Neoh. A way out of this dissimilarity is to assume that the oxidation reactions occur through OH + aryl radical. This radical recombination rate has not been measured, but we would expect it to be close to gas kinetic with little or no activation energy. The value for collision efficiency of 0.2 measured by Neoh would then represent a steric hindrance factor, or, in the case of a particle, it would be proportional to the number density of aryl radicals on the soot surface.

Molecular oxygen is present in large concentrations (order 10%) in the soot nucleation zone of the benzene flames, so it must be considered. Lin and Lin (1987) measured the rate of oxygen plus phenyl

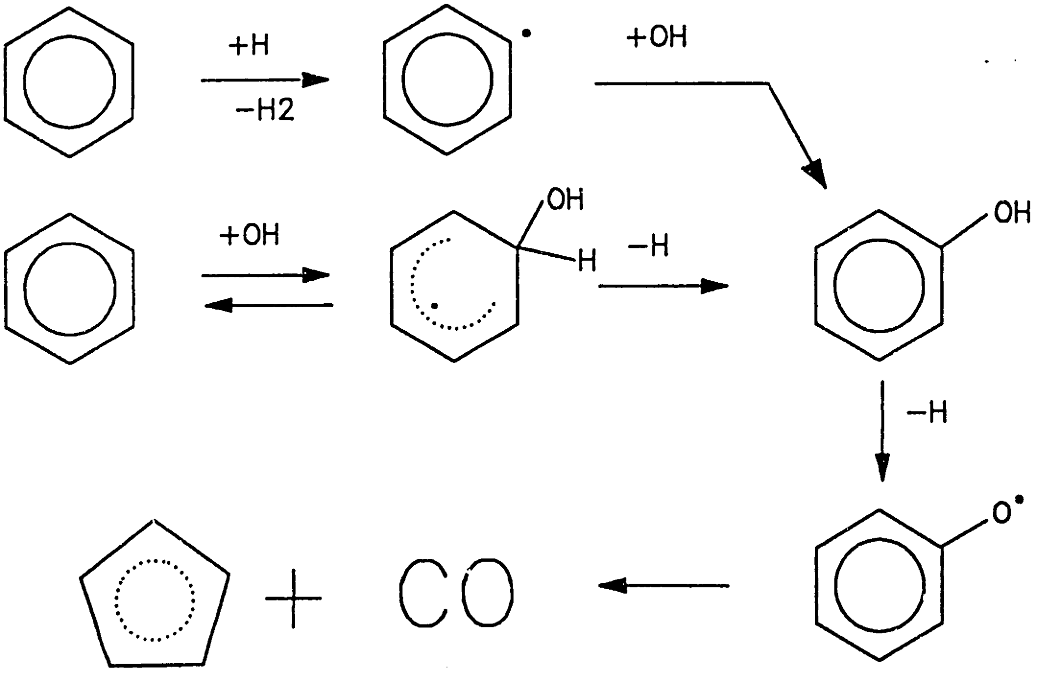

Figure 5.5 Two oxidation routes of benzene by OH. Upper mechanism adds OH through radical recombination. Lower mechanism adds OH through a displacement reaction.

in a shock tube. The phenoxy will decompose rapidly to cyclopentadienyl and carbon monoxide through the route shown in Figure 5.5.

$C_6H_5 + O_2 \Rightarrow C_6H_5O + O$ (Reaction 5.6)

$k = 2.1x10^{12} \exp(-7.5/RT)$ (cm^3/mol s; kcal/mol)

This is a fairly important oxidation channel early in the flame when the O_2 concentration is high and OH is still building. The semiemperical formula for oxidation of pyrolytic graphite by Nagle and Strickland-Constable (1962) was tested on carbon black by Park and Appleton (1973) and found to predict the data well. This formula is consistent with a mechanism of surface adsorption, reaction, and desorption. As will be seen in the next chapter, the Nagle and Strickland-Constable rate grossly overpredicts the oxidation of soot nuclei.

Neoh determined that O atom was not an important oxidant in the flame conditions she studied. We have neither direct measurements of O atom nor good estimation methods for it, so there is no way to test this observation in the present system. Two facts make the exclusion of O atom from the system suspect. First O atoms tend to be at least as reactive as OH, as can be seen by a survey of the reactions in Warnatz (1985) where both O and OH reactions are presented for the same hydrocarbon. Second, the soot nucleates in a zone where O_2 destruction rates are high. Since most of the oxygen is destroyed through the reaction $O_2 + H \Rightarrow OH + O$, the production rate of O will be the same as OH. Unfortunately O atom is experimentally inaccessible both in this experiment and in Bittner's. Since the production of O and OH are linked, the effect of leaving out O atom may just mean that the fitted OH rate constant will be too large (by twofold) to account for the destruction by O.

5.1.4 PYROLYSIS

Pyrolytic decay is a channel which removes carbon from PAH's in units of one or two carbon atoms per event, as is shown in Figure 5.6. This reaction can be thought of as the microscopic-reversibility analog to the mass growth reaction. This mechanism is speculative, since there are no prototype reactions in the literature except the pyrolysis of phenyl. The data, however, do indicate that a highly activated reaction must be present which destroys the PAH inventory. As can be seen from Figures

4.1 to 4.8, the decay of PAH at the soot nucleation zone is quite rapid. The profiles of most of the components of the flame change very little across this boundary, but the temperature is rapidly rising here. Oxidation and coagulation are two possibilities already discussed which could account for this but, as will be shown in the next chapter, they are not fast enough.

Soot, however, does not undergo rapid pyrolysis. Once formed, it can exist stably in a hot, H-atom-rich environment with no, or at most a small amount of, mass evolution. Of course the soot will oxidize if oxidant is present. The transition between the thermal instability of PAH and the stability of soot may be in the formation of a three dimensional structure. We could think of a two dimensional aryl radical breaking a C-C bond through *beta*-scission. The vinyl radical substituent which is formed can either *beta*-scission the next C-C bond and break away or reform the bond, which reverses the original reaction. In a three dimensional structure, the vinyl radical has many more sites in which to reform the bond, reducing the likelihood of fragmentation.

The experimental evidence for pyrolytic decay comes from several other areas as well. The rate benzene destruction in the benzene flame of Bittner has been shown to be consistent with a unimolecular step with an apparent activation energy of 82 kcal/mol (Bittner and Howard, 1984). The exact mechanism of the decay is not known. Looking to the high molecular weight profiles of Bittner (1981), we see evidence of the greater reactivity of the smaller PAH's relative to the heavier ones. Figure 5.7 shows the concentration profiles of three high molecular weight classes. Bittner conducted these experiments with a quadrupole mass spectrometer operating as a high-pass mass filter. Thus, each curve represents all material greater than the specified mass. The evidence for pyrolysis is in the decay or downward sloping region of the curves. The Mass>200 amu curve has the steepest decay followed by the Mass>450 amu curve. The Mass>700 amu curve has very little decay.

If oxidation were the only cause for this behavior, the slopes of these three curves on the semi-log plot would be the same, unless there was some mechanism making small PAH more reactive toward oxidation than large ones. In fact, the current model predicts just the opposite relative reactivity toward OH; the large PAH will have a greater likelihood of existing as an aryl radical (due to the higher H number) and thus be more likely to oxidize. Coagulation cannot account for the decay rate. If it were, we would see an increase in the concentration of the Mass>700 curve to offset the decrease in Mass>200 curve.

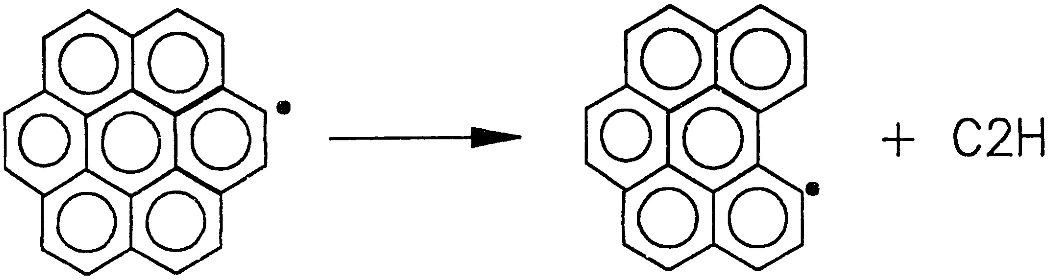

Figure 5.6 Prototype pyrolysis mechanism for PAH

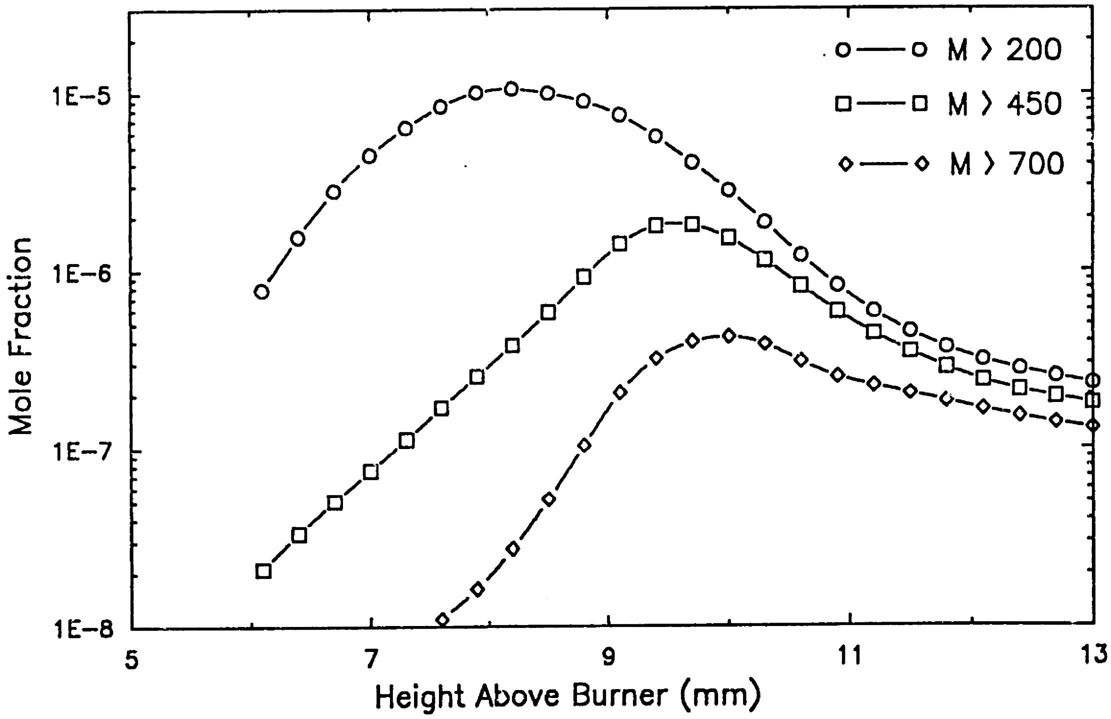

Figure 5.7 High molecular weight material profiles from Bittner (1981)

The only rate data in the literature for this type of pyrolytic reaction is on the thermal decay of phenyl radical. This has been measured in shock tubes by two groups: Kern *et al.* (1986) and Braun-Unkhoff *et al.* (1989).

$$C_6H_5 \Rightarrow C_2H_2 + C_4H_3 \qquad \text{(Reaction 5.7)}$$

Kern *et al.* $k = 1\text{x}10^{15} \exp(-82/RT)$ (cm^3/mol s; kcal/mol)

Braun-Unkhoff *et al.* $k = 4.5\text{x}10^{13} \exp(-72/RT)$ (cm^3/mol s; kcal/mol)

The decomposition of phenyl is, however, qualitatively different than the pyrolysis of larger PAH. In the former case, the total aromatic system is being destroyed, in the latter case, the aromatic network still remains, but it is smaller by two carbons. The exact effect of this on the rate is unknown.

5.2 Anomalous PAH/Soot Behavior

Given the mechanisms presented in the previous section, we can make an attempt to explain the "anomalous" behavior of the intermediate PAH as compared to the ultimate soot formed in flames of different equivalence ratio and temperature. The general model is that PAH grow through mass addition and collisions to form soot nuclei. We would expect, then, that the flames with the greatest ultimate soot loading would also have the largest inventory of intermediate PAH. As was shown in §4.2.4, this was not the case. For example, the $\varphi = 2.4$, 0% Ar flame produced more soot than the $\varphi = 2.4$, 10% Ar one, even though the intermediate PAH levels of the $\varphi = 2.4$, 10% Ar flame are greater.[4]

A possible explanation for this behavior involves both growth and pyrolysis. In the hotter flame, we have a higher peak H atom concentration. The high diffusivity of the H atom leads to higher H atom concentrations in the cooler, presooting zone of the hotter flame than in the no-diluent flame. This high H atom concentration will make a larger fraction of the aromatics exist as aryl radicals, and thus be more susceptible to growth reactions. In this way the hotter flame produces a large inventory of PAH ahead of the peak in temperature. When these PAH's are convected into the hotter region of this flame, the highly activated pyrolysis reactions destroy them much quicker than they are destroyed in the cooler

---

[4] The main effect of the diluent addition is to increase the temperature (see §3.1.4).

flame. Those PAH which have the opportunity to grow large enough to obtain three dimensional stability can survive the pyrolysis and will form soot nuclei.

5.3 Ionic Mechanisms

In the interest of completeness, we consider ionic routes to formation of soot. The ionic route to soot nucleation has a number of appealing aspects. Small ions are formed in flames through chemi-ionization (Calcote, 1962).

$$CH + O \Rightarrow CHO^{+} + e^{-} \qquad \text{(Reaction 5.8)}$$

A number of ions have aromatic character (*i.e.* follow Hückel 2(n+1) rule) which increases their stability (*e.g.* $C_3H_3^{+}$, $C_5H_5^{-}$). Stein and Kafafi (1987) have computed the thermodynamic stability of the most stable isomers (for a given C and H number) for molecules and ions. Interestingly, the ions show a monotonic increase in stability with size while the molecules show a stability barrier at the two to three ring size. This would indicate that thermodynamics would push the smallest ion to grow large without delay, but molecules may face difficulties in the growth path.

Ions have another attractive aspect with regard to growth through sticking collisions of PAH's. The effective collision cross section of for ion-molecule reactions becomes much larger than their physical dimensions due to electrostatic imaging forces. This increases the rate of coagulation and, thus, nucleation.

Several pieces of evidence argue against the importance of ions in soot formation reactions. Homann (1985) makes a convincing case that the concentrations are simply too low to be important in the nucleation process. From this work we can see that the fit to the Smoluchowski equation in Figure 4.22, which was made with a rate constant considering only van der Waals forces, is sufficiently close to the data without invoking ionic mechanisms. Lastly, as will be shown with the model, we do not need to enhance collision cross sections of PAH in order to explain the observables.

It is on this basis that ions were neglected from consideration as an important soot forming channel. It should be noted that the experimental apparatus used had no provision to make ion measurements, so their prevalence in our combustion system is not known.

Chapter Six

Numerical Model

A numerical model has been developed to describe the nucleation phase of soot formation. The model includes the following processes:

- mass growth of the PAH and nuclei through addition of C_2H_2
- oxidation of the PAH and nuclei by OH and O_2
- coagulation of the PAH and nuclei through sticking collisions
- unimolecular pyrolysis of aryl radicals

The description of the kinetics of each of these processes will be followed by some of the numerical considerations.

6.1 Model Kinetics

Almost no data exist for reactions of large PAH species which are involved in soot nucleation. Thus we had to do a great deal of extrapolation of published rate constants. Each of the reactions involved in the model had an analog reaction from the literature. Typically, these reactions involve benzene or phenyl radical plus the other reagent. The A-factors of the reactions were treated as fitted parameters, while the activation energies were kept the same as the values published for the prototype reactions. If the fit of the A-factor caused it to deviate significantly from the literature value, some attempt at rationalization based on chemical intuition was made.

6.1.1 ADDITION OF C_2H_2

Acetylene is the only molecular species present in the flame in sufficient quantities to account for molecular weight growth of the soot. While there is no direct evidence that acetylene (in molecular form) is the species which ultimately adds to the soot surface, C_2H_2 must at least involved as the carbon source in the reaction sequence.

The model assumes that all the mass growth is through C_2H_2 addition to an aryl radical site of the PAH or soot nuclei (for the rest of this discussion the term PAH will be used for the molecules as well as nuclei). The prototype reaction sequence assumed is that of Figure 5.2. This is a several step process, but can be considered as a two step operation: 1) addition of C_2H_2 to an unsubstituted aryl radical and 2) addition of C_2H_2 to the *ortho* site of an ethynyl substituted aryl radical followed immediately by ring closure. Of course, this is a major simplification which disregards all structural information. For example, addition of C_2H_2 to the 1-position of naphthalene could result in ring closure to form the 5-membered ring of acenaphthalene in one step. Six membered rings could also be formed in one step as well, as in the case of addition of C_2H_2 to the 4-position of phenanthrene to form pyrene.

The model for predicting growth up to several thousand amu cannot, however, consider this sort of fine structure for two reasons. First, adequate rate constants are not known for any of these reactions, making it senseless to try to distinguish between one- and two-step closure mechanisms. Second, the number of isomers grows exponentially with molecular weight; computer resources would rapidly be overloaded even if the programmer had the patience to evaluate all possible reactions for all possible isomers. This model makes the gross, but justifiable simplification that *one* global rate constant can hold for addition of acetylene to an aryl radical of any size or structure (as will be discussed later, no structural information whatsoever is maintained in the model).

As discussed in the preceding chapter, we have two literature rate constants to use as a prototype for this global reaction. Fahr *et al.* (1985) have measured the rate of C_2H_2 + phenyl radical. Harris and Weiner (1983b) have computed an apparent rate constant for C_2H_2 plus soot from flame data. The approach of the model toward fitting the data is to use the Arrhenius form of Fahr *et al.* along with their measured activation energy (1.4 kcal/mol) and use the A-factor as a fitting parameter.

6.1.2 OXIDATION

Two oxidants are considered in the numerical model: OH and O_2. The mechanism for both types of oxidation is the reaction of an aryl radical plus the oxidant. For the reaction of OH, no direct literature rates are available but because it is a radical recombination reaction, we could expect its rate to be near gas kinetic. As stated in the last chapter, Neoh (1980) measured the rate of OH plus soot and found it to be react with a reaction efficiency of 0.2. The reaction efficiency form of rate expression is used in the model with the efficiency as a fitted parameter.

The reaction of O_2 plus PAH uses the Lin and Lin (1987) rate coefficient. This rate parameter needed no fitting. The molecular oxygen route is more significant than the OH path early in the nucleation zone where O_2 concentration is high and OH is still building. The relative importance reverses at later times.

The Nagle and Strickland-Constable (Park and Appleton, 1973) rate for oxidation by O_2 was tried in the model. This rate expression has regions which are insensitive to oxygen concentration, indicating that some surface rate, such a desorption of product, is rate controlling. The Nagle and Strickland-Constable expression overpredicts the rate of oxidation so it was not included in the final model. This shows that the implied adsorption/desorption behavior of the Nagle and Strickland-Constable kinetics is not representative of the oxidation of large molecules/small particles.

6.1.3 COAGULATION OF PAH

The prototype reaction for growth reactions through coagulation is a PAH molecule plus an aryl radical. As was discussed in the previous chapter, there are orders of magnitude differences in the rates for single ring coagulation (benzene + phenyl) and soot coagulation. We have no way of judging, *a priori*, which rate is more appropriate. The model expresses the rate in terms of a reaction efficiency, with the efficiency being fit to the data.

6.1.4 THERMAL DECOMPOSITION OF ARYL RADICALS

Pyrolysis of phenyl and pyrolysis of soot are the two rates used for thermal decomposition of aryl radicals. The rate for phenyl decomposition is taken from Braun-Unkhoff *et al.* (in press). The observed rate for soot pyrolysis is essentially zero. In order to account for this size dependent pyrolysis rate, the model uses a ramp function to calculate rate constant as a function of size. Single ring molecules use the highest rate and species larger than 1000 amu have no pyrolysis. A linear ramp is computed between these limits. The threshold of 1000 amu was selected based on the observation that little pyrolytic decay occurs in the Mass>700 curve of Figure 5.7. The activation energy from Braun-Unkhoff *et al.* (75 kcal/mol) was used and the A-factor was fitted to the data.

6.2 Computational Concerns

The dynamics of the nucleating soot and PAH are described by a system of ordinary differential equations and integrated as an initial value problem. The molecular weight size distribution is discretized into bins of width 72 amu, which represents six carbon atoms. The particles in the bins are modeled as carbon clusters; no hydrogen content is considered and no structure is assumed.

The coagulation part of the model is computed using aerosol dynamics equations (Friedlander, 1977; Frenklach and Harris, 1987).

$$\frac{dN_1}{dt} = -N_1 \sum_{j=1}^{n_{max}} \beta_{1,j} N_j \tag{6.1}$$

$$\frac{dN_i}{dt} = \frac{1}{2} \sum_{j=1}^{i-1} \beta_{j,i-j} N_j N_{i-j} - N_i \sum_{j=1}^{n_{max}} \beta_{i,j} N_j \tag{6.2}$$

$$\beta_{i,j} = \left[\frac{8\pi kT}{\mu_{i,j}}\right]^{1/2} (r_i + r_j)^2 \eta_{i,j} (\xi_i + \xi_j - \xi_i\xi_j) \tag{6.3}$$

N_i : Number density of particles in size bin i
$\beta_{i,j}$: Second order coagulation rate constant
$\eta_{i,j}$: Collision (or reaction) efficiency
$\mu_{i,j}$: Reduced mass of colliding pair
r_i : Radius of particle
ξ_i : Fraction of PAH which exist as aryl radicals

The first component of Equation 6.2, the source term, represents the growth of bin i through collisions of two particles whose sizes sum to i. This is divided by two to avoid double counting of collisions. The second term, the sink, accounts for depletion of particles in bin i through reactive collisions with particles in any other size bin. The second order rate constant is computed as the gas kinetic collision rate times a collision efficiency. The collision efficiency, η_{ij}, can be a function of size if need be, but it was kept as a constant in this model. The factor ξ_i represents the fraction of aromatics in a given size bin which exist as aryl radicals. It is needed to account for the fraction of collisions which can be reactive. The model assumes that only aryl radical-PAH molecule collisions and radical-radical collisions are effective. ξ_i is a function of size because the larger PAH are more likely to exist as radicals due to the greater hydrogen number and it is function of height above burner because the $[H]/[H_2]$ ratio changes with height. The radii of the particles are computed by assuming the particles to be spheres with a density of 1.8 gm/cm^3. Bin 1 has to be treated differently, as shown in Equation 6.1, because there is no source term.

The other chemical reaction in the model are implemented as "stair-stepping" operations. For example, the oxidation rate of bin i includes a depletion term accounting for reactions of oxidant plus particles in bin i and a source term from particle which come from bin i+1. The effect of oxidation is to push particles "down the stairs" to smaller bins. Accounting must be made of the number of reactions to deplete a bin. Since the bin width is 72 amu, or six carbons, it takes six oxidation reactions to move a particle down. Mass growth and pyrolysis take three events each to move a particle upwards or downwards.

Mass growth:

$$\frac{dN_i}{dt} = \frac{1}{3} k(T) (\xi_{i-1} N_{i-1} - \xi_i N_i) [C_2H_2] N_{Av} \tag{6.4}$$

Oxidation:

$$\frac{dN_i}{dt} = \frac{1}{6} (\eta_{i+i} \beta_{i+1} \xi_{i+1} N_{i+1} - \eta_i \beta_i \xi_i N_i) [OH] N_{Av} \tag{6.5}$$

Pyrolysis:

$$\frac{dN_i}{dt} = \frac{1}{3} k(T) (\xi_{i+1} N_{i+1} - \xi_i N_i) \tag{6.6}$$

k(T) : rate constant computed from Arrhenius parameters. E_{act} from literature and A-factor fit to data.
η_i : reaction efficiency of OH with PAH
N_{Av} : Avagadro's number

Oxidation by molecular oxygen is not shown, but its form is quite similar to the OH oxidation, with the exception that the rate constant is of Arrhenius form rather than collision efficiency form. The four model operations, coagulation, mass growth, oxidation, and pyrolysis, are shown schematically in Figure 6.1.

The fraction of PAH which exist as aryl radicals, ξ, is computed by assuming partial equilibration of the Reaction 6.1 and the equilibrium constant computed in Equation 6.7.

$$\text{PAH molecule} + \text{H} \Leftrightarrow \text{Aryl radical} + \text{H}_2 \qquad \text{(Reaction 6.1).}$$

The thermodynamics used are those of Stein and Fahr (1985). Equation 6.7 is a three parameter fit of the equilibrium constant to temperature. The number of hydrogens is computed partly using Equation 6.9, which is the empirical fit of Pope (1988). The C/H ratio, however, is capped at 3.0 which is the value measured by Homann and Wagner (1967) for young soot.

The thermodynamic relationship computes the ratio of aryl radical to molecules, but we want the ratio of aryl radicals to total (molecule + radical). Equation 6.8, of the form x/(1+x), makes this conversion.

$$K_{eq} = 598\ T^{-0.512} \exp(-6.891/RT)\ N_H \qquad (6.7)$$

$$\xi = \frac{K_{eq}\ ([H]/[H_2])}{1 + K_{eq}\ ([H]/[H_2])} \qquad (6.8)$$

$$C/H = 0.115\ MW^{1/2} - 0.090 \qquad (6.9)$$

The profiles of C_2H_2, H, H_2, O_2, and OH are inputs to the model (see §4.4 for a description of the estimation method for H and OH). The temperature profile is also an input. The initial concentration of PAH is entered to start the integration off at time zero. Depending on the form of the data which the model was attempting to match, the output could be presented several ways. For most of the cases, the computed PAH was broken into two fractions: soluble and insoluble. The division between the two being at 900 amu.

The model uses fourth-order Runge-Kutta integration with a variable time stepping algorithm to solve the system of differential equations. The Pascal code from *Numerical Recipes* (Press *et al.*, 1986) forms the basis of the integration routine. The model was run on an IBM PC-architecture machine (Dell System 310). The number of bins could be varied depending on how much time was available. Limitations of the Pascal compiler (Borland Turbo Pascal, version 5.0) kept the maximum number of bins down to 140 (for a molecular weight range of 10,000 amu). However, we observed that there was very little change in results in going from 40 bins to 140, so most of the runs were done with the bin number at 40. Run time was less than five minutes, so rapid progress could be made in exploring the parameter space. The limitation on bin number due to software and time constraints meant that the model could not predict the number density or particle size, only volume fraction of the soot. This limitation proved not to be a significant problem because most of the experimental data to which the model is compared comes from experiments which yield volume fraction data (optical absorption or probe sampling). Diffusion was neglected in the model. In the worst case, the diffusive velocity was 10% of the convective velocity.

6.3 Model Results

The model was tested against three different flame conditions:

- $\phi=1.8$, 20 torr, 30% Ar - nearly sooting, data of Bittner (1981)
- $\phi=2.2$, 40 torr, 10% Ar - sooting, present work
- $\phi=2.4$, 40 torr, 10% Ar - sooting, present work

Although the first flame was non-sooting, profiles of high molecular weight material up to 750 amu were measured and the radical species were measured *directly*. The other two flames required that the radical profiles be *inferred* using the estimation methods presented in Chapter Four.

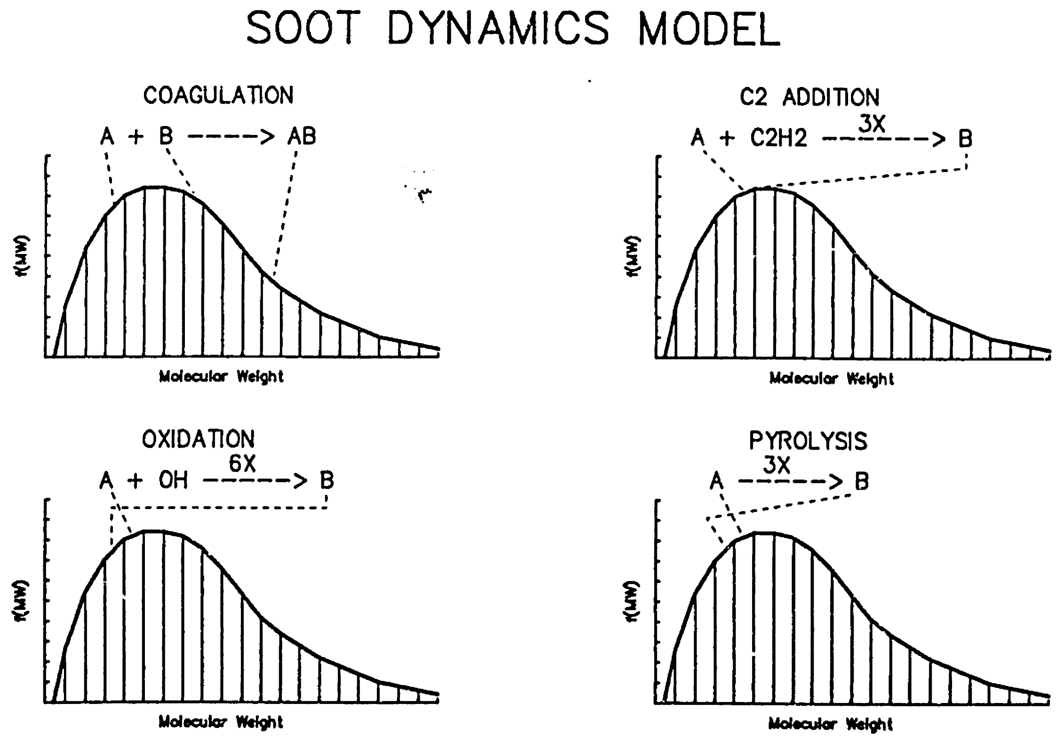

Figure 6.1 Schematic representation of model operations

The parameters adjusted in the model were:

- A-factor for the reaction C_2H_2 + aryl radical
- reaction efficiency for OH + aryl radical reaction
- collision efficiency for aryl radical + PAH molecule reaction
- A-factor for unimolecular pyrolysis

Phenyl + PAH had to be treated as a special case of aryl + PAH with its own collision efficiency. This is in line with the observation that the rate for phenyl + benzene (η = 2.6x10^{-4}) is much different than the rate for soot + soot (η = unity). A more realistic description of this class of reactions would be to make the rate constant a ramp-function with size. This, however, would add yet another parameter to set the steepness of the ramp. Aryl radical + aryl radical reactions have the same reaction efficiency as radical + molecule reactions.

Parameters were adjusted manually to achieve the best visual fit to the data. The model has built-in graphical display capability to allow this. The approach was to work with the parameters to get the best fit for each flame condition individually. Effort was made to get he location of the curve (*e.g.* the steep rise in insolubles in Figure 6.6) correct as well as the magnitudes. When a set for each flame was developed, an attempt was made to reconcile the differences. In doing this, the fit of the φ = 1.8 flame was given the most weight because the radical information here was the best. In some cases, parameters were made to converge across the three flames without severely impacting the goodness of fit. In some cases no such agreement was possible.

The lack of a consistent set of parameter values to fit all flames could be indicative of several things. First, it could be that different chemistry is operative in a sooting flame as compared to a non-sooting one. Intuition would argue against this. The model is obviously a gross oversimplification of the complex high molecular weight growth and destruction mechanisms. Perhaps it is so gross that some important process is left out. This is a likely possibility. Equally likely is that the radical (H, OH, aryl) profiles are not correct. In the φ = 2.2 and φ = 2.4 flames, a number of assumptions had to be made to calculate these profiles.

Table 6.1 lists the literature rate constants for the reactions of interest in the model. The center column lists published rates for single ring compounds. The right hand column lists the rates for soot. Table 6.2 lists the results of the model parameter fitting for the same reactions. The C_2H_2 + aryl

Table 6.1 Literature rate constants for numerical model mechanisms

Reaction	Single Ring System			Soot System	
C_2H_2 + aryl	$3.1x10^{11}$ exp(-1.4/RT)	$\eta=2.9x10^{-4}$	a	$2.5x10^{-2}\ P_{C2H2}\ S_{Soot}\ \eta=2.5x10^{-4}$	b
OH + aryl	$1.0x10^{12}$ exp(-10.7/RT)	$\eta=3x10^{-4}$	c	η = 0.13 to 0.27	d
O_2 + aryl	$2.1x10^{12}$ exp(-7.5/RT)	$\eta=5x10^{-4}$	e	$\eta = 4x10^{-3}$ to $7x10^{-3}$	f
Aryl + PAH	$3.1x10^{11}$ exp(-3.75/RT)	$\eta=2.6x10^{-4}$	a	η = unity	
Pyrolysis	$4.5x10^{13}$ exp(-72/RT)		g	no pyrolysis of soot observed	

a: Fahr *et al.* (1988)
b: Harris and Weiner (1983b); units: gm/s
c: He *et al.* (1988) Note that this rate is for OH + benzene, not phenyl
d: Neoh (1981)
e: Lin and Lin (1987)
f: Nagle and Strickland-Constable (1962) This efficiency is derived from a complex expression including apparent adsorption/desorption terms. Most likely, it is not appropriate for large molecules/small particles.
g: Braun-Unkhoff (1989)
units: A-factor - cm^3/mol s, η - dimensionless

Table 6.2 Adjusted rate constants for numerical model

Reaction	Form[1]	E_{act}	A or η		
			$\varphi=1.8$	$\varphi=2.2$	$\varphi=2.4$
C_2H_2 + aryl	A	1.4	$1x10^{12}$	$2x10^{12}$	$1x10^{12}$
OH + aryl	E	-	0.1	0.05	0.01
O_2 + aryl	A	7.5	$2.1x10^{12}$	$2.1x10^{12}$	$2.1x10^{12}$
Aryl + PAH	E	-	0.4	0.2	0.2
Phenyl + PAH	E	-	$1x10^{-4}$	$2.6x10^{-4}$	$2.6x10^{-4}$
Pyrolysis	A	72	$1x10^{13}$	$5x10^{12}$	$5x10^{12}$

[1] A = Arrhenius form, E = reation efficiency form
units: kcal/mol, cm^3/mol s

reaction rate had to be increased three to six times over the Fahr *et al.* rate. This is in line with the observation from the data of Bittner (1981, see Figure 5.3). Chemical activation is a possible explanation for this difference between the Fahr *et al.* rate and the Bittner observation. When the aryl radical is formed it is chemically "hot" and possibly is more reactive than the thermalized phenyl which was involved in the Fahr *et al.* experiments. The OH + aryl reaction efficiency had the worst agreement across the three conditions, 0.01 to 0.1, a ten-fold disparity. The magnitude is also lower than that seen by Neoh (1980) for soot. At present we have no explanation for this. The O_2 + aryl rate constant was used directly from the literature without fitting. Although this reaction is the main oxidation channel early in the flame, it is, on average, less significant than OH + aryl. The aryl + PAH collision efficiency has a fairly close agreement across the three flames (0.2 - 0.4). This rate is quite close to the observation of unity sticking efficiency for soot. The phenyl + PAH rate is either the Fahr *et al.* (1988) rate, or a value quite close to it. The pyrolysis A-factor is five to ten time less than the rate published by Braun-Unkhoff *et al.* (1989) for phenyl pyrolysis. It is not surprising that this rate has to be adjusted downwards. As was discussed in the previous chapter, the pyrolysis rate of large PAH and soot is observed to be either slow or zero. The dependence on size was assumed to linearly decrease from its initial value to zero at 1000 amu. Beyond 1000 amu no pyrolysis occurs in the model.

The measured and predicted profiles are shown in Figures 6.2, 6.4, and 6.6 for the three flames. Figures 6.3, 6.5, and 6.7 display the relative contributions from the component processes as computed by the model.

The fit of the $\varphi = 1.8$ (Figure 6.2) flame misses the peak of the Mass>200 curve by about 1 mm, but the magnitudes are hit about right. The delay in the rise of the model as compared to data could indicate an additional growth process other than through C_2H_2. Above 11 mm, too much decay through pyrolysis occurs in the model. Phenyl and C_2H_2 start out being roughly equal contributors to the high mass system at the beginning, but phenyl fails to increase as fast as C_2H_2. OH is almost always a more important oxidation channel than O_2 in this flame. By 9 mm, pyrolytic destruction becomes the dominant action in the PAH/soot system.

Figure 6.4 shows the fit of the $\varphi = 2.2$ model. The model predicts the decay of the insoluble material fairly well. The rise in the insolubles is hit almost as well, but the subsequent drop at 14 mm is totally missed. Increasing the OH reaction efficiency to make this curve drop has the effect of decimating the insolubles back at 6-7 mm.

Figure 6.6 shows the fit of the $\varphi = 2.4$ model. The data collection started earlier than in the case above (3 mm as compared to 5 mm) so we see a rise and decay of the solubles. The model fits this behavior quite well. The observed rise in insolubles is extremely rapid, increasing 4-fold in 1 mm between 8 and 9 mm. The model captures this trend as well. Excessive oxidation of the insolubles above 10 mm results in a predicted net drop which is not observed.

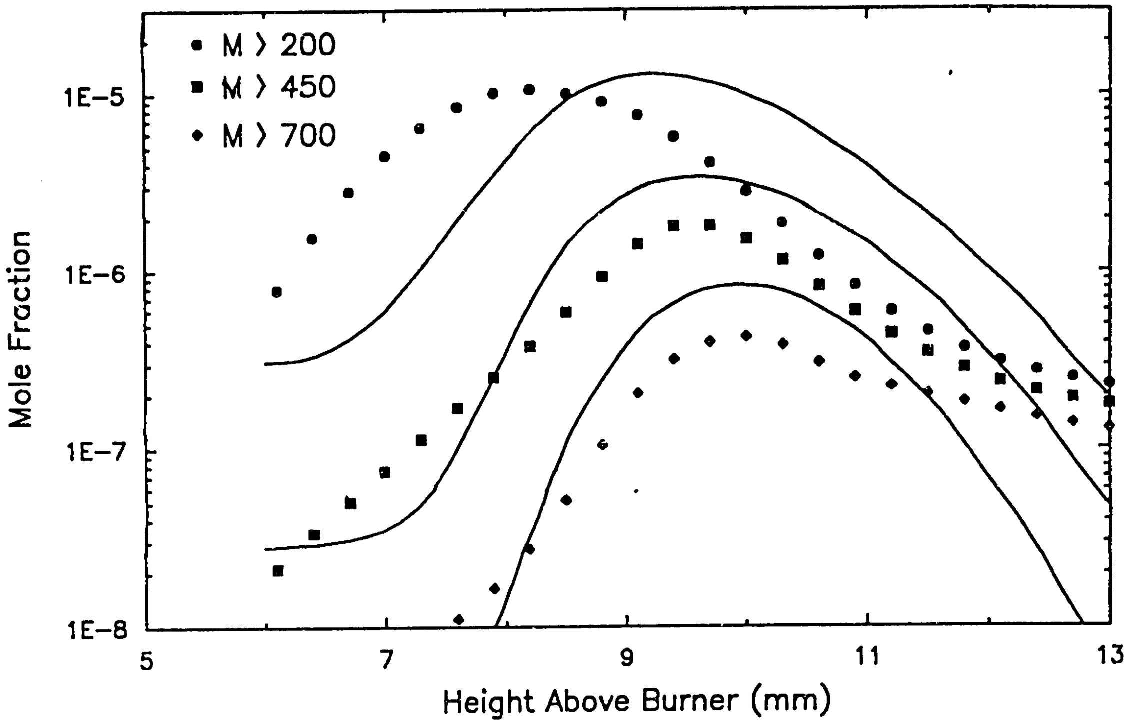

Figure 6.2 Data and model fit. $\varphi = 1.8$, 20 torr, 30% Ar

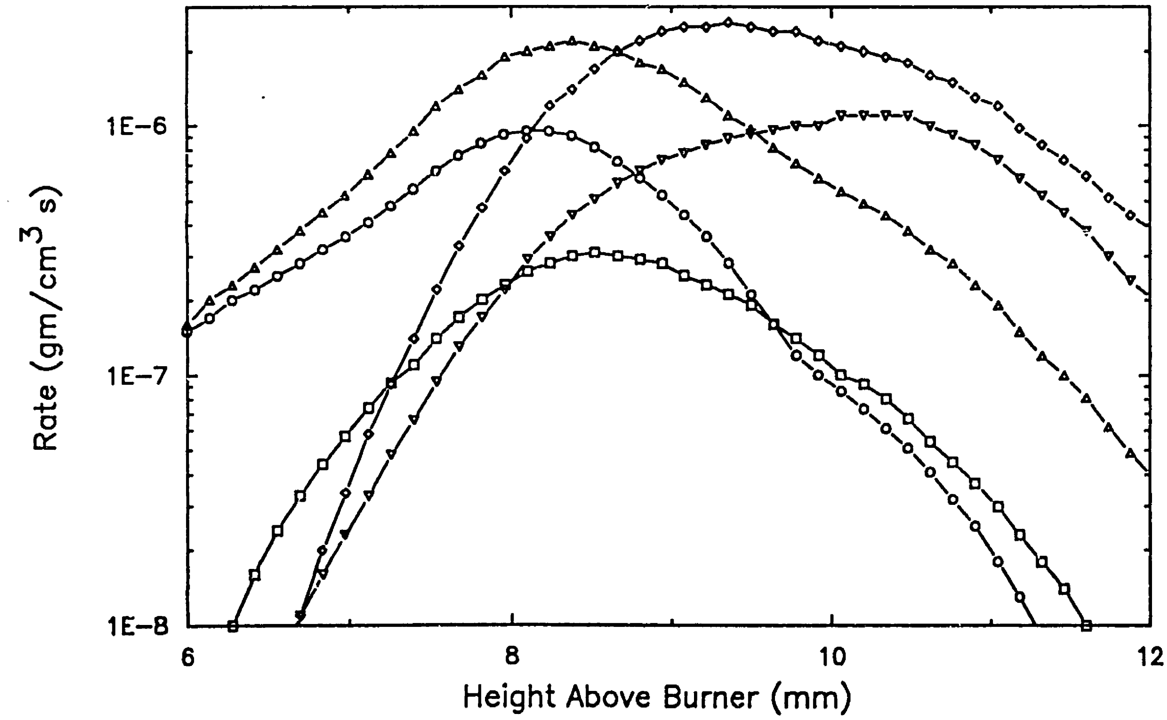

Figure 6.3 Component rates. $\varphi = 1.8$, 20 torr, 30% Ar. C_2H_2 addition (Δ), Phenyl addition (O), O_2 oxidation (□), OH oxidation (∇), Pyrolysis (◇)

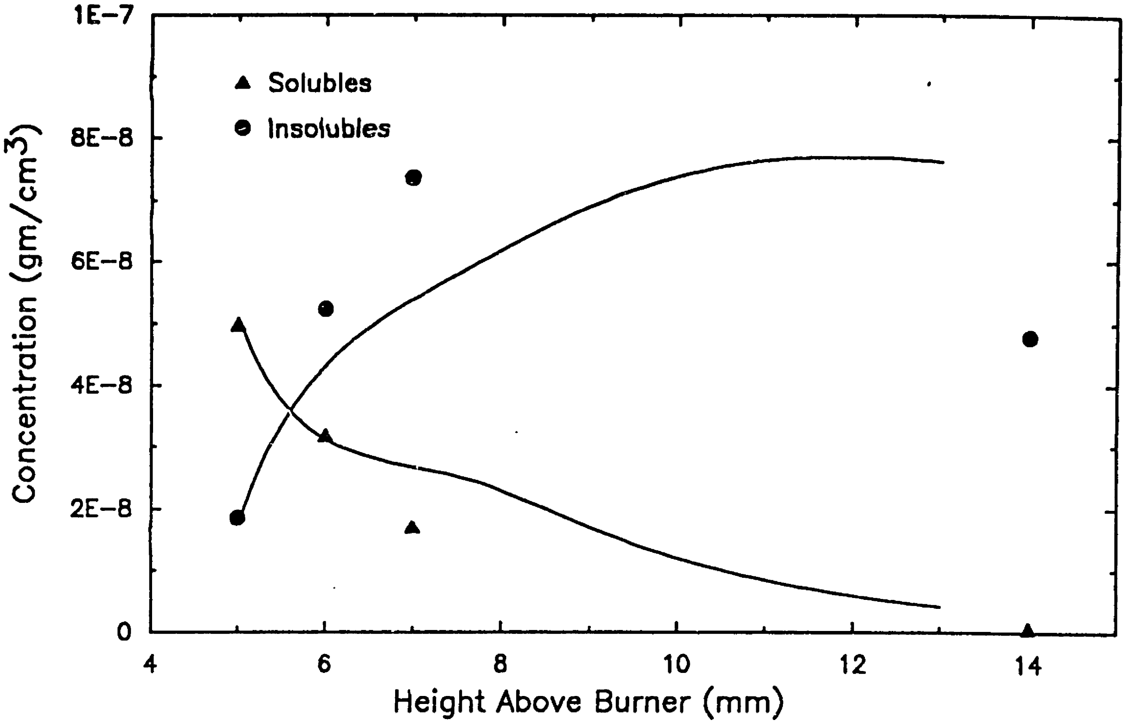

Figure 6.4 Data and model fit. $\varphi = 2.2$, 40 torr, 10% Ar

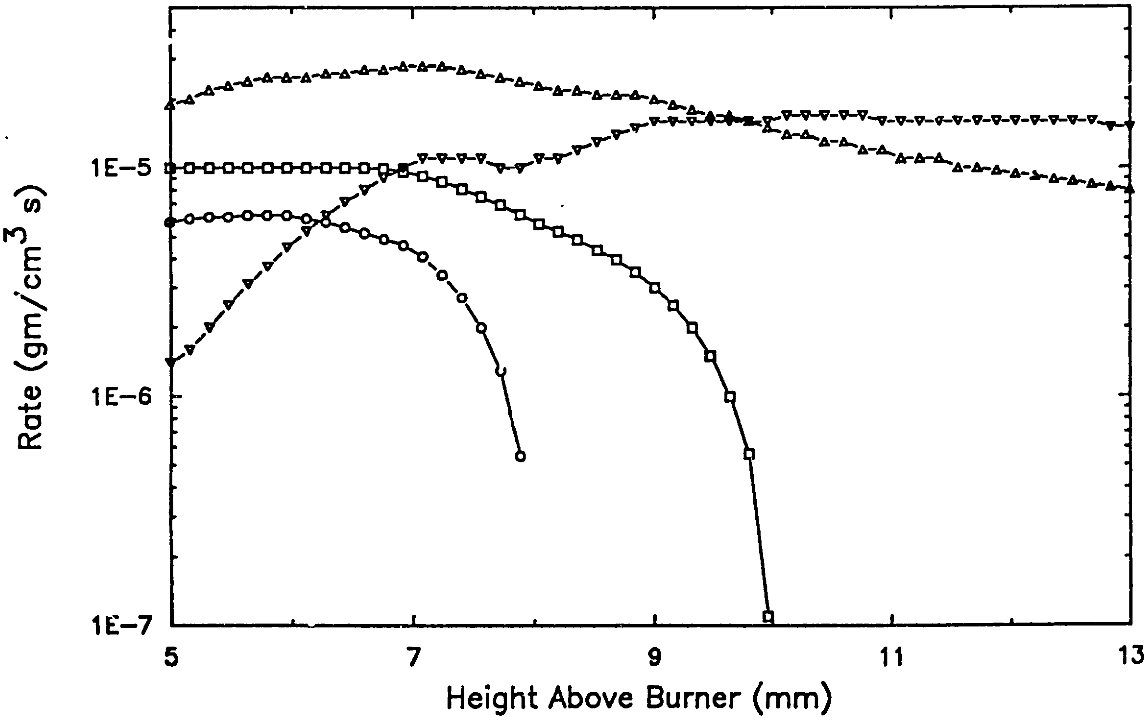

Figure 6.5 Component rates. $\varphi = 2.2$, 40 torr, 10% Ar. C_2H_2 addition (Δ), Phenyl addition (O), O_2 oxidation (□), OH oxidation (∇)

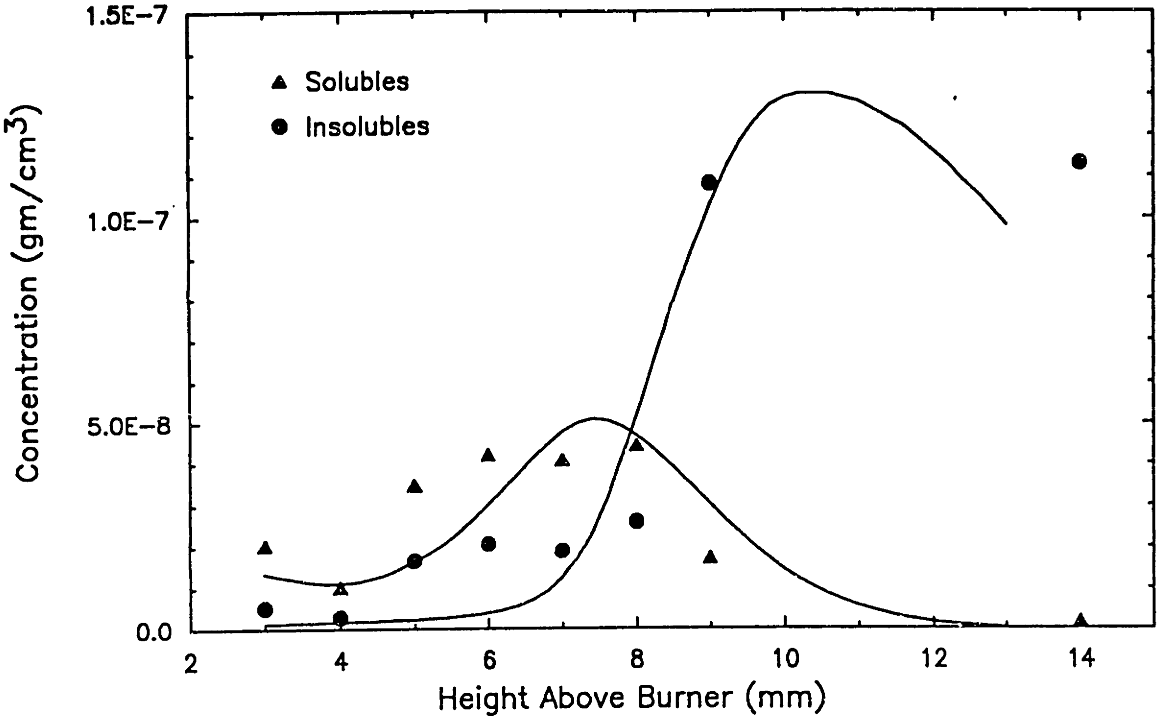

Figure 6.6 Data and model fit. φ = 2.4, 40 torr, 10% Ar

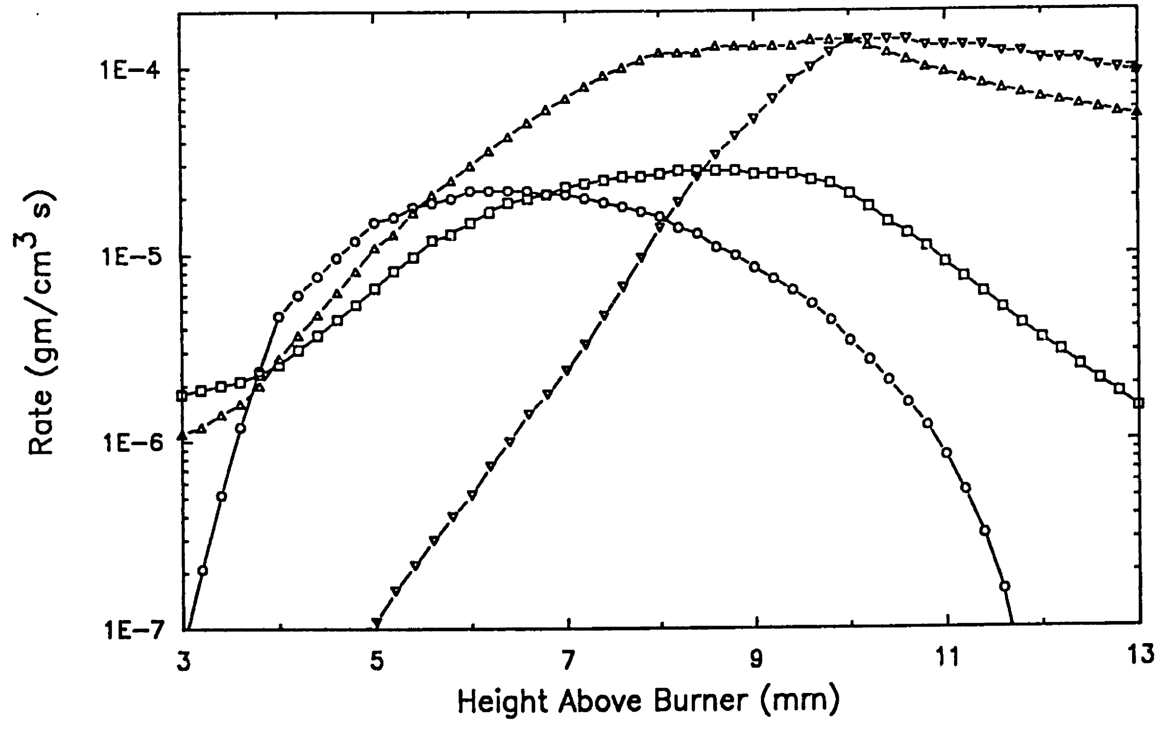

Figure 6.7 Component rates. φ = 2.4, 40 torr, 10% Ar. C_2H_2 addition (Δ), Phenyl addition (O), O_2 oxidation (□), OH oxidation (∇)

Chapter Seven

Conclusions

The results of this experimental and modeling study of soot formation indicate that the process may be broken down into four components.

- mass growth of PAH and soot through addition of C_2H_2.
- oxidation of the growing system by OH and O_2.
- coagulation of the large PAH molecules forming soot nuclei.
- unimolecular pyrolysis of the planar PAH.

Mass growth - Acetylene has long been implicated in the soot literature as the carbon source for mass growth of soot, primarily because it is the most abundant hydrocarbon in rich flames. Detailed mechanisms have been published for acetylene reactions with small PAH's to extend the aromatic network and kinetic expressions for acetylene addition to soot surfaces have been published .

This thesis has compared published rates of acetylene addition to single-ring aromatics and to soot and has found them to be similar when put on a consistent basis (*i.e.* a collision efficiency). In fitting of this rate parameter to data using the numerical model we find that the rate observed in a benzene flame is slightly higher than the published rates.

The mechanism proposed for C_2H_2 addition to soot is the same as that for C_2H_2 + phenyl radical. Thus, in the molecular regime, only aryl radicals are active at adding acetylene. In the particulate regime, localized σ-radicals on the soot surface represent the active sites.

Oxidation - OH has been identified in the literature as the primary oxidizing agent of soot in a flame. The benzene flames studied in this work have a feature unique to aromatic fuels that the soot nucleation occurs in the primary oxidation zone. As such, the large presence of molecular oxygen means that it, too, must be considered in soot destruction reactions. It is found that O_2 is a significant oxidant early in the flame when its concentration is high and before [OH] reaches relatively high levels.

In order to reconcile the near gas kinetic collision efficiency of OH with soot, we propose that only radicals are active in oxidation by OH. In a scheme very similar to that proposed above for C_2H_2 addition, we speculate that PAH's are destroyed through OH recombination with aryl radicals and that soot is destroyed through recombination of OH with σ-radicals on the soot surface.

Coagulation of PAH - It has long been observed that colliding soot particles stick with unity collision efficiency leading to a reduction in number density at gas kinetic rates. We have extended this concept into the PAH range. Mechanistically, we propose that collisions between aryl radicals and PAH molecules stick with reaction efficiencies near gas kinetic (0.2 - 0.4). Radical-radical recombinations are not treated differently than radical-molecule reactions.

This PAH coagulation concept is crucial in quantitatively explaining the observed profiles of soluble PAH's and insoluble material. Without coagulation, the inventory of PAH would need to be much higher than is observed in order to reconcile the observed soot production rates.

Pyrolysis of PAH - The rapid destruction of PAH in the soot nucleation zone can only be explained by invoking a highly activated unimolecular process. There is little change in concentrations of all gas phase species across the soot nucleation boundary with the exception of PAH's. The only change is that the temperature is rising to the 1800 to 2000 K level. The activation energy for phenyl pyrolysis has been measured to be approximately 75 kcal/mol, which has been found to work well for PAH pyrolysis. With such a high activation energy and the high observed rates, only unimolecular processes have reasonable A-factors (*i.e.* any proposed bimolecular process would have an A-factor greater than gas kinetic rates).

The pyrolytic mechanism can be thought of as the microscopic reversibility analog to the C_2H_2 addition process. As such, we propose that the mechanism involves an aryl radical undergoing a *beta*-scission reaction which splits off two carbons. It is observed that the pyrolysis channel begins to shut down as molecular size approaches 1000 amu with soot suffering little or no pyrolytic decay. We speculate that the stability imparted on large molecules could be due to the conversion from a two-dimensional PAH structure to a three-dimensional soot structure.

Many of the concepts in the above set of mechanisms have been presented before in the literature and some are new to this work. Below is a list of the features of this thesis which are unique.

- We have obtained quantitative, time-resolved profiles of PAH in well characterized benzene flames. Particularly novel are the profiles of material too heavy to be identified with chromatographic techniques.
- We have observed that ultimate soot yield is decoupled from the intermediate inventory of PAH in the flame. We propose that the highly activated pyrolytic mechanism along with oxidation by OH are responsible.
- The coagulation of PAH as a key step to nucleation has its first quantitative support from this work. The concept has existed in various forms in the literature, but never before have the quantitative data existed to validate it.
- We have identified the key role aryl radicals play in every phase of soot nucleation.
- The pyrolysis channel as a destruction mode for PAH is new. Part of the reason for its previous omission is that much of the work done on soot formation has been with cooler flames (*e.g.* ethylene). Many practical systems, such at diesel engines, operate at high temperatures where pyrolysis will be a significant channel.

Given these four processes, we can track the growth of PAH and soot as they progress through a premixed benzene/oxygen flame. This is shown in schematic form in Figure 7.1. Early in the flame, reactive species, particularly H atom, are diffusing backwards from the more vigorous and higher temperature reaction zone. In this region, the low temperature combined with relatively large H atom and C_2H_2 concentrations favor rapid growth of PAH. If the fuel is an aromatic, most of the growth starts through addition to phenyl radical. In a flame with aliphatic fuel, the phenyl radical must first form. The concentration of molecular oxygen is sufficiently high in this region of the flame to offset its relatively low reactivity, so oxidation of the aryl radicals through O_2 is important. It is important to note that the aryl radicals are the active substrates in both the growth and oxidation reactions. The concentration of H atom governs the amount of aromatic material which exists in radical form. Thus, the H atom is the species which drives the whole of the chemistry at this point.

Farther up in the flame, temperature begins to rise and the PAH's begin to become larger through C_2H_2 addition. OH concentration becomes significant as well. The larger PAH's have a greater likelihood to exist as aryl radicals due to the larger number of abstractable hydrogen atoms. This fact, combined with the larger van der Waals forces associated with large molecules, means that collisions between them have a greater chance of being reactive (*i.e.* sticking). In this way, oligomers form which create the required nuclei. OH in this region begins to be an important oxidizing species due both to its increasing concentration and its higher reactivity relative to O_2.

Progressing along in the flame the temperature begins to approach its peak value of around 2000 K. The last mechanism, pyrolysis becomes important here. Its high activation energy (72 kcal/mol) makes it the most temperature sensitive reaction class of the four. PAH species which have not yet grown to a threshold size (*ca.* 1000 amu) are susceptible to this rapid destruction path. It is proposed that the threshold of thermal stability is due to the transformation of the PAH from a two-dimensional structure to a three-dimensional structure. We know that soot is both thermodynamically stable and three-dimensional. Oxidation through OH continues in the high temperature region of the flame. Acetylene addition is no longer thermodynamically favorable, so mass growth slows.

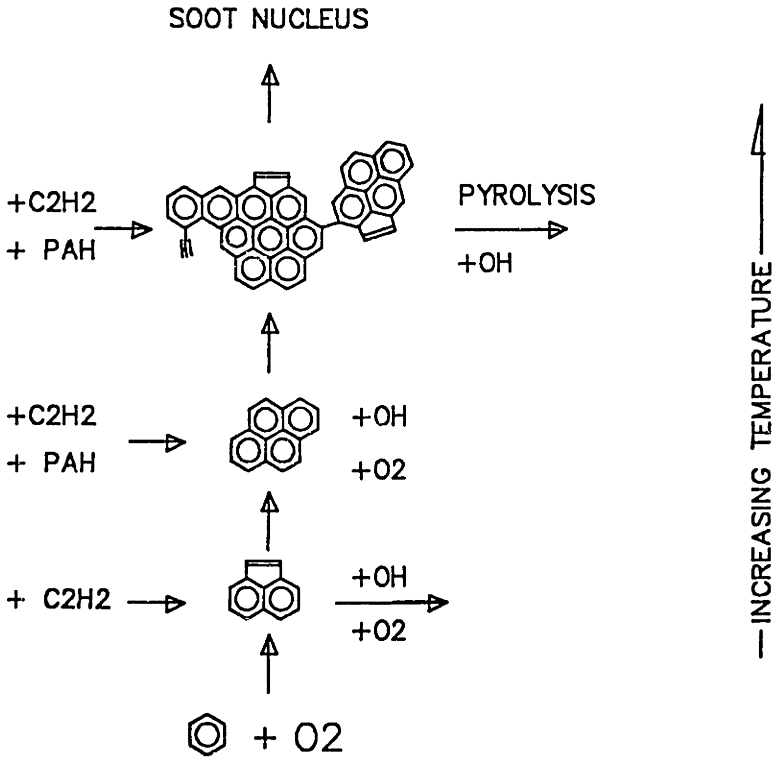

Figure 7.1 Schematic representation of soot formation in a flame

At the point of peak temperature, very little PAH remains; it has either grown to be a soot nucleus or has been destroyed by oxidation and pyrolysis. The soot nuclei continue to collide which reduces numbers and increases the size. Surface growth through addition of C_2H_2 continues, but at a reduced rate. Depending on the amount of oxidant, the soot pool can either continue to grow or can be depleted.

It is valuable to speculate on how this picture would differ in a different flame environment. In a premixed flame with an aliphatic fuel, two major factors change. First the peak temperatures are much lower. The propane flame of Bockhorn (1983) had a peak temperature of 1800 K. In this flame, the PAH's show a much more modest (twofold) reduction in the pyrolysis zone as compared to the several order of magnitude drop seen in the benzene flames of both this work and that of Bockhorn. Thus, PAH formed in a propane flame would have a greater tendency to form soot. The second fuel-related difference, however, offsets this. The first aromatic ring in the propane flame must be chemically fabricated, as opposed to a benzene system where aromatic rings enter as fuel. This slow step renders the total concentration of PAH lower in the propane system.

The last speculation will be to apply these concepts qualitatively to a totally different combustion system, the diesel engine. As a simplification, consider the diesel as a diffusion flame near the surface of a droplet of injected fuel. Upon injection to the hot cylinder, the droplet is rapidly surrounded by an oxidizing atmosphere. Fuel diffuses outward and oxygen diffuses inward to the flame front. On the fuel side we have a high temperature, very fuel rich environment with a large supply of H atom which diffuses back from the flame front. The H atoms initiate *beta*-scission reactions of the straight-chain alkane diesel fuel creating a supply of C_2H_4 which is converted to C_2H_2. Acetylene, H atoms, and the aromatic content of the diesel fuel are exactly the recipe required for rapid molecular weight growth. In addition, little if any oxidant survives through the flame front to diffuse into the fuel zone, so reactions are strictly in the forward (*i.e.* growth) direction. By the time the droplet breaks apart or burns out, the PAH have coagulated into soot spherules, reducing the surface area and thus the oxidation rate.

Strategies to control soot in diesels could concentrate in several areas. Cutting down the PAH growth rate could best be attacked by reducing the aromatic content of the fuel. This is a feasible, but expensive approach. Reducing the coagulation rate of the PAH and nuclei would enhance the oxidation rate by increasing the surface area. If the additive were effective at keeping the small PAH from growing to 3-dimensional structures, then pyrolysis could destroy them as well. An ionic fuel additive which put a charge on each nuclei could achieve this, but environmental concerns of the additive would need to be addressed. The most promising approach to diesel particulate control probably lies in oxidation. Since diesels run globally fuel lean ($\varphi_{max} < 0.7$), plenty of oxidant is available for burnout. The problem is that it exists in a relatively unreactive form, O_2. If the reaction $H + O_2 \Rightarrow OH + O$ could be driven harder, more of the highly reactive O and OH would be released. The key to all this is to generate H atom. Two possibilities exist. The first is some H-source fuel additive. The structure of this can only be guessed at. A second approach is to hydro-treat the diesel to the greatest extent possible, hydrogenating all aromatic rings.

Other combustion systems can be analyzed qualitatively in the same manner. This sort of analysis, of course, is only useful as a guide for quantitative analysis in a computer model. With the results of this thesis, a set of parameters is available for such a model.

Recommendations

- Free radicals drive the whole reaction system, as has been shown. In this work, however, no direct measure was made of the radicals, only inferences. Optical methods, such as that used by Neoh (1980) for H atom, should be applied to these flames to validate the calculated radical profiles. A direct measure of H, OH, and O would eliminate the need for partial equilibrium assumptions.

Aryl radicals are also keystones of the whole concept presented above, but we have even less information about their concentrations than we do about the small radicals. Direct measurement of these radicals represents an extreme experimental challenge. They have no unique spectral features at flame temperatures which can be exploited optically. They are reactive, so simple collection efforts will fail. Possible methods are: 1) Molecular beam collection followed by cryogenic matrix isolation. At cryogenic temperatures, a spectral feature could possibly be identified. 2) Molecular beam mass spectrometry with vacuum-UV photoionization. This ionization method has been reported to reduce or eliminate fragmentation associated with electron-impact ionization (Pfefferle, 1988). The mass spectrometer must be of sufficient quality to resolve 1 mass unit of a several hundred mass ion. 3) A scavenger which would cap the aryl radical rapidly in the bore of a sample probe and allow identification off-line would be the simplest solution. Finding such a scavenger, then, is the difficult part.

- Analysis of the chemical structure of the large PAH is of great importance. Several mysteries exist. First, we would like to know how the soot nuclei which are reported to have a C:H ratio of unity can be formed from PAH with a much lower C:H ratio. What is the oxygen content of the PAH? If oxygen is present, what is the functional form? The answers to these questions could help answer more fundamental questions about oxidation mechanisms. Knowledge of the size of the fused aromatic ring systems (which can be obtained from ^{13}C NMR) would help determine the relative significance of C_2H_2 addition and coagulation as size grow mechanisms. The existence of acetylenic substituents on PAH's larger than acenaphthalene would be further confirmation of the proposed C_2H_2 growth mechanism. Their absence is a small mystery.

- Temperature is one of the most difficult to measure, but most important parameters in the flame. Not only is measuring the quantity difficult, but alignment of the temperature profile with the probe sampling profiles is a challenge. The probe samples represent flame conditions a few (~2½) probe diameters ahead of the probe tip. Two independent temperature measurements (*e.g.* thermocouple and OH-rotational thermometry) should be performed.

- The pyrolytic decay channel needs to be evaluated more quantitatively. We have estimated the function with which the rate constant decreases with increasing molecular size. Experimental evaluation of this function would be valuable.

- The most pressing need is for more carefully taken data, of the form presented in this document, to further refine the model and concepts. In the seven years spent on this project, far too much of the effort was spent in designing, building, and testing the equipment, developing the optical and probing procedures, developing the analytical procedures, *etc.* and far too little on actual taking of data. A carefully produced set of data, with enough data points to allow numerical smoothing, in a well-designed ensemble of experiments (*i.e.* the effect of temperature, the effect of φ, *etc.*) could add invaluably in solidify the concepts presented here.

Appendices

Appendix A. Tabulation of Light PAH Data and Light Gas Data

Table A.1 Measured light PAH concentrations from $\varphi = 2.0$, 20 torr, 30% Ar flame. 8 to 11 mm.

Sample no.		192	193	190	185	191	186
HAB =>		8	9	10	10	10.5	11
Temperature =>		1100	1400	1560	1560	1650	1700
Condensibles =>		0.24	0.26	0.27	0.27	0.28	0.28
Compound	MW	gm/cc	gm/cc	gm/cc	gm/cc	gm/cc	gm/cc
Triacetylene	74	1.60E-09	9.11E-10	1.07E-09	4.41E-09	1.36E-09	0.00E+00
Toluene	92	3.56E-09	4.17E-09	4.36E-09	4.96E-09	3.78E-09	1.01E-09
Phenylacetylene	102	4.83E-09	7.89E-09	8.76E-09	1.74E-08	9.15E-09	7.53E-09
Styrene	104	1.09E-09	1.39E-09	1.43E-09	1.65E-09	1.26E-09	4.11E-10
Benzaldehyde	106	2.23E-11	2.27E-11	6.04E-11	0.00E+00	1.97E-11	9.03E-12
Indene	116	2.64E-09	3.89E-09	4.26E-09	6.13E-09	4.03E-09	2.33E-09
mm116	116	1.74E-10	0.00E+00	2.18E-10	2.45E-10	1.87E-10	0.00E+00
Diethynyl benzene	126	8.80E-10	5.46E-10	5.00E-10	4.31E-10	3.03E-10	1.55E-10
Naphthalene	128	1.84E-09	2.54E-09	2.83E-09	2.04E-09	2.83E-09	2.25E-09
Methyl indene	130	1.68E-10	2.75E-10	3.40E-10	0.00E+00	3.00E-10	1.50E-10
Ethynyl indene	140	1.08E-10	1.77E-10	2.65E-10	8.49E-10	4.04E-10	3.39E-10
Methyl naphthalene	142	1.65E-10	1.99E-10	1.70E-10	2.68E-10	1.34E-10	0.00E+00
Acenaphthalene	152	4.50E-10	8.29E-10	9.88E-10	2.22E-09	1.20E-09	2.04E-09
Ethynyl naphthalene	152	1.66E-10	2.66E-10	2.87E-10	6.17E-10	2.98E-10	4.52E-10
Acenaphthene	154	4.68E-11	2.98E-11	1.77E-11	5.01E-11	2.08E-11	1.60E-11
Biphenyl	154	1.36E-09	1.94E-09	2.17E-09	1.53E-09	2.09E-09	9.07E-10
Ethynyl acenaphthalene	164	9.90E-11	1.71E-10	2.07E-10	1.16E-09	2.20E-10	5.06E-10
Fluorene	166	1.67E-10	2.97E-10	3.37E-10	3.78E-10	3.65E-10	2.30E-10
Anthracene	178	2.12E-11	3.23E-11	2.95E-11	6.15E-11	4.25E-11	3.78E-11
Phenanthrene	178	1.57E-10	2.15E-10	2.31E-10	3.65E-10	2.80E-10	2.51E-10
Bibenzyl	184	2.06E-10	2.46E-10	2.63E-10	1.03E-11	2.40E-10	6.02E-11
Cyclopentaphenanthrene	190	6.15E-11	9.24E-11	1.15E-10	1.59E-10	5.43E-11	1.85E-10
Aceanthrylene	202	1.63E-12	4.62E-12	7.37E-12	2.14E-11	1.42E-11	4.58E-11
Acephenanthrylene	202	1.58E-11	4.08E-11	5.01E-11	9.54E-11	8.54E-11	1.33E-10
Fluoranthene	202	4.13E-11	9.49E-11	1.18E-10	1.87E-10	1.68E-10	2.39E-10
Pyrene	202	2.88E-11	7.31E-11	9.28E-11	1.71E-10	1.36E-10	3.17E-10
Phenyl naphthalene	204	3.97E-11	6.43E-11	7.37E-11	1.27E-10	9.79E-11	4.95E-11
3,6 Dimethylphenanthr.	206	1.09E-12	4.62E-12	1.44E-11	2.43E-11	7.96E-12	7.36E-12
Benzo(b)fluorene	216	9.79E-12	2.77E-11	4.38E-11	5.16E-11	5.81E-11	3.54E-11
Benzo(ghi)fluorant	226	1.47E-11	4.37E-11	4.42E-11	6.12E-11	6.09E-11	1.34E-10
Benzo(k)fluoranthe	226	5.98E-12	2.35E-11	1.22E-11	3.43E-11	4.32E-11	7.39E-11
CPEP	226	8.70E-12	4.24E-11	5.75E-11	1.28E-10	1.06E-10	3.87E-10
Chrysene	228	7.62E-12	2.81E-11	3.68E-11	2.98E-11	3.74E-11	3.11E-11
Terphenyl	230	4.19E-11	9.54E-11	1.15E-10	1.26E-10	1.32E-10	1.42E-10
1,1 binaphthyl	254	3.81E-12	6.72E-11	1.12E-10	1.06E-10	1.11E-10	2.91E-11

Table A.2 Measured light PAH concentrations from φ = 2.0, 20 torr, 30% Ar flame. 11.5 to 40 mm

Sample no.		194	184	183	182	187
HAB (mm) =>		11.5	12	13	14	40
Temperature =>		1750	1800	1850	1880	1650
Condensibles =>		0.28	0.28	0.28	0.28	0.28
Compound	MW	gm/cc	gm/cc	gm/cc	gm/cc	gm/cc
Triacetylene	74	1.08E-10	1.71E-11	2.81E-11	1.06E-11	0.00E+00
Toluene	92	1.82E-11	1.07E-11	3.46E-11	2.74E-11	9.84E-11
Phenylacetylene	102	7.76E-10	1.14E-11	8.02E-12	6.08E-12	3.46E-12
Styrene	104	4.00E-11	6.95E-12	0.00E+00	3.95E-12	0.00E+00
Benzaldehyde	106	6.83E-12	1.89E-12	0.00E+00	0.00E+00	0.00E+00
Indene	116	3.75E-10	9.47E-13	1.23E-12	0.00E+00	0.00E+00
mm116	116	1.14E-11	0.00E+00	0.00E+00	0.00E+00	0.00E+00
Diethynyl benzene	126	0.00E+00	6.32E-13	0.00E+00	0.00E+00	0.00E+00
Naphthalene	128	5.48E-10	2.21E-12	1.85E-12	0.00E+00	0.00E+00
Methyl indene	130	2.83E-11	0.00E+00	0.00E+00	0.00E+00	0.00E+00
Ethynyl indene	140	9.27E-11	0.00E+00	0.00E+00	0.00E+00	0.00E+00
Methyl naphthalene	142	0.00E+00	0.00E+00	0.00E+00	0.00E+00	0.00E+00
Acenaphthalene	152	7.16E-10	6.95E-12	3.09E-13	9.12E-13	3.12E-12
Ethynyl naphthalene	152	1.23E-10	1.26E-12	0.00E+00	0.00E+00	0.00E+00
Acenaphthene	154	1.54E-10	0.00E+00	0.00E+00	0.00E+00	0.00E+00
Biphenyl	154	1.48E-10	6.63E-12	2.47E-12	1.43E-11	3.46E-13
Ethynyl acenaphthalene	164	1.97E-10	2.53E-12	3.09E-13	4.26E-12	0.00E+00
Fluorene	166	4.78E-11	1.58E-12	9.26E-13	3.34E-12	0.00E+00
Anthracene	178	1.27E-11	0.00E+00	0.00E+00	2.13E-12	0.00E+00
Phenanthrene	178	7.87E-11	3.79E-12	5.25E-12	2.01E-11	0.00E+00
Bibenzyl	184	2.11E-11	0.00E+00	0.00E+00	9.12E-13	0.00E+00
Cyclopentaphenanthrene	190	8.68E-11	1.83E-11	6.48E-12	1.37E-11	0.00E+00
Aceanthrylene	202	1.14E-11	0.00E+00	0.00E+00	0.00E+00	0.00E+00
Acephenanthrylene	202	4.46E-11	1.26E-12	3.09E-13	3.04E-13	0.00E+00
Fluoranthene	202	9.76E-11	8.21E-12	4.94E-12	7.90E-12	0.00E+00
Pyrene	202	2.03E-10	1.58E-11	3.70E-12	4.86E-12	0.00E+00
Phenyl naphthalene	204	1.98E-11	1.26E-12	0.00E+00	0.00E+00	0.00E+00
3,6 Dimethylphenanthr.	206	1.95E-12	0.00E+00	0.00E+00	0.00E+00	0.00E+00
Benzo(b)fluorene	216	5.53E-12	0.00E+00	0.00E+00	0.00E+00	0.00E+00
Benzo(ghi)fluoranthene	226	8.10E-11	6.32E-12	0.00E+00	0.00E+00	0.00E+00
Benzo(k)fluoranthe	226	1.40E-11	1.52E-11	0.00E+00	0.00E+00	0.00E+00
CPEP	226	2.32E-10	1.42E-11	1.85E-12	0.00E+00	0.00E+00
Chrysene	228	2.21E-11	0.00E+00	0.00E+00	0.00E+00	0.00E+00
Terphenyl	230	4.03E-11	6.32E-13	0.00E+00	0.00E+00	0.00E+00
1,1 binaphthyl	254	1.50E-11	2.21E-12	9.26E-13	0.00E+00	0.00E+00

Table A.3 Measured light PAH concentrations from φ = 2.125, 40 torr, 45% Ar flame.

Sample no.		178	181	175	180	174	179	176	177
HAB =>		4	5	6	7	8	9	10	12
Compound	MW	gm/cc	gm/cc	gm/cc	gm/cc	gm/cc	gm/cc	gm/cc	gm/cc
Triacetylene	74	2.5E-10	1.2E-09	0.0E+00	1.6E-10	0.0E+00	1.9E-11	0.0E+00	0.0E+00
Toluene	92	2.4E-09	7.7E-09	8.8E-10	0.0E+00	0.0E+00	0.0E+00	1.9E-10	0.0E+00
Phenylacetylene	102	3.8E-09	8.0E-09	7.6E-09	2.6E-08	2.4E-08	1.9E-10	1.2E-10	1.3E-11
Styrene	104	8.4E-10	1.4E-09	1.0E-09	2.6E-09	0.0E+00	0.0E+00	0.0E+00	0.0E+00
Benzaldehyde	106	3.3E-11	2.9E-11	2.0E-11	0.0E+00	0.0E+00	6.3E-11	0.0E+00	0.0E+00
Indene	116	2.2E-09	4.0E-09	3.4E-09	7.9E-09	4.4E-09	8.1E-12	3.9E-11	0.0E+00
Diethynl benzene	126	5.7E-10	0.0E+00	6.5E-11	4.4E-10	5.6E-10	0.0E+00	0.0E+00	0.0E+00
Methyl indene	130	1.4E-10	3.1E-10	2.6E-10	9.8E-10	5.4E-10	0.0E+00	0.0E+00	0.0E+00
Naphthalene	128	1.6E-09	2.7E-09	2.3E-09	6.3E-09	5.3E-09	2.8E-11	3.1E-11	0.0E+00
Ethynyl indene	140	7.6E-11	2.4E-10	2.3E-10	1.4E-09	9.4E-10	0.0E+00	0.0E+00	0.0E+00
Methyl naphthale	142	3.6E-10	3.9E-10	2.9E-10	5.5E-10	0.0E+00	7.9E-12	1.6E-11	0.0E+00
Biphenyl	154	1.0E-09	1.9E-09	1.7E-09	4.9E-09	0.0E+00	0.0E+00	2.8E-11	1.6E-11
Ethynyl naphthal	152	1.4E-10	3.3E-10	2.8E-10	3.8E-11	9.5E-10	0.0E+00	0.0E+00	0.0E+00
Acenaphthalene	152	4.1E-10	1.1E-09	1.0E-09	3.8E-09	4.9E-09	2.4E-11	2.3E-11	3.8E-12
Acenaphthene	154	3.6E-11	0.0E+00	2.0E-11	0.0E+00	1.9E-11	0.0E+00	4.4E-11	0.0E+00
Bibenzyl	184	1.6E-10	2.7E-10	1.9E-10	0.0E+00	1.1E-10	0.0E+00	0.0E+00	0.0E+00
Fluorene	166	1.3E-10	3.6E-10	2.6E-10	1.3E-10	2.8E-10	8.9E-12	0.0E+00	0.0E+00
Ethynyl acenapht	164	7.6E-11	2.4E-10	3.3E-10	8.9E-10	1.4E-09	4.2E-11	4.5E-11	4.0E-11
Phenanthrene	178	9.5E-11	2.2E-10	2.0E-10	5.2E-10	4.2E-10	2.6E-11	5.7E-11	2.7E-11
Anthracene	178	1.5E-11	4.9E-11	3.5E-11	8.2E-11	6.3E-11	0.0E+00	0.0E+00	0.0E+00
Cyclopentaphenat	190	4.0E-11	9.5E-11	1.1E-10	2.5E-10	2.7E-10	0.0E+00	4.6E-11	2.3E-11
3,6 Dimethylphen	206	0.0E+00	9.5E-12	1.4E-11	1.9E-11	0.0E+00	0.0E+00	0.0E+00	0.0E+00
Fluoranthene	202	2.8E-11	1.1E-10	1.3E-10	2.8E-10	4.5E-10	8.0E-12	5.7E-12	7.6E-12
Acephenanthrylen	202	1.1E-11	3.7E-11	6.6E-11	1.7E-10	2.5E-10	0.0E+00	0.0E+00	0.0E+00
Acenanthrylene	202	0.0E+00	0.0E+00	9.5E-12	5.7E-11	4.4E-11	0.0E+00	0.0E+00	0.0E+00
Pyrene	202	2.1E-11	9.0E-11	1.2E-10	2.8E-10	5.2E-10	7.3E-12	2.5E-12	8.8E-12
Phenylnaphthalen	204	0.0E+00	1.5E-11	3.2E-11	1.1E-10	1.3E-10	0.0E+00	0.0E+00	0.0E+00
Benzo(b)fluorene	216	0.0E+00	2.7E-11	4.2E-11	7.6E-11	7.1E-11	0.0E+00	0.0E+00	0.0E+00
Benzofluoranthen	226	3.8E-12	3.1E-11	6.2E-11	1.1E-10	2.1E-10	0.0E+00	0.0E+00	0.0E+00
CPEP	226	3.2E-12	4.2E-11	1.0E-10	2.4E-10	6.0E-10	0.0E+00	0.0E+00	0.0E+00
Chrysene	228	0.0E+00	0.0E+00	2.5E-11	5.1E-11	0.0E+00	0.0E+00	0.0E+00	0.0E+00
Benzo(k)fluorant	226	0.0E+00	0.0E+00	2.0E-11	0.0E+00	7.6E-12	0.0E+00	0.0E+00	0.0E+00
Terphenyl	230	0.0E+00	7.8E-11	1.4E-10	1.8E-10	2.5E-10	0.0E+00	0.0E+00	0.0E+00
1,1 binaphthyl	254	0.0E+00	8.2E-12	8.2E-12	1.9E-11	4.9E-11	0.0E+00	5.1E-12	0.0E+00

Table A.4 Light gas mole fractions. φ = 2.4, 40 torr, 10% Ar. Measured with quadrupole mass spectrometer.

	H2	O2	CO	CO2	CH4	H2O	Ar	C2H2	C6H6
MW ->	2	32	28	44	16	18	40	26	78
Feed	0.000	0.682	0.000	0.000	0.000	0.000	0.100	0.000	0.218
1	0.054	0.390	0.225	0.000	0.007	0.100	0.078	0.008	0.137
2	0.080	0.299	0.280	0.002	0.007	0.101	0.078	0.025	0.126
3	0.066	0.374	0.234	0.000	0.006	0.079	0.081	0.016	0.145
4	0.078	0.320	0.271	0.002	0.007	0.098	0.075	0.021	0.128
5	0.093	0.247	0.321	0.013	0.008	0.106	0.071	0.029	0.108
6	0.101	0.187	0.360	0.022	0.009	0.118	0.068	0.039	0.092
7	0.107	0.095	0.436	0.048	0.011	0.148	0.061	0.058	0.041
8	0.114	0.087	0.437	0.045	0.011	0.147	0.061	0.062	0.042
9	0.120	0.064	0.469	0.048	0.013	0.137	0.058	0.071	0.025
10	0.132	0.041	0.483	0.056	0.006	0.142	0.058	0.073	0.012
11	0.144	0.018	0.498	0.065	0.000	0.147	0.057	0.074	-0.000
14	0.160	-0.000	0.536	0.066	0.000	0.124	0.059	0.058	-0.000
20	0.168	-0.000	0.552	0.065	0.000	0.104	0.058	0.055	-0.000
24	0.173	-0.000	0.562	0.065	0.000	0.090	0.057	0.053	0.000

Table A.5 Light gas fluxes. φ = 2.4, 40 torr, 10% Ar. mol/cm^2 s.

HAB mm	T K	H2 flux	O2 flux	H2O flux	CH4 flux	CO flux	C6H6 flux	C2H2 flux	CO2 flux
0.0	350	0.0E+00	4.4E-05	0.0E+00	0.0E+00	0.0E+00	1.2E-05	0.0E+00	0.0E+00
1.0	695	-4.3E-07	4.4E-05	3.1E-09	-2.3E-08	7.0E-07	1.2E-05	-1.3E-08	-1.3E-07
2.0	1040	-1.3E-06	4.3E-05	1.5E-07	-5.7E-08	2.6E-06	1.2E-05	-9.5E-08	-3.9E-07
3.0	1384	-2.2E-06	4.2E-05	6.1E-07	-5.7E-08	5.5E-06	1.2E-05	-2.3E-07	-6.4E-07
4.0	1729	-2.8E-06	4.0E-05	1.5E-06	7.6E-09	9.1E-06	1.2E-05	-3.1E-07	-7.6E-07
5.0	1879	-2.9E-06	3.7E-05	2.8E-06	1.5E-07	1.3E-05	1.1E-05	-2.1E-07	-6.6E-07
6.0	1960	-2.5E-06	3.2E-05	4.6E-06	3.9E-07	1.8E-05	1.0E-05	2.2E-07	-3.0E-07
7.0	2003	-1.5E-06	2.7E-05	6.8E-06	7.0E-07	2.2E-05	8.6E-06	1.1E-06	3.4E-07
8.0	2026	-2.0E-07	2.1E-05	9.3E-06	1.1E-06	2.7E-05	6.8E-06	2.4E-06	1.2E-06
9.0	2035	1.4E-06	1.5E-05	1.2E-05	1.4E-06	3.1E-05	4.7E-06	4.2E-06	2.4E-06
10.0	2036	3.1E-06	8.7E-06	1.4E-05	1.8E-06	3.5E-05	2.4E-06	6.2E-06	3.6E-06
11.0	2034	4.6E-06	3.5E-06	1.6E-05	2.1E-06	3.9E-05	8.2E-08	8.1E-06	4.8E-06
14.0	2021	7.6E-06	6.5E-07	1.5E-05	1.5E-06	4.7E-05	-5.3E-06	5.8E-06	6.9E-06

Appendix B. Free Radical Concentrations from Bittner (1981) Data

The data set of Bittner provide an invaluable tool for evaluating reaction mechanisms. Since free radicals were not measured directly in this experiment, we had to resort to kinetic and equilibrium concepts to *infer* the radical concentrations. The Bittner (1981) experiments were made with a molecular beam/mass spectrometer instrument. This is a device which is capable rapidly quenching and measuring free radicals present in the flame. The figures below are a comparison of the Bittner measured radical profiles against the profiles which were calculated using the methods from Chapter Four.

H atom - H atom was calculated by making use of the fact that nearly all the molecular oxygen is destroyed through Reaction 4.1.

$$H + O_2 \Rightarrow OH + O \qquad \text{(Reaction 4.1)}$$

$$[H] = -\frac{d}{dt}[O_2]/k\,[O_2] \qquad (4.12)$$

$$k = 1.2\text{x}10^{17}\,T^{-0.91}\exp(-16.9/RT) \qquad (\text{cm}^3\ \text{sec/mol; kcal})$$

Figure B.1 shows three H atom profiles - experimental, calculated, and global equilibrium. Clearly, global equilibrium is a poor choice for radical estimations. The kinetic method, however, is quite good. In the region of interest (0.6 to 1.2 cm), the measured and calculated values of [H] are within factor. The wiggles in the calculated curve are noise introduced in differentiating the data.

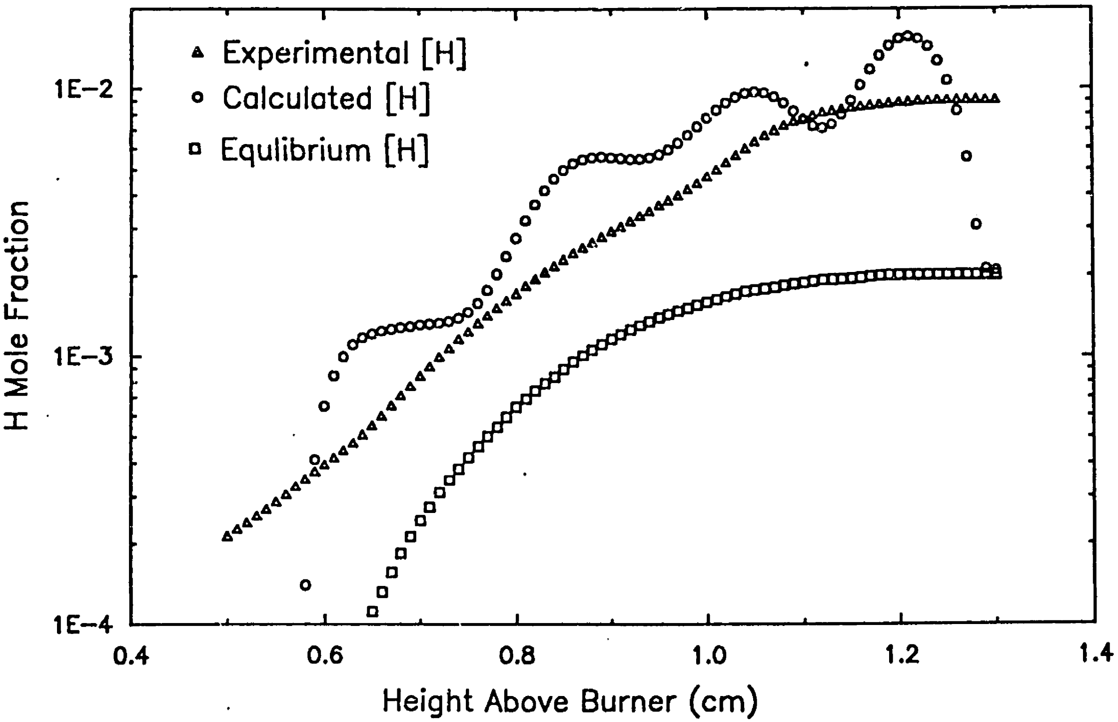

Figure B.1 H atom profiles from Bittner (1981) data

OH - OH was calculated assuming partial equilibrium of Reaction 4.2. Figure B.2 shows the approach to equilibrium of this reaction from the Bittner data. The [OH] is within a factor of five at 0.7 cm and progressively gets closer with height above burner. Figure B.3 shows the approach to equilibrium of the water gas shift system (Reaction 4.3). We can see that the radical reaction (Reaction 4.2) equilibrates before the molecular reaction (Reaction 4.3).

$$H + H_2O \Leftrightarrow H_2 + OH \qquad \text{(Reaction 4.2)}$$

$$H_2O + CO \Leftrightarrow H_2 + CO_2 \qquad \text{(Reaction 4.3)}$$

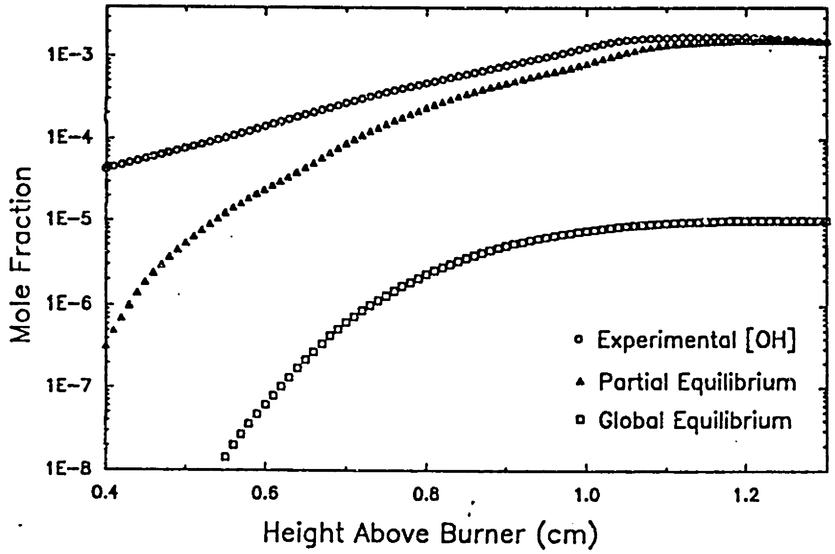

Figure B.2 OH Profiles from Bittner (1981) data.

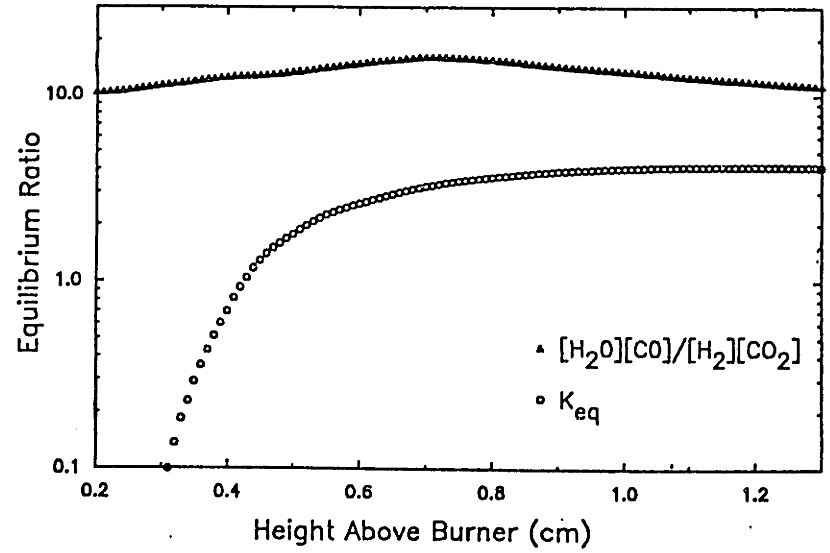

Figure B.3 Water gas shift equilibrium from Bittner (1981) data.

Appendix C. Effective Wavelength of Ge Photodiode

The sensitivity of the germanium photodiode (Hamamatusu Model B2538-05) used for the infrared absorption measurements was not sufficient to allow the use of a narrow band interference filter as in the case of the photomultiplier measurements. Knowing that the absorbing particles behave according to Rayleigh optics, we may calculate an effective wavelength for the device. Equation C.1 shows the reciprocal functionality of C_{ext} with λ. This is replaced by an integral when employed at broad-band wavelengths (Equation C.2). The sensitivity of the device is shown in Figure C.1 as a normalized distribution (adapted from Hamamatsu catalog T-3000 Dec/86). This must be multiplied by the spectral distribution of the source. In this case a the tungsten lamp with a black body temperature of 2300 K (I = 14 amp). Solving Equation C.2 for wavelength yields λ_{eff} = 1.4 μm.

$$C_{ext} = \frac{-\pi^2}{\lambda}\,\mathrm{Im}\left(\frac{m^2-1}{m^2+2}\right)\int_0^\infty f(D)D^3\,dD \qquad \text{(C.1)}$$

$$\lambda_{eff} = \left(\int_0^\infty f(\lambda)\frac{1}{\lambda}\,d\lambda\right)^{-1} \qquad \text{(C.2)}$$

C_{ext} : extinction cross section
m : complex index of refraction, n - *i*k
D : particle diameter
f(D) : particle size distribution
f(λ) : product of black body function and detector spectral sensitivity

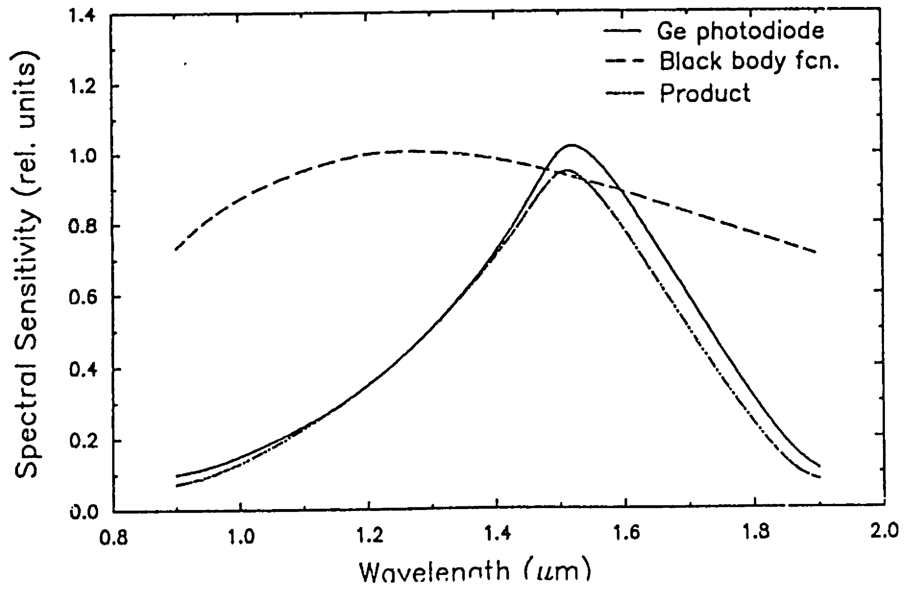

Figure C.1 Response curve of Ge photodiode

Appendix D. Evaluation of critical sooting equivalence ratio by oxidation and coagulation rates.

The process of soot nucleation is a competition between oxidation and growth reactions. We can do a simple order of magnitude evaluation of the critical sooting equivalence ratio using the mechanisms presented in this thesis. The critical sooting equivalence ratio will occur at the point where the time scale for oxidation is just balanced by the time scale for growth. If we assume that the growth is primarily due to coagulation of PAH's, then a direct quantitative comparison can be made of the two rates using the gas kinetic expression. The rate of oxidation of soot is shown in Equation D.1 with the gas kinetic rate constant presented in equation D.3. The collision efficiency used in this analysis is the value of Neoh (1980), $\eta = 0.2$. The rate of coagulation can be presented in the same gas kinetic form (Equation D.2). For this order of magnitude analysis we use a value of unity for the sticking efficiency.

In order to compare the two rates we define the coagulation time as the time required for two PAH molecules to collide. This time will be a function of [PAH] and collisional cross-section. The oxidation time is defined as the time for removal of the mass gained by the particle through that collision. If the oxidation time constant is less than the coagulation time constant, no nucleation of soot will occur. If the reverse is true, the particles will grow to form nuclei. For example, a collision between two 900 amu PAH molecules forms an 1800 amu species. Given a concentration of PAH we can calculate the coagulation time constant. For the oxidation to keep soot from nucleating, 900 amu must be removed from the particle in a time less than that coagulation time constant. The critical sooting equivalence ratio will then have relative concentrations of OH and PAH in which the calculated oxidation time constant and coagulation time constant are equal. Equation D.4 represents a rearrangement of the gas kinetic expression which shows the relative [PAH]/[OH] at critical sooting conditions. The term within the square root brackets represents the relative velocities of the colliding PAH species versus PAH-OH collisions. The term, $2^{-4/3}$, comes from the relative collisional cross-sections of the two collision types. The last term, M_C/M_{PAH}, represents the required number of effective collisions of OH with the dimer to reduce the particle back to the molecular weight of the dimer. Each effective collision of OH with the dimer removes a single carbon, so $M_C = 12$.

Table D.1 shows the results of such a calculation give the following simplifying assumptions:

- The PAH system is monodisperse with a molecular weight of 900 amu.[1]
- The OH mole fraction is 5×10^{-4}. This is fairly representative of the [OH] seen by both Bittner (1981) and the present work.

---

[1] This is obviously not meant to represent the reality system, but is merely a simplification which permits this sort of calculation.

Using this [OH] as an input, the critical [PAH] can be calculated. The table shows this critical value for PAH concentration along with the measured value in the sooting, $\varphi = 2.0$ flame. The [PAH] for the non-sooting, $\varphi = 1.8$ flame was estimated based on the observation of Bittner that the concentration of high molecular weight material in the flame increases 100 times as the fuel-oxygen ratio is increased from $\varphi = 1.8$ to $\varphi = 2.0$. We can see that the predicted [PAH] for the critical sooting equivalence ratio is exactly between the observed [PAH] in non-sooting and sooting flames. Thus, this simple analysis can predict, in this case at least, the critical concentration of soot precursors needed to form nuclei.

$$\frac{dM}{dt} = 12\,\eta_{ox}\,\beta\,N_{OH}\,N_{soot} \tag{D.1}$$

$$\frac{dN}{dt} = \beta\,N_{PAH}^{2} \tag{D.2}$$

$$\beta = \left[\frac{8kT}{\pi\mu}\right]^{1/2} \pi\,\sigma^2\,G \tag{D.3}$$

$$\frac{[PAH]}{[OH]} = \eta_{ox}\left[\frac{0.5\,M_{PAH}}{M_{OH}}\right]^{1/2} 2^{-4/3}\,\frac{M_C}{M_{OH}} \tag{D.4}$$

Table D.1 Comparison of critical sooting [PAH] with observed values in sooting and non-sooting flames.

CONDITION		[PAH] (gm/cc)
$\tau_{ox} = \tau_{coag}$	Calculated Critical Sooting [PAH]	5E-10
$\phi = 1.8$	Non-sooting	5E-11
$\phi = 2.0$	Lightly sooting	5E-9

Appendix E. Sensitivity of soot physical properties to index of refraction

Figures E.1 through E.3 show the sensitivity of the physical properties of soot to the index of refraction. Figure E.1 is a contour plot of the function $-\mathrm{Im}(m^2-1/m^2+2)$ as a function of the real and complex parts of the index of refraction ($m = n - ik$). As can be seen from Equation C.1 in Appendix C, C_{ext} and volume fraction are proportional to this function. We see that both parts of the index of refraction are relatively important in determining the volume fraction. Also shown on this figure are the values of Dalzell and Sarofim (1969) and Lee and Tien (1980) at 488 nm and 1.4 μm. The volume fraction derived from the Lee and Tien infrared is virtually the same as the Dalzell and Sarofim value.

Figure E.2 shows a contour of the function $\mathrm{Abs}(m^2-1/m^2+2)$ as a function of the real and complex parts of the index of refraction. The scattered intensity is proportional to this function as can be seen in Equation 3.5. The scattering equation is a function of both diameter and number density. Figure E.3 shows the contour of $[\mathrm{Abs}(m^2-1/m^2+2)/\mathrm{Im}(m^2-1/m^2+2)]^{1/3}$. The particle diameter is directly proportional to this function. The shape of the contours indicate that the real part of the index of refraction is more important than the imaginary part in determining particle size.

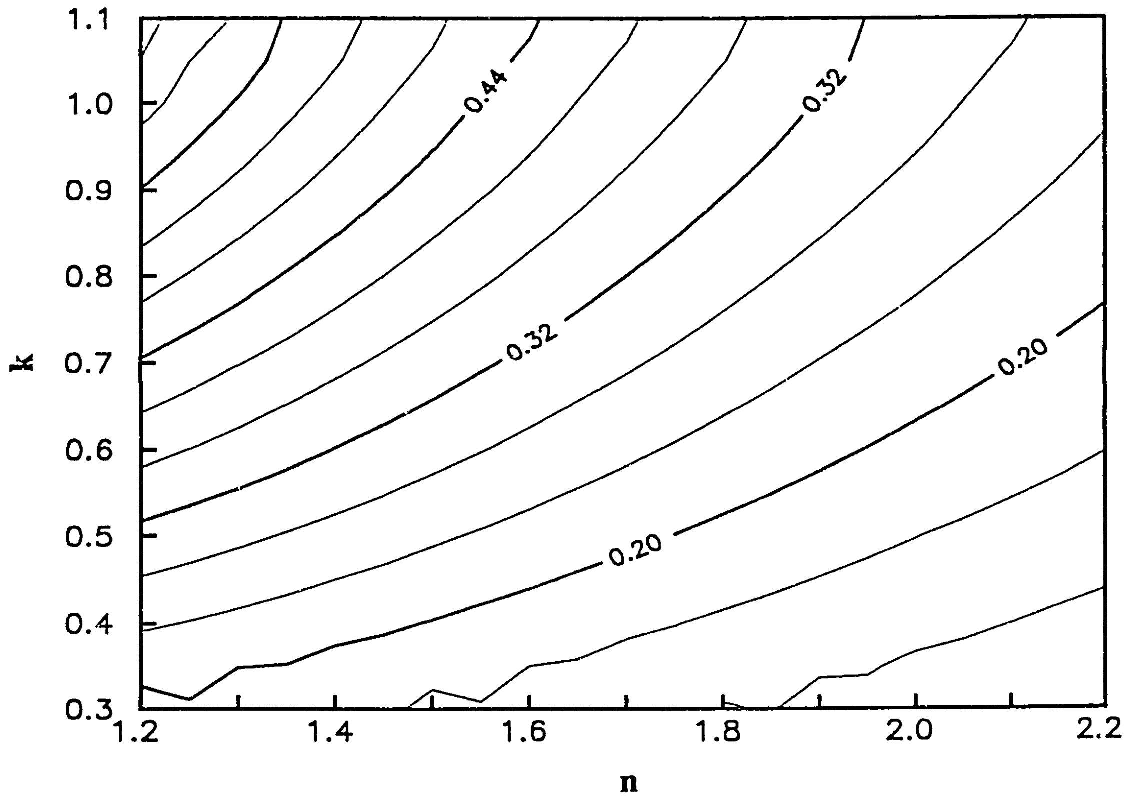

Figure E.1 Contour plot of $\mathrm{Im}(m^2-1/m^2+2)$ as a function of the real and imaginary parts of the index of refraction.

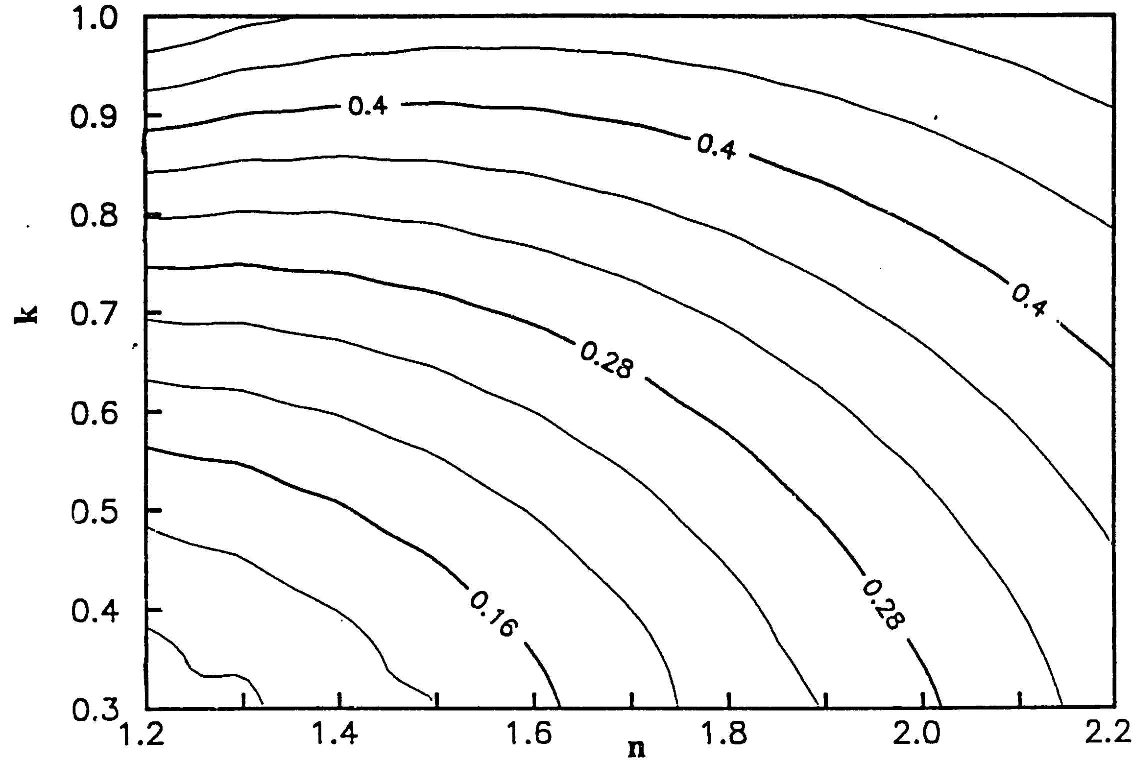

Figure E.2 Contour plot of Abs(m^2-1/m^2+2) as a function of the real and complex parts of the index of refraction.

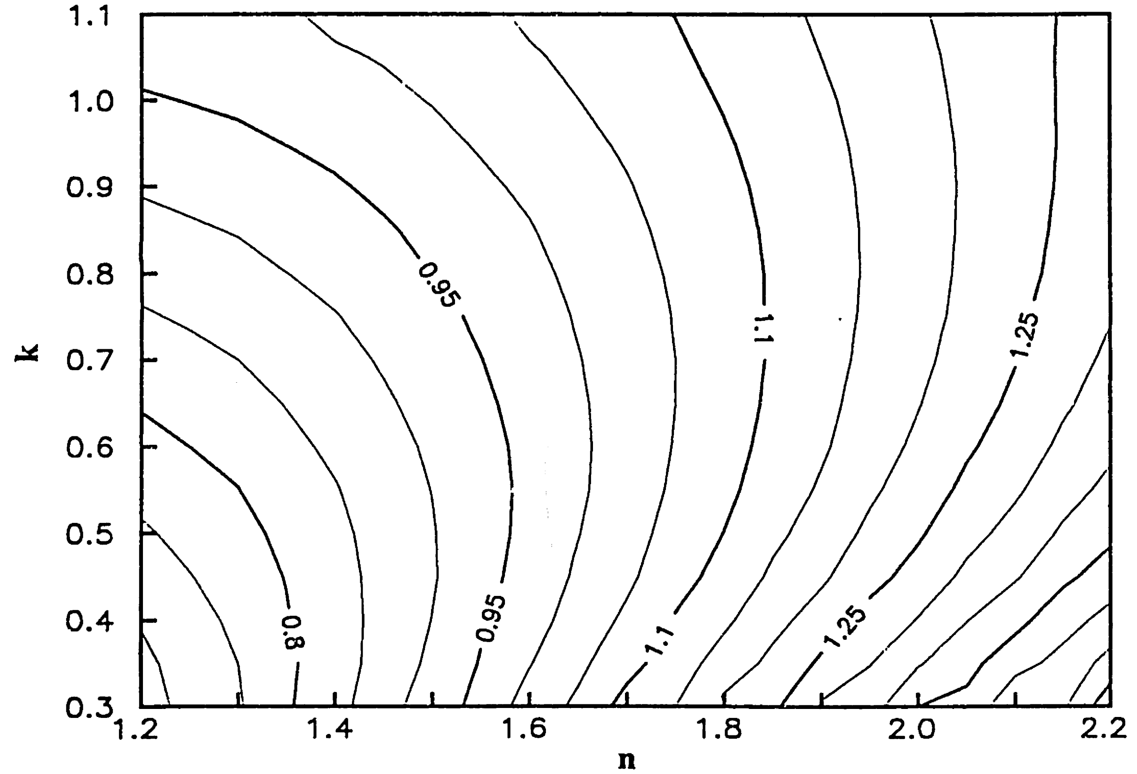

Figure E.3 Contour plot of $[\mathrm{Abs}(m^2\text{-}1/m^2+2)/\mathrm{Im}(m^2\text{-}1/m^2+2)]^{1/3}$ as a function of the real and complex parts of the index of refraction.

Appendix F. Equilibrium radical concentrations as a function of temperature and equivalence ratio.

Figures F.1 through F.3 show the equilibrium mole fractions of H, OH, and O as a function of temperature and equivalence ratio. These are calculated for a $C_6H_6/O_2/30\%$ Ar system at 20 torr using the StanJan multicomponent equilibrium solver written by W.C. Reynolds of Stanford University. The JANAF thermodynamic data set is used with this program.

At C/O ratios exceeding unity, solid carbon becomes thermodynamically stable. This transition accounts for the high sensitivity of OH and O at high equivalence ratios (C/O = 1.0 at φ = 2.5 for benzene). The equilibrium H atom is not affected by the presence of solid carbon.

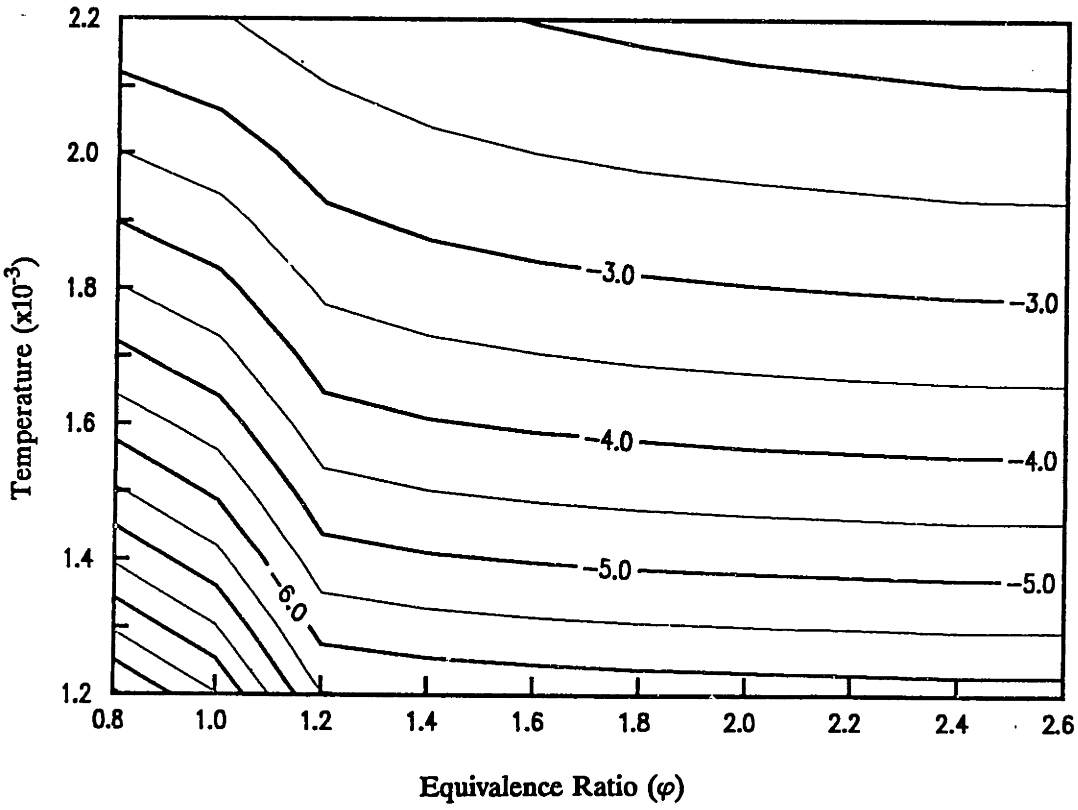

Figure F.1 Log of equilibrium H mole fraction as a function of temperature and equivalence ratio. P = 20 torr, 30% Ar diluent.

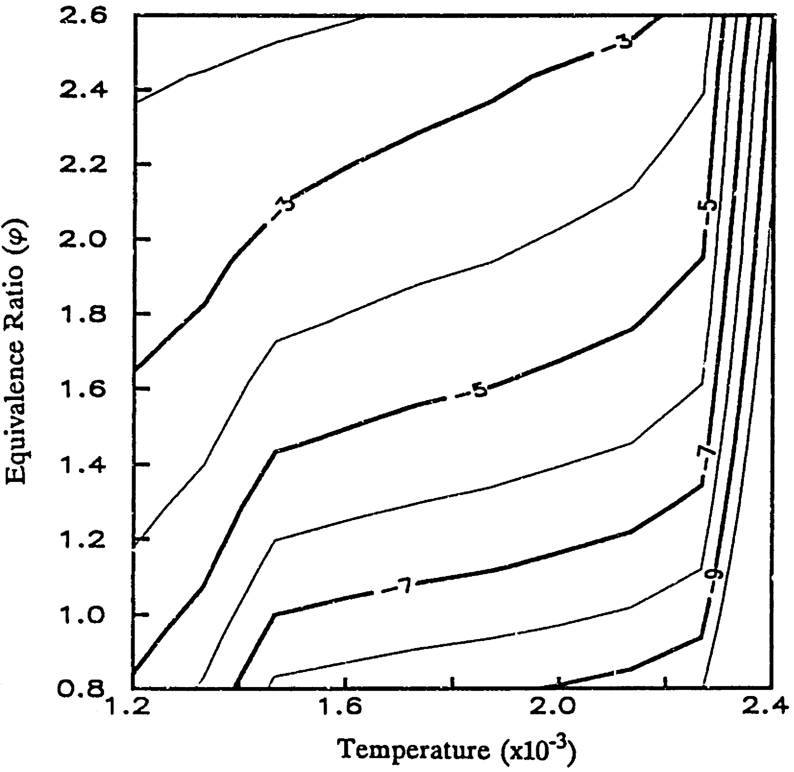

Figure F.2 Log of equilibrium OH mole fraction as a function of temperature and equivalence ratio. P = 20 torr, 30% Ar diluent.

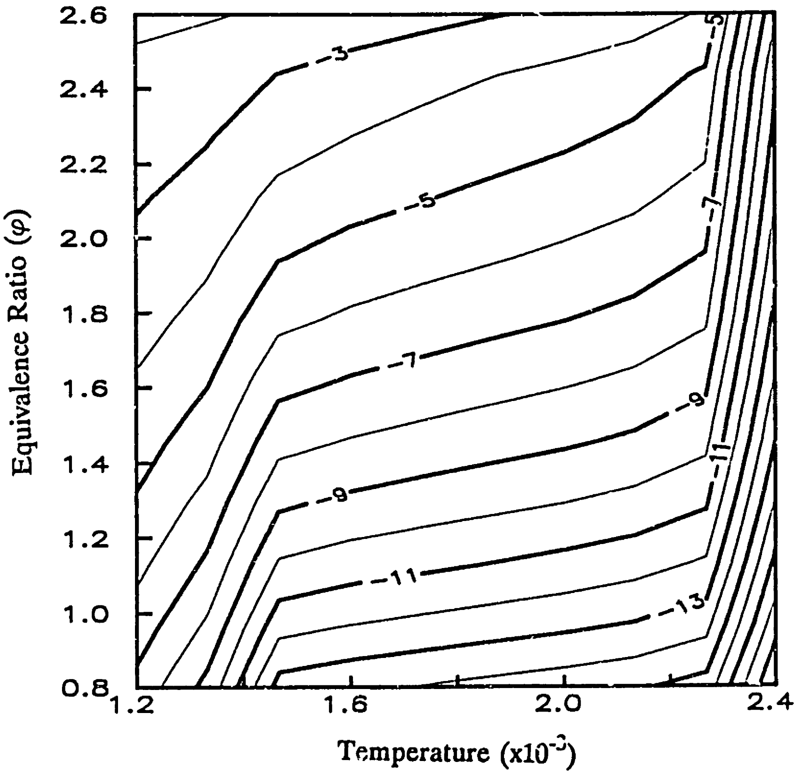

Figure F.3 Log of equilibrium O mole fraction as a function of temperature and equivalence ratio. P = 20 torr, 30% Ar diluent.

References

ASTM Standard D1322-85. "Standard Test Method for Smoke Point of Aviation Turbine Fuels" (1985).

ASTM Standard D3701-83. "Hydrogen Content of Aviation Turbine Fuels by Low-Resolution Nuclear Magnetic Resonance Spectrometry" (1983).

Badger, G.M. and Spotswood, T.M., "The Formation of Aromatic Hydrocarbons at High Temperatures. Part XI. The Pyrolysis of Buta-1,3,diene and Buta-1,3,diene with Pyrene", *J. Chem. Soc.,* 4431 (1960).

Baumgartner, L, Hess, D., Jander, H., and Wagner, H.Gg., "Rate of Soot Growth in Atmospheric Premixed Laminar Flames", *Twentieth Symposium (International) on Combustion*, p. 959-967 (1985).

Benson, S.W., *Thermochemical Kinetics*, Second edition, John Wiley and Sons, New York (1976).

Bittner, J.D. and Howard, J.B., "Pre-Particle Chemistry in Soot Formation", in *Particulate Carbon Formation During Combustion*, D.C. Siegla and G.W. Smith, Eds., Plenum Press, New York (1981).

Bittner, J.D., "A Molecular Beam Mass Spectrometer Study of Fuel-Rich and Sooting Benzene-Oxygen Flames", Ph.D. Thesis, Department of Chemical Engineering, Massachusetts Institute of Technology, (1981).

Bittner, J.D. and Howard, J.B., "Role of Aromatics in Soot Formation", in *Alternative Hydrocarbon Fuels: Combustion and Chemical Kinetics*, C.T. Bowman and J. Birkeland, Eds., Progress in Astro. and Aero., Vol. 62, p. 335, AIAA (1978).

Bittner, J.D. and Howard, J.B., "Benzene Decomposition in Flames", presented at Eastern States Section: The Combustion Institute Fall Meeting (1984).

Bittner, J.D. and Howard, J.B., "Composition Profiles and Reaction Mechanisms in a Near-sooting Premixed Benzene/Oxygen/Argon Flame", *Eighteenth Symposium (International) on Combustion*, p. 1105, (1981).

Bittner, J.D. and Howard, J.B., "Structure of Sooting Flames", in *Soot in Combustion Systems and its Toxic Properties*, J. Lahaye and G. Prado, Eds., Plenum Press, New York (1983).

Bockhorn, H., Fetting, F., and Wenz, H., "Investigation of the Formation of High Molecular Hydrocarbons and Soot in Premixed Hydrocarbons-Oxygen Flames", *Ber. Bunsenges Phys. Chem.* 87, 1067, (1983).

Bockhorn, H., Fetting, F., Heddrich, A., and Reh Ch., "Formation of High Molecular Hydrocarbons in Sooting Premixed Hydrocarbon-Oxygen Flames", Poster PS-001 presented at Twenty-First Symposium (International) on Combustion (1988).

Bohm, H., Hesse, D., Jander, H, Luers, B, Pietscher, J., Wagner, H.Gg., and Weiss, M., "The Influence of Pressure and Temperature on Soot Formation in Premixed Flames", *Twenty Second Symposium (International) on Combustion*, in press (1989).

Bohren, C.F. and Huffman, D.R., *Absorption and Scattering of Light by Small Particles*, Wiley-Interscience, New York (1983).

Bonne, U., Homann, K.H., and Wagner, H.Gg., "Carbon Formation in Premixed Flames", *Tenth*

Symposium (International) on Combustion, 503-512, (1965).

Bouquet, M. "Determination of Hydrogen Content of Petroleum Products Using a Low Resolution Pulsed NMR Spectrometer: Applications to Light Cuts, Distillates and Residues", *Fuel* 64, 226-228 (1985).

Boyland, E., "The Toxicity of Soot", in *Soot in Combustion Systems and its Toxic Properties*, J. Lahaye and G. Prado, Eds., Plenum Press, New York (1983).

Boyle, J., and Pfefferle, L., "Vacuum Ultraviolet Photo-Ionization TOF-Mass Spectrometry: A Novel Technique for Pyrolysis, Combustion, and Soot Nucleation Studies", presented at Eastern States Section: The Combustion Institute Fall Meeting (1988).

Braun-Unkhoff, M., Frank, P., and Just, Th., "A Shock Tube Study on the Thermal Decomposition of Toluene and of the Phenyl Radical at High Temperatures", *Twenty-Second Symposium (International) on Combustion*, in press (1989).

Brei, M, Jander, H., and Wagner, H.Gg., "Integral Carbon Mass Balance in Premixed Sooting Flames", *Ber. Bunsenges. Phys. Chem.* **91**, 30-36 (1987).

Brown, J.K. and Ladner, W.R. "A Study of the Hydrogen Distribution in Coal-like Materials by High-Resolution Nuclear Magnetic Resonance Spectroscopy II - A Comparison with Infrared Measurements and the Conversion of Carbon Structure", *Fuel* 39, 87 (1960)

Cabot Corporation, *Carbon Black.*

Calcote, H.F., "Ion Production and Recombination in Flames", *Eighth Symposium (International) on Combustion*, p. 184-199 (1962).

Calcote, H.F., "Ionic Mechanisms of Soot Formation in Flames", presented at Fall Technical Meeting of Eastern States Section: The Combustion Institute Fall Meeting (1978).

Chakraborty, B.B., and Long, R., "The Formation of Soot and Polycyclic Aromatic Hydrocarbons in Diffusion Flames -- Part Two", *Combustion and Flame* **12**, 237 (1968).

Charalampopoulos, T.T. and Felske, J.D., "Refractive Indices of Soot Particles Deduced from In-Situ Laser Light Scattering Measurements", *Combustion and Flame* **68**, 283-294 (1987).

Chippet, S. and Gray, W.A., "The Size and Optical Properties of Soot Particles", *Combustion and Flame* 31, 149 (1978) .

Coe, D.S., Haynes, B.S., and Steinfeld, J.I., "Identification of a Source of Argon-Ion-Laser Excited Fluorescence in Sooting Flames", *Combustion and Flame* 43, 211-214 (1981).

Coe, D.S. and Steinfeld, J.I., "Fluorescence Excitation and Emission Spectra of Polycyclic Aromatic Hydrocarbons at Flame Temperatures", *Chem. Phys. Letters* 76(3), 485-489 (1980).

Cole, J.A., Bittner, J.D., Longwell, J.P., and Howard, J.B., "Formation Mechanisms of Aromatic Compounds in Aliphatic Flames", *Combustion and Flame* **56**, 51-70, (1984).

Colket, M.B., Chiappetta, L., Guile, R.N., Zabielski, M.F., and Seery, D.J. "Measurements; Diagnostics of Internal Aerodynamics of Gas Sampling Probes", *Combustion and Flame* **44**, 3-14 (1982).

Colket, III, M.B., "The Pyrolysis of acetylene and Vinylacetylene in a Single-Pulse Shock Tube", *Twenty-First Symposium (International) on Combustion*, p. 851-864 (1988).

CRC Handbook of Chemistry and Physics, 55th edition, CRC Press, Cleveland (1974).

Crittenden, B.D., and Long, R., "The Mechanisms of Formation of Polynuclear Aromatic Compounds in Combustion Systems", in *Carcinogenesis, Vol 1., Polynuclear Aromatic Hydrocarbons: Chemistry, Metabolism, and Carcinogenesis*, R.I. Freudenthal and P.W. Jones, Eds., Raven Press, New York, (1976).

Cypres, R. and Bettens, B., "Mechanismes de Fragmentation Pyrolytique du Phenol et des Cresols", *Tetrahedron* 30, 1253-1260 (1974).

D'Alessio, Beretta, F., and Venitozzi, C., "Optical Investigation on Soot Forming Methane-Oxygen Flames", *Combustion Science and Technology* 5, 263-272 (1972).

D'Alessio, A., Di Lorenzo, A., Sarofim, A.F., Beretta, F., Masi, S., and Venitozzi, C., "Soot Formation in Methane-Oxygen Flames", *Fifteenth Symposium (International) on Combustion*, p. 1427 (1974).

D'Alessio, A., Di Lorenzo, A., Borghese, A., Beretta, F., and Masi, S., "Study of the Soot Nucleation Zone of Rich Methane-Oxygen Flames", *Sixteenth Symposium (International) on Combustion*, p. 695, The Combustion Institute, (1976).

Dalzell, W.H. and Sarofim, A.F., "Optical Constants of Soot and their Application to Heat-Flux Calculations", *Transactions of the ASME, Journal of Heat Transfer* 91, 100 (1969).

Dasch, C.J, "The Decay of Soot Surface Reactivity and Its Importance in Total Soot Formation", *Combustion and Flame* 61, 216-225 (1985).

Davies, R.A., and Scully, D.B., "Carbon Formation from Aromatic Hydrocarbons II", *Combustion and Flame* 10, 165, (1965).

Donnet, J.B. and Voet, A., *Carbon Black; Physics, Chemistry and Elastomer Reinforcement*, Marcel Dekker, New York (1976).

Drake, M.C., Grabner, L.H., and Hastie, J.W., "A Comparison of Spectroscopic Flame Temperature Measurements: Na-D Line Reversal, Rotational and Vibrational Raman, and OH Absorption", NBS Special Publication 561, Proc. of the 10th Materials Research Symposium on Characterization of High Temperature Vapors and Gases (1979).

Ebert, L.B., Scanlon, J.C., Kastrup, R.V., and Clausen, C.A. "Combustion Tube Soot from a Diesel Fuel/Air Mixture", *prepared paper - American Chemical Society, Div. Fuel Chemistry* 32(3), 440-447 (1987).

Elser, V. and Haddon, R.C., "Icosahedral C60: an Aromatic Molecule with a Vanishingly Small Ring Current Magnetic Susceptibility", *Nature* 325, 792-794 (1987).

Erickson, W., "Light Scattering: A Technique for Studying Soot in Flames", Sc.D. Thesis, Department of Chemical Engineering, Massachusetts Institute of Technology (1961).

Fahr, A., Mallard, W.G., and Stein, S.E., "Reaction of Phenyl Radicals with Ethene, Ethyne, and Benzene", *Twenty-First Symposium (International) on Combustion*, p. 825-831 (1988).

Felder, W, Madronich, S., and Olson, D.B., "Oxidation Kinetics of Carbon Blacks over 1300-1700 K", *Energy and Fuels* 2, 743-750 (1988).

Fenimore, C.P. and Jones, G.W., "Oxidation of Soot by Hydroxyl Radicals", *J. Phys. Chem.* 71(3), 593-597 (1967).

Fetzer, J.C., Biggs, W.R. and Jinno, K., "HPLC Analysis of the Large Polycyclic Aromatic Hydrocarbons in a Diesel Particulate", *Chromatographia* 21(8), 439-442 (1986).

Frazee, J.D. and Anderson, R.C., "Influence of Organic Compounds on the Formation of Gas Carbon", *Proc. Third Conf. on Carbon*, p. 405-410, Buffalo, New York (1957).

Frenklach, M., "Dynamics of Discrete Distribution for Smoluchowski Coagulation Model", *J. Colloid and Interface. Sci.* 108(1), 237-242 (1985).

Frenklach, M., Clary, D.W., Gardiner, W.C., and Stein, S.E., "Detailed Kinetic Modeling of Soot Formation in Shock-Tube Pyrolysis of Acetylene", *Twentieth Symposium (International) on Combustion*, p. 887, (1985).

Frenklach, M. and Warnatz, J, "Detailed Modeling of PAH Profiles in a Sooting Low-Pressure Acetylene Flame", *Combustion Science and Technology* 51, 265-283 (1987).

Frenklach, M. and Harris, S.J., "Aerosol Dynamics Modeling Using the Method of Moments", *J. Colloidal and Interface Science* 118(1), 252-261 (1987).

Frenklach, M. Yuan, T., and Ramachandra, M.K., "Soot Formation in Binary Hydrocarbon Mixtures", *Energy and Fuel* 2, 462-480 (1988)

Frenklach, M. and Ebert, L.B., "Comment on the Proposed Role of Spheroidal Carbon Clusters in Soot Formation", *J. Phys. Chem.*, 92, 561-563 (1988).

Frenklach, M., "On the Driving Force of PAH Production", *Twenty-Second Symposium (International) on Combustion*, in press (1989).

Friedlander, S.K., *Smoke, Dust and Haze*, Wiley-Interscience, New York (1977).

Fristrom, R.M., "Radical Concentrations and Reactions in a Methane Oxygen Flame", *Ninth Symposium (International) on Combustion*, p. 560-575 (1963).

Fristrom, R.M., "Comments on Quenching Mechanisms in the Microprobe Sampling of Flames", *Combustion and Flame* 50, 239-242 (1983).

Fristrom, R.M. and Westenberg, A.A., *Flame Structure*, McGraw-Hill, New York (1965).

Fujii, N., and Asaba, T., "Shock-Tube Study of the Reaction of Rich Mixtures of Benzene and Oxygen", *Fourteenth Symposium (International) on Combustion*, p. 433 (1973).

Gay, J.G. and Berne, B.J., "Energy Accommodation in Collisions of Small Particles", *Journal of Colloid and Interface Science* 109(1), 90-100 (1985).

Gerhardt, Ph., Loffler, S. and Homann, K.H., "Polyhedral Carbon Ions in Hydrocarbon Flames", *Chem. Phys. Letters*, 137(4), 306-310 (1987)

Gilbert, M. and Lobdell, J.H., "Resistance Thermometer Measurements in a Low Pressure Flame", *Fourth Symposium (International) on Combustion*, p. 285 (1953).

Glassman, I., "Phenomenological Models of Soot Processes in Combustion Systems", AFOSR TR-79-1147 (1979).

Glassman, I., "Soot Formation in Combustion Processes", *Twenty-Second Symposium (International)* *on Combustion*, in press (1989).

Golden, C., and Sawicki, E., "Ultrasonic Extraction of Total Particulate Aromatic Hydrocarbons (TpAH) from Airborne Particles at Room Temperature", *Intern. J. Environ. Anal. Chem.* 4, 9-23 (1975).

Gomez, A., Littman, M.G., and Glassman, I., "Comparative Study of Soot Formation on the Centerline of Axisymmetric Laminar Diffusion Flames: Fuel and Temperature Effects", *Combustion and Flame* 70, 225-241 (1987).

Graham, S.C., Homer, J.B., and Rosenfeld, J.L.J., "The Formation and Coagulation of Soot Aerosols Generated by the Pyrolysis of Aromatic Hydrocarbons", *Proceedings of the Royal Society of London* 344, 259, (1975).

Greist, W.H., Tomkins, B.A., Epler, J.L. and Rao, T.K, "Characterization of Multialkylated Polycyclic Aromatic Hydrocarbons and Energy-Related Materials", in *Polynuclear Aromatic Hydrocarbons*, P.W. Jones and P. Leber, Eds., Ann Arbor Sciences Publishers, Inc. Ann Arbor, MI (1979).

Harris, M.M., King, G.B., and Laurendeau, N.M., "Influence of Temperature and Hydroxyl Concentration on Incipient Soot Formation in Premixed Flames", *Combustion and Flame* 64, 99-112 (1986).

Harris, S.J. and Weiner, A.M., "Surface Growth of Soot Particles in Premixed Ethylene/Air Flames", *Combustion Science and Technology* 31, 155-167 (1983a).

Harris, S.J. and Weiner, A.M., "Determination of the Rate Constant for Soot Surface Growth", *Combustion Science and Technology* 32, 267-275 (1983b).

Harris, S.J. and Weiner, A.M., "Soot Particle Growth in Premixed Toluene/Ethylene Flames", *Combustion Science and Technology* 38, 75 (1984).

Harris, S.J. and Weiner A.M., "Some Constraints on Soot Particle Inception in Premixed Ethylene Flames", *Twentieth Symposium (International) on Combustion*, p. 969-978, (1985).

Harris, S.J., Weiner, A.M., and Ashcroft, C.C., "Soot Particle Inception Kinetics in a Premixed Ethylene Flame", *Combustion and Flame* 64, 65-81, (1986).

Harris, S.J., Weiner, A.M., and Blint, R.J., "Formation of Small Aromatic Molecules in a Sooting Ethylene Flame", *Combustion and Flame* 72, 91-109, (1988).

Harris, S.J., "A Picture of Soot Particle Inception", *Twenty-Second Symposium (International) on Combustion*, in press (1989).

Haynes, B.S., and Wagner, H.Gg., "Soot Formation", *Progress in Energy and Combustion Science* 7, 229-273 (1980).

He, Y.Z., Mallard, W.G., and Tsang, W., "Kinetics of Hydrogen and Hydroxyl Radical Attack on Phenol at High Temperatures", *Journal of Physical Chemistry* 92, 2196-2201 (1988).

Heilbronner, E. and Straub, H., *Hückel Molecular Orbitals*, Springer-Verlag, New York (1966).

Homann, K.H., and Wagner, H.Gg., "Some New Aspects of the Mechanism of Carbon Formation in Premixed Flames", *Eleventh Symposium (International) on Combustion*, p. 371 (1967).

Homann, K.H., "Formation of Large Molecules, Particulates, and Ions; Progress and Unresolved Questions", *Twentieth Symposium (International) on Combustion*, p. 857, The Combustion Institute, (1985).

Howard, J.B. and Kausch, W.J., "Soot Control by Fuel Additives", *Progress in Energy and Combustion Science* **6**, 263-276 (1980).

Howard, J.B. and Longwell, J.P., "Formation Mechanisms of PAH and Soot in Flames", *Seventh International Symposium on Polynuclear Aromatic Hydrocarbons*, Battelle Press, Columbus, OH, (1982).

Howarth, C.R., Foster, P.J., and Thring, M.W., "The Effect of Temperature on the Extinction of Radiation by Soot Particles", *Proc. Third Int'l. Heat Transfer Conf.*, Vol 5, p. 122-128 (1966).

Hura, H.S. and Glassman, I., "Fuel Oxygen Effects on Soot Formation in Counterflow Diffusion Flames", *Combustion Science and Technology* **54**, 1-21 (1987).

Jones, K.C., Stratford, J.A., Waterhouse, K.S., Furlong, E.T., Giger, W., Hites, R.A., Schaffner, C., and Johnston, A.E., "Increases in the Polynuclear Aromatic Hydrocarbon Content of an Agricultural Soil over the Last Century", *Environ. Sci. Technol.* **28**(1), 95-101 (1989).

Karcher, W., Fordham, R.J., Dubois, J.J., Glause, P.G.J.M., and Lighardt, J.A.M., *Spectral Atlas of Polycyclic Aromatic Compounds*, D. Reidel Publ. Co. Dordrecht/Boston/Lancaster (1985).

Kent, J.H and Wagner, H.Gg., "Why Do Diffusion Flames Emit Smoke?", *Combustion Science and Technology* **41**, 245-269 (1984).

Kern, R.D., Wu, C.H., Skinner, G.B., Rao, V.S., Kiefer, J.H, Towers, J.A., and Mizerka, L.J., "Collaborative Shock Tube Studies of Benzene Pyrolysis", *Twentieth Symposium (International) on Combustion*, p. 789-797 (1985).

Kiefer, J.H., Mizerka, L.J., Patel, M.R., and Wei, H.C., "A Shock Tube Investigation of Major Pathways in the High Temperature Pyrolysis of Benzene", *Journal of Physical Chemistry* **89**(10), 2013-2019 (1985).

Kostkowski, H.J. and Lee, R.D., "Theory and Methods of Optical Pyrometry", NBS Monograph 41, issued March 1, 1962.

Kroto, H.W., Heath, J.R., O'Brien S.C., Curl, R.F., and Smalley, R.E., "C60: Buckminsterfullerene", *Nature* **318**, 162 (1985).

Lafleur, A.L., Gagel, J.J., Longwell, J.P., and Monchamp, P.A., "Identification of Aromatic Alkynes and Polyunsaturated Acetylenes in the Output of a Jet-Stirred Combustor", *Energy and Fuels* **2**, 709-716 (1988).

Lafleur, A.L. and Wornat, M.J., "Multimode Separation of Polycyclic Aromatic Compounds in High-Performance Size Exclusion Chromatography with Polydivinylbenzene", *Anal. Chem.*, in press (1988).

Lafleur, A.L., Monchamp, P.A., Chang, N.S., Plummer, E.F., and Wornat, M.J., "Evaluation of Cyano Bonded Phases for the Fractionation of Bioactive Complex Mixtures", *Journal of Chromatographic Science*, in press (1988).

Lafleur, A.L., Monchamp, P.A., Plummer, E.F., and Kruzel, E.L., "Evaluation of Gravimetric Methods for Dissoluble Matter in Extracts of Environmental Samples", *Analytical Letters* **19**, 2013-2119 (1986).

Lahaye, J., and Prado, G., "Mechanisms of Carbon Black Formation", in *Chemistry and Physics of Carbon*, Vol. 14, P.L. Walker and P.A. Thrower, Eds., p. 168, Marcel Dekker, New York, (1978).

Lam, F.W., "The Formation of Polycyclic Aromatic Hydrocarbons and Soot in a Jet-Stirred/Plug-Flow

Reactor", Ph.D. Thesis, Department of Chemical Engineering, Massachusetts Institute of Technology (1988).

Lampe, F.W., Franklin, J.L, and Field, F.H., "Cross Sections for Ionization by Electrons", *J. American Chemical Society* 79, 6129 (1957).

Larsson, S., Volosov, A., and Rosen, A., "Optical Spectrum of the Icosahedral C60 - "Follene-60"", *Chem. Phys. Letters*, 137(6), 501-504 (1987).

Lee, M.L., Vassilaros, D.L., White, C.M., and Novotny, M., "Retention Indices for Programmed-Temperature Capillary Column Gas Chromatography of Polycyclic Aromatic Hydrocarbons", *Analytical Chemistry* **51**(6) 768, (1979).

Lee, S.C. and Tien, C.L., "Optical Constants of Soot in Hydrocarbon Flames", *Eighteenth Symposium (International) on Combustion*, p. 1159-1166 (1980).

Lee, M.L., Novotny, M.V., and Bartle, K.D., *Analytical Chemistry of Polycyclic Aromatic Compounds*, Academic Press, New York (1981).

Lee, M.L. and Wright, B.W., "Capillary Column Gas Chromatography of Polycyclic Aromatic Compounds: A Review", *Journal of Chromatographic Science* **18**, 345-358 (1980).

Lin, C.Y. and Lin, M.C., "Unimolecular Decomposition of the Phenoxy Radicals in Shock Waves", *Int. J. Chem. Kin.* **17**, 1025-1028 (1985).

Lin, C.Y. and Lin, M.C., "Kinetics of the C_6H_5 + O_2 Reaction", Abstract 7, Presented at Eastern States Section: The Combustion Institute Fall Meeting (1987).

Longwell, J.P., "The Formation of Polycyclic Aromatic Hydrocarbons by Combustion", *Nineteenth Symposium (International) on Combustion*, p. 1339-1350 (1982).

Longwell, J.P., "Polycyclic Aromatic Hydrocarbons and Soot from Practical Combustion Systems", in *Soot in Combustion Systems and its Toxic Properties*, J. Lahaye and G. Prado, Eds., Plenum Press, New York, (1983).

Lucht, R.P., Sweeny, D.W., and Laurendeau, N.M., "Laser-Saturated Fluorescence Measurements of OH in Atmospheric Pressure $CH_4/O_2/N_2$ Flames Under Sooting and Non-Sooting Conditions", *Combustion Science and Technology* **42**, 259-281 (1985).

Mallion, R.B., "Ring Current Effects in C60", *Nature* **325**, 760-761 (1987).

Miller, J.H., Mallard, W.G., and Smyth, K.C., "Intermolecular Potential Calculations for Polycyclic Aromatic Hydrocarbons", *J. Phys. Chem.* **88**, 4963-4970 (1984).

Miller, J.H., Smyth, K.C., and Mallard, W.G., "Calculations of the Dimerization of Aromatic Hydrocarbons: Implications for Soot Formation", *Twentieth Symposium (International) on Combustion*, p. 1139-1147 (1985).

Millikan, R.C., "Non-Equilibrium Soot Formation in Premixed Flames", *J. Phys. Chem.* **66**, 794 (1962).

Millikan, R.C. and Foss, W.I., "Non-equilibrium Effects in Soot Deposition", *Combustion and Flame* **6**, 210-211 (1962).

Nagle, J. and Strickland-Constable, R.F., "Oxidation of Carbon Between 1000-2000°C", *Proc. of Fifth Carbon Conf*, p. 154-164 (1962).

Neoh, K.G., "Soot Burnout in Flames", Ph.D. Thesis, Department of Chemical Engineering, Massachusetts Institute of Technology, (1980).

Nicovich, J.M. and Ravishankara, A.R., "Reaction of Hydrogen Atom with Benzene: Kinetics and Mechanism", *J. Phys. Chem.* **88**, 2534-2541 (1984).

Olson, D.B., and Madronich, S., "The Effect of Temperature on Soot Formation in Premixed Flames", *Combustion and Flame* **60**, 203-213 (1985).

Otvos, J.W. and Stevenson, D.P., "Cross-sections of Molecules for Ionization by Electrons", *J. American Chemical Society* **78**, 546 (1956).

Page, F.M. and Ates, F., "Oxidation of Soot in Fuel-Rich Flames", *Evaporation-Combustion of Fuels*, ACS Advances in Chemistry Series, no. 166, p. 190-197, J.T. Zang, Ed., ACS, Washington, DC (1978).

Palmer, H.B., and Cullis, C.F., "The Formation of Carbon from Gases", in *Chemistry and Physics of Carbon*, Vol. 1, P.L. Walker, Ed., p. 265-325, Marcel Dekker, New York (1965).

Park, C. and Appleton, J.P., "Shock Tube Measurements of Soot Oxidation Rates", *Combustion and Flame* **20**, 369-379 (1973).

Perry, R.H. and Chilton, C.H., *Chemical Engineers' Handbook*, Fifth edition, McGraw-Hill, New York (1973).

Pope, C.J., "Fluxes and Net Reaction Rates of High Molecular Weight Material in a Near-Sooting Benzene-Oxygen Flame", M.S. Thesis, Department of Chemical Engineering, Massachusetts Institute of Technology, (1988).

Porter, G., "Carbon Formation in the Combustion Wave", *Fourth Symposium (International) on Combustion*, p. 248-252 (1953).

Pott, P., *Chirugical Observations*, p. 63, Hawkes, Clarke and Collins, London (1975).

Prado, G., Lahaye, J., and Haynes, B.S., "Soot Particle Nucleation and Agglomeration", in *Soot in Combustion Systems and Its Toxic Properties*, J. Lahaye and G. Prado, Eds., Plenum Press, New York (1983).

Press, W.H., Flannery, B.P., Teukolsky, S.A., and Vetterling, W.T., *Numerical Recipes*, Cambridge University Press, Cambridge (1986).

Reid, R.C., Prausnitz, J.M., and Sherwood, T.K., *The Properties of Gases and Liquids*, Third edition, McGraw-Hill, New York (1977).

Reisch, M.S., "Top 50 Chemicals Production Reaches Record High", *Chemical and Engineering News*, p. 11-14, April 10, 1989.

Reynolds, W.C., STANJAN Multicomponent Equilibrium Program V.3.60, available on disk (1986).

Ritrievi, K.E., "The Effect of Iron on Soot Particle Formation and Growth", Ph.D. Thesis, Department of Chemical Engineering, Massachusetts Institute of Technology (1984).

Rivin, D. and Medalia, A.I., "A Comparative Study of Soot and Carbon Black", in *Soot in Combustion Systems and Its Toxic Properties*, J. Lahaye and G. Prado, Eds., Plenum Press, New York (1983).

Savitsky, A., and Golay, M.J.E., "Smoothing and Differentiation of Data by Simplified Least Squares Procedures", *Analytical Chemistry* 36(8), 1627-1639 (1964).

Schmidt, W, Grimmer, G., Jacob, J., Dettbarn, G. and Naujack, K.W., "Polycyclic Aromatic Hydrocarbons with Mass Number 300 and 302 in Hard-Coal Flue Gas Condensate", *Fresenius. Z. Anal. Chem.* 326, 401-413 (1987).

Schott, G.L., "Further Studies of Exponential Branching Rates in Reflected-Shock Heated, Nonstoichiometric H_2-CO-O_2 Systems", *Combustion and Flame* 21, 357-370 (1973).

Scully, D.B., and Davies, R.A., "Carbon Formation from Aromatic Hydrocarbons", *Combustion and Flame* 9, 185 (1964).

Shreve, N.R. and Brink, J.A., *Chemical Process Industries*, Fourth edition, McGraw-Hill, New York (1977).

Smoluchowski, M.V., "Versuch einer mathematischen Theorie der Koagulationskinetik kolloider Lösungen (Essay on the Mathematical Theory of Coagulation Kinetics for Colloidal Solutions)", *Z. Phys. Chem* 92, 129-168 (1917).

Stehling, F.C., Frazee, J.D., and Anderson, R.C., "Mechanisms of Nucleation in Carbon Formation", *Eighth Symposium (International) on Combustion*, p. 774 (1962).

Stein, S.E. and Kafafi, S.A., "Thermochemistry of Soot Formation", presented at Eastern States Section: The Combustion Institute Fall Meeting (1987).

Stein, S.E., and Fahr, A., "High Temperature Stabilities of Hydrocarbons", *Journal of Physical Chemistry* 89(17), 3714-3725, (1985).

Stenhagen, E., Abrahamson, S., and McLafferty, F.W., *Registry of Mass Spectral Data*, Wiley-Interscience, New York (1974).

Street, J.C., and Thomas, A., "Carbon Formation in Premixed Flames", *Fuel* 34, 4 (1955).

Streitwieser, A., *Molecular Orbital Theory for Organic Chemists*, Wiley, New York (1961).

Stull, V.R. and Plass, G.N., "Emissivity of Dispersed Carbon Particles", *J. Opt. Soc. Amer.* 50, 121-129 (1960).

Takahashi, F. and Glassman, I., "Sooting Correlations for Premixed Flames", *Combustion Science and Technology* 37, 1 (1987).

Tanzawa, T., and Gardiner, W.C. Jr., "Reaction Mechanism of the Homogeneous Thermal Decomposition of Acetylene", *Journal of Physical Chemistry*, 84, 236-239 (1980).

Tompkins, E.E., and Long, R., "The Flux of Polycyclic Aromatic Hydrocarbons and of Insoluble Material in Premixed Acetylene-Oxygen Flames", *Twelfth Symposium (International) on Combustion*, p. 625 (1969).

van de Hulst, H.C., *Light Scattering by Small Particles*, Dover, New York (1957).

Vaughn, C.B., "Formation of Soot and Polycyclic Aromatic Hydrocarbons in a Jet/Stirred Reactor", Ph.D. Thesis, Department of Chemical Engineering, Massachusetts Institute of Technology, (1985).

Volponi, J.V., McLean, W.J., Fristrom,R.M. and Munir, Z.A., "Determination of H, OH, and O Species

Concentrations by Deuterium Scavenging in Low Pressure Acetylene-Oxygen-Argon Flames", *Combustion and Flame* 65, 243-248 (1986).

Wagner, H.Gg., "Soot Formation - An Overview", in *Particulate Carbon Formation During Combustion*, D.C. Siegla and G.W. Smith, Eds., Plenum Press, New York (1981).

Wagner, H.Gg., "Mass Growth of Soot", p. 171-195 in *Soot in Combustion Systems and its Toxic Properties*, J. Lahaye and G. Prado, Eds., Plenum Press, New York (1983).

Wagner, H.Gg., "Soot Formation in Combustion", *Seventeenth Symposium (International) on Combustion*, p. 3-19 (1979).

Wall, J.C. and Hoekman, S.K., "Fuel Composition Effects on Heavy-Duty Diesel Particulate Emission", SAE Technical Paper Series 841364, presented at Fuel and Lubricant Meeting and Exposition, Baltimore, MD, 8-11 October 1984.

Warnatz, J., "Rate Coefficients in the C/H/O System", Chapter 5 in *Combustion Chemistry*, W.C. Gardiner, Ed., Springer-Verlag, New York (1984).

Weiner, A.M. and Harris, S.J., "Optical Detection of Large Soot Precursors", *Combustion and Flame*, submitted (1988).

Wicke, B.G., Wong, C., and Grady, K.A., "Room Temperature Oxidation of Soot by Oxygen Atoms", *Combustion and Flame* 66, 37-46 (1986).

Wicke, B. G., and Grady, K.A., "Oxidation of Soot by Oxygen Atoms at Temperatures between 525 K and 873 K", Poster P-32, Twenty-Second Symposium (International) on Combustion, (1988).

Wieschnowsky, U., Bockhorn, H, and Fetting, F., "Some New Observations Concerning the Mass Growth of Soot in Premixed Hydrocarbon-Oxygen Flames", *Twenty-Second Symposium (International) on Combustion*, in press (1989).

Wright, F.J., "The Oxidation of Soot by O Atoms", *Fifteenth Symposium (International) on Combustion*, p. 1449-1460 (1975).

Wu, S.C., Jelski, D.A., and George, T.F., "Vibrational Motions of Buckminsterfullerene", *Chem. Phys. Letters*, 137(3), 291-294 (1987).